NUREG/CR-6854

Fracture Analysis of Vessels – Oak Ridge FAVOR, v04.1, Computer Code: Theory and Implementation of Algorithms, Methods, and Correlations

U.S. Nuclear Regulatory Commission
Office of Nuclear Regulatory Research
Washington, DC 20555-0001

AVAILABILITY OF REFERENCE MATERIALS IN NRC PUBLICATIONS

NRC Reference Material

As of November 1999, you may electronically access NUREG-series publications and other NRC records at NRC's Public Electronic Reading Room at http://www.nrc.gov/reading-rm.html.
Publicly released records include, to name a few, NUREG-series publications; *Federal Register* notices; applicant, licensee, and vendor documents and correspondence; NRC correspondence and internal memoranda; bulletins and information notices; inspection and investigative reports; licensee event reports; and Commission papers and their attachments.

NRC publications in the NUREG series, NRC regulations, and *Title 10, Energy*, in the Code of *Federal Regulations* may also be purchased from one of these two sources:

1. The Superintendent of Documents
   U.S. Government Printing Office
   Mail Stop SSOP
   Washington, DC 20402–0001
   Internet: bookstore.gpo.gov
   Telephone: 202-512-1800
   Fax: 202-512-2250
2. The National Technical Information Service
   Springfield, VA 22161–0002
   www.ntis.gov
   1–800–553–6847 or, locally, 703–605–6000

A single copy of each NRC draft report for comment is available free, to the extent of supply, upon written request as follows:
Address: Office of the Chief Information Officer,
Reproduction and Distribution
Services Section
U.S. Nuclear Regulatory Commission
Washington, DC 20555-0001
E-mail: DISTRIBUTION@nrc.gov
Facsimile: 301–415–2289

Some publications in the NUREG series that are posted at NRC's Web site address http://www.nrc.gov/reading-rm/doc-collections/nuregs are updated periodically and may differ from the last printed version. Although references to material found on a Web site bear the date the material was accessed, the material available on the date cited may subsequently be removed from the site.

Non-NRC Reference Material

Documents available from public and special technical libraries include all open literature items, such as books, journal articles, and transactions, *Federal Register* notices, Federal and State legislation, and congressional reports. Such documents as theses, dissertations, foreign reports and translations, and non-NRC conference proceedings may be purchased from their sponsoring organization.

Copies of industry codes and standards used in a substantive manner in the NRC regulatory process are maintained at—
The NRC Technical Library
Two White Flint North
11545 Rockville Pike
Rockville, MD 20852–2738

These standards are available in the library for reference use by the public. Codes and standards are usually copyrighted and may be purchased from the originating organization or, if they are American National Standards, from—
American National Standards Institute
11 West 42nd Street
New York, NY 10036–8002
www.ansi.org
212–642–4900

Legally binding regulatory requirements are stated only in laws; NRC regulations; licenses, including technical specifications; or orders, not in NUREG-series publications. The views expressed in contractor-prepared publications in this series are not necessarily those of the NRC.

The NUREG series comprises (1) technical and administrative reports and books prepared by the staff (NUREG–XXXX) or agency contractors (NUREG/CR–XXXX), (2) proceedings of conferences (NUREG/CP–XXXX), (3) reports resulting from international agreements (NUREG/IA–XXXX), (4) brochures (NUREG/BR–XXXX), and (5) compilations of legal decisions and orders of the Commission and Atomic and Safety Licensing Boards and of Directors' decisions under Section 2.206 of NRC's regulations (NUREG–0750).

NUREG/CR-6854
ORNL/TM-2004/244

Fracture Analysis of Vessels – Oak Ridge FAVOR, v04.1, Computer Code: Theory and Implementation of Algorithms, Methods, and Correlations

Manuscript Completed: September 2004
Date Published: ???? 2006

Prepared by

P. T. Williams, T. L. Dickson, and S. Yin

Oak Ridge National Laboratory
Managed by UT-Battelle, LLC
Oak Ridge National Laboratory
Oak Ridge, TN 37831-8063

Prepared for
Division of Fuel, Engineering, and Radiological Research
Office of Nuclear Regulatory Research
U.S. Nuclear Regulatory Commission
Washington, DC 20555-0001
NRC Job Code Y6533

Abstract

The current regulations to insure that nuclear reactor pressure vessels (RPVs) maintain their structural integrity when subjected to transients such as pressurized thermal shock (PTS) events were derived from computational models developed in the early-to-mid 1980s. Since that time, advancements and refinements in relevant technologies that impact RPV integrity assessment have led to an effort by the NRC to re-evaluate its PTS regulations. Updated computational methodologies have been developed through interactions between experts in the relevant disciplines of thermal hydraulics, probabilistic risk assessment, materials embrittlement, fracture mechanics, and inspection (flaw characterization). Contributors to the development of these methodologies include the NRC staff, their contractors, and representatives from the nuclear industry. These updated methodologies have been integrated into the **F**racture **A**nalysis of **V**essels – **O**ak **R**idge (FAVOR, v04.1) computer code developed for the NRC by the Heavy Section Steel Technology (HSST) program at Oak Ridge National Laboratory (ORNL). The FAVOR, v04.1, code represents the baseline NRC-selected applications tool for re-assessing the current PTS regulations. Intended to document the technical bases for the assumptions, algorithms, methods, and correlations employed in the development of the FAVOR, v04.1, code, this report is one of a series of software quality assurance documentation deliverables being prepared according to the guidance provided in IEEE Std. 730.1-1995, *IEEE Guide for Software Quality Assurance Planning.* Additional documents in this series include (1) *FAVOR, v01.1, Computer Code: Software Requirements Specification,* (2) *FAVOR, v01.1, Computer Code: Software Design Description*, and (3) *FAVOR, v04.1, Computer Code: User's Guide.*

Foreword

The reactor pressure vessel is exposed to neutron radiation during normal operation. Over time, the vessel steel becomes progressively more brittle in the region adjacent to the core. If a vessel had a preexisting flaw of critical size and certain severe system transients occurred, this flaw could propagate rapidly through the vessel, resulting in a through-wall crack. The severe transients of concern, known as pressurized thermal shock (PTS), are characterized by rapid cooling (i.e., thermal shock) of the internal reactor pressure vessel surface that may be combined with repressurization. The simultaneous occurrence of critical-size flaws, embrittled vessel, and a severe PTS transient is a very low probability event. The current study shows that U.S. pressurized-water reactors do not approach the levels of embrittlement to make them susceptible to PTS failure, even during extended operation well beyond the original 40-year design life.

Advancements in our understanding and knowledge of materials behavior, our ability to realistically model plant systems and operational characteristics, and our ability to better evaluate PTS transients to estimate loads on vessel walls have shown that earlier analyses, performed some 20 years ago as part of the development of the PTS rule, were overly conservative, based on the tools available at the time. Consistent with the NRC's Strategic Plan to use best-estimate analyses combined with uncertainty assessments to resolve safety-related issues, the NRC's Office of Nuclear Regulatory Research undertook a project in 1999 to develop a technical basis to support a risk-informed revision of the existing PTS Rule, set forth in Title 10, Section 50.61, of the Code of Federal Regulations (10 CFR 50.61).

Two central features of the current research approach were a focus on the use of realistic input values and models and an explicit treatment of uncertainties (using currently available uncertainty analysis tools and techniques). This approach improved significantly upon that employed in the past to establish the existing 10 CFR 50.61 embrittlement limits. The previous approach included unquantified conservatisms in many aspects of the analysis, and uncertainties were treated implicitly by incorporating them into the models.

This report is one of a series of 21 reports that provide the technical basis that the staff will consider in a potential revision of 10 CFR 50.61. The risk from PTS was determined from the integrated results of the Fifth Version of the Reactor Excursion Leak Analysis Program (RELAP5) thermal-hydraulic analyses, fracture mechanics analyses, and probabilistic risk assessment. This report is the theory manual for the probabilistic fracture mechanics code Fracture Analysis of Vessels, Oak Ridge (FAVOR). The FAVOR code is used to assess structural integrity of pressurized-water reactor pressure vessels during postulated pressurized thermal shock transients.

Brian W. Sheron, Director
Office of Nuclear Regulatory Research
U.S. Nuclear Regulatory Commission

Contents

Page

Abstract iii

Foreword v

Contents vii

List of Tables ix

List of Figures x

Executive Summary xiii

Abbreviations xv

Acknowledgments xvii

1 . Introduction 1

2 . Pressurized Thermal Shock Events 5

2.1 Historical Review 5
2.2 Current NRC Regulatory Approach to PTS 6
2.3 Contributions of Large-Scale Experiments to the Technical Basis for PTS Assessment 7

3 . Structure and Organization of the FAVOR Code 10

3.1 FAVOR – Computational Modules and Data Streams 10
3.2 FAVOR Load Module (FAVLoad) 11
3.2.1 Thermal-Hydraulic Transient Definitions 11
3.2.2 Required Vessel Geometry and Thermo-Elastic Property Data 12
3.2.3 Deterministic Analyses 12
3.2.4 Flaw Categories Used in FAVOR 13
3.3 FAVOR PFM Module (FAVPFM) 14
3.3.1 FAVPFM Flowchart 16
3.3.2 Beltline Configurations and Region Discretization 18
3.3.3 Treatment of the Fusion-Line Along Welds 20
3.3.4 Warm Prestressing 22
3.3.5 Probability Distributions 25
3.3.6 Truncation Protocol 30
3.3.7 Conditional Probability of Initiation (*CPI*) 30
3.3.8 Post-Initiation Flaw Geometries and Orientations 35
3.3.9 Conditional Probability of Failure (*CPF*) by Through-Wall Cracking 37
3.3.10 Multiple Flaws 38
3.3.11 Ductile-Tearing Models in FAVOR 38
3.3.11.1 Ductile-Tearing Model No. 1 (implemented in FAVOR, v04.1) 43
3.3.11.2 Ductile-Tearing Model No. 2 (implemented in FAVOR, v03.1) 45
3.3.12 Initiation-Growth-Arrest (*IGA*) Submodel 50
3.3.13 Ductile-Tearing Submodel 61

3.3.14 Ductile Tearing as an Initiating Event 64
3.4 FAVOR Post Module – FAVPost 65

4 . Probabilistic Fracture Mechanics 67

4.1 Deterministic Analyses 67
4.1.1 Thermal Analysis 68
4.1.2 Stress Analysis 71
4.1.3 Linear-Elastic Fracture Mechanics (LEFM) 74
4.1.3.1 Mode I Stress-Intensity Factors 74
4.1.3.2 Inner Surface-Breaking Flaw Models –Semi-Elliptic and Infinite Length 74
4.1.3.3 Embedded Flaw Model 81
4.1.3.4 Inclusion of Residual Stresses in Welds 84
4.1.3.5 Inclusion of Crack-Face Pressure Loading for Surface-Breaking Flaws ... 86
4.2 Sampled LEFM Material and Correlative Properties 87
4.2.1 Reference Nil-Ductility Transition Temperature, RT_{PTS}, at EOL Fluence 87
4.2.2 Radiation Embrittlement 88
4.2.3 Fast-Neutron Fluence Attenuation and Sampling Distribution 92
4.2.4 ORNL 99/27 K_{Ic} and K_{Ia} Databases 92
4.2.5 Index Temperature RT_{NDT} – Uncertainty Classification and Quantification 98
4.2.6 Index Temperature RT_{Arrest} – Uncertainty Classification and Quantification 103
4.2.7 Plane-Strain Static Cleavage Initiation Toughness – K_{Ic} 107
4.2.8 Plane-Strain Crack Arrest Toughness – K_{Ia} 109
4.2.9 Material Chemistry –Sampling Protocols 112
4.3 NRC RVID2 Database 117
4.4 Discrete Flaw Density and Size Distributions 117
4.5 Summary of Sampling Distributions and Protocols 121

5 . Summary and Conclusions 128

References 129

Appendix A – Background and Antecedents of FAVOR, v04.1 138

Appendix B – Stress-Intensity Factor Influence Coefficients 143

Appendix C – Listings of K_{Ic} And K_{Ia} Extended Databases 157

Appendix D – Summary of RVID2 Data for Use in FAVOR Calculations 169

Appendix E – Statistical Point-Estimation Techniques for Weibull Distributions 171

Appendix F – Development of Stochastic Models for $\Delta RT_{epistemic}$ and ΔRT_{arrest} 174

List of Tables

Table **Page**

1. Large-Scale PTS Experiments and Performing Organizations 9
2. Illustration of Computational Procedure to Determine *CPI* and *CPF* for a Postulated Flaw (Warm Prestress Not Included).....33
3. Applied Flaw Orientations by Major Region.....35
4. Sources for Ductile-Tearing Data 39
5. Chemical Composition of Materials Used in the Ductile-Tearing Model Development 39
6. Summary of Ductile-Tearing Data Used in the Ductile-Tearing Model Development 39
7. Summary of ORNL 99/27 K_{Ic} Extended Database.....96
8. Summary of K_{Ia} Extended Database.....96
9. Chemistry and Heat Treatment of Principal Materials: ORNL 99/27 Database 97
10. Materials Used from the ORNL 99/27 K_{Ic} Extended Database 100
11. Values of Lower-Bounding Reference Temperature 101
12. ORNL 99/27 K_{Ia} Database – Reference-Transition Temperatures 105
B1. Influence Coefficients for Inside Axial and Circumferential Semi-elliptical Surface Flaws: R / t = 10 and a / t = 0.01 144
B2. Influence Coefficients for Inside Axial and Circumferential Semi-elliptical Surface Flaws: R / t = 10 and a / t = 0.0184 145
B3. Influence Coefficients for Inside Axial and Circumferential Semi-elliptical Surface Flaws: R / t = 10 and a / t = 0.05 146
B4. Influence Coefficients for Inside Axial and Circumferential Semi-elliptical Surface Flaws: R / t = 10 and a / t = 0.075 147
B5. Influence Coefficients for Inside Axial and Circumferential Semi-elliptical Surface Flaws: R / t = 10 and a / t = 0.1 148
B6. Influence Coefficients for Inside Axial and Circumferential Semi-elliptical Surface Flaws: R / t = 10 and a / t = 0.2 149
B7. Influence Coefficients for Inside Axial and Circumferential Semi-elliptical Surface Flaws: R / t = 10 and a / t = 0.3 150
B8. Influence Coefficients for Inside Axial Semi-elliptical Surface Flaws: R / t = 10 and a / t = 0.5 151
B9. Influence Coefficients for Inside Circumferential Semi-elliptical Surface Flaws: R / t = 10 and a / t = 0.5.....152
B10. Influence Coefficients for Inside Axial Infinite-Length Surface Flaws, R / t = 10 153
B11. Influence Coefficients for Inside Circumferential 360 Degree Surface Flaws, R / t = 10155
C1. Static Initiation Toughness K_{Ic} Extended Database.....158
C2. Crack Arrest Toughness K_{Ia} ORNL 99/27 Database.....164
C3. Crack Arrest Toughness K_{Ia} Extended K_{Ia} Database – Large Specimen Data.....167
F1. $\Delta RT_{epistemic}$ Ranked Data with Order-Statistic Estimates of P.....175
F2. ODRPACK Results of ODR Analysis of $\Delta RT_{epistemic}$ Model Equation 179
F2. ODRPACK Results of ODR Analysis of $\Delta RT_{epistemic}$ Model Equation (continued).....180
F3. Data Used in the Development of the ΔRT_{arrest} Model 185
F4. ODRPACK Results of ODR Analysis of ΔRT_{arrest} Model Equation 186
F4. ODRPACK Results of ODR Analysis of ΔRT_{arrest} Model Equation (continued).....187
F4. ODRPACK Results of ODR Analysis of ΔRT_{arrest} Model Equation (continued).....188

List of Figures

Figure **Page**

1. The beltline region of the reactor pressure vessel wall extends from approximately one foot above the active reactor core to one foot below the core 2

2. FAVOR data streams flow through three modules: (1) FAVLoad, (2) FAVPFM, and (3) FAVPost. 10

3. The FAVOR load generator module FAVLoad performs deterministic analyses for a range of thermal-hydraulic transients.....11

4. Flaw models in FAVOR include infinite-length surface breaking flaws, finite-length semi-elliptic surface flaws (with aspect ratios L / a = 2, 6, and 10), and fully elliptic embedded flaws. All flaw models can be oriented in either the axial or circumferential directions..13

5. The FAVPFM module takes output from FAVLoad and user-supplied data on flaw distributions and embrittlement of the RPV beltline and generates PFMI and PFMF arrays.....15

6. Flow chart for improved PFM model implemented in FAVPFM showing the four primary nested loops – (1) *RPV Trial Loop*, (2) *Flaw Loop*, (3) *Transient Loop*, and (4) *Time Loop* 17

7. Fabrication configurations of PWR beltline shells (adapted from [3]): (a) rolled-plate construction with axial and circumferential welds and (b) ring-forging construction with circumferential welds only.....19

8. FAVOR uses a discretization of the RPV beltline region to resolve the variation in radiation damage in terms of plate, axial weld, and circumferential weld major regions which are further discretized into multiple subregions. 21

9. Example of warm prestressing: (a) loading history with pressure applied to the inner surface and the temperature at the crack tip, (b) load path for a flaw showing two WPS regions. (*cpi* is the instantaneous conditional probability of initiation). 24

10. Example probability density functions for (a) normal and logistic and (b) uniform, Weibull, and lognormal continuous distributions. 29

11. Interaction of the applied K_I time history and the Weibull K_{Ic} statistical model for an example flaw. 32

12. The parameter $cpi(\tau)_{(i,j,k)}$ is the instantaneous conditional probability of initiation (*cleavage fracture*) obtained from the Weibull K_{Ic} cumulative distribution function. $CPI_{(i,j,k)}$ is the maximum value of $cpi(\tau)_{(i,j,k)}$. (Note: i = transient index, j = RPV trial index, and k = flaw index) 34

13. $\Delta cpi(\tau^n)_{(i,j,k)}$ is the increase in $cpi(\tau^n)_{(i,j,k)}$ that occurs during each discrete time step. When the maximum value of $cpi(\tau^n)_{(i,j,k)}$ is reached, negative values of $\Delta cpi(\tau^n)_{(i,j,k)}$ are set to zero. (Note: i = transient index, j = RPV trial index, and k = flaw index) 34

14. At the time of initiation, the three categories of flaws are transformed into infinite-length flaws: (a) Category 1 semi-elliptic surface breaking circumferential flaws become 360 degree circumferential flaws, (b) and (c) Category 2 and 3 embedded flaws become inifinite-length axial or 360 degree circumferential flaws at the same depth. Category 1 flaws are only oriented in the circumferential direction.....36

15. Given a J_R curve in power-law model form and current flow stress, σ_f, the initiation toughness, J_{Ic} , and local tearing modulus, T_R, are uniquely defined). 42

16. Flowchart for PFM model – the Initiation-Growth-Arrest (*IGA*) submodel can be viewed as a Monte Carlo model nested within the larger PFM Monte Carlo model. For a

given flaw, the *IGA* submodel is called after the *CPI* for the current transient has been calculated. Note: ++ notation indicates increment index by 1, e.g., *i*++ means *i*=*i*+1.....51
17. (a) Flow chart for Initiation-Growth-Arrest Model – The *IGA Propagation* submodel is only called for flaws with increasing *CPIs*. The weld-layering scheme is also shown for *Initiation-Growth-Arrest* Model. No through-wall resampling is carried out for plates or forgings.....52
17 (continued) (b) *IGA Propagation* submodel to test for Stable Arrest (no failure) and Vessel Failure.....53
17 (continued) (c) *Unstable-Ductile-Tearing* submodel to test for either stable tearing to a new flaw position, *a, or unstable ductile tearing that fails the vessel. 54**
18. An example Category 2 flaw (a) initiates, (b) expands into an infinite-length flaw, (c) advances to new weld layer and resamples chemistry content to calculate new RT_{NDT}, (d) continues growth until either failure by net-section plastic collapse of remaining ligament or stable crack arrest. The potential for arrest and subsequent re-initiation is also modeled.....55
19. *IGA* mesh used to estimate $dJ_{applied}$ / d*a* using second order central finite-difference ratio.64
20. The FAVOR post-processor FAVPost combines the distributions of conditional probabilities of initiation and failure calculated by FAVPFM with initiating frequency distributions for all of the transients under study to create distributions of frequencies of RPV fracture and failure.....66
21. Isoparametric mapping from parameter space to axisymmetric $\square^1$ Euclidean space using 3-node quadratic basis functions. 69
22. One-dimensional axisymmetric finite-element model used in FAVOR to calculate both temperature and stress histories through the wall of an RPV. 70
23. Influence coefficients, *K, have been calculated for finite semi-elliptical flaws with aspect ratios *L* / *a* = 2, 6, and 10 for R_i / *t* = 10.....77**
24. Crack-surface loading cases for determining finite 3D flaw influence coefficients: (a) uniform unit load, (b) linear load, (c) quadratic load, and (d) cubic load.....77
25. Influence coefficients have been computed for both infinite axial and 360 degree circumferential flaws. 79
26. Superposition allows the use of an equivalent problem to compute the stress intensity factor.....80
27. Influence coefficients, *K, represent stress intensity factor per unit load applied to the crack face. 80**
28. Geometry and nomenclature used in embedded flaw model.....82
29. Resolution of computed nonlinear stress profile into the linear superposition of effective membrane and bending stresses. 82
30. Weld residual stress through-thickness distribution developed for use in RPV integrity analyses.....85
31. Relationship between the change in the fracture-toughness index temperature ($\Delta T_0 \approx \Delta RT_{NDT}$) change in the 30 ft-lbf CVN transition temperature (ΔT_{30}) for welds and plates/forgings produced by irradiation. The difference in the best-fit slopes is statistically significant.....91
32. ORNL 99/27 K_{Ic} database including modified ASME K_{Ic} curve that served as a lower-bounding reference curve in the development of a new transition index temperature. ...94
33. K_{Ia} databases (a) ORNL 99/27 K_{Ia} database and (b) Extended K_{Ia} database.....95
34. Cumulative distribution function of the observed difference in RT_{NDT} $_0$ and T_o (with a size of 1T) using data in the ORNL 99/27 database. 99
35. Cumulative distribution function of the difference (designated as $\Delta RT_{epistemic}$) between RT_{NDT0} and a new lower-bounding reference index designated RT_{LB}. 99
36. The ΔRT_{LB} for HSST Plate 02. The lower-bounding transition reference temperature, RT_{LB}, was developed from 18 materials in the ORNL 99/27 database, where for each material $RT_{LB} = RT_{NDT0} - \Delta RT_{LB}$ 100

37. Comparison of cumulative distribution functions developed for RT_{NDT0}-T_0 and RT_{NDT0}-RT_{LB} 102
38. Lognormal distribution of $\Delta RT_{ARREST} = T_{K_{Ia}} - T_0$ as a function of T_0 105
39. Lognormal probability densities for ΔRT_{Arrest} as function of T_0. 105
40. Proposed adjustment to RT_{LB} arises from observed offset between ΔRT_{LB} CDF and $RT_{NDT} - T_0$ CDF at median (P = 0.5). 106
41. Weibull statistical distribution for plane-strain cleavage initiation fracture toughness, K_{Ic}, with prescribed validity bounds. The ORNL 99/27 K_{Ic} database was used in the construction of the model. 108
42. Lognormal statistical distribution for plane-strain crack arrest fracture toughness, K_{Ia}, constructed using the (a) Model 1: ORNL 99/27 K_{Ia} database normalized by the arrest reference temperature, RT_{Arrest} and (b) Model 2: Extended K_{Ia} database normalized by the arrest reference temperature, RT_{Arrest}. 110
43. Weld fusion area definitions for (a) axial-weld subregion elements and (b) circumferential subregion elements. 119
43. (continued) (c) Plate subregion element. 120
A1. Depiction of the development history of the FAVOR code 140
F1. Comparison of the initial Weibull model, W_0, for $\Delta RT_{epistemic}$ with the ODR model: (a) probability density functions and (b) cumulative distribution functions. 191
F2. Comparison of ODR Weibull model, W_{ODR}, for $\Delta RT_{epistemic}$ with the models for Case 1 (W_1) and Case 2 (W_2): (a) probability density functions and (b) cumulative distribution functions. 192
F3. Comparison of initial model in FAVOR, W_0, with Case 2, W_2. 193
F4. Comparison of ODR model, W_{ODR}, with Case 2, W_2. 194
F5. Data used to develop the lognormal statistical model for ΔRT_{arrest} as a function of T_0 .195
F6. Model developed from ODR analysis of log-transformed data. 196
F7. Variance of ODR model compared to final model. 197
F8. Comparison of ODR model with final model. 198

Executive Summary

This report is one of a series of reports that summarize the results of a 5-year project conducted by the U.S. Nuclear Regulatory Commission's (NRC) Office of Nuclear Regulatory Research. This study sought to develop a technical basis to support revision of Title 10, Section 50.61, of the Code of Federal Regulations (10 CFR 50.61), which is known as the pressurized thermal shock (PTS) rule and the associated PTS screening criteria in a manner consistent with current NRC guidelines on risk-informed regulation. The figure below illustrates how this report fits into the overall project documentation.

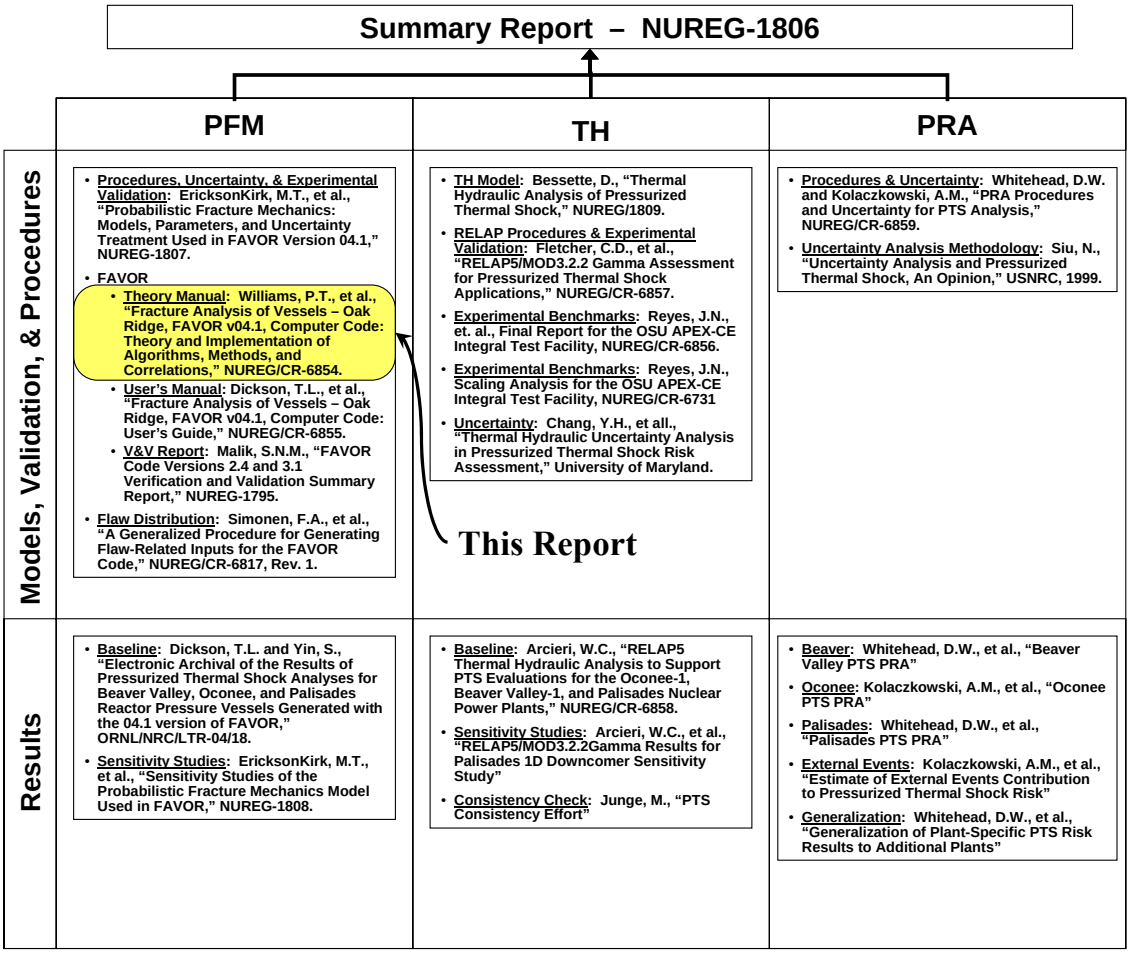

The **F**racture **A**nalysis of **V**essels – **O**ak **R**idge (**FAVOR**, v04.1) computer program has been developed to perform a risk-informed probabilistic analysis of the structural integrity of a nuclear reactor pressure vessel (RPV) when subjected to an overcooling event. The focus of this analysis is the beltline region of the RPV wall. Overcooling events, where the temperature of the coolant in contact with the inner surface of the RPV wall rapidly decreases with time, produce temporally dependent temperature gradients that induce biaxial stress states varying in magnitude through the vessel wall. Near the inner surface and through most of the wall thickness, the stresses are tensile, thus generating Mode I opening driving forces that can act on possible surface-breaking or

embedded flaws. If the internal pressure of the coolant is sufficiently high, then the combined thermal plus mechanical loading results in a transient condition known as a pressurized-thermal shock (PTS) event.

In 1999 ORNL, working in cooperation with the NRC staff and with other NRC contractors, illustrated that the application of fracture-related technology developed since the derivation of the current pressurized-thermal-shock (PTS) regulations (established in the early-mid 1980s) had the potential for providing a technical basis for a re-evaluation of the current PTS regulations. Motivated by these findings, the U.S. Nuclear Regulatory Commission (NRC) began the PTS Re-evaluation Project to establish a technical basis rule within the framework established by modern probabilistic risk assessment techniques and advances in the technologies associated with the physics of PTS events. An updated computational methodology has been developed through research and interactions among experts in the relevant disciplines of thermal-hydraulics, probabilistic risk assessment (PRA), materials embrittlement, probabilistic fracture mechanics (PFM), and inspection (flaw characterization). Major differences between this methodology and that used to establish the technical basis for the current version of the PTS rule include the following:

- The ability to incorporate new detailed flaw-characterization distributions from NRC research (with Pacific Northwest National Laboratory, PNNL),
- the ability to incorporate detailed neutron fluence regions – detailed fluence maps from Brookhaven National Laboratory, BNL,
- the ability to incorporate warm-prestressing effects into the analysis,
- the ability to include temperature-dependencies in the thermo-elastic properties of base and cladding,
- the ability to include crack-face pressure loading for surface-breaking flaws,
- a new ductile-fracture model simulating stable and unstable ductile tearing,
- a new embrittlement correlation,
- the ability to include multiple transients in one execution of FAVOR,
- input from the Reactor Vessel Integrity Database, Revision 2, (RVID2) of relevant RPV material properties,
- fracture-toughness models based on extended databases and improved statistical distributions,
- removal of the implicit conservatism in the RT_{NDT} transition temperature,
- a variable failure criterion, i.e., how far must a flaw propagate into the RPV wall for the vessel simulation to be considered as “failed” ?
- semi-elliptic surface-breaking and embedded-flaw models,
- through-wall weld residual stresses, and an
- improved PFM methodology that incorporates modern PRA procedures for the classification and propagation of input uncertainties and the characterization of output uncertainties as statistical distributions.

This updated methodology has been implemented in the Fracture Analysis of Vessels – Oak Ridge (FAVOR, v04.1) computer code developed for the NRC by the Heavy Section Steel Technology (HSST) program at Oak Ridge National Laboratory (ORNL). The FAVOR, v04.1, code represents the baseline NRC-selected applications tool for re-assessing the current PTS regulations. This report documents the technical bases for the assumptions, algorithms, methods, and correlations employed in the development of the FAVOR code.

Abbreviations

ASME	American Society of Mechanical Engineers
ASTM	American Society for Testing and Materials
BNL	Brookhaven National Laboratory
CCA	compact crack-arrest test specimen
C(T)	compact tension fracture-toughness test specimen
CDF	cumulative distribution function
CPI	conditional probability of initiation
CPF	conditional probability of failure (as indicated by through-wall cracking)
CRP	copper-rich precipitate
CVN	Charpy V-Notch test specimen
DTE	differential-thermal expansion
EFPY	effective full-power years
EPFM	elastic-plastic fracture mechanics
EPRI	Electric Power Research Institute
EOL	end-of-licensing
FAVOR	Fracture Analysis of Vessels – Oak Ridge
FEM	finite-element method
HAZ	heat-affected zone
HSST	Heavy Section Steel Technology Program
IPTS	Integrated Pressurized Thermal Shock Program
LEFM	linear-elastic fracture mechanics
LOCA	loss-of-coolant accident
NESC	Network for Evaluating Structural Components
NIST	National Institute for Standards and Technology
NRC	United States Nuclear Regulatory Commission
ORNL	Oak Ridge National Laboratory
PDF	probability density function
PFM	probabilistic fracture mechanics
PNNL	Pacific Northwest National Laboratory
PRA	Probabilistic Risk Assessment
PTS	pressurized thermal shock
PWHT	post-weld heat treatment
PWR	pressurized water reactor
RCW	recirculating cooling water
RG1.99	NRC Regulatory Guide 1.99, Revision 2, Ref. [12]
RG1.154	NRC Regulatory Guide 1.154, Ref. [11]
RPV	reactor pressure vessel
RVID	Reactor Vessel Integrity Database, Version 2, Ref. [129]
SIFIC	stress-intensity influence coefficients
SMD	stable matrix defect
10CFR50.61	Title 10 of the *Code of Federal Regulations*, Part 50, Section 50.61, Ref. [10]
TMI	Three-Mile-Island nuclear reactor
T-E	thermo-elastic

T-H	thermal-hydraulic
UMD	unstable matrix defect
WOL	wedge-open loading test specimen for fracture toughness
WPS	warm prestressing

Acknowledgments

The development of the new methodologies and models incorporated into FAVOR, v04.1, has been the result of a long and fruitful collaboration with many colleagues. The contributions of the NRC staff including Dr. L. Abramson, D. Bessette, Dr. N. Chokshi, Dr. E. Hackett, D. Jackson, W. Jones, D. Kalinousky, Dr. M. Kirk, Dr. S. Malik, M. Mayfield, T. Santos, Dr. N. Siu, and R. Woods are gratefully acknowledged. The new approaches to conditional probability of initiation and failure and the treatment of multiple flaws were developed in collaboration with Professors M. Modarres, A. Mosleh, and Dr. F. Li of the University of Maryland Center for Technology Risk Studies. The new flaw-characterization distributions were developed by D. Jackson of the NRC and Drs. F. Simonen, S. Doctor, and G. Schuster at Pacific Northwest National Laboratory, and the new detailed fluence maps were developed by W. Jones and T. Santos of the NRC and Dr. J. Carew of Brookhaven National Laboratory. Dr. K. Bowman of the Computer Science and Mathematics Division at Oak Ridge National Laboratory (ORNL) developed the statistical procedures that were applied in the development of the Weibull fracture-toughness model for FAVOR. Drs. M. Sokolov and S. K. Iskander of the Metals and Ceramics Division at ORNL carried out the survey of fracture-toughness data that produced the ORNL 99/27 extended fracture-toughness database. Dr. B. R. Bass, head of the Heavy Section Steel Technology Program at ORNL, provided the survey of fracture-arrest data from the Large-Specimen experiments carried out in the 1980s. Drs. E. Eason and J. Wright of Modeling and Computing Services, Boulder, Colorado and Prof. G. R. Odette of the University of California at Santa Barbara developed the new irradiation-shift model implemented in FAVOR, v04.1. In addition to developing the ductile-tearing model implemented in this version of FAVOR, Dr. M. Kirk of the NRC led a Working Group in the development of the new fracture-toughness models in FAVOR. Other members of this Working Group included, in addition to the authors, Dr. R. K. Nanstad and J. G. Merkle of the Metals and Ceramics Division at ORNL, Professor Modarres and Dr. F. Li of the University of Maryland Center for Technology Risk Studies, Dr. M. Natishan of PEAI, and Dr. B. R. Bass. J. G. Merkle with Dr. Nanstad developed the lower-bounding reference temperature approach that was adopted in the uncertainty analysis of the reference-nil-ductility transition temperature. Several conversations with Prof. R. Dodds of the University of Illinois, Prof. K. Wallin of VTT, Finland, and Dr. C. Faidy of Electricité de France were most helpful in the course of this effort. There were also contributions from many members of the nuclear industry.

1. Introduction

The **F**racture **A**nalysis of **V**essels – **O**ak **R**idge (FAVOR, v04.1) computer program has been developed to perform a risk-informed probabilistic analysis of the structural integrity of a nuclear reactor pressure vessel (RPV) when subjected to an overcooling event. The focus of this analysis is the *beltline* region of the RPV wall as shown in Fig. 1. *Overcooling events*, where the temperature of the coolant in contact with the inner surface of the RPV wall rapidly decreases with time, produce temporally dependent temperature gradients that induce biaxial stress states varying in magnitude through the vessel wall. Near the inner surface and through most of the wall thickness, the stresses are tensile, thus generating Mode I opening driving forces that can act on possible surface-breaking or embedded flaws. If the internal pressure of the coolant is sufficiently high, then the combined thermal plus mechanical loading results in a transient condition known as a pressurized-thermal shock (PTS) event.

In 1999, Dickson et al. [1] illustrated that the application of fracture-related technology developed since the derivation of the current pressurized-thermal-shock (PTS) regulations (established in the early-mid 1980s) had the potential for providing a technical basis for a re-evaluation of the current PTS regulations. Based on these results, the U.S. Nuclear Regulatory Commission (NRC) began the *PTS Re-evaluation Project* to establish a technical basis rule within the framework established by modern probabilistic risk assessment techniques and advances in the technologies associated with the physics of PTS events. An updated computational methodology has been developed over the last four years through research and interactions among experts in the relevant disciplines of thermal-hydraulics, probabilistic risk assessment (PRA), materials embrittlement, probabilistic fracture mechanics (PFM), and inspection (flaw characterization). This updated methodology has been implemented in the **F**racture **A**nalysis of **V**essels – **O**ak **R**idge (FAVOR, v04.1) computer code developed for the NRC by the Heavy Section Steel Technology (HSST) program at Oak Ridge National Laboratory (ORNL). The FAVOR, v04.1, code represents the baseline NRC-selected applications tool for re-assessing the current PTS regulations. This report is intended to document the technical bases for the assumptions, algorithms, methods, and correlations employed in the development of the FAVOR code.

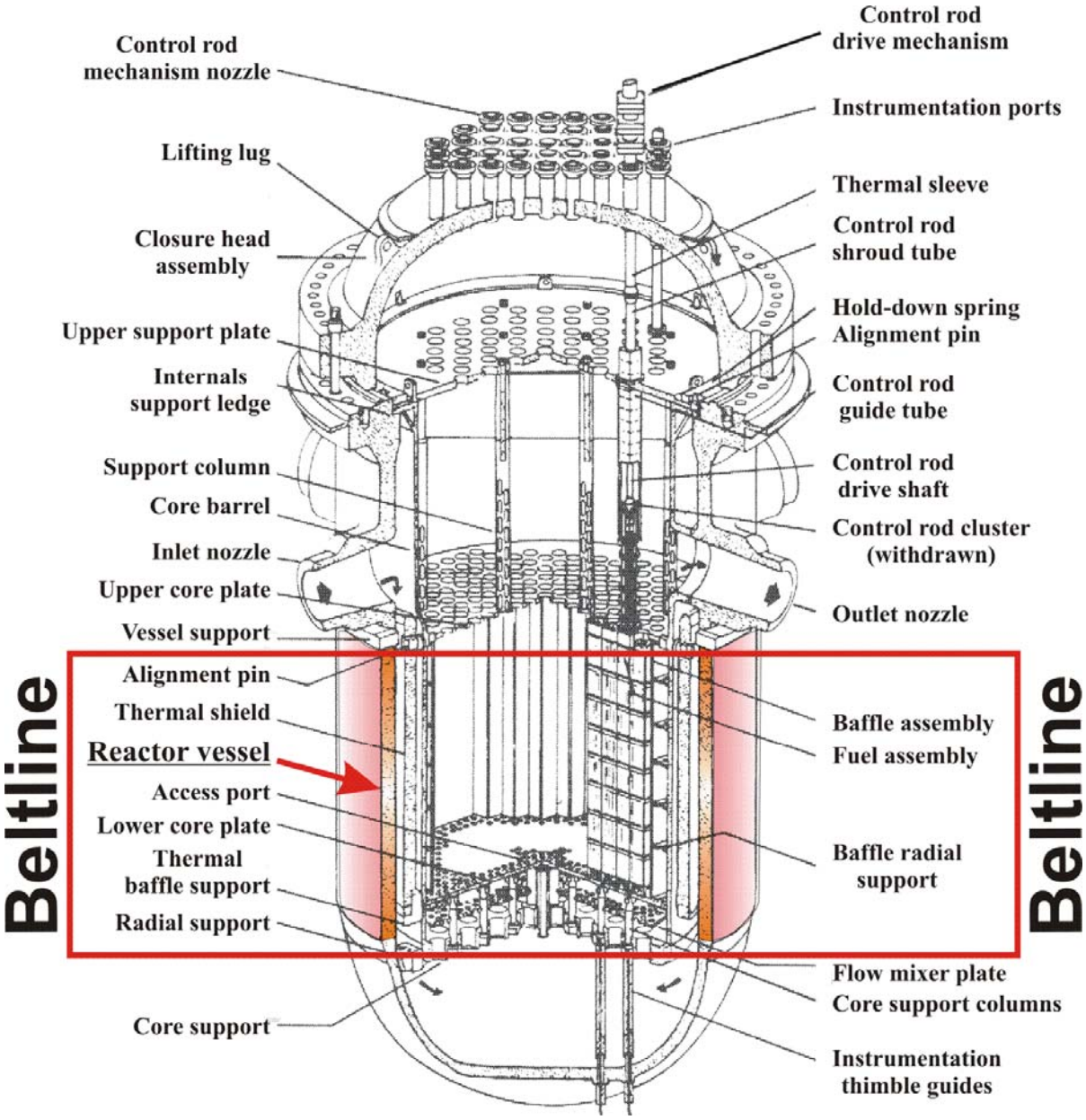

Fig. 1. The beltline region of the reactor pressure vessel wall extends from approximately one foot above the active reactor core to one foot below the core (adapted from [2]).

This baseline release of the new FAVOR (version-control code v04.1) implements the results of the preparatory phase of the PTS Re-evaluation Project in an improved PFM model for calculating the conditional probability of crack initiation (by plane-strain cleavage initiation) and the conditional probability of vessel failure (by through-wall cracking). Although the analysis of PTS has been the primary motivation in the development of FAVOR, it should also be noted that the problem class for which FAVOR is applicable encompasses a broad range of events that include normal operational transients (such as start-up and shut-down) as well as additional upset conditions beyond PTS. Essentially any event in which the reactor pressure vessel (RPV) wall is exposed to time-varying thermal-hydraulic boundary conditions could be an appropriate candidate for a FAVOR analysis of the vessel's structural integrity.

In support of the PTS Re-evaluation Project, the following advanced technologies and new capabilities have been incorporated into FAVOR, v04.1:

- **the ability to incorporate new detailed flaw-characterization distributions from NRC research (with Pacific Northwest National Laboratory, PNNL),**
- **the ability to incorporate detailed neutron fluence regions – detailed fluence maps from Brookhaven National Laboratory, BNL,**
- **the ability to incorporate warm-prestressing effects into the analysis,**
- **the ability to include temperature-dependencies in the thermo-elastic properties of base and cladding,**
- **the ability to include crack-face pressure loading for surface-breaking flaws,**
- **a new ductile-fracture model simulating stable and unstable ductile tearing,**
- **a new embrittlement correlation,**
- **the ability to include multiple transients in one execution of FAVOR,**
- **input from the Reactor Vessel Integrity Database, Revision 2, (RVID2) of relevant RPV material properties,**
- **fracture-toughness models based on extended databases and improved statistical distributions,**
- **a variable failure criterion, i.e., how far must a flaw propagate into the RPV wall for the vessel simulation to be considered as "failed" ?**
- **semi-elliptic surface-breaking and embedded-flaw models,**
- **through-wall weld residual stresses, and an**
- **improved PFM methodology that incorporates modern PRA procedures for the classification and propagation of input uncertainties and the characterization of output uncertainties as statistical distributions.**

Chapter 2 of this report provides a short historical perspective for viewing the pressurized-thermal-shock problem, including a summary of events leading to the current regulations. This chapter is followed by a full description of the analytical models employed in the FAVOR code, described in

Chapters 3 and 4. In that presentation, particular emphasis is given to the new features of the code that were highlighted above. A summary and conclusions are given in Chapter 5. Appendix A gives a summary of the development history of FAVOR and its antecedents. Appendix B presents the database of stress-intensity-factor influence coefficients that has been implemented in FAVOR for its surface-breaking flaw models. The database of plane-strain static initiation fracture toughness, K_{Ic}, and plane-strain crack arrest, K_{Ia}, properties for pressure vessel steels is given in Appendix C. This fracture-toughness database was used in the construction of the statistical models for crack initiation and arrest that are implemented in FAVOR. Appendix D presents a summary of RVID2 data to be used in FAVOR analyses for the PTS Re-evaluation Project. The point-estimation techniques used in the development of the Weibull cumulative distribution functions that estimate the epistemic uncertainty in the fracture initiation and arrest reference temperatures are given in Appendix E. The development of the sampling protocols for the epistemic uncertainties in two important reference temperatures is given in Appendix F.

2. Pressurized Thermal Shock Events

Overcooling events, where the temperature of the coolant in contact with the inner surface of the reactor pressure vessel (RPV) wall rapidly decreases with time, produce temporally dependent temperature gradients that induce biaxial stress states varying in magnitude through the vessel wall. Near the inner surface and through most of the wall thickness the stresses are tensile, thus presenting Mode I opening driving forces that can act on possible surface-breaking or embedded flaws. The combined thermal plus mechanical loading results in a transient condition known as a pressurized thermal shock (PTS) event.

Concern with PTS results from the combined effects of (1) simultaneous pressure and thermal-shock loadings, (2) embrittlement of the vessel material due to cumulative irradiation exposure over the operating history of the vessel, and (3) the possible existence of crack-like defects at the inner surface of or embedded within the RPV heavy-section wall. The decrease in vessel temperature associated with a thermal shock also reduces the fracture toughness of the vessel material and introduces the possibility of flaw propagation. Inner surface-breaking flaws and embedded flaws near the inner surface are particularly vulnerable, because at the inner surface the temperature is at its minimum and the stress and radiation-induced embrittlement are at their maximum.

2.1 Historical Review

The designers of the first pressurized-water reactor (PWR) vessels in the late 1950s and early 1960s were cognizant of PTS as a reactor vessel integrity issue where nonductile fracture was evaluated as a part of the design basis using a transition-temperature approach [3]. Continued concerns about vessel failure due to overcooling events motivated a number of advances in fracture mechanics technology in the late 1960s and the 1970s. Before the late 1970s, it was postulated that the most severe thermal shock challenging a PWR vessel would occur during a large-break loss-of-coolant accident (LOCA), where room-temperature emergency core-cooling water would flood the reactor vessel within a few minutes, rapidly cooling the wall and inducing tensile thermal stresses near the inner surface of the vessel [4]. However, the addition of pressure loading to the thermal loading was not typically considered, since it was expected that during a large-break LOCA the system would remain at low pressure. Two events in the late 1970s served to raise the concern of PTS to a higher priority in the 1980s, and this concern continues to the present.

In 1978, the occurrence of a non-LOCA event at the Rancho Seco Nuclear Power Plant in California showed that during some types of overcooling transients, the rapid cooldown could be accompanied by repressurization of the primary recirculating-cooling-water (RCW) system, compounding the effects of the thermal stresses. The Three-Mile-Island (TMI) incident in 1979, which also involved a cooldown event at high RCW system pressure, drew additional attention to the impact of operator action and control system effects on transient temperature and pressure characteristics for PTS events [3].

Following these two events, the U.S. Nuclear Regulatory Commission (NRC) designated PTS as an unresolved safety issue (A-49). Questions also arose concerning the mixing (or lack of mixing) of cold safety injection water with reactor coolant in the vessel, leading to an amplification of the PTS effect. In late 1980, the NRC issued NUREG 0737-Item II.K.2.13, which required that the operators of all PWRs and all applicants for licenses evaluate reactor vessel integrity following a small-break LOCA as part of the TMI action plan [5]. Additional potential transients were added in March of 1981. At the end of 1981, the nuclear power industry submitted its response to NUREG 0737 to the NRC. These submittals were based primarily on deterministic analyses using conservative thermal-hydraulic and fracture-mechanics models of postulated design-basis transients and the temperature and pressure time-histories from some of the PTS events that had actually been experienced in operating PWR plants [3]. On the basis of these analyses, the NRC concluded that no event having a significant probability of occurring could cause a PWR vessel to fail at that time or within the next few years. However, the NRC continued to be concerned that other events with more limiting transient characteristics in combination with the impact of operator action and control system effects were not being addressed. As a result, greater emphasis was placed on Probabilistic Risk Assessment (PRA) combined with thermal-hydraulic (T-H) analysis and probabilistic fracture mechanics (PFM) as primary vessel-integrity assessment tools.

2.2 Current NRC Regulatory Approach to PTS

During the 1980s, in an effort to establish generic limiting values of vessel embrittlement, the NRC funded the Integrated Pressurized Thermal Shock (IPTS) Program [4, 6, 7] which developed a comprehensive probabilistic approach to risk assessment. Current regulatory requirements are based on the resulting *risk-informed* probabilistic methodology. In the early 1980s, extensive analyses were performed by the NRC and others to estimate the likelihood of vessel failure due to PTS events in PWRs. Though a large number of parameters governing vessel failure were identified, the single most significant parameter was a correlative index of the material that also serves as a measure of embrittlement. This material index is the reference nil-ductility transition temperature, RT_{NDT}. The NRC staff and others performed analyses of PTS risks on a conservative and generic basis to bound

the risk of vessel failure for any PWR reactor. The NRC staff approach to the selection of the RT_{NDT} screening criteria is described in SECY-82-465 [8]. Reference [9] is a short review of the derivation of the PTS *screening criteria* from both deterministic and probabilistic fracture mechanics considerations. The analyses discussed in SECY-82-465 led to the establishment of the *PTS rule* [10], promulgated in Title 10 of the *Code of Federal Regulations*, Chapter I, Part 50, Section 50.61 (10CFR50.61), and the issuance of NRC Regulatory Guide 1.154 (RG1.154) [11].

The *PTS rule* specifies *screening criteria* in the form of limiting irradiated values of RT_{NDT} (designated by the rule as RT_{PTS}) of 270 °F for axially oriented welds, plates, and forgings and 300 °F for circumferentially oriented welds. The PTS rule also prescribes a method to estimate RT_{PTS} for materials in an RPV in Regulatory Guide 1.99, Revision 2 [12]. For nuclear power plants to operate beyond the time that they exceed the screening criteria, the licensees must submit a plant-specific safety analysis to the NRC three years before the screening limit is anticipated to be reached. Regulatory Guide 1.154 recommends the content and format for these plant-specific integrated PTS analyses with the objective of calculating an estimate for the frequency of vessel failure caused by PTS events. RG1.154 also presents the *primary PTS acceptance criterion* for acceptable failure risk to be a mean frequency of less than 5×10^{-6} vessel failures per year.

2.3 Contributions of Large-Scale Experiments to the Technical Basis for PTS Assessment

A number of large-scale experiments conducted internationally over the past 30 years have contributed significantly to a better understanding of the factors influencing the behavior of RPVs subjected to postulated PTS scenarios [13]. These experiments, several of which are summarized in Table 1, reflect different objectives that range from studies of "separate effects" to others that integrate several features into a single experiment. In Table 1, the experiments are organized in terms of four specimen groups: (1) pressure-vessel specimens, (2) cylindrical specimens, (3) plate specimens, and (4) beam specimens. The actual test specimens were fabricated from prototypical RPV steels, including plate, forgings, and weld product forms. Some of the specimens included prototypical cladding, and others used steels that had been heat-treated or were fabricated with a special chemistry to simulate near-end-of-licensing (degraded properties) conditions.

In recent years, these large-scale experiments have provided a catalyst in western Europe and the United States for intensive international collaboration and for the formation of multinational networks to assess and extend RPV/PTS technology. Project FALSIRE [14-17] was initiated in 1989 through support provided by governmental agencies within Germany and the U. S., under sponsorship of the OECD/Nuclear Energy Agency. Within FALSIRE, researchers from a large number of international organizations used selected large-scale experiments to evaluate levels of conservatism in RPV

integrity assessment methodologies. In 1993, the Joint Research Centre of the European Commission launched the Network for Evaluating Structural Components (NESC) to study the entire process of RPV integrity assessment. The NESC projects brought together a large number of leading international research organizations to evaluate all aspects of the assessment process (i.e., fracture methodologies, material properties characterization, inspection trials, and experimental techniques) through a large-scale PTS spinning cylinder experiment [18, 36]. Issues receiving special attention in the NESC experiment included (1) effects of constraint, (2) effects of cladding and HAZ regions, and (3) behavior of sub-clad flaws under simulated PTS loading.

The large-scale experimental database and extensive body of associated analytical interpretations have provided support for the technical basis that underpins various elements of the fracture models implemented in the FAVOR code. In particular, these results have contributed significantly to confirming the applicability of fracture methodologies to cleavage fracture events in RPV steels, including crack initiation and crack arrest. References [14-18, 36] (and references given therein) provide comprehensive evaluations of RPV integrity assessment methodologies applied to a broad selection of experiments.

Within the HSST Program, the large-scale experiments are contributing to a framework for future integration of advanced fracture techniques into RPV integrity assessment methodology. These advanced techniques provide a sharp contrast to the current approach to RPV integrity assessment as exemplified by the methodology implemented in the FAVOR code (described herein). The FAVOR code executes probabilistic defect assessments of RPVs using (1) linear-elastic stress analysis methods and (2) conventional, high-constraint fracture-toughness data. The advanced fracture-mechanics methodologies currently under development depart from the latter approach in three major components: (1) stress analyses of cracked regions to include plasticity, (2) constraint adjustments to material toughness values for shallow surface and embedded flaws, and (3) probabilistic descriptions of material fracture toughness in the transition temperature region consistent with the methodologies embodied by ASTM Standard E-1921 (i.e., the Master Curve). Development of an updated analytical tool incorporating these advanced techniques and providing extended applicability to RPV integrity assessments is envisioned for the near future.

Table 1. Large-Scale PTS Experiments and Performing Organizations

ID No.	Experiment Title	Research Organization	Country	Refs.
Tests with Pressurized Vessels				
ITV 1-8	Intermediate Test Vessels	Oak Ridge National Laboratory	USA	19-25
PTSE-1	Pressurized Thermal Shock Experiments	Oak Ridge National Laboratory	USA	26
PTSE-2	Pressurized Thermal Shock Experiments	Oak Ridge National Laboratory	USA	27
PTS I/6	Pressurized Thermal Shock Experiment I/6	Central Research Institute for Structural Materials (CRISM)	Russia	28, 29
Tests with Cylindrical Specimens				
NKS-3	Thermal Shock Experiment 3	Materialprüfungsanstalt (MPA)	Germany	30
NKS-4	Thermal Shock Experiment 4	Materialprüfungsanstalt (MPA)	Germany	30
NKS-5	Thermal Shock Experiment 5	Materialprüfungsanstalt (MPA)	Germany	31
NKS-6	Thermal Shock Experiment 6	Materialprüfungsanstalt (MPA)	Germany	29, 31
SC-1	Spinning Cylinder PTS Experiment 1	AEA Technology	UK	32
SC-2	Spinning Cylinder PTS Experiment 2	AEA Technology	UK	32
SC-4	Spinning Cylinder PTS Experiment 4	AEA Technology	UK	33
TSE-6	Thermal Shock Cylinders (Cylinder with Short Flaws)	Oak Ridge National Laboratory (ORNL)	USA	34
TSE-7	Thermal Shock Cylinders (Clad Cylinder)	Oak Ridge National Laboratory (ORNL)	USA	35
TSE-8	Thermal Shock Cylinders (Clad Cylinder)	Oak Ridge National Laboratory (ORNL)	USA	35
NESC-1	NESC-1 Spinning Cylinder PTS Experiment	Network for Evaluating Steel Components (NESC)	International Network	36
Tests with Plate Specimens				
PTS Step B	Wide-Plate PTS Step B Experiment	Japan Power and Engineering Inspection Corporation (JAPEIC)	Japan	37
WP-1 & 2	Wide-Plate Crack Arrest Tests of A533B and LUS Steels	Oak Ridge National Laboratory (ORNL)	USA	38, 39
GP-1	Wide Plate Test	Materialprüfungsanstalt (MPA)	Germany	40
Tests with Beam Specimens				
DD-2 & DSR-3	Clad-beam experiments	Electricité de France (EdF)	France	29, 41
SE(B) RPV Steel	Full-Thickness Clad Beam Experiments	National Institute of Standards and Testing (NIST) and ORNL	USA	42, 43
CB	Cruciform Beam (CB) Experiments	Oak Ridge National Laboratory (ORNL)	USA	44

3. Structure and Organization of the FAVOR Code

3.1 FAVOR – Computational Modules and Data Streams

As shown in Fig. 2, FAVOR is composed of three computational modules: (1) a deterministic load generator (**FAVLoad**), (2) a Monte Carlo PFM module (**FAVPFM**), and (3) a post-processor (**FAVPost**). Figure 2 also indicates the nature of the data streams that flow through these modules.

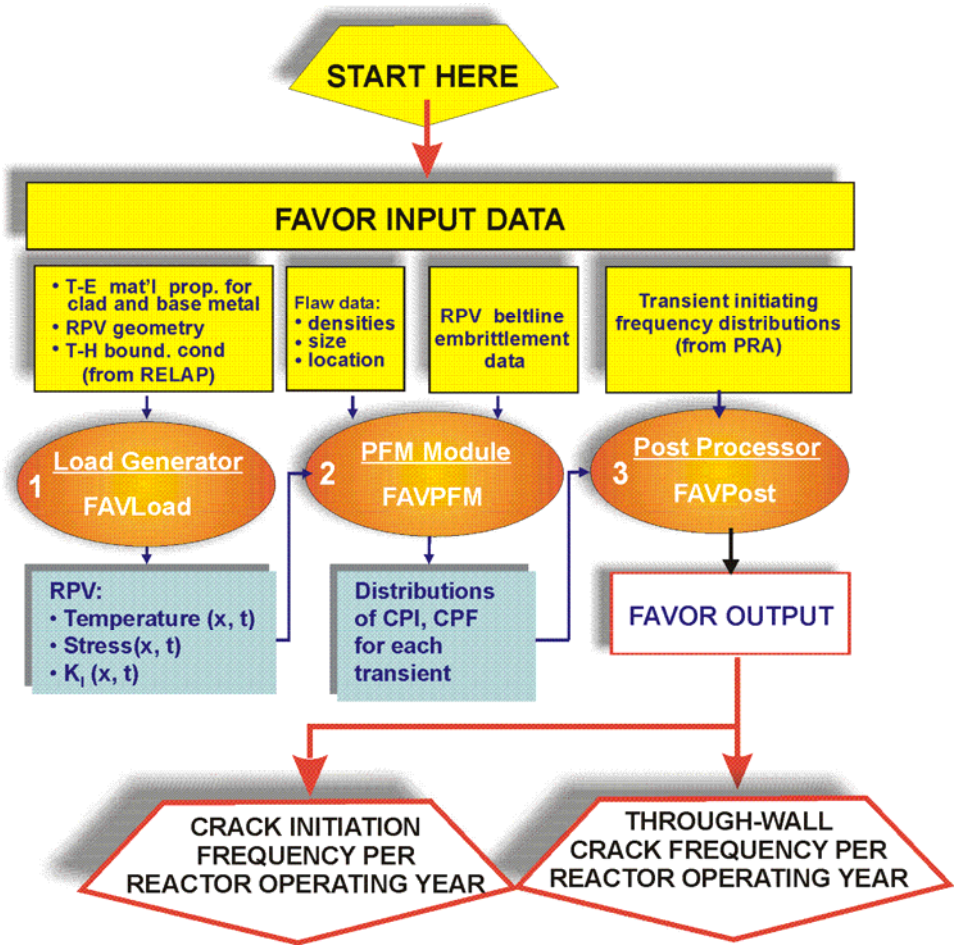

Fig. 2. FAVOR data streams flow through three modules: (1) FAVLoad, (2) FAVPFM, and (3) FAVPost.

The formats of the required user-input data files are discussed in detail in the companion report *FAVOR (v04.1): User's Guide* [45].

3.2 FAVOR Load Module (FAVLoad)

The functional structure of the FAVOR load module, FAVLoad, is shown in Fig. 3, where multiple thermal-hydraulic transients are defined in the input data. The number of transients that can be analyzed in a single execution of FAVLoad is dependent upon the memory capacity of the computer being used for the analysis. For each transient, deterministic calculations are performed to produce a load-definition input file for FAVPFM. These load-definition files include time-dependent through-wall temperature profiles, through-wall circumferential and axial stress profiles, and stress-intensity factors for a range of axially and circumferentially oriented inner surface-breaking flaw geometries (both infinite- and finite-length).

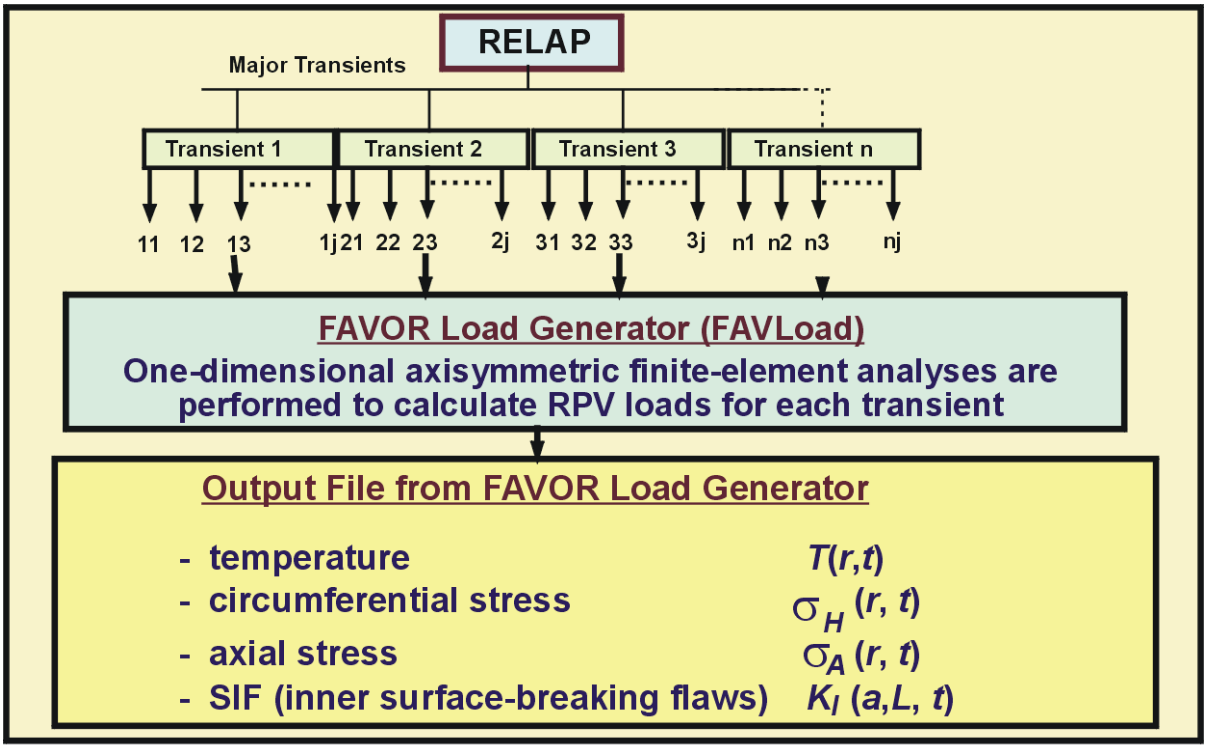

Fig. 3. The FAVOR load generator module FAVLoad performs deterministic analyses for a range of thermal-hydraulic transients.

3.2.1 Thermal-Hydraulic Transient Definitions

The thermal-hydraulic (T-H) definitions required by FAVLoad are supplied by the user in the form of digitized tables of bulk coolant temperature, convective heat-transfer coefficient, and internal pressure, all as functions of elapsed time for the transient. Time-history data pairs can be input for each of the three variables, allowing a very detailed definition of the thermal-hydraulic loading imposed on the RPV internal wall. An option is also available to specify a stylized exponentially decaying coolant temperature-time history.

3.2.2 Required Vessel Geometry and Thermo-Elastic Property Data

The FAVLoad module requires fundamental vessel geometry data, including the vessel's inner radius, wall thickness, and cladding thickness. Temperature-dependent thermo-elastic properties are also input for the cladding and base materials. These geometric descriptions and property data for the RPV are treated as fixed parameters in all subsequent analyses.

3.2.3 Deterministic Analyses

Finite-element analyses are carried out on a one-dimensional axisymmetric model of the vessel wall. The transient heat conduction equation with temperature-dependent properties is solved for the combined cladding and base materials to produce time-varying temperature profiles through the wall. The finite-element stress analysis calculates radial displacements and then, through strain-displacement and linear-elastic stress-strain relationships, time-varying axial and hoop stress profiles are also calculated. These stresses include the effects of thermal and mechanical loading (internal pressure applied to the inner vessel surface and exposed crack face) along with the option of superimposed weld-residual stress profiles developed by the HSST program. The stress discontinuity at the clad-base interface is also captured by the finite-element stress model. Through the specification of a selected stress-free temperature by the user, the effects of an initial thermal-differential expansion between the cladding and base materials can also be included in the quasi-static load path. The finite-element thermal and stress models use the same quadratic elements and graded-mesh discretization.

The finite-element method (FEM), together with the very detailed definition of the thermal-hydraulic boundary conditions, provides the capability to generate accurate thermal, stress, and applied stress-intensity factor, K_I, solutions. The application of FEM in this way allows the resolution of complex thermal-hydraulic transients that exhibit discontinuities in the boundary condition time-histories, e.g., transients with late repressurizations.

Time-dependent stress-intensity factors for infinite-length and finite-length (semi-elliptical) surface-breaking flaws are calculated for a range of flaw depths, sizes, and aspect ratios. Due to its generality, the embedded-flaw model was implemented in the FAVPFM module, rather than FAVLoad. The details of these deterministic analyses are given in Chapter 4. See Fig. 4 for a summary of the flaw models available in FAVOR.

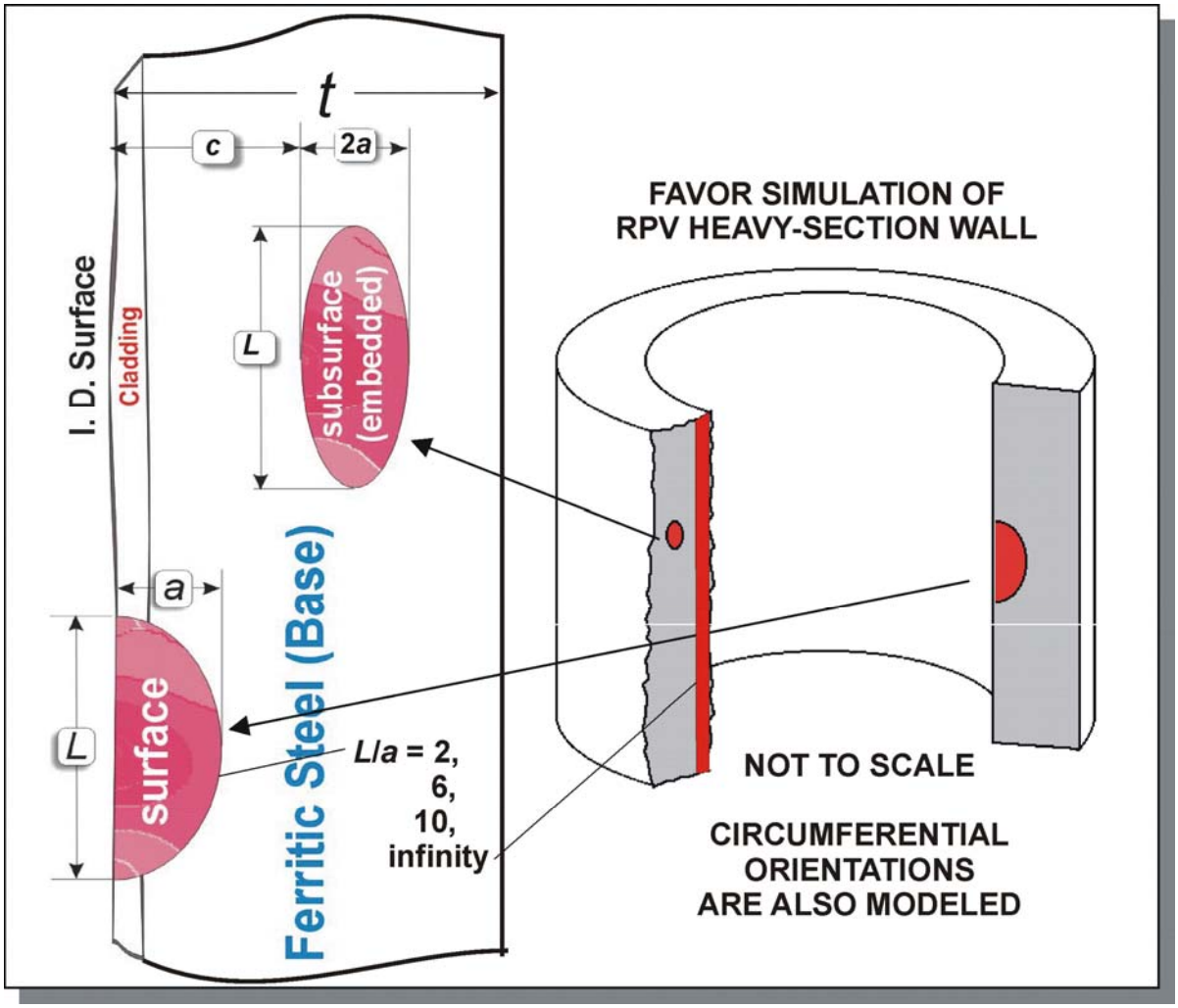

Fig. 4. Flaw models in FAVOR include infinite-length surface breaking flaws, finite-length semi-elliptic surface flaws (with aspect ratios *L* / *a* = 2, 6, and 10), and fully elliptic embedded flaws. All flaw models can be oriented in either the axial or circumferential directions.

3.2.4 Flaw Categories Used in FAVOR

As indicated in Fig. 4, three categories of flaws are available in FAVOR:

- **Category 1 – surface-breaking flaws**

  infinite length – aspect ratio $L/a = \infty$
  semi-elliptic – aspect ratio $L/a = 2$
  semi-elliptic – aspect ratio $L/a = 6$
  semi-elliptic – aspect ratio $L/a = 10$

- **Category 2 – embedded flaws – fully elliptic geometry with inner crack tip located between the clad/base interface and 1/8*t* from the inner surface (*t* = thickness of the RPV wall)**

- **Category 3 – embedded flaws – fully elliptic geometry with inner crack tip located between 1/8*t* and 3/8*t* from the inner surface**

3.3 FAVOR PFM Module (FAVPFM)

The FAVOR PFM model is based on the Monte Carlo technique, where deterministic fracture analyses are performed on a large number of stochastically generated RPV *trials* or *realizations*. Each vessel realization can be considered a perturbation of the *uncertain* condition of the specific RPV under analysis. The condition of the RPV is considered uncertain in the sense that a number of the vessel's properties along with the postulated flaw population have uncertainties associated with them. These input uncertainties are described by statistical distributions. The RPV trials propagate the input uncertainties with their interactions through the model, thereby determining the probabilities of crack initiation and through-wall cracking for a set of postulated PTS events at a selected time in the vessel's operating history. The improved PFM model also provides estimates of the uncertainties in its outputs in terms of discrete statistical distributions. By repeating the RPV trials a large number of times, the output values constitute a random sample from the probability distribution over the output induced by the combined probability distributions over the several input variables [46].

The assumed fracture mechanism is stress-controlled cleavage initiation (in the lower-transition-temperature region of the vessel material) modeled under the assumptions of linear-elastic fracture mechanics (LEFM). The failure mechanism by through-wall cracking is the prediction of sufficient flaw growth either (1) to produce a net-section plastic collapse of the remaining ligament or (2) to advance the crack tip through a user-specified fraction of the wall thickness. Flaw growth can be due to either cleavage propagation or stable ductile tearing. In addition, if the conditions for unstable ductile tearing are satisfied, then vessel failure by through-wall cracking is assumed to occur.

The Monte Carlo method involves sampling from appropriate probability distributions to simulate many possible combinations of flaw geometry and RPV material embrittlement subjected to transient loading conditions. The PFM analysis is performed for the beltline of the RPV, usually assumed to extend from one foot below the reactor core to one foot above the reactor core. The RPV beltline can be divided into *major regions* such as axial welds, circumferential welds, and plates or forgings that may have their own embrittlement-sensitive chemistries. The major regions may be further discretized into *subregions* to accommodate detailed neutron fluence maps that can include significant details regarding azimuthal and axial variations in neutron fluence. The general data streams that flow through the FAVPFM module are depicted in Fig. 5.

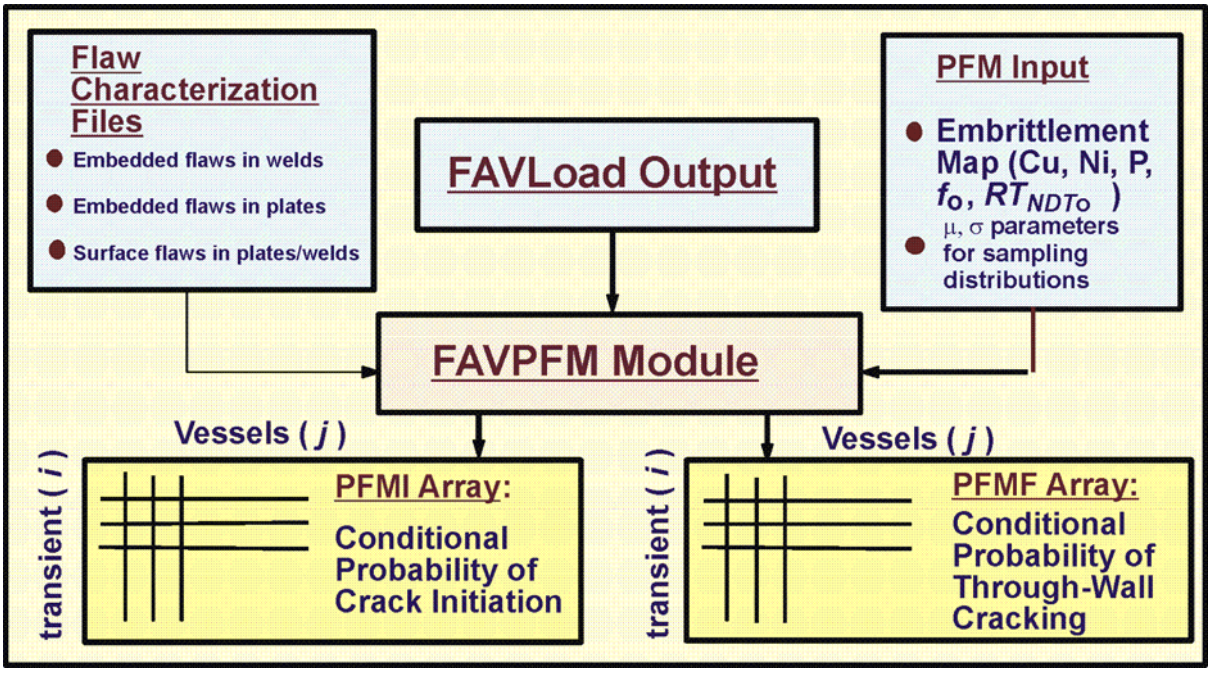

Fig. 5. The FAVPFM module takes output from FAVLoad and user-supplied data on flaw distributions and embrittlement of the RPV beltline and generates PFMI and PFMF arrays.

As shown in Fig. 5, the FAVPFM module requires, as input, load-definition data from FAVLoad and user-supplied data on flaw distributions and embrittlement of the RPV beltline. FAVPFM then generates two matrices: (1) the conditional probability of crack initiation (PFMI) matrix and (2) conditional probability of through-wall cracking (PFMF) matrix. The (i, j)th entry in each array contains the results of the PFM analysis for the jth vessel simulation subjected to the ith transient.

Current PTS regulations are based on analyses from PFM models that produced a Bernoulli sequence of boolean results for cleavage fracture initiation and RPV failure by through-wall cracking; i.e., the outcome for each RPV trial in the Monte Carlo analysis was either crack initiation or no crack initiation and either failure or no failure. The conditional probability of initiation, $P(I|E)$, was calculated simply by dividing the number of RPV trials predicted to experience cleavage fracture by the total number of trials. Similarly, the conditional probability of failure, $P(F|E)$, was calculated by dividing the number of RPV trials predicted to fail by the total number of trials. The final results were discrete values for $P(I|E)$ and $P(F|E)$, without any quantification of the uncertainty in the solution. The improved PFM model in the new FAVPFM (v04.1) module provides for the calculation of discrete probability *distributions* of RPV fracture and failure along with the estimation of uncertainties in the results. In this improved PFM model, values for the conditional probability of initiation ($0 \le CPI \le 1$) and conditional probability of failure ($0 \le CPF \le 1$) by through-wall cracking are calculated for each flaw subjected to each transient.

3.3.1 FAVPFM Flowchart

Figure 6 is a flowchart illustrating the essential elements of the nested-loop structure of the PFM Monte Carlo model – (1) *RPV Trial Loop*, (2) *Flaw Loop*, (3) *Transient Loop*, and (4) *Time-integration Loop*. The outermost *RPV Trial Loop* is indexed for each RPV trial included in the analysis, where the number of RPV trials is specified by the user in the FAVPFM input stream. Since each RPV trial can be postulated to contain multiple flaws, the next innermost loop (the *Flaw Loop*) is indexed for the number of flaws for this trial. Each postulated flaw is positioned (through sampling) in a particular RPV beltline subregion having its own distinguishing embrittlement-related parameters. Next, the flaw geometry (depth, length, aspect ratio, and location within the RPV wall) is determined by sampling from appropriate distributions derived from expert judgment [47] and non-destructive and destructive examinations [48-50] of RPV steels. Each of the embrittlement-related parameters [nickel (an alloying element), copper and phosphorus (contaminants), neutron fluence, and an estimate of the *epistemic* and *aleatory* uncertainties in the unirradiated RT_{NDT0}] are sampled from appropriate distributions.[1] The neutron fluence is attenuated to the crack-tip location, and a value for the irradiated reference index, RT_{NDT} (serving as a quantitative estimate of radiation damage), is calculated.

A deterministic fracture analysis is then performed on the current flaw for each of the postulated PTS transients; thus, the deterministic component of the analysis involves two inner nested loops – a *Transient Loop* and a *Time-integration Loop*. The temporal relationship between the applied Mode I stress intensity factor (K_I) and the static cleavage fracture initiation toughness (K_{Ic}) at the crack tip is calculated at discrete transient time steps. The fracture-toughness, K_{Ic}, statistical model is a function of the normalized temperature, $T(\tau) - RT_{NDT}$, where $T(\tau)$ is the time-dependent temperature at the crack tip. Analysis results are used to calculate the conditional probability of crack initiation (*CPI*)[2], i.e., the probability that pre-existing fabrication flaws will initiate in cleavage fracture. Also, the PFM model calculates the conditional probability of failure (*CPF*)[2] by through-wall cracking, i.e., the probability that an initiated flaw will propagate through the RPV wall. These probabilities are conditional in the sense that the transients are assumed to occur and that the postulated flaws do in fact exist. In the treatment of multiple flaws to be discussed in Sect. 3.3.10, the values of *CPI* and *CPF* calculated for individual flaws become the *statistically independent marginal* probabilities used in the construction of the joint conditional probabilities of initiation and failure.

---

[1] The details of the protocols and statistical distributions for all sampled parameters are given in Chapter 4.

[2] The notations of *CPI* and *CPF* are used here rather than the older $P(I|E)$ and $P(F|E)$ notations in order to highlight the fact that a new PFM methodology is being applied.

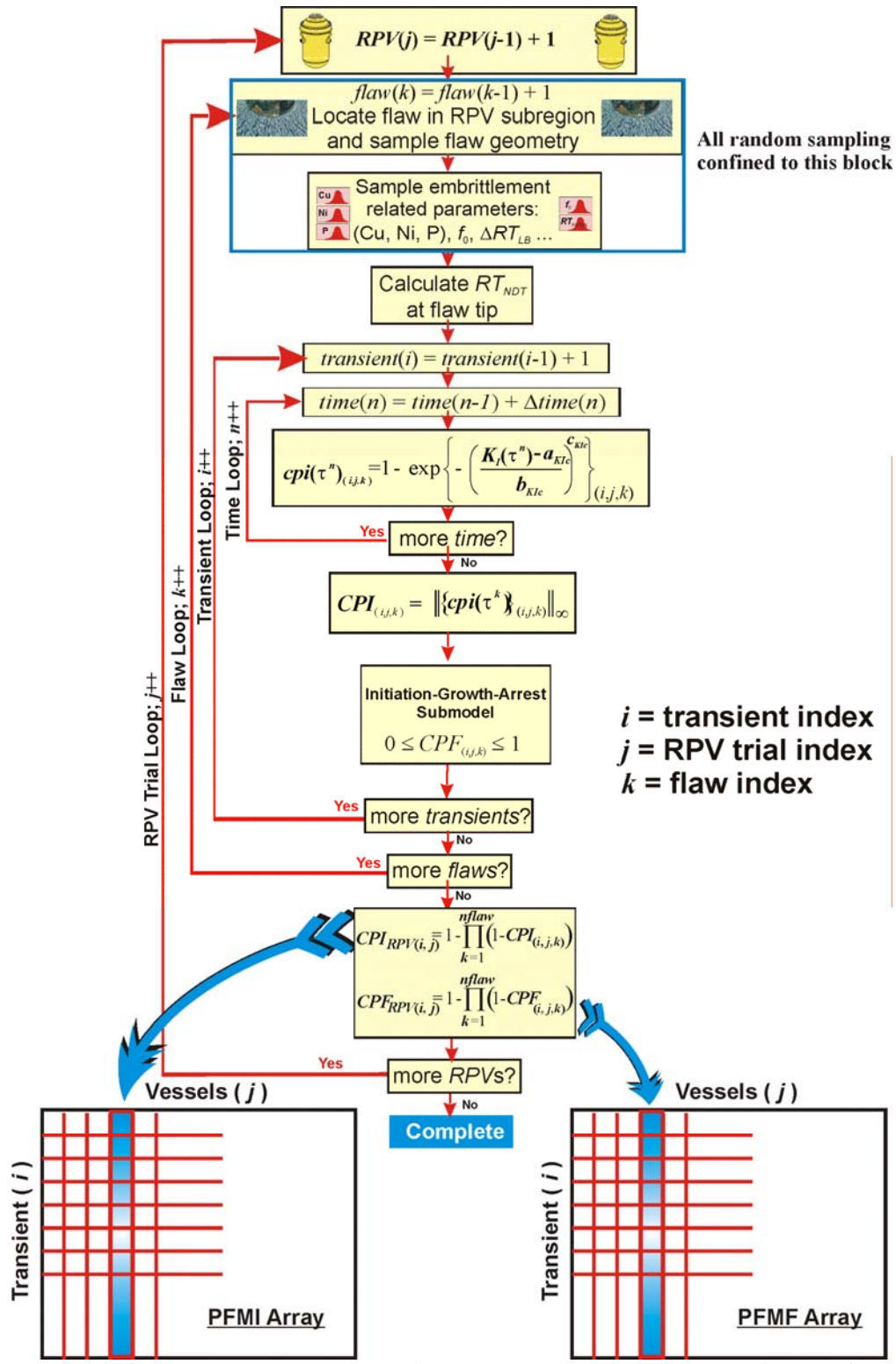

Fig. 6. Flow chart for improved PFM model implemented in FAVPFM showing the four primary nested loops – (1) *RPV Trial Loop*, (2) *Flaw Loop*, (3) *Transient Loop*, and (4) *Time Loop*. Note: ++ notation indicates increment index by 1, e.g., *i*++ means *i*=*i*+1.

Great care was taken in the construction of the nested-loop structure shown in Fig. 6 to preclude the introduction of a bias in the results due to the arbitrary ordering of the transients. In other words, for a given RPV trial, flaw, and transient, the same value of *CPI* and *CPF* will be calculated irrespective of the position of the transient (or the number of transients) in the load-definition transient stack. This objective was accomplished by confining all random sampling to the *sampling block* located at the point of entry into the flaw loop. Any sampling required in the crack *Initiation-Growth-Arrest* submodel[3] draws from sets of random number sequences derived in the sampling block. These set-aside random number sequences remain fixed for the current flaw and are reset to the start of the sequence as each transient is incremented in the *Transient Loop*. New random number sequences are constructed (resampled) for each increment in the *Flaw Loop*. The above approach involves an implementation of a variance reduction technique called *common random numbers* (CRN) which, in the terminology of classical experimental design, is a form of *blocking*. CRN has also been called *correlated sampling* or *matched streams* in some statistical simulation contexts [51].

3.3.2 Beltline Configurations and Region Discretization

The FAVOR code provides the capability to model the variation of radiation damage in the *beltline region* of an RPV with as much detail as the analyst considers necessary. In this section, a description of the beltline region is given, focusing on those aspects that are relevant to a FAVOR PFM analysis.

The beltline region of an RPV is fabricated using either forged-ring segments or rolled-plate segments [4]. The vessels are typically constructed of a specialty pressure vessel ferritic steel (e.g., A533-B, Class 1 plate or A508, Class 2 forging) as the base material. The heavy-section steel wall is lined with an internal cladding of austenitic stainless steel. Vessels made with forgings have only circumferential welds, and plate-type vessels have both circumferential welds and axial welds, as shown in Fig. 7. Therefore, beltline shells of a plate-type vessel contain three *major region* categories to model: (1) axial welds, (2) circumferential welds, and (3) plate segments. Only that portion of a weld that is within the axial bounds of the core need be considered, because the fast-neutron flux (and thus the radiation damage) experiences a steep attenuation beyond the fuel region. The extended surface length of an axially oriented flaw in a plate segment is also limited by the height of the core but not by the height of the shell course; therefore, the surface length of axial flaws in plate segments can be greater than those in axial welds [4]. Circumferential flaws in circumferential welds can be assumed to be limited by the full 360-degree arc-length of the weld. Due to the fabrication procedures for applying the cladding on the inner surface of the vessel, FAVOR assumes all pre-existing surface-

[3] As will be discussed in Chapter 4, resampling of weld chemistry is required in the through-wall crack growth protocol as the crack front advances into a different weld layer.

breaking flaws (in plate or weld subregions) are circumferential flaws. Embedded flaws can be either axially or circumferentially oriented.

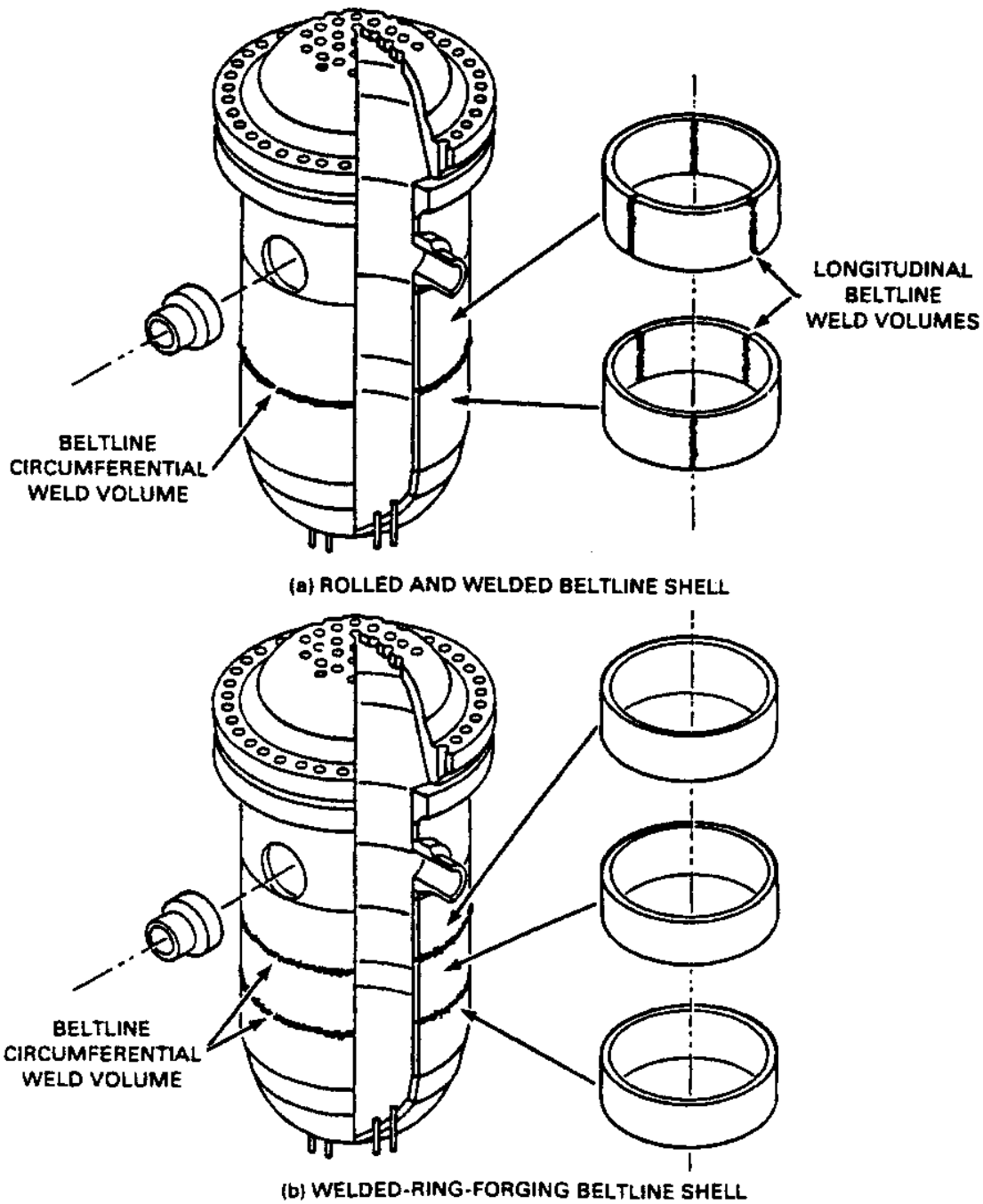

Fig. 7. Fabrication configurations of PWR beltline shells (adapted from [3]): (a) rolled-plate construction with axial and circumferential welds and (b) ring-forging construction with circumferential welds only.

Given the above considerations, the beltline region in FAVOR is defined as that portion of the RPV shell (including plate segments and welds) that extends from one foot below the bottom of the active core to one foot above the core. It is this region of the RPV wall that is explicitly modeled in FAVOR. As will be discussed in later sections, the assumption applied in the crack *Initiation-Growth-Arrest* submodel is that all finite-length flaws (both surface-breaking and embedded) instantly upon initiation become infinite-length flaws at depths corresponding to the locations of their outer crack tips at the time of initiation. This assumption that there is lateral extension of finite flaws before they extend through the vessel wall is supported by experimental observations made during large-scale PTS experiments (discussed in Chapter 2) conducted at ORNL in the 1980s.

Figure 8 shows a typical rollout section of the beltline region. The user is required to discretize (subdivide) the beltline into several major regions that contain plates (or forgings), axial welds, and circumferential welds. These major regions are further discretized into subregions for greater resolution of the variation in radiation-induced embrittlement. An embrittlement-distribution map is defined in the input data for FAVPFM using these major region and subregion definitions.

3.3.3 Treatment of the Fusion-Line Along Welds

The discretization and organization of major regions and subregions in the beltline includes a special treatment of weld *fusion lines* These fusion lines can be visualized as approximate boundaries between the weld subregion and its neighboring plate or forging subregions. FAVOR checks for the possibility that the plate subregions adjacent to a weld subregion could have a higher degree of radiation-induced embrittlement than the weld. The irradiated value of RT_{NDT} for the weld subregion of interest is compared to the corresponding values of the adjacent (i.e., nearest-neighbor) plate subregions. Each weld subregion will have at most two adjacent plate subregions. The embrittlement-related properties of the most limiting (either the weld or the adjacent plate subregion with the highest value of irradiated RT_{NDT}) material are used when evaluating the fracture toughness of the weld subregion. These embrittlement-related properties include the unirradiated value of $\bar{RT}_{NDT0}$, the fast-neutron fluence, $\bar{f}_0$, product form, and chemistry content, $\bar{Cu}$, $\bar{Ni}$, and $\bar{P}$ wt %, as discussed in Steps 3 and 4 and Eqs. (120) and (121) of Sect. 4.5. Flaw type and pre- and post-initiation orientation (see Sect. 3.3.8 and Table 3) of flaws are not transferred from a dominant plate subregion to a weld subregion.

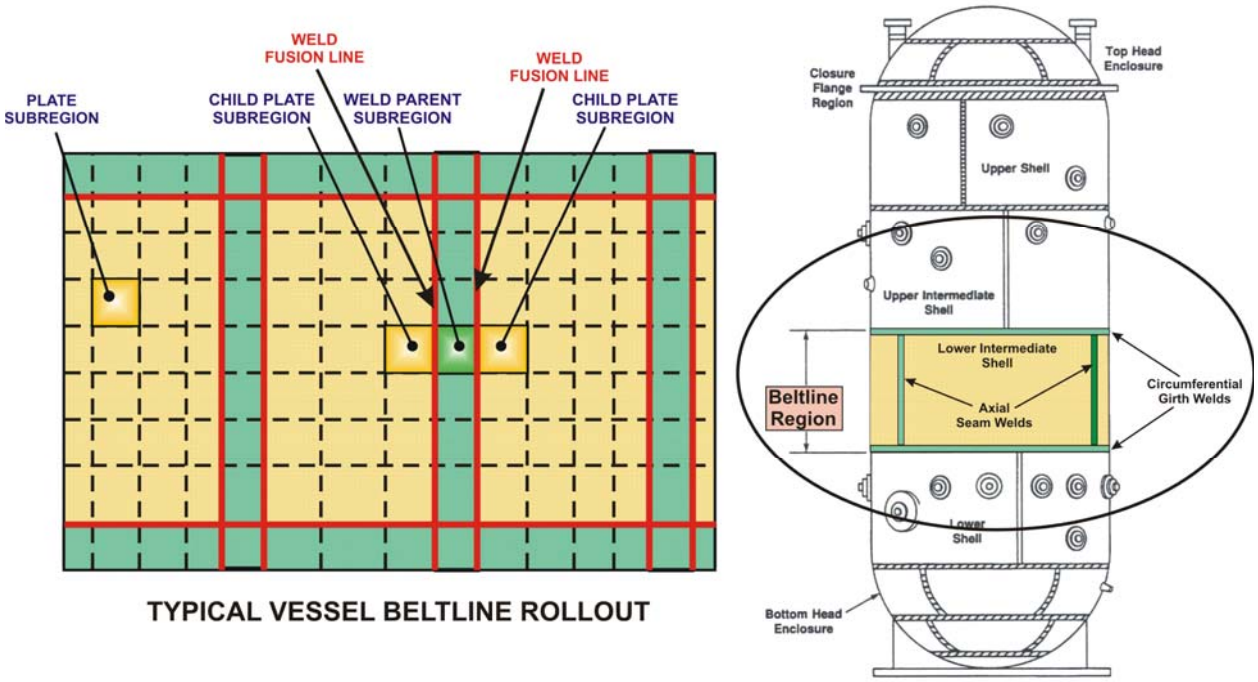

Fig. 8. FAVOR uses a discretization of the RPV beltline region to resolve the variation in radiation damage in terms of plate, axial weld, and circumferential weld major regions which are further discretized into multiple subregions.

For the Ductile Tearing Model No. 2, implemented in FAVOR, v03.1 (see the discussion in Sect. 3.3.11), a second *weld-fusion-line dependency structure* is created based on the irradiated upper-shelf energy, *USE*. This weld-fusion-line dependency structure for sampling ductile-tearing properties is independent of the embrittlement-related dependency structure discussed above. For Ductile-tearing Model No. 2, the ductile-tearing-related properties of the most limiting (either the weld or the adjacent plate subregion with the lowest value of irradiated *USE*) material are used when evaluating ductile-tearing of a flaw located in the weld subregion. As with the embrittlement-related weld-fusion-line treatment, the flaw type and pre- and post-initiation orientation of flaws are not transferred from a dominant plate subregion to a weld subregion. Ductile-Tearing Model No. 1, implemented in FAVOR, v04.1, this second weld-fusion-line dependency structure for sampling ductile-tearing properties is not required.

For those conditions in which plate embrittlement properties are used to characterize the weld subregion fracture toughness, the weld chemistry re-sampling protocols continue to be applied.

3.3.4 Warm Prestressing

Experimental evidence for the warm prestressing (WPS) effect in ferritic steels was first reported almost 40 years ago [52]. Since then, this phenomena has been the subject of extensive research; e.g., see [53-62]. The technical basis for the inclusion of warm prestressing effects in FAVOR is presented in detail in [63]. The following is a summary of the discussion in [63].

The WPS phenomena can be characterized as an increase in the apparent fracture toughness of a ferritic steel after first being "prestressed" at an elevated temperature. Three mechanisms have been identified [53, 57, 61] to produce the WPS phenomena:

1. Preloading at an elevated temperature *work-hardens the material ahead of the crack tip*. The increase in yield strength with decreasing temperature "immobilizes" the dislocations in the plastic zone [55,56]. Consequently, an increase in applied load is needed for additional plastic flow (a prerequisite for fracture) to occur at the lower temperature.
2. Preloading at an elevated temperature *blunts the crack tip*, reducing the geometric stress concentration making subsequent fracture more difficult.
3. Unloading after or during cooling from the elevated WPS temperature down to a reduced temperature *produces residual compressive stresses ahead of the crack tip*. The load applied at the reduced temperature must first overcome these compressive stresses before the loading can produce additional material damage and possibly fracture. The residual compressive stresses associated with the unloaded initial plastic zone can be viewed as protecting the crack tip, since higher applied loads are required to achieve a given level of crack driving force compared to the condition before preloading [59].

Heretofore, probabilistic fracture mechanics calculations performed in the United States have typically not included the WPS phenomena as a part of the PFM model. This omission was based on the following considerations:

1. Thermal-hydraulic (TH) transients were often represented as smooth temporal variations of both pressure and coolant temperature; however, data taken from operating nuclear power plants demonstrate that actual overcooling events are not necessarily so well behaved. This non-smoothness of these fundamental mechanical and thermal loads created the possibility that, due to short-duration time-dependent fluctuations of pressure and/or coolant temperature, the criteria for WPS might be satisfied by the idealized transient but not satisfied by the real transient.
2. Previous PRA models of human reliability (HR) were typically not sufficiently sophisticated to capture the potential for plant operators to repressurize the primary coolant system as part of their response to an RPV-integrity challenge. Since such a repressurization would largely nullify the benefit of WPS, it was viewed as nonconservative to account for WPS within a model that may also ignore the potentially deleterious effects of operator actions.

FAVOR, v04.1, addresses both of these concerns by allowing as input data (1) more realistic and detailed representations of the postulated PTS transients and (2) more sophisticated PRA/HR models that explicitly consider both acts of omission and commission on the part of plant operators.

The FAVOR WPS-modeling option implements the *conservative WPS principle* first proposed by McGowan [54]. This principle states that for cleavage crack initiation to be possible the following criteria must be met: (1) the applied-K_I at the crack tip must exceed some minimum value of K_{Ic} and (2) the applied-K_I must be increasing with time (i.e., $dK_I / d\tau > 0$) when the load path first enters the finite K_{Ic} probability space. Equivalently, a flaw is assumed by FAVOR to be in a state of WPS when either of the two following conditions are met:

1. the time-rate-of-change of the applied-K_I is nonpositive ($dK_I / d\tau \leq 0$), or
2. the applied K_I is less than the maximum K_I experienced by the flaw up to the current time in the transient, where this $K_{I(max)}$ must be greater than the current value of $K_{Ic(\min)}$ as defined by the location parameter of the statistical model (to be discussed in Sect. 3.3.7) for cleavage-fracture initiation.

Figures 9a and b present an example of a PTS transient (Fig. 9a) applied to a flaw with its resulting load path (Fig. 9b). At Point 1 in Fig. 9b, the load path for the flaw enters finite K_{Ic} probability space, and, shortly thereafter, $dK_I / d\tau$ becomes negative. The flaw is in a state of WPS from Point 1 to Point 2. At Point 2, the applied-K_I at the crack tip exceeds the current $K_{I(max)}$ (established at Point 1).

Along the load path between Points 2 and 3, the flaw is no longer in a state of WPS and has a finite probability of crack initiation. At Point 3, a new $K_{I(max)}$ is established, and, since $dK_I / d\tau \leq 0$ or $K_I < K_{I(max)}$ for the remainder of the load path, the flaw returns to and remains in a state of WPS. While the WPS condition is in effect, the instantaneous conditional probability of initiation, $cpi(\tau)$, for the flaw is set to zero, even though the applied K_I of the flaw is within the finite K_{Ic} probability space ($K_I > K_{Ic(min)}$). To assess the impact of including WPS in the analysis, WPS has been implemented in FAVOR as a user-set option, thus allowing cases to be run with and without WPS effects.

If the WPS option is activated, the applied K_I of an arrested flaw must also be greater than the previous maximum K_I (of the arrested flaw geometry since the time of the arrest) for the flaw to reinitiate.

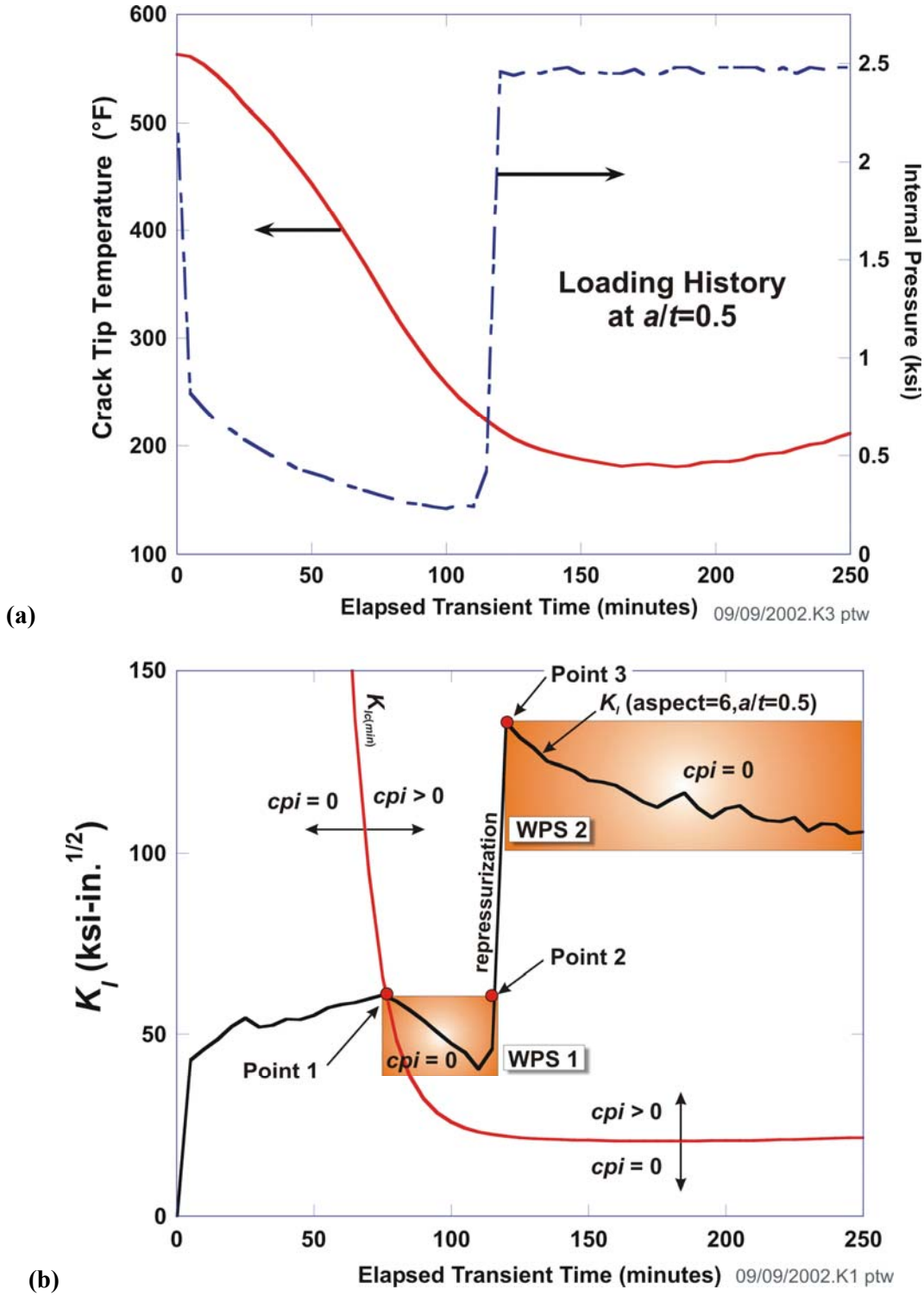

Fig. 9. Example of warm prestressing: (a) loading history with pressure applied to the inner surface and the temperature at the crack tip, (b) load path for a flaw showing two WPS regions. (*cpi* is the instantaneous conditional probability of initiation).

3.3.5 Probability Distributions

The sampled variables used in FAVPFM are drawn from a range of specified statistical distributions. The following presents general information about these distributions including, the form of their probability density function (PDF), cumulative distribution function (CDF), first and second moments, and sampling methods used in FAVOR. The notation $X_i \leftarrow N(\mu,\sigma)$ signifies that a random variate is drawn as a sample from a population described by the specified distribution. In this example, the population is described by a two-parameter normal distribution with mean, μ, and standard deviation, σ. Other distributions applied in FAVOR include the standard *uniform* distribution for a unit open interval, $U(0,1)$; the two-parameter *lognormal* distribution, $\Lambda(\mu_{\log},\sigma_{\log})$; the three-parameter *Weibull* distribution, $W(a,b,c)$; and the two-parameter *logistic* distribution, $L(\alpha,\beta)$.

A standard uniform distribution on the interval $U(0,1)$ is the starting point for all of the transformation methods that draw random variates from nonuniform continuous distributions. A uniform distribution is defined by the following:

<u>Uniform Distribution</u> – $U(a,b)$

PDF:

$$f_U(x \mid a,b) = \begin{cases} 0 & ; \quad x < a \\ \dfrac{1}{b-a} & ; \quad a \le x \le b \\ 0 & ; \quad x > b \end{cases}$$

CDF:

$$\Pr(X \le x) = F_U(x \mid a,b) = \begin{cases} 0 & ; \quad x < a \\ \dfrac{x-a}{b-a} & ; \quad a \le x \le b \\ 1 & ; \quad x > b \end{cases}$$

Moments:

Mean $$\mu = \frac{a+b}{2}$$

Variance $$\sigma^2 = \frac{(b-a)^2}{12}$$

Sampling from a two-parameter Uniform Distribution: $U_i \leftarrow U(0,1)$

Sampling from a standard uniform distribution, $U(0,1)$, is accomplished computationally with a *Random Number Generator* (RNG). A portable random number generator [64-66], written in Fortran, has been implemented and tested in FAVOR. This portable generator, based on a composite of two multiplicative linear congruential generators using 32 bit integer arithmetic, has a reported theoretical minimum period of 2.3×10^{18}. This implementation was successfully tested by the HSST Program at ORNL for statistical randomness using the NIST *Statistical Test Suite for Random and Pseudorandom Number Generators* [67].

<u>Normal Distribution</u> – $N(\mu,\sigma)$

PDF: $$f_N(x \mid \mu,\sigma) = \frac{1}{\sigma\sqrt{2\pi}} \exp\left[-\frac{(x-\mu)^2}{2\sigma^2}\right]; \quad -\infty < x < +\infty$$

CDF: $$\Pr(X \le x) = \Phi(z) = \frac{1}{\sqrt{2\pi}} \int_{-\infty}^{z} \exp\left(-\frac{\xi^2}{2}\right) d\xi \ ; \quad z = \frac{x-\mu}{\sigma}; \quad -\infty < x < +\infty$$

Moments:

Mean μ

Variance σ^2

Sampling from a two-parameter Normal Distribution: $X_i \leftarrow N(\mu,\sigma)$

Earlier versions of FAVOR used the Box-Müller *Transformation Method* [68-70] to sample from a standard normal distribution, $N(0,1)$. Beginning with FAVOR, v04.1, the more computationally efficient Forsythe's method (as extended by Ahrens and Dieter [71]) for sampling from a standard normal distribution has been implemented. The sampled standard normal deviate, Z_i, is then scaled to the required random normal deviate with mean, μ, and standard deviation, σ, by.

$$\begin{aligned} Z_i &\leftarrow N(0,1) \\ X_i &= Z_i\sigma + \mu \end{aligned} \tag{1}$$

The extended Forsythe's method is computationally very efficient; however, one problem with the method is that there is no direct connection between the standard normal deviate and its associated *p-value* in the normal cumulative distribution function. When this relationship between the *p-value* and the deviate is required, an alternative method for expressing the inverse of a standard normal

CDF (also known as a percentile function) is applied in FAVOR. The following rational function [72] represents an accurate approximation of the standard normal percentile function:

$$
\begin{aligned}
x &= \begin{cases} p & \text{for } p < \frac{1}{2} \\ 1-p & \text{for } p \geq \frac{1}{2} \end{cases} \\
y &= \sqrt{-2\ln(x)} \\
Z_p &= \operatorname{sgn}\left(p - \frac{1}{2}\right)\left(y + \frac{a_0 + a_1 y + a_2 y^2 + a_3 y^3 + a_4 y^4}{b_0 + b_1 y + b_2 y^2 + b_3 y^3 + b_4 y^4}\right)
\end{aligned}
\tag{2}
$$

where

$$
\operatorname{sgn}(x) = \begin{cases} -1 & \text{if } x < 0 \\ +1 & \text{if } x \geq 0 \end{cases}
$$

and the coefficients of the rational function are:

$$
\begin{aligned}
a_0 &= \text{-}0.3222324310880000 & b_0 &= 0.0993484626060 \\
a_1 &= \text{-}1.0000000000000000 & b_1 &= 0.5885815704950 \\
a_2 &= \text{-}0.3422420885470000 & b_2 &= 0.5311034623660 \\
a_3 &= \text{-}0.0204231210245000 & b_3 &= 0.1035377528500 \\
a_4 &= \text{-}0.0000453642210148 & b_4 &= 0.0038560700634
\end{aligned}
$$

The standard normal deviate is then scaled to obtain the required quantile

$$
X_p = Z_p \sigma + \mu \tag{3}
$$

<u>Lognormal Distribution</u> $-\Lambda\left(\mu_{\log}, \sigma_{\log}\right)$

PDF:

$$
f_\Lambda(x \mid \mu_{\log}, \sigma_{\log}) = \begin{cases} 0 & ; \quad x \leq 0 \\ \dfrac{1}{\sigma_{\log} x \sqrt{2\pi}} \exp\left[-\dfrac{\left(\ln x - \mu_{\log}\right)^2}{2\sigma_{\log}^2}\right] & ; \quad 0 < x < \infty \end{cases}
$$

CDF:

$$
\Pr(X \leq x) = \Phi(z) = \begin{cases} 0 & ; \quad x \leq 0 \\ \dfrac{1}{\sqrt{2\pi}} \displaystyle\int_{-\infty}^{z} \exp\left(-\frac{\xi^2}{2}\right) d\xi \; ; \quad z = \dfrac{\ln x - \mu_{\log}}{\sigma_{\log}} & , \quad 0 < x < \infty \end{cases}
$$

Moments:

Mean

$$
\mu = \exp\left(\mu_{\log} + \frac{\sigma_{\log}^2}{2}\right)
$$

Variance $\sigma^2 = \omega(\omega - 1)\exp(2\mu_{\log}); \quad \omega = \exp(\sigma_{\log}^2)$

Sampling from a two-parameter Lognormal Distribution: $X_i \leftarrow \Lambda(\mu_{\log}, \sigma_{\log})$

The log-transformed deviate is sampled from a normal distribution with mean equal to the lognormal mean, $\mu_{\log}$, and standard deviation equal to the lognormal standard deviation, $\sigma_{\log}$. The log-transformed deviate is then converted into the required random deviate by the exponential function.

$$\begin{aligned} Y_i &\leftarrow N(\mu_{\log}, \sigma_{\log}) \\ X_i &= \exp(Y_i) \end{aligned} \tag{4}$$

<u>Weibull Distribution</u> – $W(a,b,c)$

(a = location parameter, b = scale parameter, c = shape parameter)

PDF: $$f_w(x|a,b,c) = \begin{cases} 0 \quad ; & x \le a \\ \frac{c}{b} y^{c-1} \exp\left(-y^c\right); & (y = (x-a)/b, x > a,\ b,c > 0) \end{cases}$$

CDF: $$\Pr(X \le x) = F_w(x \mid a,b,c) = \begin{cases} 0 \quad ; & x \le a \\ 1 - \exp\left[-y^c\right]; & (y = (x-a)/b, x > a,\ b,c > 0) \end{cases}$$

Moments:

Mean $\mu = a + b\,\Gamma\left(1 + \frac{1}{c}\right)$

Variance $\sigma^2 = b^2\left[\Gamma\left(1 + \frac{2}{c}\right) - \Gamma^2\left(1 + \frac{1}{c}\right)\right]$

where $\Gamma(x)$ is Euler's gamma function.

Sampling from a three-parameter Weibull Distribution: $X_i \leftarrow W(a,b,c)$

A random number is drawn from a uniform distribution on the open interval (0,1) and then transformed to a Weibull variate with the Weibull percentile function.

$$\begin{aligned} U_i &\leftarrow U(0,1) \\ X_i &= a + b\left[-\ln(1 - U_i)\right]^{1/c} \end{aligned} \tag{5}$$

<u>Logistic Distribution</u> – $L(\alpha,\beta)$

PDF: $$f_L(x\,|\,\alpha,\beta)=\frac{z}{\beta(1+z)^2};\quad z=\exp\left[-\left(\frac{x-\alpha}{\beta}\right)\right],\quad -\infty<x<\infty$$

CDF: $$\Pr(X\le x)=F_L(x\,|\,\alpha,\beta)=\frac{1}{1+z};\quad z=\exp\left[-\left(\frac{x-\alpha}{\beta}\right)\right],\quad -\infty<x<\infty$$

Moments:

Mean $\mu=\alpha$

Variance $\sigma^2=\dfrac{\pi^2\beta^2}{3}$

Sampling from a two-parameter Logistic Distribution $X_i \leftarrow L(\alpha,\beta)$

A random number is drawn from a uniform distribution on the open interval (0,1) and then transformed to a logistic variate by the logistic percentile function.

$$\begin{aligned} U_i &\leftarrow U(0,1) \\ X_i &= \alpha-\beta\ln\left(\frac{1}{U_i}-1\right) \end{aligned} \tag{6}$$

Figure 10 gives examples of PDFs for each of these continuous probability distributions.

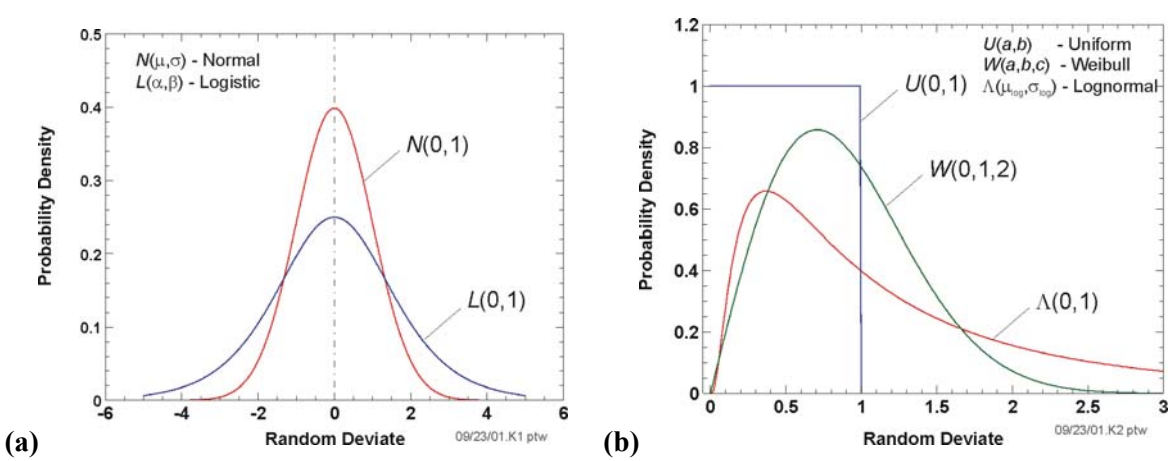

Fig. 10. Example probability density functions for (a) normal and logistic and (b) uniform, Weibull, and lognormal continuous distributions.

3.3.6 Truncation Protocol

When sampling physical variables from statistical distributions, it is sometimes necessary to truncate the distribution to preclude the sampling of nonphysical values. When truncation is required in FAVOR, the truncation bounds, either symmetric or one-sided, are explicitly stated in the sampling protocols presented in Chapters 3 and 4. The truncation rule applied in FAVOR requires a sampled variable that exceeds its truncation bounds to be replaced by the boundary value. This exception-handling protocol ensures that the integrated area under the truncated probability density function remains equal to unity; however, the shape of the resulting sampled density distribution will have a step-function rise at the truncated boundaries.

3.3.7 Conditional Probability of Initiation (*CPI*)

As discussed above, a deterministic fracture analysis is performed by stepping through discrete transient time steps to examine the temporal relationship between the applied Mode I stress intensity factor (K_I) and the static cleavage fracture initiation toughness (K_{Ic}) at the crack tip. The computational model for quantification of fracture-toughness uncertainty has been improved (relative to the models used in the 1980s to derive the current PTS regulations) in three ways: (1) the K_{Ic} and K_{Ia} databases were extended by 84 and 62 data values, respectively, relative to the databases in the EPRI NP-719-SR[4] report [73]; (2) the statistical representations for K_{Ic} and K_{Ia} were derived through the application of rigorous mathematical procedures; and (3) a method for estimating the *epistemic* uncertainty in the transition-reference temperature was developed. Bowman and Williams [74] provide details regarding the extended database and mathematical procedures employed in the derivation of a Weibull distribution for fracture-toughness data. Listings of the extended ORNL 99/27 K_{Ic} and K_{Ia} database are given in Appendix C. A Weibull distribution, in which the parameters were calculated by the *Method of Moments* point-estimation technique, forms the basis for the new statistical model of K_{Ic}. For the Weibull distribution, there are three parameters to estimate: the location parameter, a, of the random variate; the scale parameter, b, of the random variate; and the shape parameter, c. The Weibull probability density, f_W, is given by:

$$f_w(x|a,b,c) = \begin{cases} 0 \quad ; & x \le a \\ \dfrac{c}{b} y^{c-1} \exp\left(-y^c\right); & (y = (x-a)/b, x > a,\ b,c > 0) \end{cases} \tag{7}$$

where the parameters of the K_{Ic} distribution are a function of $\Delta T_{RELATIVE}$:

[4] The fracture-toughness database given in EPRI NP-719-SR (1978) [73] served as the technical basis for the statistical K_{Ic} / K_{Ia} distributions used in the IPTS studies of the 1980s.

$$
\boxed{\begin{aligned}
a_{K_{Ic}}(\tilde{\Delta T}_{RELATIVE}) &= 19.35 + 8.335\exp\left[0.02254(\tilde{\Delta T}_{RELATIVE})\right] \ [\text{ksi}\sqrt{\text{in.}}] \\
b_{K_{Ic}}(\tilde{\Delta T}_{RELATIVE}) &= 15.61 + 50.132\exp\left[0.008(\tilde{\Delta T}_{RELATIVE})\right] \ [\text{ksi}\sqrt{\text{in.}}] \\
c_{K_{Ic}} &= 4
\end{aligned}} \tag{8}
$$

where $\tilde{\Delta T}_{RELATIVE} = (T(t) - \tilde{RT}_{NDT})$ in °F. The curve, "$\tilde{X}$", above a variable indicates that it is a randomly sampled value. The details of the development of Eq. (8) will be given in Chapter 4 along with a discussion of the sampling methods for $\tilde{RT}_{NDT}$.

For each postulated flaw, a deterministic fracture analysis is performed by stepping through the transient time history for each transient. At each time step, τ^n, for the *i*th transient and *j*th RPV trial, an instantaneous $cpi(\tau^n)_{(i,j,k)}$ is calculated for the *k*th flaw from the Weibull K_{Ic} cumulative distribution function at time, τ, to determine the fractional part (or fractile) of the distribution that corresponds to the applied $K_I(\tau^n)_{(i,j,k)}$:

$$
\Pr\left(K_{Ic} \le K_I(\tau^n)_{(i,j,k)}\right) = cpi(\tau)_{(i,j,k)} = \begin{cases} 0 \ ; & K_I(\tau^n)_{(i,j,k)} \le a_{K_{Ic}} \\ 1 - \exp\left\{-\left[\dfrac{K_I(\tau^n)_{(i,j,k)} - a_{K_{Ic}}}{b_{K_{Ic}}}\right]^{c_{K_{Ic}}}\right\} ; & K_I(\tau^n)_{(i,j,k)} > a_{K_{Ic}} \end{cases} \tag{9}
$$

Here, $cpi(\tau^n)_{(i,j,k)}$ is the instantaneous conditional probability of initiation at the crack tip at time τ^n. Figure 11 illustrates the interaction of the applied K_I time history and the Weibull K_{Ic} distribution for an example case, in which an embedded flaw 0.67-in. in depth, 4.0-in. in length, with the inner crack tip located 0.5-in. from the inner surface, is subjected to a severe PTS transient. The RT_{NDT} of the RPV material is 270 °F. A Weibull distribution, as a lower-bounded continuous statistical distribution, has a lower limit (referred to as the *location parameter,* $a_{K_{Ic}}$) such that any value of K_I below the location parameter has a zero probability of initiation. As described in Fig. 11, the applied K_I must be greater than the local value of $a_{K_{Ic}}$ before $cpi > 0$. The region designated as $cpi > 0$ in the figure represents the finite probability K_{Ic} initiation space, and outside of this region $cpi = 0$.

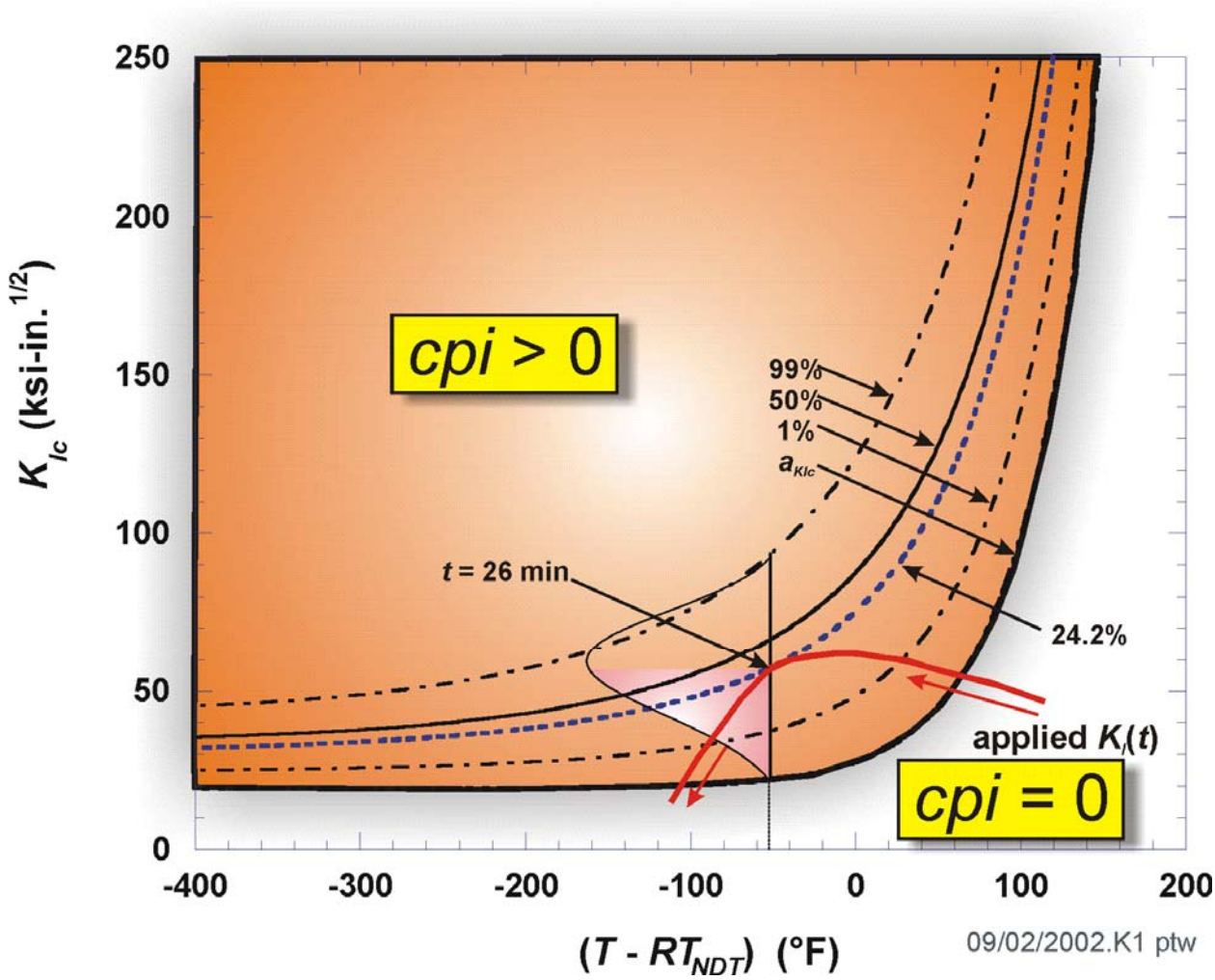

Fig. 11. Interaction of the applied K_I time history and the Weibull K_{Ic} statistical model for a postulated flaw.

Table 2. Illustration of Computational Procedure to Determine *CPI* and *CPF* for a Postulated Flaw (Warm Prestress Not Included)

Time(τ^n) (min)	$T(\tau^n)$ (°F)	RT_{NDT} (°F)	$T(\tau^n)$-RT_{NDT} (°F)	K_{Ic} Weibull Parameters a (ksi√in)	b (ksi√in)	c (-)	$K_I(\tau^n)$ (ksi√in)	$cpi(\tau^n)$ (-)	$\Delta cpi(\tau^n)$ (-)	$P(F\|I)$ (-)	$\Delta cpf(\tau^n)$ (-)	$cpf(\tau^n)$ (-)
8	360.68	270.0	90.68	83.70	119.16	4	50.90	0	0	0	0	0
10	328.28	270.0	58.28	50.35	95.52	4	55.70	9.82E-06	9.82E-06	0	0	0
12	302.18	270.0	32.18	36.57	80.46	4	59.20	6.24E-03	6.23E-03	0.20	0.0012	0.0012
14	281.48	270.0	11.48	30.15	70.56	4	61.00	3.59E-02	2.96E-02	0.25	0.0074	0.0087
16	264.74	270.0	-5.26	26.75	63.68	4	61.80	8.77E-02	5.18E-02	0.30	0.0155	0.0242
18	251.24	270.0	-18.76	24.81	58.76	4	61.70	1.44E-01	5.62E-02	0.40	0.0225	0.0467
20	240.44	270.0	-29.56	23.63	55.18	4	61.10	1.91E-01	4.76E-02	0.50	0.0238	0.0705
22	231.62	270.0	-38.38	22.86	52.49	4	60.10	2.24E-01	3.24E-02	0.60	0.0194	0.0899
24	224.24	270.0	-45.76	22.32	50.37	4	58.80	2.40E-01	1.66E-02	0.70	0.0116	0.1015
26	218.12	270.0	-51.88	21.94	48.71	4	57.30	2.42E-01	2.04E-03	0.80	0.0016	0.1031

Notes:
$cpi(\tau^n)$ – instantaneous conditional probability of initiation
$\Delta cpi(\tau^n)$ – incremental change in instantaneous conditional probability of initiation
$P(F|I)$ - the number of flaws that propagated through the wall thickness divided by the total number of initiated flaws
$\Delta cpf(\tau^n) = P(F|I) \times \Delta cpi(t^n)$
$cpf(\tau^n)$ = instantaneous conditional probability of failure by through-wall cracking
CPI = *sup*-norm[5] of the vector $\{cpi(\tau^n)\}$
CPF = *sup*-norm of the vector $\{cpf(\tau^n)\}$
The transient index, *i*, RPV trial index, *j*, and flaw index, *k*, are implied.

Table 2 summarizes results of the PFM model for the postulated flaw. The transient index, *i*, RPV trial index, *j*, and flaw index, *k*, are implied for all variables. The column headed $cpi(\tau^n)$ is the instantaneous value of the conditional probability of initiation determined from Eq. (9) (see Fig.12). The next column headed $\Delta cpi\ (\tau^n)$ is the increase in $cpi(\tau^n)$ that occurred during the discrete time step, $\Delta\tau^n$, as illustrated in Fig. 13. The current value of $CPI_{(i,j,k)}$ is

$$CPI_{(i,j,k)} = \left\| \left\{ cpi(\tau^m) \right\}_{(i,j,k)} \right\|_\infty \quad \text{for } 1 \le m \le n \tag{10}$$

For the example flaw in Table 2, *CPI* = 0.242 occurs at a transient time of 26 minutes. The last three columns in Table 2 are used in the determination of the conditional probability of vessel failure, *CPF*, by through-wall cracking, as will be discussed below.

[5] the *sup*-norm is the maximum-valued element (in absolute value) in the vector

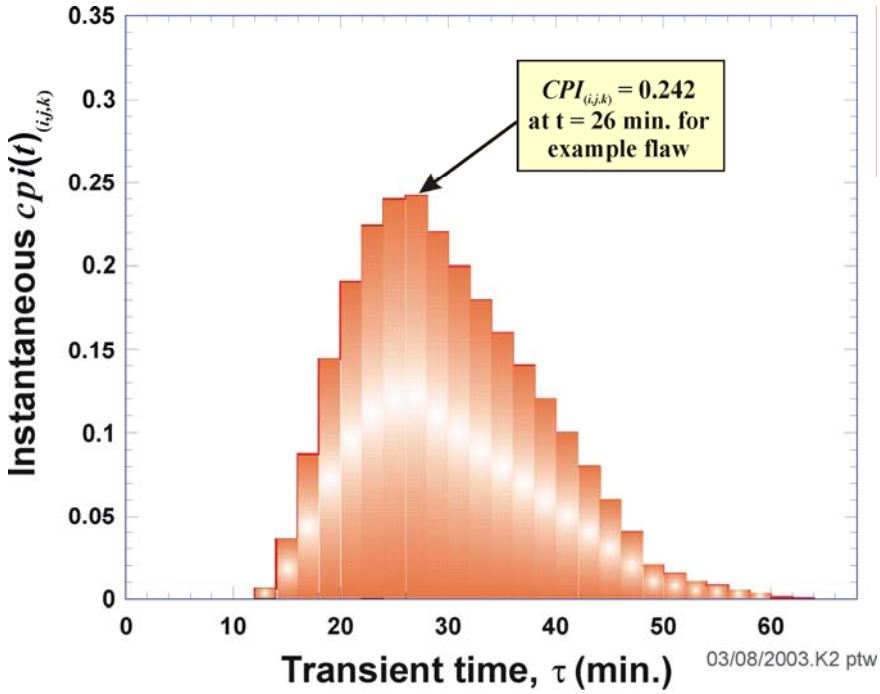

Fig. 12. The parameter $cpi(\tau)_{(i,j,k)}$ is the instantaneous conditional probability of initiation (*cleavage fracture*) obtained from the Weibull K_{Ic} cumulative distribution function. $CPI_{(i,j,k)}$ is the maximum value of $cpi(\tau)_{(i,j,k)}$. (Note: i = transient index, j = RPV trial index, and k = flaw index)

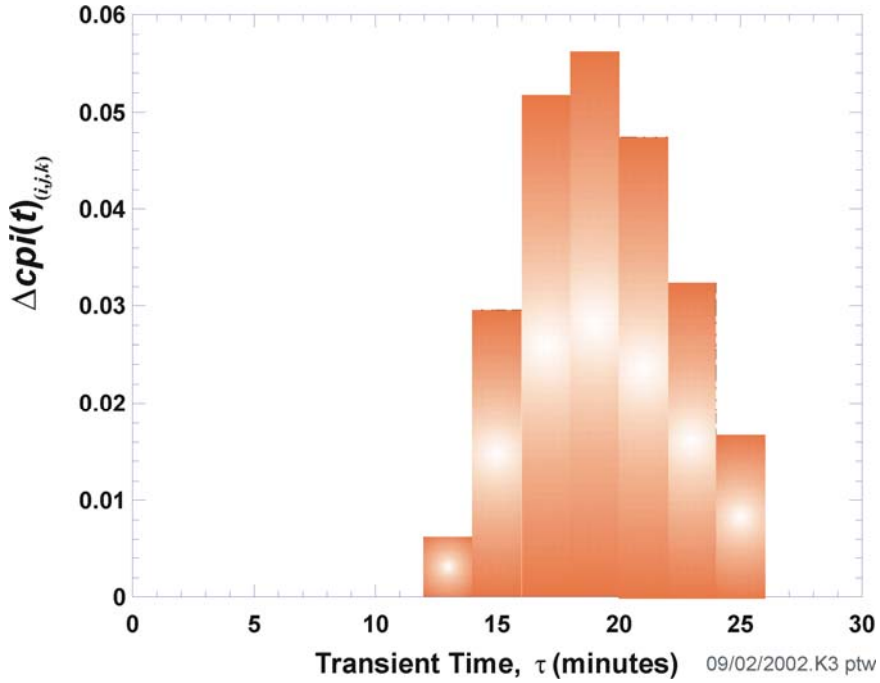

Fig. 13. $\Delta cpi(\tau^n)_{(i,j,k)}$ is the increase in $cpi(\tau^n)_{(i,j,k)}$ that occurs during each discrete time step. When the maximum value of $cpi(\tau^n)_{(i,j,k)}$ is reached, negative values of $\Delta cpi(\tau^n)_{(i,j,k)}$ are set to zero. (Note: i = transient index, j = RPV trial index, and k = flaw index)

3.3.8 Post-Initiation Flaw Geometries and Orientations

A flaw that initiates in cleavage fracture is assumed to become an infinite-length inner surface-breaking flaw, regardless of its original geometry (see Fig. 14). This assumption is consistent with the results of large-scale fracture experiments in which flaws, initiated in cleavage fracture, were observed to extend in length before propagating through the wall thickness [75]. For example, a circumferentially oriented semi-elliptical surface-breaking flaw ½-inch in depth is assumed to become a ½-inch deep 360-degree circumferential flaw. An embedded flaw ½-inch in depth with its inner crack tip located at ½-inch from the RPV inner surface becomes a 1-inch deep infinite-length flaw, since it is assumed that an initiated embedded flaw first propagates through the clad, thus becoming an infinite-length surface-breaking flaw before advancing into the vessel wall.

All surface-breaking semi-elliptic flaws in FAVOR are assumed to be pre-existing fabrication flaws that are circumferentially oriented; see Table 3. This restriction is based on the assumption that Category 1 flaws were created during vessel fabrication, as the austenitic stainless-steel cladding was being applied to the inner surface of the vessel. This assumption introduces a preferred orientation for these flaws. Embedded flaws may be oriented either axially or circumferentially. Upon initiation, the transformed infinite-length flaws retain the orientation of the parent initiating flaw.

Table 3. Applied Flaw Orientations by Major Region

Major Region	Flaw Category 1	Flaw Category 2	Flaw Category 3
axial weld	circumferential	axial	axial
circumferential weld	circumferential	circumferential	circumferential
plate/forging	circumferential	axial/circumferential*	axial/circumferential*

Flaw Category 1 – surface-breaking flaw

Flaw Category 2 – embedded flaw in the base material between the clad/base interface and $\frac{1}{8}t$

Flaw Category 3 – embedded flaw in the base material between $\frac{1}{8}t$ and $\frac{3}{8}t$

*Flaw Categories 2 and 3 in plates/forgings are equally divided between axial and circumferential orientations

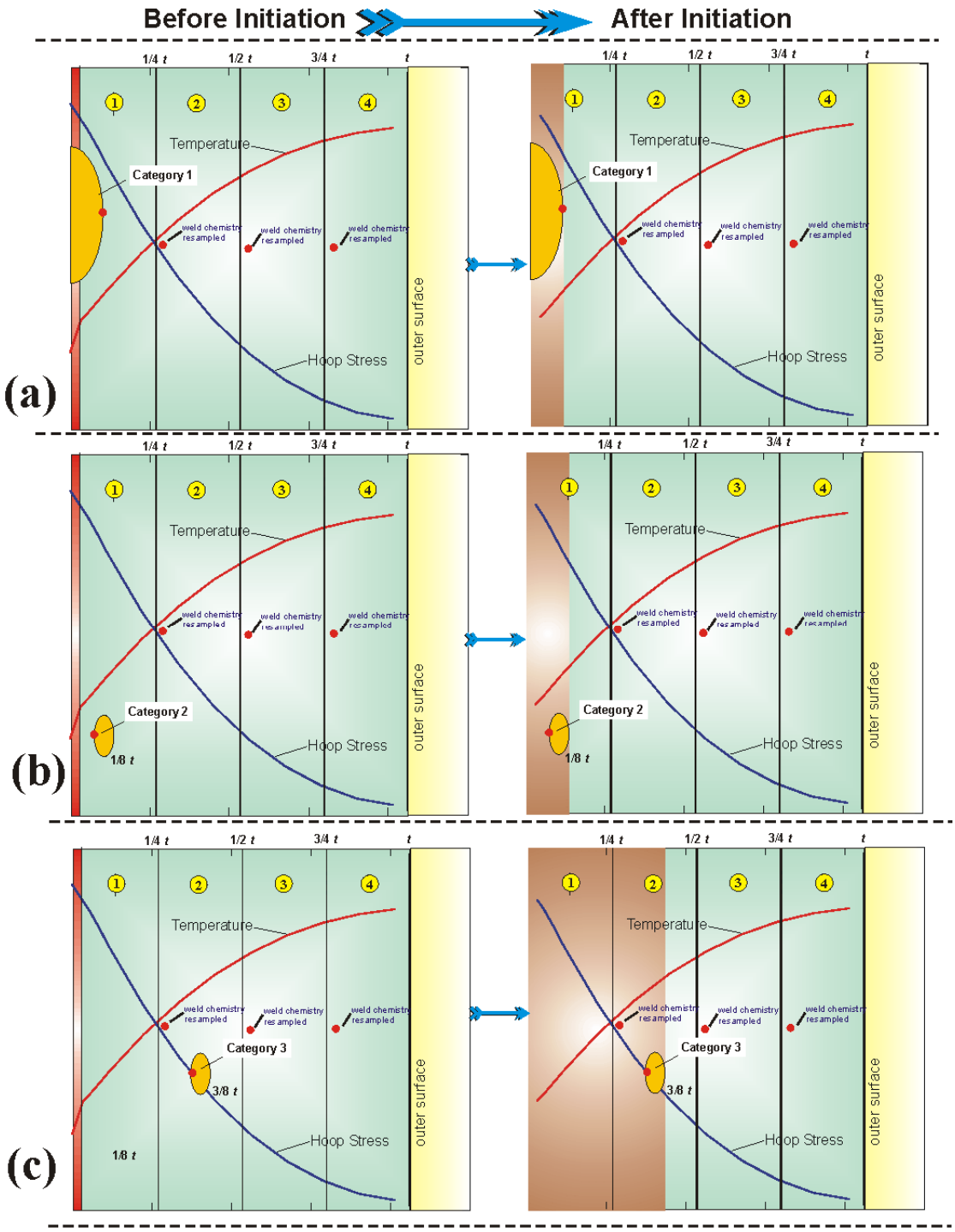

Fig. 14. At the time of initiation, the three categories of flaws are transformed into infinite-length flaws: (a) Category 1 semi-elliptic surface-breaking circumferential flaws become 360 degree circumferential flaws, (b) and (c) Category 2 and 3 embedded flaws become inifinite-length axial or 360 degree circumferential flaws at the same depth. Category 1 flaws are only oriented in the circumferential direction.

3.3.9 Conditional Probability of Failure (*CPF*) by Through-Wall Cracking

A flaw that has initiated in cleavage fracture has two possible outcomes for the time remaining in the transient. The newly-formed infinite-length flaw either propagates through the entire wall thickness causing RPV failure by through-wall cracking, or it experiences a stable arrest at some location in the wall. In either case, the advancement of the crack tip through the RPV wall may involve a sequence of *initiation* / *arrest* / *re-initiation* events as discussed in the following section. In the discussion in this section, the transient index, *i*, RPV trial index, *j*, and flaw index, *k*, are implied for all variables. They have been left off to simplify the notation.

Table 2 summarizes the calculation of RPV failure in the improved PFM model. The column headed $P(F \mid I)$ is the conditional probability of failure given initiation; $P(F \mid I)$ is equal to the fraction of initiated flaws that propagate through the wall thickness causing RPV failure. At the current time, τ^n, the increment in the conditional probability of failure, $\Delta cpf(\tau^n)$, is the product of $P(F \mid I)$ and $\Delta cpi(\tau^n)$. The instantaneous value of the conditional probability of failure at time τ^n, $cpf(\tau^n)$, is therefore

$$cpf(\tau^n) = \sum_{m=1}^{n_{\max}} P(F \mid I) \times \Delta cpi(\tau^m) = \sum_{m=1}^{n_{\max}} \Delta cpf(\tau^m) \tag{11}$$

where $n_{\max}$ is the time step at which the current value of *CPI* occurred, i.e., the time at which the maximum value of $cpi(\tau)$ occurred.

The fraction of flaws that would fail the RPV is determined (at each time step for each flaw) by performing a Monte Carlo analysis of through-wall propagation of the infinite-length flaw. In each analysis, the infinite-length flaw is incrementally propagated through the RPV wall until it either fails the RPV or experiences a stable arrest. In each analysis, a K_{Ia} curve is sampled from the lognormal K_{Ia} distribution (to be discussed). The applied K_I for the growing infinite-length flaw is compared to K_{Ia} as the flaw propagates through the wall. If crack arrest does not occur ($K_I \geq K_{Ia}$), the crack tip advances another small increment, and again a check is made for arrest. If the crack does arrest ($K_I \leq K_{Ia}$), the simulation continues stepping through the transient time history checking for re-initiation of the arrested flaw. At the end of the Monte Carlo analysis, $P(F|I)$ is simply the number of flaws (that initiated at time τ^n) that propagated through the wall thickness causing RPV failure, divided by the total number of simulated flaws. See Sect. 3.3.12 for details of the Initiation-Growth-Arrest (*IGA*) submodel.

The *sup*-norm of the vector $\{cpf(\tau^n)\}$, *CPF*, occurs at the same time step as the *CPI*. In Table 2, for the example flaw, *CPF* is 0.103 and occurs at a transient elapsed time of 26 minutes.

3.3.10 Multiple Flaws

The technical basis for the treatment of multiple flaws in the beltline region of an RPV is given in [76,77]. For each *j*th RPV trial and *i*th transient, the process described above is repeated for all postulated flaws, resulting in an array of values of $CPI_{(i,j,k)}$, for each *k*th flaw, where the value of $CPI_{(i,j,k)}$ is the *sup*-norm of the vector $\{cpi(\tau^n)_{(i,j,k)}\}$ (0.242 for the example in Table 2).

If $CPI_{(i,j,1)}$ is the *probability of initiation* of a flaw in an RPV trial that contains a single flaw, then $(1\text{-}CPI_{(i,j,1)})$ is the *probability of non-initiation*. If $CPI_{(i,j,1)}$ and $CPI_{(i,j,2)}$ are the *marginal* probabilities of initiation of two flaws in an RPV trial that contains two flaws, then $(1\text{-}CPI_{(i,j,1)})\times\ (1\text{-}CPI_{(i,j,2)})$ is the total probability of non-initiation, i.e., the joint probability that neither of the two flaws will fracture. This can be generalized to an RPV simulation with *nflaw* flaws, so that the total joint probability that none of the flaws will initiate is:

$$\begin{aligned}\left\{\begin{matrix}\text{Conditional probability}\\ \text{of non-initiation}\end{matrix}\right\}_{(i,j)} &= \prod_{k=1}^{nflaw}(1-CPI_{(i,j,k)})\\ &= (1-CPI_{(i,j,1)})(1-CPI_{(i,j,2)})\ldots(1-CPI_{(i,j,nflaw)})\end{aligned} \tag{12}$$

Therefore, for the *i*th transient and *j*th RPV trial with *nflaw* flaws, the total probability that at *least one of the flaws* will fracture is just the complement of Eq. (12):

$$\begin{aligned}CPI_{RPV(i,j)} &= 1\text{-}\prod_{k=1}^{nflaw}(1-CPI_{(i,j,k)})\\ &= 1-\left[\left(1-CPI_{(i,j,1)}\right)(1-CPI_{(i,j,2)})\ldots(1-CPI_{(i,j,nflaw)})\right]\end{aligned} \tag{13}$$

The method described here for combining the values of *CPI* for multiple flaws in an RPV is also used for combining the values of *nonfailure* to produce *CPFs* for multiple flaws.

3.3.11 Ductile-Tearing Models in FAVOR

Two ductile-tearing models have been implemented into FAVOR. Ductile-Tearing Model No. 1, implemented in the FAVOR, v04.1, is the recommended model to estimate the effects of ductile tearing in the *Initiation-Growth-Arrest* model. Ductile-Tearing Model No. 2 was implemented in FAVOR, v03.1, and is retained in the current release for the purposes of backward compatibility with previous analyses carried out using FAVOR, v03.1.

Ductile-tearing property data were obtained from the PTSE-1 [26] and PTSE-2 [27] studies carried out in the late 1980s along with additional data collected in [82-84] and applied in the model development. A summary of the major materials and data sources is presented in Table 4 along with the chemistry composition and relevant ductile-tearing properties in Tables 5 and 6.

Table 4. Sources for Ductile-Tearing Data [26, 27, 78, 79, 80, 116]

Materials	Reference
61-67W	NUREG/CR-3506
Midland Weld	NUREG/CR-5736
P02, 68-71W	NUREG/CR-4880
PTSE-1 Post Test	NUREG/CR-4106
PTSE-2 Post Test	NUREG/CR-4888
W8A & W9A	NUREG/CR-5492

Table 5. Chemical Composition of Materials Used in the Ductile-Tearing Model Development

HSST	Weld Flux	Chemistry Composition (wt %)									
ID	Lot ID	C	Mn	P	S	Si	Cr	Ni	Mo	Cu	V
Plate 02	(-)	0.230	1.550	0.009	0.014	0.200	0.040	0.670	0.530	0.140	0.003
Midland Beltine	Linde 80	0.083	1.607	0.017	0.006	0.622	0.100	0.574	0.410	0.256	0.006
Midland Nozzle	Linde 80	0.083	1.604	0.016	0.007	0.605	0.110	0.574	0.390	0.290	0.008
W8A	Linde 80	0.083	1.330	0.011	0.016	0.770	0.120	0.590	0.470	0.390	0.003
W9A	Linde 0091	0.190	1.240	0.010	0.008	0.230	0.100	0.700	0.490	0.390	
68W	Linde 0091	0.150	1.380	0.008	0.009	0.160	0.040	0.130	0.600	0.040	0.007
69W	Linde 0091	0.140	1.190	0.010	0.009	0.190	0.090	0.100	0.540	0.120	0.005
70W	Linde 0124	0.100	1.480	0.011	0.011	0.440	0.130	0.630	0.470	0.056	0.004
71W	Linde 80	0.120	1.580	0.011	0.011	0.540	0.120	0.630	0.450	0.046	0.005
61W	Linde 80 btwn A533B	0.090	1.480	0.020	0.014	0.570	0.160	0.630	0.370	0.280	0.005
62W	Linde 80 btwn A508	0.083	1.510	0.160	0.007	0.590	0.120	0.537	0.377	0.210	0.010
63W	Linde 80 btwn A508	0.098	1.650	0.016	0.011	0.630	0.095	0.685	0.427	0.299	0.011
64W	Linde 80 btwn A508	0.085	1.590	0.014	0.015	0.520	0.092	0.660	0.420	0.350	0.007
65W	Linde 80 btwn A508	0.080	1.450	0.015	0.015	0.480	0.088	0.597	0.385	0.215	0.006
66W	Linde 80 btwn A508	0.092	1.630	0.018	0.009	0.540	0.105	0.595	0.400	0.420	0.009
67W	Linde 80 btwn A508	0.082	1.440	0.011	0.012	0.500	0.089	0.590	0.390	0.265	0.007

Table 6. Summary of Ductile-Tearing Data Used in the Ductile-Tearing Model Development

Material ID	Size	Fluence 10^{19} n/cm^2	Temp. (°C)	J_{Ic} (kJ/m^2)	Avg. T_R (-)	Avg. USE (ft-lbf)	Material ID	Size	Fluence 10^{19} n/cm^2	Temp. (°C)	J_{Ic} (kJ/m^2)	Avg. T_R (-)	Avg. USE (ft-lbf)	Material ID	Size	Fluence 10^{19} n/cm^2	Temp. (°C)	J_{Ic} (kJ/m^2)	Avg. T_R (-)	Avg. USE (ft-lbf)
61W	0.8	0	75	142.3	89	62	64W	0.5	0.582	177	119.1	36	75	Mid-Belt	NA	0	21	167.4	71	65
61W	0.5	0	75	143.4	106	62	64W	4	0.66	200	78.7	50	75	Mid-Belt	NA	0	21	116.4	84	65
61W	0.8	0	121	123.9	74	62	64W	4	0.64	200	94.9	49	75	Mid-Belt	NA	0	21	131.4	76	65
61W	0.5	0	121	130.6	90	62	64W	1.6	0.623	200	57.3	46	75	Mid-Belt	NA	0	21	164.7	70	65
61W	4	0	200	97.4	100	62	64W	1.6	0.671	200	80.2	50	75	Mid-Belt	NA	0	150	133.4	41	65
61W	4	0	200	128.1	72	62	64W	0.8	0.773	200	101.9	31	75	Mid-Belt	NA	0	150	125.1	44	65
61W	1.6	0	200	78.3	70	62	64W	0.5	0.672	200	99.4	23	75	Mid-Belt	NA	0	150	141.1	60	65
61W	0.8	0	200	89.5	52	62	64W	0.8	0.773	288	46	15	75	Mid-Belt	NA	0	288	86.4	32	65
61W	0.5	0	200	89.1	66	62	64W	0.5	0.672	288	66.3	18	75	Mid-Belt	NA	0	288	103.3	33	65
61W	1.6	0	288	57.7	68	62	65W	1.6	0	132	123.4	120	108	Mid-Nozz	NA	0	21	126.6	47	64
61W	0.8	0	288	66.1	47	62	65W	0.8	0	132	147.2	97	108	Mid-Nozz	NA	0	21	113.0	57	64
61W	0.5	0	288	75	53	62	65W	0.5	0	132	118.5	130	108	Mid-Nozz	NA	0	150	102.8	39	64
61W	0.5	0	288	76.5	53	62	65W	4	0	177	80.4	138	108	Mid-Nozz	NA	0	150	89.9	43	64
61W	0.8	1.1	121	103.1	51	52	65W	0.8	0	177	117.6	76	108	Mid-Nozz	NA	0	288	69.1	32	64
61W	1.6	1.3	121	83	41	52	65W	0.5	0	177	114.8	102	108	Mid-Nozz	NA	0	288	64.5	39	64
61W	0.5	1.6	121	76.4	22	52	65W	4	0	200	69.3	114	108	Mid-Nozz	NA	0	288	64.3	37	64
61W	0.5	1	200	96.4	60	52	65W	1.6	0	200	104.1	72	108	Plate 02	NA	0	50	117.3	197	105
61W	4	1.1	200	52.4	38	52	65W	0.8	0	200	128.9	84	108	Plate 02	NA	0	50	189.9	164	105
61W	1.6	1.2	200	63.6	31	52	65W	0.5	0	200	94.8	111	108	Plate 02	NA	0	50	191.8	154	105
61W	0.8	1.2	200	69.5	44	52	65W	4	0	288	120.1	73	108	Plate 02	NA	0	50	205.1	141	105
61W	4	1.4	200	61.3	30	52	65W	1.6	0	288	71.9	73	108	Plate 02	NA	0	50	218.9	153	105
61W	0.8	1.1	288	46.4	15	52	65W	1.6	0	288	74.2	69	108	Plate 02	NA	0	121	111.0	156	105
61W	0.5	1.4	288	44.6	17	52	65W	0.8	0	288	73.5	56	108	Plate 02	NA	0	121	137.1	178	105
62W	0.5	0	75	121.7	119	93	65W	0.5	0	288	83.8	69	108	Plate 02	NA	0	121	161.7	147	105
62W	1.6	0	149	114.5	124	93	65W	1.6	0.67	132	106.2	77	72	Plate 02	NA	0	121	168.3	133	105
62W	0.8	0	149	150.1	139	93	65W	0.8	0.744	132	113.6	54	72	Plate 02	NA	0	121	171.4	138	105
62W	0.5	0	149	91.4	99	93	65W	0.5	0.767	132	110.3	48	72	Plate 02	NA	0	204	132.1	118	105
62W	4	0	177	107.6	154	93	65W	4	0.74	177	53.1	89	72	Plate 02	NA	0	204	134.7	99	105
62W	0.8	0	177	160.3	115	93	65W	0.8	0.744	177	104.8	45	72	Plate 02	NA	0	204	139.2	115	105
62W	0.5	0	177	101	94	93	65W	0.5	0.629	177	114.7	47	72	Plate 02	NA	0	204	140.4	113	105
62W	4	0	200	145.5	140	93	65W	4	0.61	200	85.6	61	72	Plate 02	NA	0	204	181.0	100	105
62W	1.6	0	200	154.4	117	93	65W	1.6	0.62	200	70.4	56	72	Plate 02	NA	0	288	111.8	81	105
62W	1.6	0	200	128.7	133	93	65W	0.8	0.756	200	91.5	41	72	Plate 02	NA	0	288	112.1	73	105
62W	0.8	0	200	150.8	99	93	65W	0.5	0.629	200	107	54	72	Plate 02	NA	0	288	118.1	92	105
62W	0.5	0	200	78.4	83	93	65W	0.8	0.756	288	41	23	72	Plate 02	NA	0	288	121.9	73	105
62W	0.5	0	200	113.8	87	93	65W	0.5	0.767	288	43.9	32	72	Plate 02	NA	0	288	132.6	89	105
62W	4	0	288	87.3	112	93	66W	0.5	0	100	94.4	41	76	68W	NA	0	23	160.1	219	147
62W	1.6	0	288	101	118	93	66W	1.6	0	200	67	55	76	68W	NA	0	121	151.1	204	147
62W	0.8	0	288	93.8	59	93	66W	0.8	0	200	103.6	50	76	68W	NA	0	121	196.9	204	147
62W	0.5	0	288	83.6	59	93	66W	0.5	0	200	73	42	76	68W	NA	0	200	223.5	111	147
62W	0.5	0	288	85	84	93	66W	0.8	0	288	73.8	40	76	68W	NA	0	288	121.3	132	147

Table 6. (cont.) Summary of Ductile-Tearing Data Used in the Ductile-Tearing Model Development

Material ID	Size	Fluence 10^{19} n/cm^2	Temp. (°C)	J_{Ic} (kJ/m^2)	Avg. T_R (-)	Avg. USE (ft-lbf)
62W	1.6	1.4	149	118.3	60	80
62W	0.8	1.3	149	118.7	91	80
62W	0.5	1.6	149	96.2	32	80
62W	0.5	1.3	176	94.1	50	80
62W	4	1.4	177	105.9	62	80
62W	0.8	1.5	177	127.4	45	80
62W	0.5	0.8	177	95.9	34	80
62W	4	1.5	200	90	62	80
62W	1.6	1.6	200	85	52	80
62W	0.8	1.3	200	115.9	69	80
62W	0.5	1	200	63.3	29	80
62W	0.8	1.5	288	60.9	24	80
62W	0.5	1.5	288	61.9	24	80
63W	1.6	0	100	118	120	87
63W	0.8	0	100	141.2	95	87
63W	0.5	0	100	131.1	86	87
63W	4	0	171	148.4	100	87
63W	1.6	0	171	103.5	97	87
63W	0.8	0	171	112.4	77	87
63W	0.5	0	171	113.2	88	87
63W	4	0	200	77.7	113	87
63W	1.6	0	200	79.6	94	87
63W	0.8	0	200	120.3	69	87
63W	0.5	0	200	89.2	70	87
63W	0.5	0	200	98.4	80	87
63W	4	0	288	88.4	62	87
63W	1.6	0	288	122.4	64	87
63W	0.8	0	288	66.8	57	87
63W	0.5	0	288	59.1	55	87
63W	0.5	0	288	66.7	52	87
63W	0.5	1.1	149	68.4	43	68
63W	1.6	1.3	171	79.2	49	68
63W	0.8	1.1	171	89.7	32	68
63W	0.5	1.3	171	78.9	27	68
63W	4	1.25	200	72.7	16	68
63W	1.6	1.4	200	62.2	29	68
63W	0.8	1.1	200	75.8	33	68
63W	0.5	0.9	200	77	49	68
63W	0.5	1	204	56.3	42	68
63W	0.8	1.4	288	42.7	19	68
63W	0.5	1.2	288	51.5	23	68
64W	1.6	0	100	105.7	148	100
64W	0.8	0	100	160.4	105	100
64W	0.5	0	100	116	89	100
64W	4	0	177	117.4	146	100
64W	1.6	0	177	134.6	103	100
64W	0.8	0	177	114.9	83	100
64W	0.5	0	177	125	73	100
64W	4	0	200	161.4	96	100
64W	1.6	0	200	67.8	97	100
64W	0.8	0	200	118.8	76	100
64W	0.5	0	200	115.8	54	100
64W	4	0	288	85.5	96	100
64W	1.6	0	288	76.6	83	100
64W	0.8	0	288	75.9	54	100
64W	0.5	0	288	74.2	44	100
64W	0.8	0.773	177	92.9	37	75

Material ID	Size	Fluence 10^{19} n/cm^2	Temp. (°C)	J_{Ic} (kJ/m^2)	Avg. T_R (-)	Avg. USE (ft-lbf)
66W	0.5	0	288	61.9	25	76
66W	1.6	0.854	200	68.4	31	58
66W	1.6	0.944	200	66.4	29	58
66W	0.8	1.022	200	75.2	22	58
66W	0.5	0.896	200	67.4	18	58
66W	0.8	1.03	288	42.8	17	58
66W	0.5	0.896	288	51.6	16	58
67W	1.6	0	100	130.4	164	103
67W	0.8	0	100	166.5	112	103
67W	0.5	0	100	132.8	98	103
67W	4	0	200	97.4	121	103
67W	1.6	0	200	84.1	116	103
67W	0.8	0	200	118	85	103
67W	0.5	0	200	102.1	76	103
67W	0.5	0	200	92	69	103
67W	4	0	288	97.9	58	103
67W	1.6	0	288	63.4	83	103
67W	0.8	0	288	82.6	56	103
67W	0.5	0	288	80	51	103
67W	4	0.86	200	67.3	45	73
67W	4	0.96	200	56.7	57	73
67W	0.8	1.022	200	76.3	45	73
67W	0.5	0.834	200	92.2	32	73
67W	0.8	1.03	288	58.6	23	73
67W	0.5	0.617	288	80	24	73
W8A	1	0	0	104.4	72	58
W8A	1	0	75	94.4	81	58
W8A	1	0	200	79.7	57	58
W8A	1	0	288	58.6	34	58
W8A	1	2.1	125	69.9	16	36
W8A	1	2.1	200	54.1	14	36
W8A	1	2.1	288	38.6	9	36
W8A	1	1.5	30	80.8	54	40
W8A	1	1.5	75	84.6	28	40
W8A	1	1.5	200	60	17	40
W8A	1	1.5	200	57.4	18	40
W8A	1	1.5	288	41.6	11	40
W9A	1	0	-40	207.4	NA	115
W9A	1	0	0	255	173	115
W9A	1	0	75	195.9	170	115
W9A	1	0	200	147.9	130	115
W9A	1	0	288	92.9	120	115
W9A	1	0	288	116	97	115
W9A	1	2.1	75	156.2	42	74
W9A	1	2.1	200	124.1	37	74
W9A	1	2.1	200	147.7	40	74
W9A	1	2.1	288	81.5	31	74
W9A	1	1.5	75	167.7	52	84
W9A	1	1.5	200	146.4	46	84
W9A	1	1.5	200	127.2	47	84
W9A	1	1.5	288	96.1	36	84
PTSE-2	NA	0	100	64	120	46.4
PTSE-2	NA	0	100	55.6	145	46.4
PTSE-2	NA	0	175	58.3	106	46.4
PTSE-2	NA	0	175	68.4	105	46.4
PTSE-2	NA	0	250	52.8	67	46.4
PTSE-2	NA	0	250	52.2	61	46.4

Material ID	Size	Fluence 10^{19} n/cm^2	Temp. (°C)	J_{Ic} (kJ/m^2)	Avg. T_R (-)	Avg. USE (ft-lbf)
68W	NA	0	288	190.7	138	147
69W	NA	0	50	143.0	87	147
69W	NA	0	50	147.9	80	147
69W	NA	0	50	163.7	70	147
69W	NA	0	121	139.5	89	147
69W	NA	0	121	141.7	93	147
69W	NA	0	121	142.7	82	147
69W	NA	0	121	158.9	88	147
69W	NA	0	200	174.5	54	147
69W	NA	0	204	98.9	76	147
69W	NA	0	204	117.5	61	147
69W	NA	0	288	89.7	56	147
69W	NA	0	288	94.1	49	147
69W	NA	0	288	103.8	56	147
69W	NA	0	288	129.4	56	147
70W	NA	0	50	106.2	188	74
70W	NA	0	50	177.8	163	74
70W	NA	0	121	127.5	159	74
70W	NA	0	121	131.1	148	74
70W	NA	0	121	142.8	140	74
70W	NA	0	204	103.3	108	74
70W	NA	0	204	112.0	133	74
70W	NA	0	204	121.0	110	74
70W	NA	0	288	89.0	79	74
70W	NA	0	288	105.6	93	74
70W	NA	0	288	106.2	88	74
71W	NA	0	30	128.0	186	81
71W	NA	0	50	97.9	144	81
71W	NA	0	50	121.0	98	81
71W	NA	0	121	110.8	153	81
71W	NA	0	121	126.7	105	81
71W	NA	0	121	131.0	155	81
71W	NA	0	204	77.6	66	81
71W	NA	0	204	84.7	87	81
71W	NA	0	204	115.4	90	81
71W	NA	0	288	64.5	72	81
71W	NA	0	288	77.4	71	81
71W	NA	0	288	80.2	61	81

In conjunction with the ductile-tearing model development, a revised fracture arrest toughness stochastic model has also been implemented in FAVOR. A discussion of this new arrest model is given in Sect. 4.2.8.

One of the constraints in developing a ductile-tearing model for FAVOR is that the required material properties should currently be available for the four plants being studied in the PTS Re-evaluation project. The relevant information available from RVID2 [129] includes Cu, Ni, and P content; the upper-shelf Charpy V-notch (CVN) energy, *USE*; and the unirradiated flow stress of the RPV steels. Consequently, all ductile fracture toughness properties used in FAVOR need to be derived from this information.

The following models are required:

- a model for the variation of ductile crack initiation toughness, J_{Ic} , with temperature and irradiation, and
- a model for the variation of ductile-tearing resistance as a function of temperature, irradiation, and accumulated ductile tearing, Δa .

These two models are connected in that they both can be derived from a J_R curve, expressed in a power-law model form by:

$$J_R = C(\Delta a^m) \tag{14}$$

where the tearing resistance is characterized by the material's local tearing modulus, T_R, defined by

$$T_R = \left(\frac{E}{\sigma_f^2}\right)\left(\frac{dJ_R}{da}\right) = \left(\frac{E}{\sigma_f^2}\right) \times m \times C \times \Delta a^{(m-1)} \tag{15}$$

Given the elastic modulus, E, and sampled irradiated flow stress, σ_f , the remaining three variables required by the ductile-tearing model are J_{Ic}, C, and m, where all three are a function of temperature and level of irradiation damage.

Applying the definition of J_{Ic} in ASTM E-1820 [81], estimates of two of the variables allows the calculation of the third. In Fig. 15, the ductile-tearing initiation toughness, J_{Ic}, is defined in ASTM E-1820 as the intersection of the J_R curve with a 0.2 mm offset blunting line given by

$$J_{(0.2\text{ mm offset})} = 2\sigma_f(\Delta a - \Delta a_0) \tag{16}$$

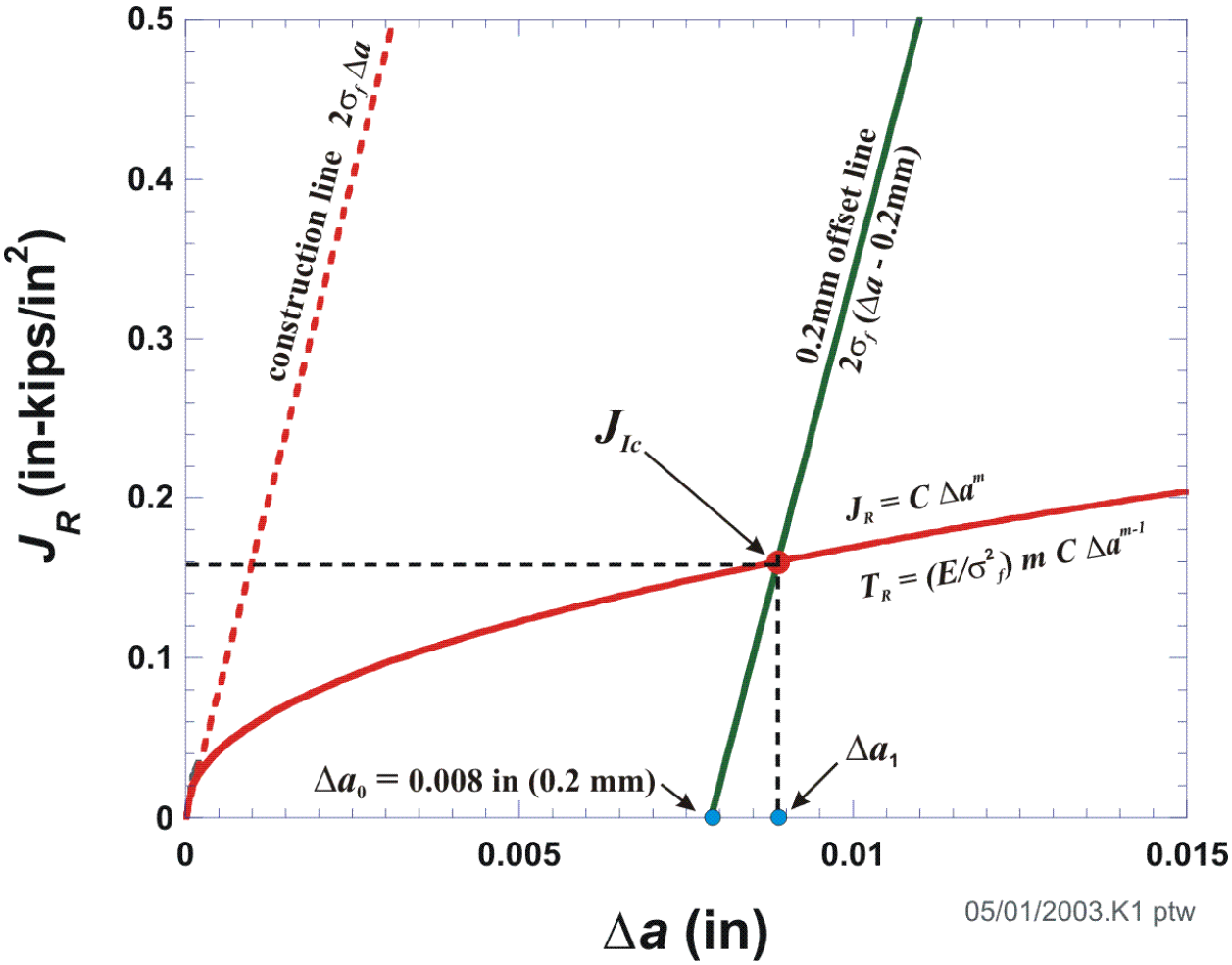

Fig. 15. Given a J_R curve in power-law model form and current flow stress, σ_f, the initiation toughness, J_{Ic}, and local tearing modulus, T_R, are uniquely defined (see ASTM E-1820 [81]).

where the prescribed offset is $\Delta a_0 = 0.2\text{ mm}\ (0.008\text{ in})$. Therefore, with an estimate of J_{Ic} and the power-law exponent, m, the power-law coefficient, C, is

$$J_{Ic} = C\Delta a^m \Rightarrow C = \frac{J_{Ic}}{\Delta a^m}$$

$$J_{Ic} = 2\sigma_f(\Delta a - \Delta a_0) \Rightarrow \Delta a = \frac{J_{Ic}}{2\sigma_f} + \Delta a_0 \tag{17}$$

$$\therefore\ C = \frac{J_{Ic}}{\left(\dfrac{J_{Ic}}{2\sigma_f} + \Delta a_0\right)^m}$$

The local tearing modulus then follows from Eq. (15). The focus of model development was, therefore, placed on providing methods of estimating the initiation fracture toughness, J_{Ic}, and the power-law exponent, m, as a function of temperature and irradiation damage.

3.3.11.1 Ductile-Tearing Model No. 1 (implemented in FAVOR, v04.1)

The recommended Ductile-Tearing Model No. 1 was developed from the research described in [82,83]. The following is a summary of the model described in these references.

A model of ferritic steel toughness that accounts for fracture mode transition behavior, upper shelf behavior, and the interaction between these two different fracture modes can be constructed based on Wallin's Master Curve [124], the relationship between the upper-shelf temperature, T_{US}, the Master Curve reference temperature, T_0, and the upper-shelf Master Curve. Using these relationships it is possible, as described below, to estimate the complete variation of initiation fracture toughness, J_{Ic}, with temperature in both the transition regime and on the upper shelf based only on an estimate of T_0.

The following sampling protocols are taken from [83]:

<u>Step 1. – Estimate a Value for T_0</u>

Given a sampled value of $\widehat{RT}_{NDT0}\left[°\mathrm{F}\right]$, adjusted for the effects of irradiation damage, an estimate for T_0 (for a reference size of 1T) can be sampled using Eq. (89) (see Sect. 4.2.5)

$$\widehat{T}_0 = \frac{\left\langle \widehat{RT}_{NDT-DT} + 27.82 - \left\{ 122.4 \left[\left(-\ln(1-P_{T_0}) \right)^{\frac{1}{2.25}} \right] \right\} \right\rangle - 32}{1.8} \quad \left[°\mathrm{C}\right] \tag{18}$$

Where $\widehat{RT}_{NDT-DT}\left(r,\ldots\right) = \widehat{RT}_{NDT0} + \widehat{\Delta RT}_{NDT}\left(r,\ldots\right)$, (see Eq. (91)) with $\widehat{RT}_{NDT0}$ equal to the sampled unirradiated value of $RT_{NDT,}$ $\widehat{\Delta RT}_{NDT}\left(r,\ldots\right)$ equal to the shift due to radiation embrittlement, and $P_{T_0} = \Phi$ is the fractile drawn for the epistemic uncertainty in RT_{NDT} in Eq. (90).

<u>Step 2. – Estimate a Value for the Upper-Shelf Temperature, T_{US}</u>

From the relationship developed in [83], an estimate for the upper-shelf temperature associated with this sampled value for T_0 can be calculated from

$$\widehat{T}_{US} = 50.1 + \left(0.794\,\widehat{T}_0\right) \quad \left[°\mathrm{C}\right] \tag{19}$$

Step 3. – Calculate a Value for J_C Using the Master Curve at T_{US}

Using a plane strain conversion from K_{Jc} to J_c, we have, from the Master Curve model [124]

$$J_{c(med)} = \frac{1000\left\{30 + 70\exp\left[0.019\left(T_{US} - T_0\right)\right]\right\}^2\left(1-\nu^2\right)}{E} \quad \left[\frac{\text{kJ}}{\text{m}^2}\right]$$

where (20)

$$E = 207200 - \left(57.1\,T_{US}\right) \quad [\text{MPa}] \text{ and } \nu = 0.3$$

Step 4. – Calculate an Estimate for ΔJ_{Ic} at T_{US}

Using the relationship derived in [83] to characterize the temperature dependence of J_{Ic}

$$\Delta J_{Ic} = J_{Ic}^{meas} - J_{Ic}^{288°\text{C}} = 2.09\left\{C_1 \exp\left[-C_2\left(T_{US} + 273.15\right) + C_3\left(T_{US} + 273.15\right)\ln\left(\dot{\varepsilon}\right)\right] - \sigma_{ref}\right\} \tag{21}$$

where $C_1 = 1033$ MPa, $C_2 = 0.00698$ K^{-1}, $\dot{\varepsilon} = 0.0004$ sec^{-1}, $C_3 = 0.000415$ K^{-1}, $\sigma_{ref} = 3.3318$ MPa

Step 5. – Calculate an Estimated Mean and Standard Deviation for the Aleatory Uncertainty in J_{Ic}

At a given wall temperature, $T_{wall}(R,t)$ [°C], an estimated mean value for J_{Ic} can now be estimated by

$$\overline{J_{Ic}} = J_{c(med)} - \Delta J_{Ic} + 2.09\left\{C_1 \exp\left[-C_2\left(T_{wall} + 273.15\right) + C_3\left(T_{wall} + 273.15\right)\ln\left(\dot{\varepsilon}\right)\right] - \sigma_{ref}\right\} \quad \left[\frac{\text{kJ}}{\text{m}^2}\right] \tag{22}$$

Where an estimate for the standard deviation is given in [83] by

$$\sigma_{J_{Ic}} = 62.023\exp\left(-0.0048\,T_{wall}\right) \quad \left[\frac{\text{kJ}}{\text{m}^2}\right] \tag{23}$$

Step 6. – Sample a Value for J_{Ic} from a Normal Distribution

The aleatory uncertainty in J_{Ic} is now estimated by sampling from the following normal distribution

$$\widehat{J}_{Ic} \leftarrow N\left(\overline{J_{Ic}}, \sigma_{J_{Ic}}\right) \quad \left[\frac{\text{kJ}}{\text{m}^2}\right] \tag{24}$$

where the sampled value is truncated at $\overline{J_{Ic}} - 2\sigma_{J_{Ic}} \le \hat{J}_{Ic} \le \overline{J_{Ic}} + 2\sigma_{J_{Ic}}$ using the truncation protocol of Sect. 3.3.6.

<u>Step 7. – Calculate an Estimate for the Power-Law Exponent, *m*, and Coefficient, *C*</u>

The mean value of the *J-R* curve exponent *m* (as in $J_R = C\left(\Delta a^m\right)$) is estimated based on the sampled value of J_{Ic} and the local value of the wall temperature, $T_{wall}(R,t)$, from the following equation (developed from the data given in [83])

$$\begin{gathered} \overline{m} = a + b\exp\left(\frac{T_{wall}\left[^\circ\mathrm{C}\right]}{d}\right) + c\left(\hat{J}_{Ic}\left[\mathrm{kJ/m^2}\right]\right)^3 \\ a = 0.1117 \quad c = 5.8701\times10^{-09} \\ b = 0.4696 \qquad d = -758.19 \\ \sigma_{\text{std-error}} = 0.08425 \\ R^2 = 0.2992 \end{gathered} \tag{25}$$

The *J-R* curve exponent *m* with aleatory uncertainty can then be sampled from the following normal distribution:

$$\hat{m} \leftarrow N(\overline{m}, 0.08425) \tag{26}$$

The *J-R* curve coefficient, *C*, then follows from

$$\hat{C} = \frac{\hat{J}_{Ic\ (\text{at } T_{wall})}}{\left(\dfrac{\hat{J}_{Ic\ (\text{at } T_{wall})}}{2\hat{\sigma}_f} + \Delta a_0\right)^{\hat{m}}} \tag{27}$$

where $\hat{\sigma}_f$ is the sampled flow stress and $\Delta a_0 = 0.2\ \mathrm{mm}$.

3.3.11.2 Ductile-Tearing Model No. 2 (implemented in FAVOR, v03.1)

Pursuant to the proposal in [84], a preliminary ductile-tearing model was developed and implemented into FAVOR, v03.1, for a scoping study of the effects of tearing resistance associated with RPV materials.

3.3.11.2.1 Upper-Shelf Irradiation Effects Model

The following discussion is taken from [84]:

To date, efforts to trend the effects of irradiation damage on RPV steels have focused predominantly on predicting the joint effects of radiation (as quantified by the fast-neutron fluence, energy > 1 MEv)

and chemical composition on the energy absorbed by a Charpy V-notch (CVN) specimen on the upper shelf (i.e., the upper shelf energy, or *USE*). This focus occurs because CVN specimens are placed into surveillance capsules that are used to assess the effect of irradiation damage on the RPV steel. It should be emphasized that the *USE* is ***not*** the initiation fracture toughness (J_{Ic}) or the tearing modulus (T_R) information needed by FAVOR to assess the probability of through-wall cracking of the RPV arising from a PTS event. Nevertheless, without significant additional research the only way to predict the effect of irradiation on J_{Ic} and T_R is to first predict the effect of irradiation on *USE* and then correlate J_{Ic} and T_R with *USE*.

In 1998, Eason, Wright, and Odette [85, 86] proposed the following relation between *USE*, chemical composition, and fluence based on the *USE* data available from domestic nuclear RPV surveillance programs at that time (692 data records) (NUREG/CR-6551) [86]. This model is given by the following equation

$$USE_{(i)} = A + 0.0570 \cdot USE_{(u)}^{1.456} - \left[17.5 \cdot f\left(Cu\right) \cdot \left(1 + 1.17 Ni^{0.8894}\right) + 305P\right]\left(\frac{\phi t}{10^{19}}\right)^{0.2223} \quad \text{[ft-lbf]} \qquad (28)$$

where USE_u is the unirradiated upper-shelf energy in ft-lbf; *Cu*, *Ni*, and *P* are the copper, nickel, and phosphorous content in wt %; ϕt is the fast-neutron fluence in neutrons/cm^2; *A* is a product-form constant; and *f*(*Cu*) is a function of copper content defined as

$$A = \begin{cases} 55.4 & \text{for welds} \\ 61.0 & \text{for plates} \\ 66.3 & \text{for forgings} \end{cases}$$

$$f\left(Cu\right) = \frac{1}{2} + \frac{1}{2}\tanh\left[\frac{Cu - 0.138}{0.0846}\right]$$

Reference [84] proposes the following method to simulate upper-shelf energies and address uncertainties in $USE_{(u)}$:

Step 1. Input a best-estimate value for the unirradiated upper-shelf energy for a given major region in the FAVOR embrittlement map of the beltline. Treat this value as the mean of a normal distribution of $USE_{(u)}$ values, $\mu_{USE_{(u)}}$.

Step 2. At this value of $\mu_{USE_{(u)}}$, sample a value for the standard deviation from a normal distribution given by

$$\begin{aligned} \sigma_{USE_{(u)}(mean)} &= 4.3296 - 0.0857\mu_{USE_{(u)}} + 0.0012\mu_{USE_{(u)}}^2 \\ \widehat{\sigma}_{USE_{(u)}} &\leftarrow N(\sigma_{USE_{(u)}(mean)}, 2.2789) \end{aligned} \qquad (29)$$

Step 3. Sample a value for the unirradiated upper-shelf energy, $\widehat{USE}_{(u)}$, from the following normal distribution

$$\widehat{USE}_{(u)} \leftarrow N(\mu_{USE_{(u)}}, \widehat{\sigma}_{USE_{(u)}}) \tag{30}$$

Step 4. The irradiated value for the upper-shelf energy is then estimated from Eq. (28), or, applying sampling notation:

$$\widehat{USE}_{(i)} = A + 0.0570 \cdot \widehat{USE}_{(u)}^{1.456} - \left[17.5 \cdot f\left(\widehat{Cu}\right) \cdot \left(1 + 1.17\widehat{Ni}^{0.8894}\right) + 305\widehat{P}\right]\left(\frac{\widehat{\phi t}}{10^{19}}\right)^{0.2223} \quad \text{[ft-lbf]} \tag{31}$$

where the chemistry and attenuated fluence have been previously sampled.

3.3.11.2.2 Model for Initiation Ductile Fracture Toughness, J_{Ic}

The sampling protocol for J_{Ic} developed in [84] is as follows:

Step 1. Determine a value of $\widehat{USE}_{(u)}$ using the sampling protocol outlined in Sect. 3.3.11.2.1 and Eqs. (29) and (30).

Step 2. Apply this sampled value of $\widehat{USE}_{(u)}$ along with sampled values of $\widehat{Cu}$, $\widehat{Ni}$, $\widehat{P}$ and $\widehat{\phi t}$ to estimate a value of $\widehat{USE}_{(i)}$ using Eq. (31).

Step 3. Convert this estimate of $\widehat{USE}_{(i)}$ value to a value of $\widehat{K}_{J_{Ic}(i)(\text{at } 550°\text{F})}$ at 550°F using the mean curve established in [84], where the uncertainty in $\widehat{K}_{J_{Ic}(i)(\text{at } 550°\text{F})}$ is ***not*** sampled,

$$\widehat{K}_{J_{Ic}(i)(\text{at } 550°\text{F})} = 70.855 + \left(0.5784 \times \widehat{USE}_{(i)}\right) \quad [\text{ksi}\sqrt{\text{in}}] \tag{32}$$

Step 4. Convert the $\widehat{K}_{J_{Ic}(i)(\text{at } 550°\text{F})}$ value to a $\widehat{K}_{J_{Ic}(i)(\text{at } T_{wall})}$ value at the wall temperature of interest using the mean curve from [84]:

$$\begin{aligned} \widehat{\Delta K}_{J_{Ic}} &= K_{J_{Ic}(\text{at } T_{wall})} - \widehat{K}_{J_{Ic}(\text{at } 550°\text{F})} = \\ &= 1.35\left\{1033 \cdot \exp\left[\begin{array}{c} 0.000415\left(\dfrac{T_{wall} + 459.69}{1.8}\right) \cdot \ln\left(0.0004\right) \\ -0.00698\left(\dfrac{T_{wall} + 459.69}{1.8}\right) \end{array}\right] - \sigma_{ref}\right\} \quad [\text{ksi}\sqrt{\text{in}}] \end{aligned} \tag{33}$$

where σ_{ref} is

$$\sigma_{ref} = 1033 \cdot \exp\left[\begin{array}{c} 0.000415\left(\dfrac{550 + 459.69}{1.8}\right) \cdot \ln\left(0.0004\right) \\ -0.00698\left(\dfrac{550 + 459.69}{1.8}\right) \end{array}\right] = 3.331798 \tag{34}$$

and T_{wall} is the wall temperature at the crack tip in °F. Therefore

$$\hat{K}_{J_{Ic}(\text{at } T_{wall})} = \hat{K}_{J_{Ic}(\text{at } 550°\text{F})} + \hat{\Delta K}_{J_{Ic}} \qquad [\text{ksi}\sqrt{\text{in}}] \tag{35}$$

The required sampled value of J_{Ic} follows from the plane strain conversion

$$\hat{J}_{Ic(\text{at } T_{wall})} = \left(\frac{1-\nu^2}{E}\right)\hat{K}^2_{J_{Ic}(\text{at } T_{wall})} \quad [\text{in-kips/in}^2] \tag{36}$$

3.3.11.2.3 Model for Normalized Average Tearing Resistance, T_{mat} , and J_R Curve Power-Law Exponent, m

In the analysis of ductile-tearing data in [84], the exponent, m, of the J_R power-law curve (see Eq. (14)) has been correlated with the material's estimated value for the average tearing modulus, T_{mat} , which is the normalized linear slope of all the J-Δa data between the 0.15 and 1.5 mm exclusion lines in the ASTM E-1820 determination of J_{Ic}.

The sampling protocol for estimating a value for T_{mat} is the following:

Step 1. Determine a value of $\hat{USE}_{(u)}$ using the sampling protocol outlined in Sect. 3.3.11.2.1 and Eqs. (29) and (30).

Step 2. Apply this sampled value of $\hat{USE}_{(u)}$ along with sampled values of $\hat{Cu}$, $\hat{Ni}$, $\hat{P}$ and $\hat{\phi t}$ to estimate a value of $\hat{USE}_{(i)}$ using Eq. (31).

Step 3. Convert this estimate of $\hat{USE}_{(i)}$ value to a value of $\hat{T}_{mat(i)(\text{at } 550°\text{F})}$ at 550 °F using the mean curve established in [84], where the uncertainty in $\hat{T}_{mat(i)(\text{at } 550°\text{F})}$ is ***not*** sampled

$$\hat{T}_{mat(i)(\text{at } 550°\text{F})} = 3.9389 + \left(0.5721 \times \hat{USE}_{(i)}\right) \tag{37}$$

Step 4. Convert the $\hat{T}_{mat(i)(\text{at } 550°\text{F})}$ value to a $\hat{T}_{mat(i)(\text{at } T_{wall})}$ value at the wall temperature of interest using the mean curve from [84]:

$$\hat{\Delta T}_{mat} = T_{mat(i)(\text{at } T_{wall})} - \hat{T}_{mat(i)(\text{at } 550°\text{F})} =$$

$$= 1.38\left\{1033 \cdot \exp\left[\begin{array}{c} 0.000415\left(\dfrac{T_{wall}+459.69}{1.8}\right)\cdot \ln\left(0.0004\right) \\ -0.00698\left(\dfrac{T_{wall}+459.69}{1.8}\right) \end{array}\right] - \sigma_{ref}\right\} \quad [-] \tag{38}$$

where σ_{ref} is

$$\sigma_{ref} = 1033 \cdot \exp\left[\begin{array}{c} 0.000415\left(\dfrac{550+459.69}{1.8}\right)\cdot \ln\left(0.0004\right) \\ -0.00698\left(\dfrac{550+459.69}{1.8}\right) \end{array}\right] = 3.331798 \tag{39}$$

and T_{wall} is the wall temperature at the crack tip in °F. Therefore

$$\widehat{T}_{mat(i)(\text{at } T_{wall})} = \widehat{T}_{mat(i)(\text{at } 550°\text{F})} + \Delta T_{mat} \qquad [-] \tag{40}$$

Step 5. Calculate an estimated value of the J_R power-law exponent, m, using the correlation developed in [84], where the uncertainty in $\widehat{m}$ is not sampled.

$$\widehat{m} = 0.3214 + \left(0.0019 \times \widehat{T}_{mat(i)}\right) \tag{41}$$

Step 6. Calculate a value for the J_R power-law coefficient, C, from the definition of J_{Ic} in ASTM E-1820

$$\widehat{C} = \frac{\widehat{J}_{Ic(i)(\text{at } T_{wall})}}{\left(\dfrac{\widehat{J}_{Ic(i)(\text{at } T_{wall})}}{2\widehat{\sigma}_f} + \Delta a_0\right)^{\widehat{m}}} \tag{42}$$

where $\Delta a_0 = 0.2 \text{ mm } (0.008 \text{ in})$ and $\widehat{\sigma}_f$ is the sampled flow stress.

3.3.12 Initiation-Growth-Arrest (*IGA*) Submodel

As shown in Fig. 16, after the value of *CPI* has been calculated for the current flaw and transient, the conditional probability of vessel failure, *CPF*, by through-wall cracking is determined by the flaw Initiation-Growth-Arrest (*IGA*) submodel. The *IGA* submodel may be viewed as a small Monte Carlo model nested within the larger PFM Monte Carlo model. The following steps in the *IGA* submodel are shown in Fig. 17a:

Step G1. The *IGA* submodel is entered from the *PFM* model with a given flaw and transient. The *IGA* trial counter, *NTRIAL*, is initialized to zero. The pointer to the vector holding the random number sequence containing the values of P_f [6] is reset to 1. Each transient for this flaw will start with the same random number sequence for internal sampling; however, each flaw has a different vector of random numbers. Go to Step G2.

Step G2. The *NTRIAL* counter is incremented; the time-step counter *NSTEP* is initialized to zero; and a random number P_f is drawn from a uniform distribution on the open interval (0,1). Go to Step G3.

Step G3. The time-step counter is incremented up to the time step corresponding to when CPI occurred; time advances to the next time step. Go to Step G4.

Step G4. For the given flaw, subjected to the current transient, the change in *cpi* with respect to time is checked. If $\mathrm{d}cpi/dt > 0$, then the flaw becomes a candidate for propagation through the wall. (This submodel will be described in detail in the following.) If $\mathrm{d}cpi/\mathrm{d}t \le 0$, then control branches to Step G8.

Step G5. The *IGA Propagation* submodel is entered for this flaw, providing the submodel with the current time step, flaw depth, and value of P_f. Go to Step G6.

Step G6. Control returns from the *IGA Propagation* submodel with the fate of the flaw, either a vessel failure or a stable arrest (no failure). If a vessel failure occurred, control is transferred to Step G7. If a stable arrest occurred, control is transferred to Step G8.

Step G7. The vessel failure counter, *NFAIL*(*NSTEP*), for this time step is incremented. Go to Step G8.

Step G8. If the transient has completed, i.e., $NSTEP > NSTEP_{CPI}$, branch to Step G9. If the transient is not finished, cycle to Step G3. Note that $NSTEP_{CPI} = NSTEP$ at which $cpi(t) = \|cpi(t)\|_\infty = CPI$.

---

[6] The value of P_f represents the percentile used in sampling ΔRT_{ARREST} (see Step 11 in Sect. 4.5) and K_{Ia} (see Step 15 in Sect. 4.5) in Step P6 and in sampling K_{Ic} in Step P8 of the *IGA Propagation Submodel*, and is used to ensure that the calculated initiation and failure probabilities are not affected by the order in which transients are analyzed. The *IGA Propagation Submodel* is an embedded Monte Carlo model that is repeated a user-set number of times using a different value of P_f each time. See the discussion in the final paragraph of Sect. 3.3.1.

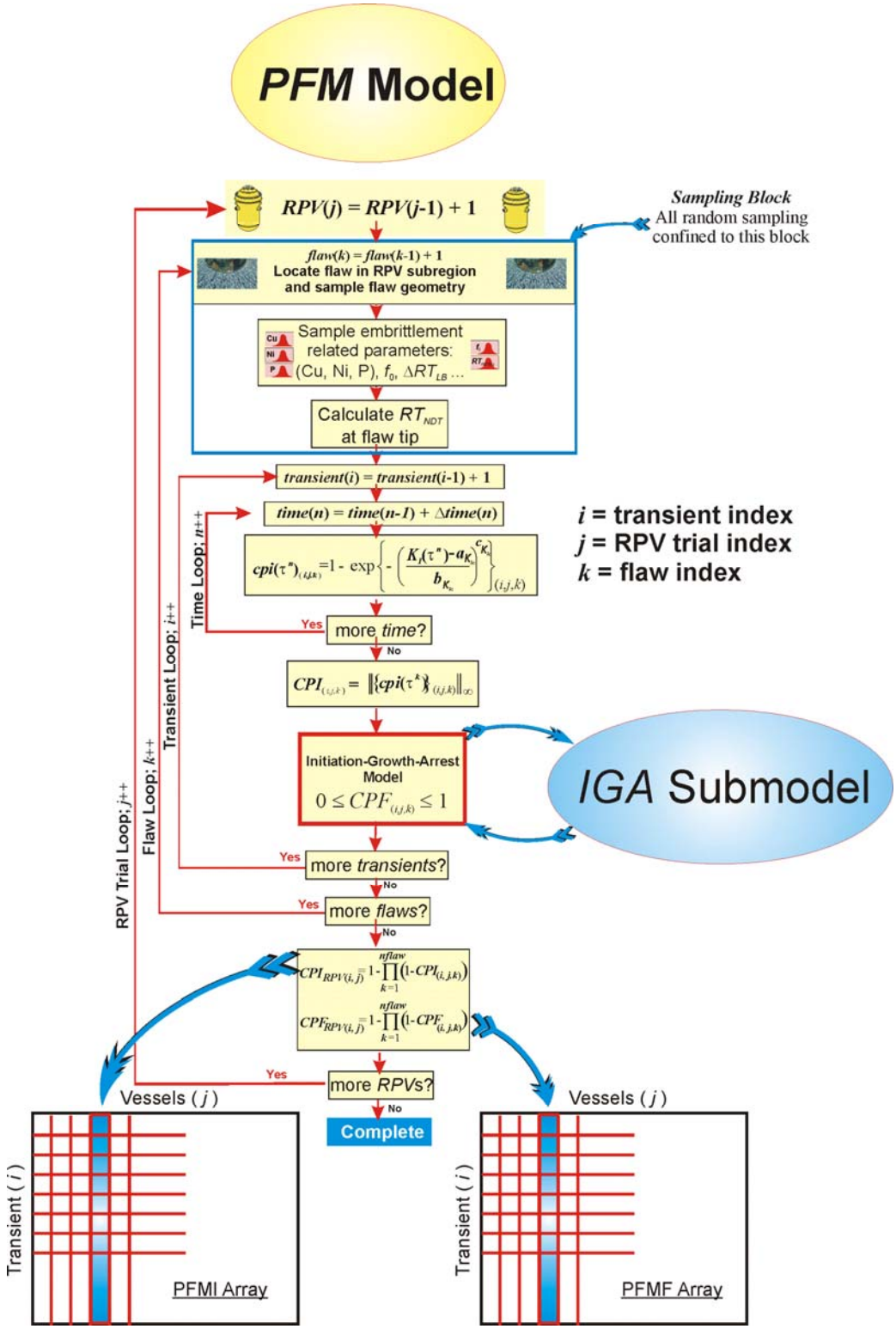

Fig. 16. Flowchart for PFM model – the Initiation-Growth-Arrest (*IGA*) submodel can be viewed as a Monte Carlo model nested within the larger PFM Monte Carlo model. For a given flaw, the *IGA* submodel is called after the *CPI* for the current transient has been calculated. Note: ++ notation indicates increment index by 1; e.g., *i*++ means *i*=*i*+1.

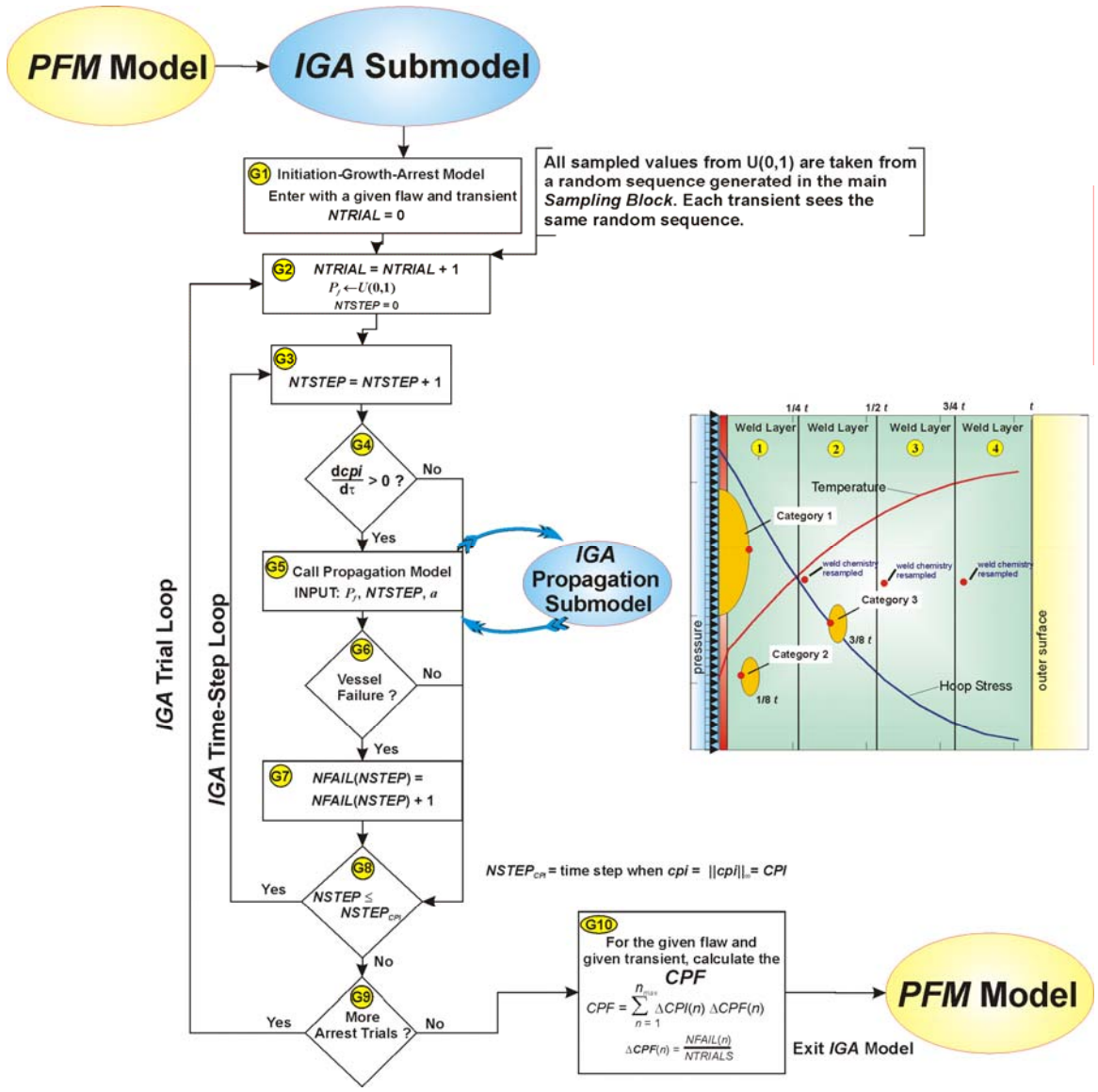

(a)

Fig 17. (a) Flow chart for Initiation-Growth-Arrest Submodel – The *IGA Propagation* submodel is only called for flaws with increasing *CPIs*. The weld-layering scheme is also shown for *Initiation-Growth-Arrest* Model. No through-wall resampling is carried out for plates or forgings.

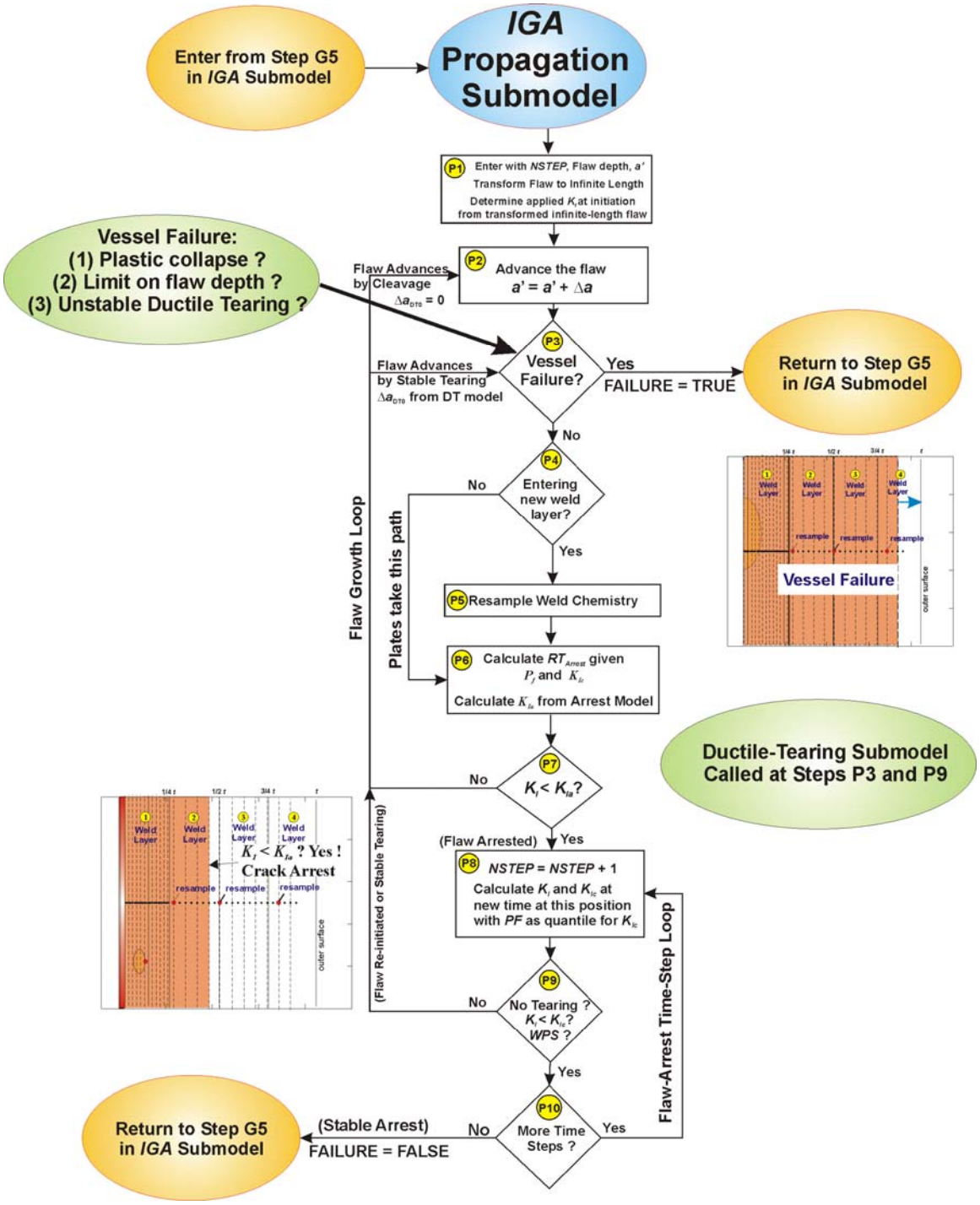

(b)

Fig. 17 (continued) (b) *IGA Propagation* submodel to test for Stable Arrest (no failure) and Vessel Failure.

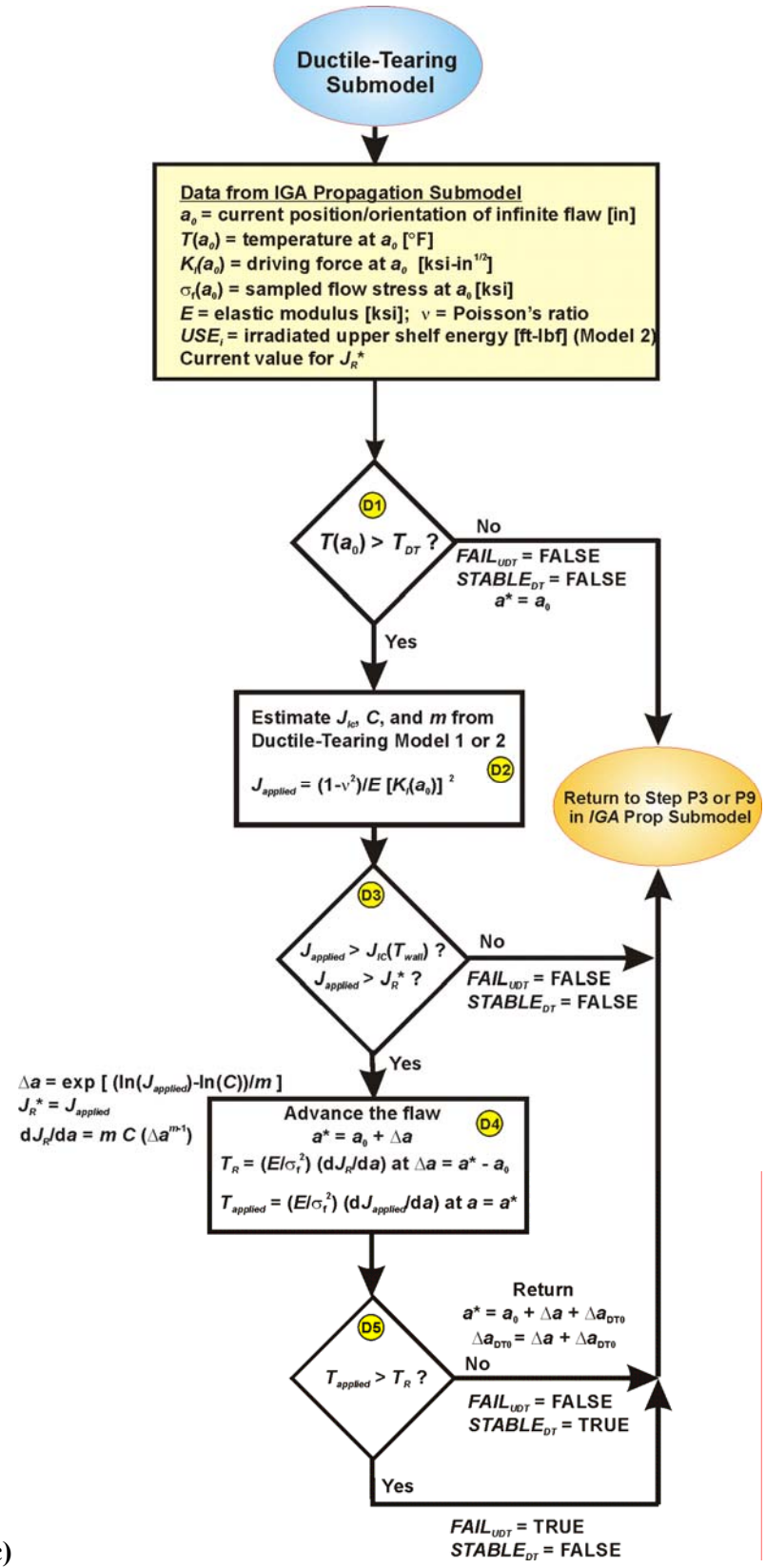

(c)

Fig. 17 (continued) (c) *Unstable-Ductile-Tearing* submodel to test for either stable tearing to a new flaw position, *a, or unstable ductile tearing that fails the vessel.**

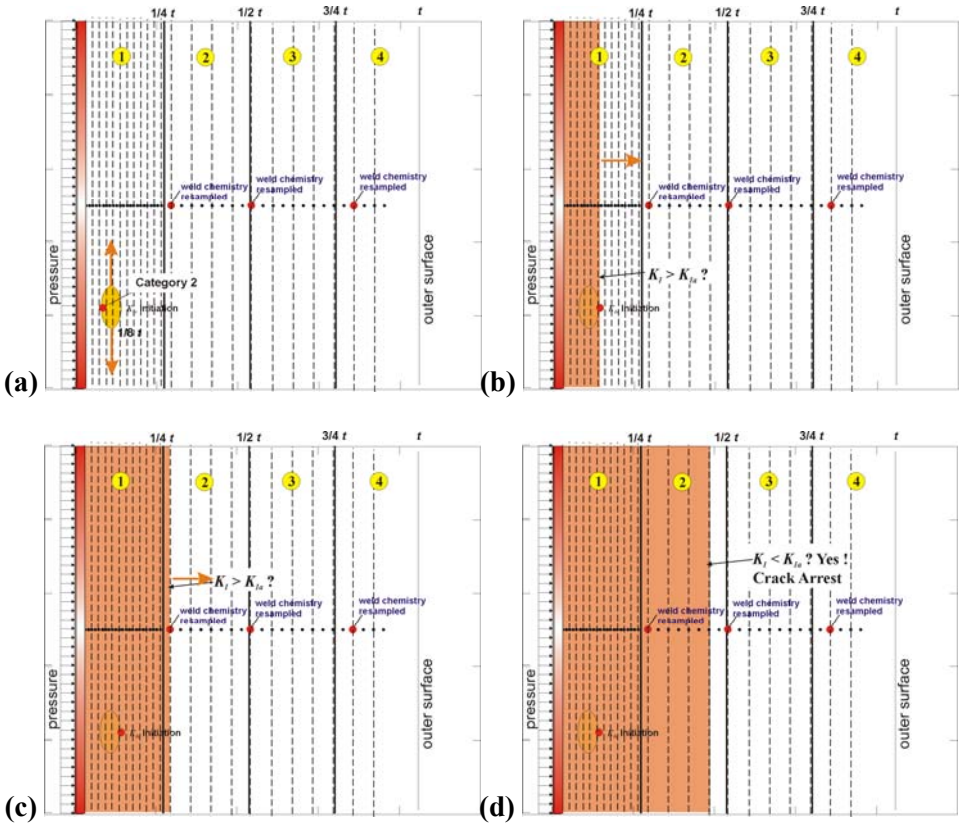

Fig. 18. An example Category 2 flaw (a) initiates, (b) expands into an infinite-length flaw, (c) advances to new weld layer and resamples chemistry content to calculate new RT_{NDT}, (d) continues growth until either failure by net-section plastic collapse of remaining ligament or stable crack arrest. The potential for arrest and subsequent re-initiation is also modeled.

Step G9. A check is made to see if the required number of trials has been completed. If there are more *NTRIALS* to be run, control is transferred to Step G2. If the *IGA* submodel has completed its sample trials for the current transient, then control is transferred to Step G10.

Step G10. The $CPF_{(i,j,k)}$ for the *i*th transient, and *j*th RPV trial, and *k*th flaw is calculated by the following:

$$CPF_{(i,j,k)} = \sum_{m=1}^{NSTEP_{CPI}} \Delta cpi(t^m)_{(i,j,k)} P(F \mid I)^m$$
$$P(F \mid I)^m = \frac{NFAIL(m)}{NTRIALS} \tag{43}$$

where $NSTEP_{CPI}$ is the time step at which the value of $CPI_{(i,j,k)}$ was calculated for this *i*th transient, *j*th RPV trial, and *k*th flaw.

Steps G2 through G9 are repeated *NTRIAL* cycles through the *IGA* submodel.

Figure 17b presents the control structure of the *IGA Propagation* submodel. This submodel proceeds in the following manner:

IGA Propagation Submodel

Step P1. Enter the submodel with the initiating time step, *NSTEP*, and the flaw depth. Transform the Category 1, 2, or 3 flaw into its corresponding infinite-length flaw, and calculate the applied stress-intensity factor, K_I, for the transformed flaw at this time and designate it $K_{I\text{-}initiation}$. This value of K_I will be higher than the K_I for the finite-flaw at initiation. Go to Step P2.

Step P2. Advance the infinite-length flaw to its next position in the *IGA* mesh (see Fig. 18). Proceed to Step P3.

Step P3. Check for vessel failure by through-wall cracking. At this new flaw depth and current time, calculate the current sampled estimate for the flow stress of the material. The current sampled value of ΔT_{30} (to be discussed in Chapter 4) is also used to estimate the effects of irradiation on the unirradiated flow stress, $\sigma_{flow(u)}$. After each resampling of ΔT_{30}, the flow stress will have been adjusted by the following relation:

$$\sigma_{flow} = \sigma_{flow(u)} + \gamma \Delta T_{30} \text{ where } \gamma = \begin{cases} 0.112 \text{ ksi/°F for welds} \\ 0.131 \text{ ksi/°F for plates} \end{cases}$$

This sampled value of σ_{flow} is then used in the vessel-failure test against the pressure-induced membrane stress in the remaining ligament, checking for net-section plastic collapse. The membrane stress is equal to

$$\sigma_m(t) = \frac{p_i(\tau)\left(R_i + a\right)}{\beta\left(R_o - R_i - a\right)}; \quad \beta = \begin{cases} 1 & \text{hoop stress} \\ 2 & \text{axial stress} \end{cases}$$

where $p_i(\tau)$ is the time-dependent internal pressure, R_i and R_o are the inner and outer vessel radii, respectively, and a is the current flaw depth.

For the initial entry into the *IGA Propagation* submodel, the flaw is growing due to a cleavage initiation; therefore, the ductile-tearing model will not be applied until the flaw has experienced its first arrest event. After the flaw has arrested, the ductile-tearing model is called at this point to check for unstable ductile tearing. This check for unstable tearing is made only if the flaw has re-initiated in ductile tearing. If the flaw has re-initiated as a cleavage event, the ductile-tearing submodel is not called. If the conditions for unstable ductile tearing are encountered, the logical variable FAIL_UDT is set to TRUE in the ductile-tearing submodel and returned to the IGA Propagation Submodel.

The vessel failure criterion is

if REINITIATED_BY_DUCTILE_TEARING is TRUE then

$$\text{if} \left\{ \begin{array}{c} \sigma_m > \bar{\sigma}_{flow} \\ \text{or} \\ FAIL_UDT \text{ is TRUE} \\ \text{or} \\ \left(\dfrac{a}{R_o - R_i} \right) > FAILCR \end{array} \right\} \text{then}$$

vessel failure = TRUE during ductile tearing

return to Step G5 in *IGA* Model

$$\text{elseif} \left\{ \begin{array}{c} \sigma_m > \bar{\sigma}_{flow} \\ or \\ \left(\dfrac{a}{R_o - R_i} \right) > FAILCR \end{array} \right\} \text{then}$$

vessel failure = TRUE during flaw growth by cleavage

return to Step G5 in *IGA* Model

else

vessel failure = FALSE

proceed to Step P4

where $0.25 \le FAILCR \le 0.95$ is a user-supplied failure criterion.

Step P4. If the material is a plate or forging product form, proceed directly to Step P6. If the material is a weld, check to see if the flaw has advanced into a new weld layer. Weld subregions are sectioned into through-wall quadrants to simulate, in an approximate manner, multiple weld layers. As the flaw advances from one weld-layer quadrant into the next, the weld chemistry will be resampled with the attenuated fluence. If the flaw has just advanced into a new weld layer, go to Step P5. If not, then proceed to Step P6.

Step P5. Resample the weld chemistry (Cu, Ni, and P) using the sampling distributions given in Chapter 4. Update the irradiation shift, $\bar{\Delta RT}_{NDT}$, and the irradiated value of the upper shelf energy, $\bar{USE}_{(i)}$, using the resampled weld chemistry. If the weld-layer-resampling option is turned on and the flaw has just entered layer 2, 3, or 4, then resample for a new value of P_f to replace the value of P_f sampled in Step G2 of the *IGA* submodel. The random iterate P_f is drawn from a uniform distribution on the open interval $U(0,1)$.

Step P6. Using the current chemistry content and current value of P_f, recalculate the arrest reference temperature. The details are given in Chapter 4; however, the equations are given here for completeness. Calculate the epistemic uncertainty in the arrest reference temperature by Eqs. (119) and (125) given in Sect. 4.5.

$$\bar{\Delta RT}_{epistemic} = -45.586 + 131.27\left[-\ln\left(1-\bar{\Phi}\right)\right]^{\frac{1}{2.177}} \quad [°\text{F}]$$

$$\bar{\Delta RT}_{epistemic-arrest} = \bar{\Delta RT}_{epistemic} - 14.4 \quad [°\text{F}]$$

Retrieve the previously sampled unirradiated value of RT_{NDTo} for this subregion and the sampled value of the irradiation shift for this flaw, $\Delta RT_{NDT}(r,\ldots)$, determined from the embrittlement model applied for this flaw at its current position in the RPV wall or from weld-chemistry resampling if Step P5 was executed. Calculate the shift in the arrest reference temperature, relative to the initiation reference temperature using Eqs. (126) in Step 11 of Sect. 4.5

$$\Delta RT_{ARREST} \leftarrow \Lambda(\mu_{\ln(\Delta RT_{ARREST})}, \sigma_{\ln(\Delta RT_{ARREST})}) \quad [°\mathrm{F}]$$

where (see Appendix F for the development of this protocol)

$$\mu_{\ln(\Delta RT_{ARREST})} = \ln\left[\Delta RT_{ARREST(mean)}\right] - \frac{\sigma^2_{\ln(\Delta RT_{ARREST})}}{2}$$

$$\Delta RT_{ARREST(mean)} = 44.122\exp\left[-0.005971 \times T_0\right] \quad [°\mathrm{C}]$$

$$T_0 = \left(RT_{NDT_0} - \Delta RT_{epist-arrest} - 32\right)/1.8 \quad [°\mathrm{C}]$$

$$\sigma_{\ln(\Delta RT_{ARREST})} = \sqrt{\ln\left\{\exp\left[0.38998^2 + 2\ln(\Delta RT_{ARREST(mean)})\right] - \mathrm{var}\left(T_0\right)\right\} - 2\ln\left[\Delta RT_{ARREST(mean)}\right]}$$

$$\mathrm{var}(T_0) = \begin{cases} (12.778)^2 & \text{for } T_0 < -35.7\ °\mathrm{C} \\ 99.905972 - 1.7748073 T_0 & \text{for } -35.7\ °\mathrm{C} \le T_0 \le 56\ °\mathrm{C} \\ 0 & \text{for } T_0 > 56\ °\mathrm{C} \end{cases}$$

Calculate the estimated arrest temperature[7] by Eq. (127) in Step 12 of Sect. 4.5

$$RT_{ARREST}(r,\ldots) = RT_{NDT_0} - \Delta RT_{epist-arrest} + \Delta RT_{ARREST} + \Delta RT_{NDT}(r,\ldots)$$

Calculate the normalized (relative to RT_{ARREST}) temperature of the vessel at the current location, *r*, in the RPV wall by Eq. (128) in Step 13 of Sect. 4.5

$$\Delta T_{RELATIVE}(r,\ldots) = T(r,t) - RT_{ARREST}(r,\ldots)$$

If this is the first pass through the submodel for this flaw, calculate (by Eqs. (129) and (130) in Steps 14 and 15 in Sect. 4.5) the fractile, $\Phi_{K_{I-initiation}}$, associated with this value of $K_{I\text{-}initiation}$ from the arrest model, given the current value of the applied $K_{I\text{-}initiation}$ from the infinite-length flaw in the *IGA* submodel

$$\Phi_{K_{I-initiation}} = \frac{1}{2}\left[\mathrm{erf}\left(\frac{\ln(K_{I-initiation}) - \mu_{\ln(K_{Ia})}(\Delta T_{RELATIVE})}{\sigma_{\ln(K_{Ia})}\sqrt{2}}\right) + 1\right]$$

where

[7] The subregion value of RT_{NDTo} is not re-sampled in this step.

$$\mathrm{erf}(x) = \text{ error function} = \frac{2}{\sqrt{\pi}}\int_0^x \exp(-\xi^2)\,\mathrm{d}\xi;\ \ \mathrm{erf}(-x) = -\mathrm{erf}(x)$$

if K_{Ia}_Model is equal to 1

$$K_{Ia(\mathrm{mean})}(\Delta T_{RELATIVE}) = 27.302 + 69.962\exp\left[0.006057(\Delta T_{RELATIVE})\right]\ \ [\mathrm{ksi}\sqrt{\mathrm{in.}}]$$

$$\sigma_{\ln(K_{Ia})} = 0.18$$

else if K_{Ia}_Model is equal to 2

$$K_{Ia(\mathrm{mean})}(\Delta T_{RELATIVE}) = 27.302 + 70.6998\exp\left[0.008991(\Delta T_{RELATIVE})\right]\ \ [\mathrm{ksi}\sqrt{\mathrm{in.}}]$$

$$\sigma_{\ln(K_{Ia})} = 0.34$$

$$\mu_{\ln(K_{Ia})}(\Delta T_{RELATIVE}) = \ln\left[K_{Ia(\mathrm{mean})}(\Delta T_{RELATIVE})\right] - \frac{\sigma^2_{\ln(K_{Ia})}}{2}$$

In the above relation for $\Phi_{K_{I-initiation}}$, $\mu_{\ln(K_{Ia})}$ is calculated at the location of the initiation of the flaw. For this flaw, the value of $\Phi_{K_{I-initiation}}$ remains fixed in the *IGA Propagation* submodel until P_f is resampled in Step G2 of the *IGA* submodel. Using the current value of P_f, scale by $\Phi_{K_{I-initiation}}$ (if this is the weld layer in which the crack initiation originally occurred) such that (from Eq. (131) in Step 15 of Sect. 4.5)

$$\Phi_{K_{Ia}} = (P_f)(\Phi_{K_{I-initiation}})$$

For subsequent weld layers do not perform the above scaling. When the flaw advances into a new weld layer, any linkage between the flaw's initiation and its continued propagation is assumed to be broken.

With this $\Phi_{K_{Ia}}$ fractile, draw a value of K_{Ia} from its lognormal distribution as given by Eq. (132) of Step 15 in Sect. 4.5

$$K_{Ia}(\Phi_{K_{Ia}}, \Delta T_{RELATIVE}) = \exp\left[\sigma_{\ln(K_{Ia})} Z_{\Phi K_{Ia}} + \mu_{\ln(K_{Ia})}(\Delta T_{RELATIVE})\right]$$

$$Z_{\Phi_{K_{Ia}}} = \text{ standard normal deviate corresponding to the } \Phi_{K_{Ia}} \text{ fractile}$$

In the above relation for K_{Ia}, $\mu_{\ln(K_{Ia})}$ is calculated at the current location of the flaw. The scaling procedure in Step P6 ensures that the initial value of K_{Ia}, calculated immediately after initiation, does not exceed the initiating value of $K_{I\text{-}initiation}$, thus producing an initial extension. Once the value of $Z_{\Phi_{K_{Ia}}}$ has been determined for this *IGA* trial, the arrest toughness during flaw advancement through the wall changes due to changes in $\Delta T_{RELATIVE}$ only. These changes are caused by variations in $T(r,t)$ and RT_{Arrest} (due to the resampling of the weld chemistry when passing into new weld layers).

For Ductile-Tearing Model No. 2, update the current value of the irradiated upper-shelf energy by

$$USE_{(i)} = A + 0.0570 \cdot USE_{(u)}^{1.456} - \left[17.5 \cdot f\left(Cu\right) \cdot \left(1 + 1.17Ni^{0.8894}\right) + 305\hat{P}\right]\left(\frac{\phi t}{10^{19}}\right)^{0.2223} \quad \text{[ft-lbf]}$$

Go to Step P7.

Step P7. Check the current applied K_I for the advancing flaw against the current value of the arrest fracture toughness K_{Ia}.

if $K_I < K_{Ia}$ then
  the flaw has arrested
  proceed to Step P8
else
  the flaw has not arrested
  proceed to Step P2

Step P8. Hold the flaw at this position, and advance the time to check for re-initiation or new ductile tearing.

$$NSTEP = NSTEP + 1$$

For this new time station, bring up the wall temperature, $T(r,\tau)$, at this position along with the current irradiated and attenuated value of RT_{NDT} to calculate

$$\Delta T_{RELATIVE}(r,\ldots) = T(r,\tau) - RT_{RTNDT}(r,\ldots)$$

Now calculate the parameters of the K_{Ic} model

$$a_{K_{Ic}}(\Delta T_{RELATIVE}) = 19.35 + 8.335\exp\left[0.02254(\Delta T_{RELATIVE})\right] \text{ [ksi}\sqrt{\text{in.}}\text{]}$$
$$b_{K_{Ic}}(\Delta T_{RELATIVE}) = 15.61 + 50.132\exp\left[0.008(\Delta T_{RELATIVE})\right] \text{ [ksi}\sqrt{\text{in.}}\text{]}$$
$$c_{K_{Ic}} = 4$$

with K_{Ic} in ksi√in and $\Delta T = (T\text{-}RT_{NDT})$ in °F.

The static initiation toughness, K_{Ic}, is calculated from its Weibull distribution by

$$K_{Ic}(\Delta T_{RELATIVE}) = a_{K_{Ic}}(\Delta T_{RELATIVE}) + b_{K_{Ic}}(\Delta T_{RELATIVE})\left[-\ln(1-P_f)\right]^{1/c_{K_{Ic}}}$$

for $a_{K_{Ic}}(\Delta T_{RELATIVE}) \le K_{Ic} \le K_{Ic(\max)}$

Proceed to Step P9.

Step P9. If the warm prestressing (WPS) analysis option has been turned on by the user (see Sect. 3.3.4 for details on WPS effects as implemented in FAVOR), check to see if the flaw is in a state of WPS. If the ductile-tearing option is turned on, then call the ductile-tearing model to determine if there is stable or unstable ductile tearing. If the WPS option is on and WPS = TRUE, go to Step P10. If the WPS option is off or WPS = FALSE, check the current applied K_I for re-initiation by the test

if $K_I < K_{Ic}$ and $STABLE_DT$ and $FAIL_UDT$ are both FALSE then
  No re-initiation.
  Proceed to Step P10.
else if WPS_OPTION is on and WPS is TRUE then
  No re-initiation
  Proceed to Step P10
else if $FAIL_UDT$ is TRUE then
  the vessel has failed by unstable ductile tearing
  set vessel failure to TRUE
  return to Step G5 of *IGA* model
else if $STABLE_DT$ is TRUE and $K_{J_{Ic}}$ is less than K_{Ic} then
  the flaw has re-initiated by a ductile-tearing event
  REINITIATED_BY_DUCTILE_TEARING = TRUE
  the current level of tearing Δa_0 is set by the ductile-tearing model
  Proceed to Step P3
else
  The flaw has re-initiated by a cleavage event.
  REINITIATED_BY_DUCTILE_TEARING = FALSE
  Reset the current level of tearing $\Delta a_0 = 0$
  Proceed to Step P2 and advance the flaw

Step P10. If there are time steps remaining in the transient, proceed to Step P8 and advance the time. If the transient is complete, set vessel failure = FALSE, and return to Step 5 of the *IGA* submodel.

Note that in the *IGA Propagation* submodel, the flaw is assumed to advance instantaneously; i.e., the time station remains fixed during flaw growth. Time will advance only if the flaw is in a state of arrest. If the flaw remains in arrest until the end of the transient, then the flaw is said to have experienced a *Stable Arrest*.

3.3.13 Ductile-Tearing Submodel

Figure 17c presents a flowchart of the *Ductile-Tearing Submodel*.

Step D1. The program enters the submodel with the current position and orientation of the crack tip and the time within the selected transient. The submodel first checks the current wall

temperature at the crack tip with the ductile-tearing transition temperature, T_{DT}. Based on a previous study, the value of T_{DT} is set to $200\ °\mathrm{F}$. If this is not the first entry into the model, a current value of J_R^* will be known, where J_R^* is a measure of the current deformation state due to tearing.

if $T_{wall} < T_{DT}$ then

$FAIL_UDT = \text{FALSE}$

$STABLE_DT = \text{FALSE}$

Return to Step P3 or P9 of *IGA* Submodel

else

Proceed to Step D2

Step D2. Given the location and orientation of the flaw tip, the submodel converts the known value of $K_{I\text{-}applied}$ to $J_{applied}$ using a plane-strain conversion. The submodel then proceeds to calculate/sample estimates for the J_R-curve parameters, J_{Ic}, C, and m.

$$J_{applied} = \frac{(1-\nu^2)}{E} K_{I-applied}^2 \ [\text{in-kips/in}^2]$$

get $\widehat{J}_{Ic}$ from either Ductile-Tearing Model No. 1 or 2

get $\widehat{C}$, and $\widehat{m}$ from either Ductile-Tearing Model No. 1 or 2

Proceed to Step D3

Step D3. The submodel then compares the $J_{applied}$ to the estimated value of J_{Ic} obtained in Step D2 and the known value of J_R^*. If this is the first entry into the model or if a cleavage reinitiation has occurred since the last entry into the model, then $J_R^* = 0$. J_R^* is the value of $J_{applied}$ corresponding to a previous time step at which a stable ductile tear ocurred. For a ductile tear to occur at the current time, it is necessary for $J_{applied}$ to be equal to or greater than the current value of J_R^*.

if $(J_{applied} < J_{Ic})$ or $(J_{applied} \le J_R^*)$ then

$FAIL_UDT = \text{FALSE}$

$STABLE_DT = \text{FALSE}$

Return to Step P3 or P9 of *IGA* Submodel

else

Proceed to Step D4

Step D4. The submodel then advances the position of the flaw, a_0, using the known value of $J_{applied}$, and then calculates the local tearing modulus, T_R, characterizing the tearing resistance of the material.

$$J_R^* = J_{applied}$$

$$\Delta a = \exp\left[\frac{\ln(J_R^*) - \ln(C)}{m}\right], \text{[in]}$$

$$a^* = a_0 + \Delta a$$

$$T_R = \left(\frac{E}{\sigma_{flow}^2}\right)\frac{dJ_R^*}{da}\bigg|_{\Delta a^*} = \left(\frac{E}{\sigma_{flow}^2}\right) \times m \times C \times (\Delta a)^{m-1}$$

The *IGA Propagation* submodel mesh is searched to find the closest node point, node *n*, to the current flaw position. The flaw is then repositioned to this node point (see Fig. 19). Based on the new position of the flaw, the applied tearing modulus is estimated from a second-order finite-difference ratio.

$$\frac{dJ_{applied}}{da} \approx \frac{J_{n+1} + (\alpha - 1)J_n - \alpha^2 J_{n-1}}{\alpha(\alpha+1)\Delta x} \quad , \quad O\left(\Delta x^2\right)$$

where

$$\Delta x = x_n - x_{n-1}$$

$$\alpha = \frac{x_{n+1} - x_n}{x_n - x_{n-1}}$$

$$T_{applied} = \left(\frac{E}{\sigma_{flow}^2}\right)\frac{dJ_{applied}}{da}\bigg|_{a=a^*}$$

Step D5. A check is now made for unstable ductile tearing. If the applied tearing modulus is greater than T_R , then a state of unstable ductile tearing is declared.

if $T_{applied} > T_R$ then

$FAIL_UDT$ = TRUE

$STABLE_DT$ = FALSE

Return to Step P3 or Step P9 in the *IGA Propagation* Submodel

else

$FAIL_UDT$ = FALSE

$STABLE_DT$ = TRUE

$\Delta a_0 = \Delta a$

$a_0 = a^*$

Return to Step P3 or Step P9 in the *IGA Propagation* Submodel

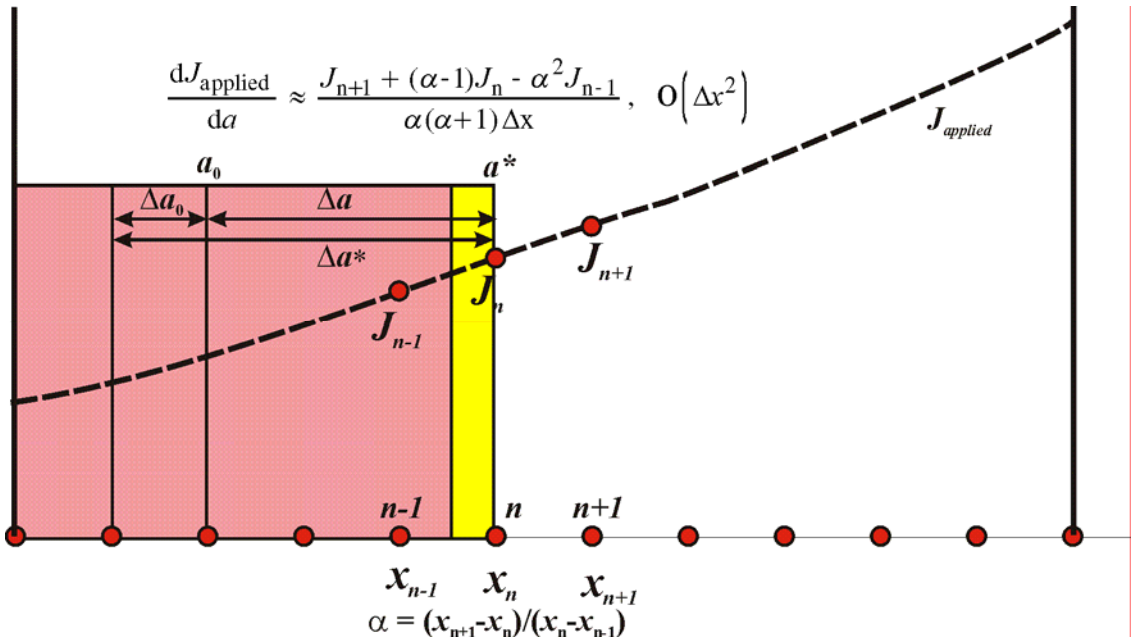

Fig. 19. ***IGA Propagation*** **submodel mesh used to estimate d$J_{applied}$ / d*a* using a second-order central finite-difference ratio.**

3.3.14 Ductile Tearing as an Initiating Event

The ductile-tearing model, as implemented, should have no effect on the values of *CPI* produced by FAVOR, and this was verified in a preliminary scoping study. However, a counter was implemented into FAVOR at the point where the conditional probability of initiation, *cpi*, by cleavage is calculated to determine if initiation of flaw growth by ductile tearing was a potential issue. In all of the studies carried out to date using the ductile-tearing models described in Sect. 3.3.11, no ductile-tearing initiating events were discovered.

3.4 FAVOR Post Module – FAVPost

The distribution of the transient initiating frequencies obtained from PRA studies, the values of conditional probability of fracture (contained in the FAVPFM-generated matrix *PFMI*), and the values of the conditional probability of vessel failure (contained in the FAVPFM-generated matrix *PFMF*) are combined in the FAVPost module to generate discrete distributions of the frequency of vessel initiation, $\Phi(I)$, and frequency of vessel failure, $\Phi(F)$. This process is described by the following *pseudo code*:

For j = 1, N_{SIM} vessel simulations, increment by 1

For i = 1, N_{TRAN} transients, increment by 1

Sample the discrete cumulative distribution function of the transient-initiating frequency for this transient to generate a sample initiating frequency (in events per reactor year).

$\phi(E)_{(i)} \leftarrow CDF_{(i,j)}$ of transient-i initiating frequency

End of Transient Loop

The above loop generates a vector of transient-initiating frequencies for this vessel simulation, $\left\{\phi(E)\right\}_{(1\times N_{TRAN})}$.

For the jth vessel, take the inner product of the transient initiating frequencies vector times the jth column-vectors in the *PFMI* and *PFMF* matrices.

$$\Phi(I)_{(j)} = \sum_{i=1}^{N_{TRAN}} \phi(E)_{(i)} PFMI(i,j)$$

$$\Phi(F)_{(j)} = \sum_{i=1}^{N_{TRAN}} \phi(E)_{(i)} PFMF(i,j)$$

End of Vessel Simulation Loop

The inner product of the row-vector of the sampled transient initiating frequencies and the jth column-vector of *PFMI* produces the frequency of crack initiation for the jth vessel simulation, $\Phi(I)_{(j)}$. Likewise, the inner product of the row-vector of sampled transient initiating frequencies and the jth column-vector of *PFMF* results in the frequency of vessel failure for the jth vessel simulation, $\Phi(F)_{(j)}$. The (i, j) entry in matrix *PFMI* represents the conditional probability of crack initiation of

the *j*th vessel simulation subjected to the *i*th transient. The units are *crack initiations per event*. Therefore, the frequency of crack initiation, as determined from the inner product of the transient-initiating frequency and the conditional probability of crack initiation, is the number of *crack initiations per reactor year*. Likewise, the frequency of vessel failure, as determined from the inner product of the transient-initiating frequency and the conditional probability of vessel failure is the number of vessel *failures per reactor year*.

At the end of this process, there are discrete distributions of sample size N_{SIM} for the frequency of crack initiation, $\{\Phi(I)\}_{N_{SIM}\times 1}$, and the frequency of vessel failure, $\{\Phi(F)\}_{N_{SIM}\times 1}$. The above process is described in Fig. 20.

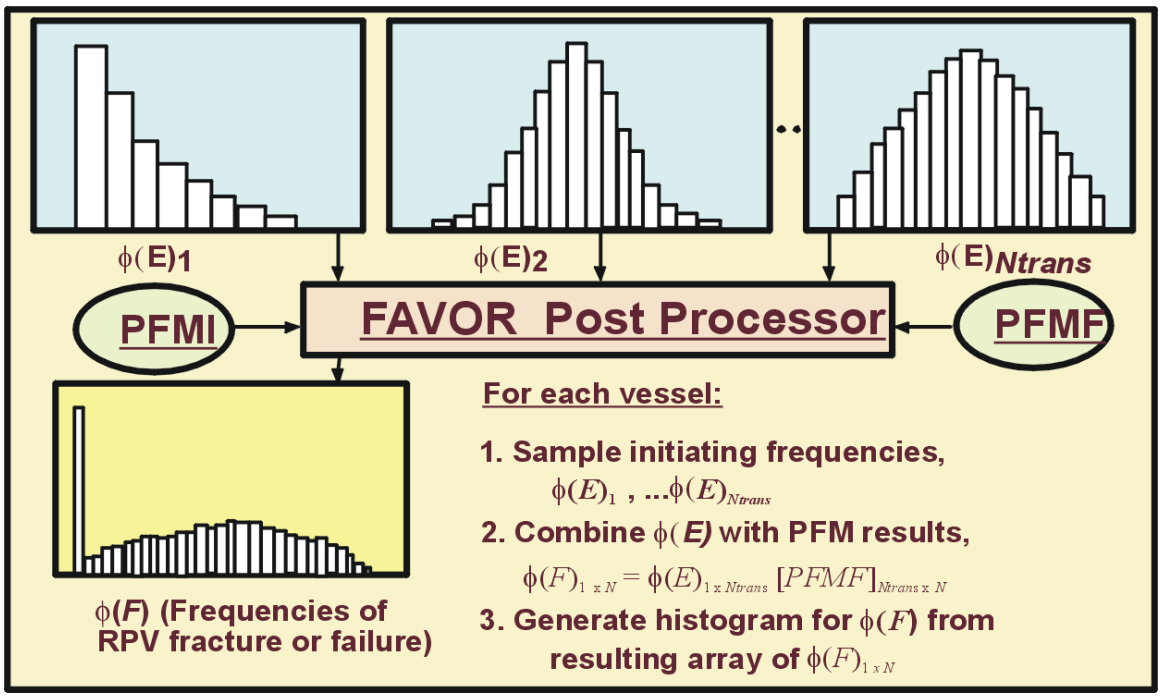

Fig. 20. The FAVOR post-processor FAVPost combines the distributions of conditional probabilities of initiation and failure calculated by FAVPFM with initiating frequency distributions for all of the transients under study to create distributions of frequencies of RPV fracture and failure.

4. Probabilistic Fracture Mechanics

A central feature of modern PRA/PFM analyses is an explicit treatment of model uncertainties with two types being distinguished, *aleatory* and *epistemic* [87]. *Aleatory uncertainties* arise due to the randomness inherent in any physical or human process, whereas *epistemic uncertainties* are caused by a limitation in the current state of knowledge (or understanding) of that process. Epistemic uncertainties can therefore, in principle, be reduced by an increased state of knowledge, whereas aleatory uncertainties are fundamentally irreducible. Playing a central role in the PTS Re-evaluation Project, the identification and classification of epistemic and aleatory uncertainties is a crucial aspect of PRA/PFM analyses, because the mathematical procedures used to account for them are different. A major effort in the development of improved fracture mechanics models for FAVOR has been the attempt to identify and classify the uncertainties in these models. Sections 4.2 through 4.5 will present the results of this effort. The deterministic analyses carried out to create a *loading definition* for each PTS transient are first discussed in Section 4.1.

It should be noted that during the investigation of new models for the FAVOR code, the basic requirements of the PTS Re-evaluation Project played a key role in the development process. To enable all commercial operators of pressurized water reactors to assess the state of their RPV relative to the new PTS screening criteria without the need to make new material property measurements, the initiation fracture toughness of the RPV needs to be estimated using only currently available RT_{NDT} values. Moreover, to be consistent with the LEFM principals on which the FAVOR code is based, this RT_{NDT} -based model needs to estimate K_{Ic} values. These restrictions suggested that only very limited information, specifically a value of RT_{NDT}, would be available to define the initiation fracture-toughness model appropriate to a given steel in a plant-specific RPV.

4.1 Deterministic Analyses

The FAVLoad module carries out both thermal and stress analyses of a one-dimensional axisymmetric model of the RPV wall. The time-dependent temperature and stress distributions through the wall constitute the thermal and mechanical loading that will be applied to postulated flaws. In addition, Mode I stress-intensity factors are generated for a range of axially and circumferentially oriented infinite-length and finite-length (semi-elliptical) flaw geometries (flaw depths and lengths). The following subsections describe how these deterministic calculations are carried out in the FAVLoad module. The embedded-flaw model to be discussed has been implemented in the FAVPFM module.

4.1.1 Thermal Analysis

The temperature time-history, $T(r,\tau)$, for the vessel is determined by modeling the RPV wall as an axisymmetric one-dimensional structure with the temperature profile being dependent on the radial position, r, and elapsed time, τ, in the transient. In the absence of internal heat generation, the transient heat conduction equation is a second-order parabolic partial differential equation:

$$\rho\, c_p(T)\, \frac{\partial T}{\partial \tau} = \frac{1}{r}\frac{\partial}{\partial r}\left[k(T)\, r \frac{\partial T}{\partial r} \right] \tag{44}$$

where ρ is the mass density, $c_p(T)$ is the temperature-dependent mass-specific heat capacity, and $k(T)$ is the temperature-dependent thermal conductivity. Note that any temperature dependencies in the mass density should be included in the characterization of the mass-specific heat capacity, leaving the mass density as a constant in the problem formulation. Equation (44) can be expressed in the following canonical form

$$\frac{\partial T}{\partial \tau} - \frac{1}{r}\frac{\partial}{\partial r}\left[\lambda(T)\, r \frac{\partial T}{\partial r} \right] = 0 \text{ for } r \in \square^{1}; \tau \in (0,\infty) \tag{45}$$

where the property grouping $\lambda(T) = k(T) \big/ \rho\, c_p(T)$ is the temperature-dependent thermal diffusivity of the material. For Eq. (45) to be well posed, initial and boundary conditions must be applied.

<u>Initial Condition</u>

$$T(r,0) = T_{initial} \text{ for } R_i \le r \le R_o \tag{46}$$

<u>Boundary Conditions</u>

$$q(R_i,t) = h(t)\big(T_\infty(t) - T(R_i,t)\big) \text{ at } r = R_i \tag{47}$$
$$q(R_o,t) = 0 \text{ at } r = R_o$$

where in Eqs. (46)-(47), q is a prescribed boundary heat flux, $h(\tau)$ is the time-dependent convective film coefficient, $T_\infty(\tau)$ is the time-dependent bulk coolant temperature, and R_i and R_o are the inner and outer radii of the vessel wall, respectively. Input data to the thermal model include the mesh definition, property data, and prescribed time-histories for $h(\tau)$ and $T_\infty(\tau)$.

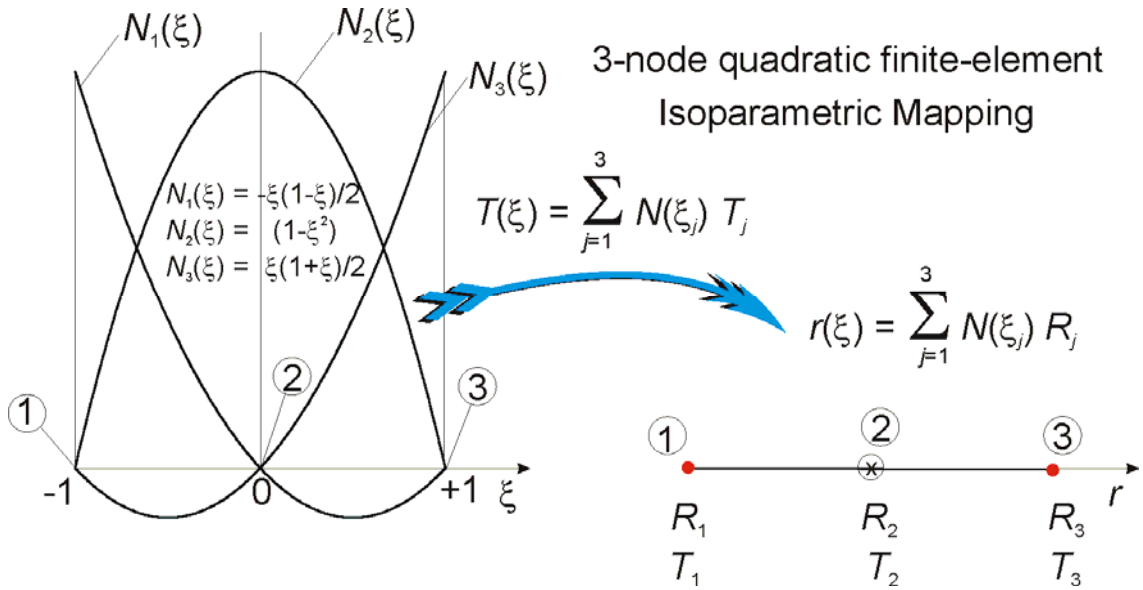

Fig. 21. Isoparametric mapping from parameter space to axisymmetric $\square^1$ Euclidean space using three-node quadratic basis functions.

Eqs. (45)-(47) can be solved using the finite-element method, where the variational formulation for the transient heat conduction equation is given in Ref. [88]. The fundamental decisions required to implement the finite-element method are (1) choice of basis functions, (2) choice of mapping, and (3) choice of method for element integration. As shown in Fig. 21, FAVOR uses an isoparametric mapping with 3-node quadratic cardinal basis functions, specifically

$$\{N(\xi)\} = \begin{Bmatrix} N_1(\xi) \\ N_2(\xi) \\ N_3(\xi) \end{Bmatrix} = \frac{1}{2}\begin{Bmatrix} -\xi(1-\xi) \\ 2(1-\xi^2) \\ \xi(1+\xi) \end{Bmatrix}; \quad \left\{\frac{dN}{d\xi}\right\} = \begin{Bmatrix} \dfrac{dN_1}{d\xi} \\ \dfrac{dN_2}{d\xi} \\ \dfrac{dN_3}{d\xi} \end{Bmatrix} = \frac{1}{2}\begin{Bmatrix} (-1+2\xi) \\ -4\xi \\ (1+2\xi) \end{Bmatrix} \tag{48}$$

The elements of the thermal stiffness matrix [88] are calculated using a full-integration fourth-order Gauss-Legendre quadrature rule with the following weights, ω_i, and Gauss sampling points, ξ_i,

$$\int_{-1}^{+1} g(\xi)d\xi \approx \sum_{i=1}^{4} \omega_i g(\xi_i) \quad \text{where} \quad \{\xi_i\} = \begin{Bmatrix} -\sqrt{\dfrac{3+2\sqrt{6/5}}{7}} \\ -\sqrt{\dfrac{3-2\sqrt{6/5}}{7}} \\ \sqrt{\dfrac{3-2\sqrt{6/5}}{7}} \\ \sqrt{\dfrac{3+2\sqrt{6/5}}{7}} \end{Bmatrix}; \{\omega_i\} = \begin{Bmatrix} \dfrac{1}{2} - \dfrac{1}{6\sqrt{6/5}} \\ \dfrac{1}{2} + \dfrac{1}{6\sqrt{6/5}} \\ \dfrac{1}{2} + \dfrac{1}{6\sqrt{6/5}} \\ \dfrac{1}{2} - \dfrac{1}{6\sqrt{6/5}} \end{Bmatrix} \tag{49}$$

In FAVOR, a graded mesh (see Fig. 22) is generated through the wall thickness using ten three-noded quadratic isoparametric axisymmetric elements (21 nodes). Note that the FEM model does not use the same discretization applied in the *IGA* submodel. The first two elements represent the cladding, and the remaining eight elements model the base material. Explicit forward time integration is employed with a fixed time step of 1.0 second. Temperature and hoop-stress profiles are plotted in Fig. 22 for a fixed time in an example transient.

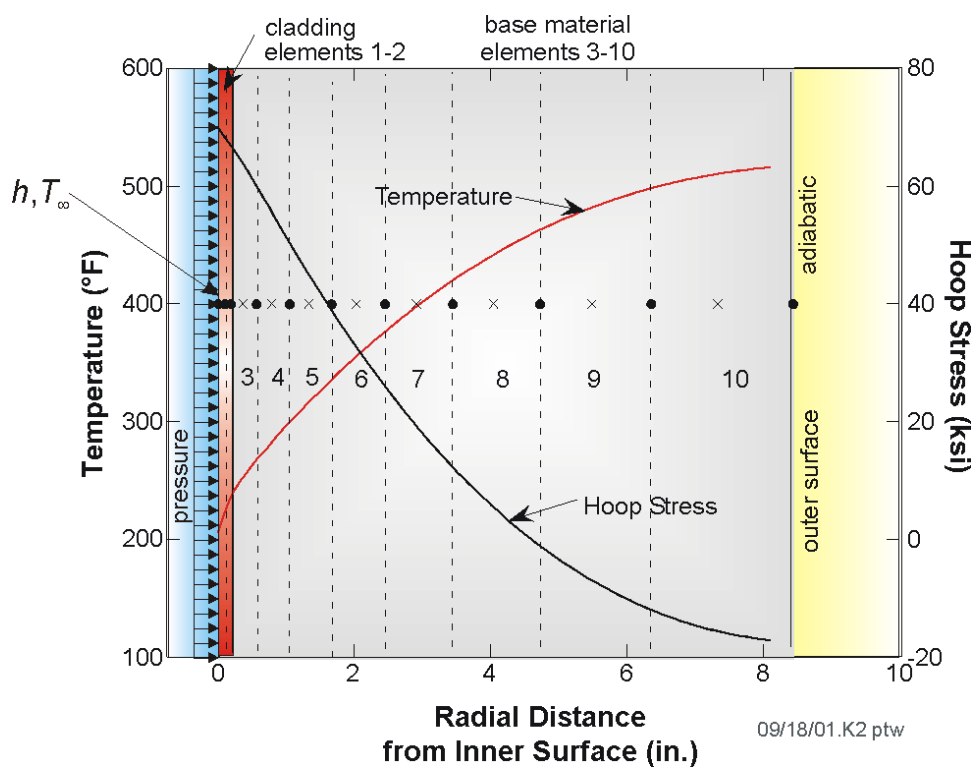

Fig. 22. One-dimensional axisymmetric finite-element model used in FAVOR to calculate both temperature and stress histories through the wall of an RPV.

4.1.2 Stress Analysis

FAVLoad carries out a displacement-based finite-element analysis of the vessel using a one-dimensional axisymmetric model of the vessel wall. The calculated displacements are converted into strains using strain-displacement relationships, and the associated stresses are then calculated using linear-elastic stress-strain relationships. At each time station during the transient, the structure is in a state of static equilibrium; thus the load history is considered *quasi-static.*

Let (u, v, w) be the radial, circumferential, and axial displacements, respectively, of a material point in a cylindrical (r, θ, z) coordinate system. The general two-dimensional axisymmetric case requires that

$$v = 0; \tau_{r\theta} = \tau_{\theta z} = 0; \gamma_{r\theta} = \gamma_{\theta z} = 0 \tag{50}$$

where $\tau_{r\theta}, \tau_{\theta z}$ are shear stresses and $\gamma_{r\theta}, \gamma_{\theta z}$ are engineering shear strains. The strain-displacement relationships for the two-dimensional case are

$$\begin{Bmatrix} \varepsilon_{rr} \\ \varepsilon_{\theta\theta} \\ \varepsilon_{zz} \\ \gamma_{zr} \end{Bmatrix} = \begin{bmatrix} \frac{\partial}{\partial r} & 0 \\ \frac{1}{r} & 0 \\ 0 & \frac{\partial}{\partial z} \\ \frac{\partial}{\partial z} & \frac{\partial}{\partial r} \end{bmatrix} \begin{Bmatrix} u \\ w \end{Bmatrix} \tag{51}$$

For the one-dimensional axisymmetric case, (r, θ, z) are principal directions, and $w = 0; \partial/\partial z = 0;$ such that

$$\varepsilon_{rr} = \frac{\partial u}{\partial r}; \quad \varepsilon_{\theta\theta} = \frac{u}{r}; \quad \varepsilon_{zz} = \frac{\partial w}{\partial z} = 0; \quad \gamma_{zr} = \frac{\partial u}{\partial z} + \frac{\partial w}{\partial r} = 0 \tag{52}$$

For the case of a long cylinder with free ends and no axial or circumferential variations in temperature or material properties and with no radial variation in material properties, the radial and circumferential stresses for the one-dimensional axisymmetric case are calculated from the strains by

$$\sigma_{rr} = \frac{E}{(1+\nu)(1-2\nu)}\left[(1-\nu)\varepsilon_{rr} + \nu\varepsilon_{\theta\theta}\right] - \frac{\alpha E}{1-2\nu}(T - T_{ref}) \tag{53}$$

$$\sigma_{\theta\theta} = \frac{E}{(1+\nu)(1-2\nu)}\left[(1-\nu)\varepsilon_{\theta\theta} + \nu\varepsilon_{rr}\right] - \frac{\alpha E}{1-2\nu}(T - T_{ref}) \tag{54}$$

where

σ_{rr} = radial normal stress
$\sigma_{\theta\theta}$ = circumferential (hoop) normal stress
ε_{rr} = radial normal strain
$\varepsilon_{\theta\theta}$ = circumferential (hoop) normal strain
T = wall temperature as a function of r
T_{ref} = thermal stress-free reference temperature
r = radial position in wall
E = Young's modulus of elasticity
ν = Poisson's ratio
α = linear coefficient of thermal expansion

For generalized plane-strain conditions, the stress in the axial direction, σ_{zz}^{PS}, is given by

$$\sigma_{zz}^{PS} = \nu(\sigma_{rr} + \sigma_{\theta\theta}) - \alpha E(T - T_{ref}) \tag{55}$$

To obtain the axial stresses with the ends free (assuming no cap load), it is necessary to remove the net end force associated with the plane-strain condition. This net load is

$$f^{PS} = 2\pi \int_{R_i}^{R_o} \sigma_{zz}^{PS} r dr \tag{56}$$

where R_i and R_o are the inner and outer radii of the cylinder.

In FAVOR, the radial and hoop stresses are calculated using the finite-element method in which Eqs. (53) and (54) apply to each finite element, and thus radial variations in the material properties E, α, and ν can be included by letting the properties vary from one element material group to another. To account for radial variations in properties when calculating the axial stresses, Eq. (55) is applied to each element j such that

$$\sigma_{zz-j}^{PS} = \nu_j(\sigma_{rr-j} + \sigma_{\theta\theta-j}) - \alpha_j E_j (T_j - T_{ref}) \tag{57}$$

is the axial stress in each element under plane-strain conditions. To achieve a free-end condition, the force f_j^{PS} [Eq. (56)] must be released in such a manner that the change in axial strain (displacement) is the same for each element, because it is assumed that initial planes remain in plane under load. If Δf_j is the reduction in the plane-strain force, f_j^{PS}, on element j, then

$$\frac{\Delta f_1}{A_1 E_1} = \frac{\Delta f_2}{A_2 E_2} = \cdots \frac{\Delta f_{nele}}{A_{nele} E_{nele}} \tag{58}$$

and

$$\sum_{j=1}^{nele} (f_j^{PS} + \Delta f_j) = 0 \tag{59}$$

where

$$f_j^{PS} = A_j\left[\nu_j\left(\sigma_{rr-j} + \sigma_{\theta\theta-j}\right) - \alpha_j E_j (T_j - T_{ref})\right]$$

$$A_j = \pi(r_{o-j}^2 - r_{i-j}^2) \tag{60}$$

where r_o and r_i are the outer and inner radii of element j, respectively. Let f_{p-j} be the axial forces that are the result of adding internal pressure, p. Specifying that the axial displacements for each element be the same gives

$$\frac{f_{p-1}}{A_1 E_1} = \frac{f_{p-2}}{A_2 E_2} = \cdots \frac{f_{p-nele}}{A_{nele} E_{nele}} \tag{61}$$

and

$$\sum_{j=1}^{nele} f_{p-j} = \pi R_o^2 p \tag{62}$$

where

$$f_j = \Delta f_j + f_{p-j}$$

Recalling that the uniform change in axial strain has no effect on σ_{rr} and $\sigma_{\theta\theta}$, Eqs. (60), (61), and (62) can be solved for f_j after calculating values of σ_{rr-j} and $\sigma_{\theta\theta-j}$; then the axial stress is calculated from

$$\sigma_{zz-j} = \frac{\left(f_j^{PS} + f_j\right)}{A_j} \tag{63}$$

FAVOR uses a reduced-integration two-point Gauss-Legendre quadrature rule for the calculation of σ_{rr} and $\sigma_{\theta\theta}$ in each element. The Gauss sample points and weights for two-point quadrature are:

$$\int_{-1}^{+1} g(\xi)d\xi \approx \sum_{i=1}^{2} \omega_i g(\xi_i) \text{ where } \{\xi_i\} = \begin{Bmatrix} -\sqrt{\frac{1}{3}} \\ +\sqrt{\frac{1}{3}} \end{Bmatrix}; \{\omega_i\} = \begin{Bmatrix} 1 \\ 1 \end{Bmatrix} \tag{64}$$

For the calculation of the axial stresses, each of the elements is divided into two sub-elements, each containing one of the two Gauss points, and the axial stresses are calculated at each of the Gauss points. Stresses at the nodes of the finite-element mesh are obtained by interpolation and extrapolation using a cubic spline fit of the stresses at the Gauss points. The stress analysis uses the same mesh and quadratic elements that are applied in the thermal analysis described in the previous section. Details regarding the formation and assembly of the stiffness matrix and load vector for a static stress analysis are given in any text on finite-element methods. See, for example, ref. [89].

4.1.3 Linear-Elastic Fracture Mechanics (LEFM)

The FAVOR code's linear-elastic stress model treats axial flaws exposed to a one-dimensional axisymmetric stress field and circumferential flaws exposed to a generalized-plane-strain stress field. These flaws are, therefore, assumed to experience only a Mode I loading, where the principal load is applied normal to the crack plane, thus tending to open the crack. It is also assumed that the plastic zone around the crack tip is fully contained, and the overall deformation-load response of the structure is linear. For these high-constraint conditions, the principles of linear-elastic fracture mechanics (LEFM) apply when calculating driving forces for the crack.

4.1.3.1 Mode I Stress-Intensity Factors

For the cracked structure under LEFM conditions, the singular stress field in the vicinity of the crack tip can be characterized by a single parameter. This one-parameter model has the form

$$\begin{aligned} \sigma_{\theta\theta} &= \frac{K_I}{\sqrt{2\pi r}} \quad \text{for axial flaws} \\ \sigma_{zz} &= \frac{K_I}{\sqrt{2\pi r}} \quad \text{for circumferential flaws} \end{aligned} \tag{65}$$

where r is the radial distance from the crack tip, and the crack plane is assumed to be a principal plane. The critical fracture parameter in Eq. (65) is the Mode I stress-intensity factor, K_I. When the conditions for LEFM are met, the problem of calculating the stress-intensity factor can be formulated solely in terms of the flaw geometry and the stress distribution of the uncracked structure.

FAVOR, v04.1, has an extensive stress-intensity-factor-influence coefficient (SIFIC) database for finite- and infinite-length surface flaws that has been implemented in the FAVLoad module for R_i/t = 10 only. The HSST program at ORNL has also developed a similar database for R_i/t = 20, which was implemented in earlier versions of FAVOR and could be re-installed for future releases if the need arises.

4.1.3.2 Inner Surface-Breaking Flaw Models –Semi-Elliptic and Infinite Length

For inner surface-breaking flaws, the stress-intensity-factor, K_I, is calculated in FAVOR using a weighting-function approach originally introduced by Bückner [90] and applied by other researchers [91-94], including the developers of OCA-I [95] and OCA-P [96]. The HSST Program at ORNL generated a database of SIFICs for axial infinite-length [97] and axial semi-elliptical [98] surface flaws along with circumferential 360-degree [97] and circumferential semi-elliptical [99] surface flaws. These databases have been implemented in the FAVLoad module.

Semi-Elliptic Finite Surface Flaws

As mentioned above, the stress-intensity factor, K_I, is calculated by a linear superposition technique proposed by Bückner [90], where, instead of analyzing the cracked structure using actual loads, the analysis is performed with a distributed pressure loading applied to the crack surfaces only. This pressure is opposite in sign, but equal in magnitude and distribution, to the stresses along the crack line that are calculated for the uncracked structure with the actual loads applied. For an arbitrary stress distribution and for the case of a three-dimensional semi-elliptical surface flaw, the truncated stress distribution can be approximated by a third-order polynomial of the form

$$\sigma(a') = C_0 + C_1(a'/a) + C_2(a'/a)^2 + C_3(a'/a)^3 \tag{66}$$

where $\sigma(a')$ is the stress normal to the crack plane at radial position, a'. The variables a' and a are defined in Fig. 23, and the coefficients (C_0, C_1, C_2, C_3) are calculated by a generalized least squares regression analysis in the FAVLoad module for the stress distribution calculated for the uncracked structure across the crack depth. The K_I values are determined for each of the individual terms (stress distributions) in Eq. (66) and then added to obtain the total K_I value as follows:

$$K_I(a) = \sum_{j=0}^{3} K_{Ij}(a) = \sum_{j=0}^{3} C_j \sqrt{\pi a} K_j^*(a) \tag{67}$$

where

$$K_j^*(a) = \frac{K_{Ij}^{'}(a)}{C_j^{'}\sqrt{\pi a}} \tag{68}$$

Values of $K_{Ij}^{'}(a)/C_j^{'}\sqrt{\pi a}$ were calculated for each of the normalized stress distributions corresponding to each term in Eq. (66) (see Fig. 24), using three-dimensional finite-element analysis results and an arbitrary value of $C_j^{'} = 1$. The dimensionless quantity $K_j^*(a)$ is referred to as the *influence coefficient*. For semi-elliptic flaws, $K_j^*(a)$ values can be calculated for several points along the crack front, in which case Eq. (67) becomes

$$K_I(\phi) = \sum_{j=0}^{3} C_j \sqrt{\pi a} K_j^*(\phi) \tag{69}$$

where ϕ is the elliptical angle denoting the point on the crack front, and the crack-depth notation (a) has been dropped. Although SIFICs are available in the database for a range of elliptical angles, this baseline release of FAVOR only calculates the value of K_I at the deepest point along the flaw front (i.e., $\varphi = 90°$).

The presence of a thin layer of stainless steel cladding on the inner surface of reactor pressure vessels has a significant effect on the K_I values for inner-surface flaws because of very high thermal stresses generated in the cladding during a thermal transient. When using influence coefficients for three-

dimensional flaws, it is necessary to represent the stress distribution in the uncracked cylinder with a third-order polynomial, and thus the discontinuity in the thermal stress at the clad-base material interface presents a problem. To accommodate the stress discontinuity associated with the cladding, influence coefficients were calculated for the cladding stresses alone; the corresponding K_I value can then be superimposed on the K_I value due to the stresses in the base material. This is accomplished by first calculating a K_I value for a continuous-function stress distribution obtained by a linear extrapolation of the stress distribution in the base material to the clad-base interface. Then a K_I value is calculated for the stress distribution in the cladding by subtracting the extrapolated distribution from the actual assumed-linear distribution in the cladding. The total K_I value is simply the sum of the two. Because the stress distribution in the cladding is essentially linear, only a first-order polynomial is used for the cladding stress-intensity-factor-influence coefficients.

The influence coefficients implemented in FAVOR were calculated using the ABAQUS [100] finite-element code. Three-dimensional finite-element models were generated for a range of relative crack depths (a / t) and aspect ratios (L / a) (see Fig. 23). The analysis matrix included relative crack depths of $0.01 \le (a/t) \le 0.5$ and aspect ratios of $L/a = 2, 6, 10$. In the process of calculating the SIFICs, careful attention was paid to using adequately converged finite-element meshes and an appropriate cylinder length. The number of elements in the circumferential and axial directions and around the crack front was increased, one at a time, until the addition of one element changed the value of K_I by less than one percent. With regard to cylinder length, a minimum incremental length of the cylinder that could be added to the length of the flaw to negate end effects was estimated from Eq. (70) [101]

$$\ell = 2\pi \left[\frac{R_i^2 t^2}{3(1-\nu^2)} \right]^{1/4} \tag{70}$$

where ν is Poisson's ratio, R_i is the inner radius of the vessel, and t is the wall thickness.

The analysis results in Ref. [99] demonstrated that there were essentially no differences in SIFICs between the axial and circumferential orientations for relative flaw depths of $0.01 \le a/t < 0.5$ and flaw aspect ratios of $L/a = 2$, 6, and 10. This important finding implies that SIFICs for axial flaws can be used for circumferential flaws up to a relative flaw depth of 0.5 with very little error. The greatest difference ($\square$ 5%) between the two orientations occurs for flaw geometries with an a/t = 0.5 and L/a = 10. In Appendix B, SIFICs for both axial and circumferential orientations for relative flaw depths of a/t = 0.01, 0.0184, 0.05, 0.075, 0.1, 0.2, and 0.3 are presented in Tables B1-B7, respectively. Table B8 presents the SIFICs for an axial flaw with a/t = 0.5, and Table B9 presents the SIFICs for a circumferential flaw with a/t = 0.5.

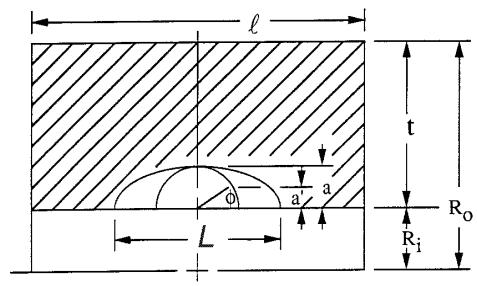

The truncated stress distribution is approximated with a third order polynomial

$$\sigma(a') = C_0 + C_1(a'/a) + C_2(a'/a)^2 + C_3(a'/a)^3$$

K_I values are calculated for each of the individual terms and then added to obtain the total K_I value

$$K_I(a) = \sum_{j=0}^{3} C_j \sqrt{\pi a} K_j^*(a)$$

for 3-D flaws

$$K_I(\phi) = \sum_{j=0}^{3} C_j \sqrt{\pi a} K_j^*(\phi)$$

Fig. 23. Influence coefficients, *K, have been calculated for finite semi-elliptical flaws with aspect ratios *L* / *a* = 2, 6, and 10 for R_i / *t* = 10.**

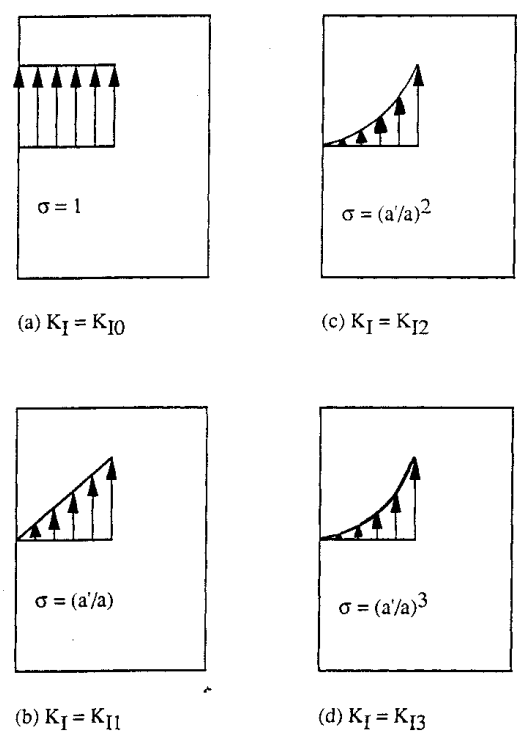

Fig. 24. Crack-surface loading cases for determining finite 3D flaw influence coefficients: (a) uniform unit load, (b) linear load, (c) quadratic load, and (d) cubic load.

Infinite-Length Surface Flaws

Figure 25 shows the geometries for the axial and circumferential infinite-length flaws. Figure 26 illustrates the decomposition of a cracked structure under actual loads into an equivalent problem with two components. One component is an uncracked structure under actual loads for which $K_I = 0$, since there is no crack. The second component is a cracked structure having a crack face loading equal in magnitude and opposite in direction to the stress distribution in the uncracked structure at the location of the crack. Therefore, the problem of interest reduces to the calculation of the K_I for the second component. This calculation can be accomplished by computing K^* values for each of several unit loads applied at specified points along the crack face (see Fig. 27) and then weighting them by the truncated crack-free stress distribution associated with the equivalent problem [95]. The procedure can be summarized as follows:

axial flaws

$$K_I(a) = \sum_{i=1}^{n} \sigma_i \Delta a_i K_i^*(a_i', a) \tag{71}$$

circumferential flaws

$$K_I(a) = \sum_{i=1}^{n} 2\pi(R + a_i')\sigma_i \Delta a_i K_i^*(a_i', a) \tag{72}$$

where

$\Delta a_i =$ an increment of a about a_i' such that $\sum_{i=1}^{n} \Delta a_i = a$

$a_i' =$ radial distance from open end of crack to point of application of unit load,

$\sigma_i =$ average crack-free stress over Δa_i for equivalent problem

$K_I =$ opening Mode I stress-intensity factor

$K_I^* =$ stress-intensity factor per unit load applied at a_i' , where load has dimensions of force/length for axial flaws and force for circumferential flaws

$n =$ number of points along length of crack for which K_i^* are available,

$R =$ inside radius of vessel.

The ABAQUS (version 4.9.1) finite-element code was used to calculate the influence coefficients presented in Appendix B. The general procedure consisted of developing a finite-element model for each crack depth and then individually applying unit loads at corner nodes located along the crack face. The axial stress-intensity-factor influence coefficients given in Table B10 have been nondimensionalized by multiplying by the factor ($0.1\, t^{1/2}$), where t is the wall thickness, and the circumferential stress-intensity-factor influence coefficients given in Table B11 have been nondimensionalized by multiplying by the factor ($10\, t^{3/2}$). These normalizing factors account for the

fact that the applied load in the generalized plane-strain analyses for axial flaws is 1.0 kip/in. of model thickness, and the applied load in the axisymmetric analyses of the circumferential flaws is a 1.0 kip total "ring" load. For both orientations, the range of relative flaw depths are $a / t = \{0.01, 0.02, 0.03, 0.05, 0.075, 0.1, 0.2, 0.3, 0.4, 0.5, 0.6, 0.7, 0.8, 0.9, \text{and } 0.95\}$. It should be noted that values in Tables B10 and B11 for $a'/a \geq 0.95$ represent "fitted" or extrapolated values rather than directly computed ones. ABAQUS version 4.9.1 did not correctly compute the *J*-integral for *J*-paths in which the load on the crack face was contained within the contour itself.

Finally, it should be pointed out that, as with the finite-surface flaws, great care was exercised in developing finite-element meshes that would produce converged solutions. Higher-order meshes were employed throughout the modeling. Starter finite-element meshes for each crack depth were examined for convergence by approximately doubling the mesh refinement, i.e., the number of nodes and elements, and performing a representative K^* calculation with the more refined model. This procedure was repeated until the difference in K^* values between successive models was less than one percent, at which time the more refined model was selected for the final computation.

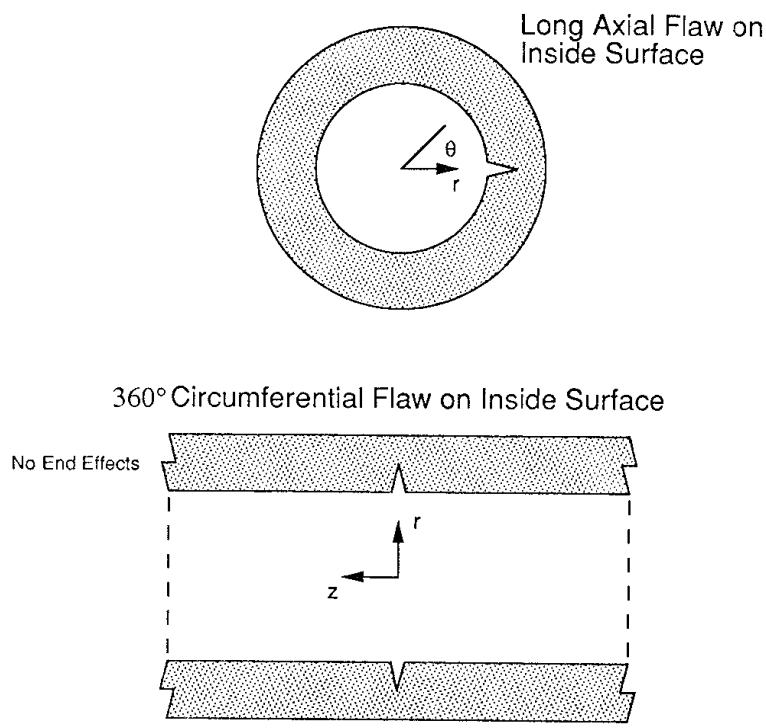

Fig. 25. Influence coefficients have been computed for both infinite axial and 360-degree circumferential flaws.

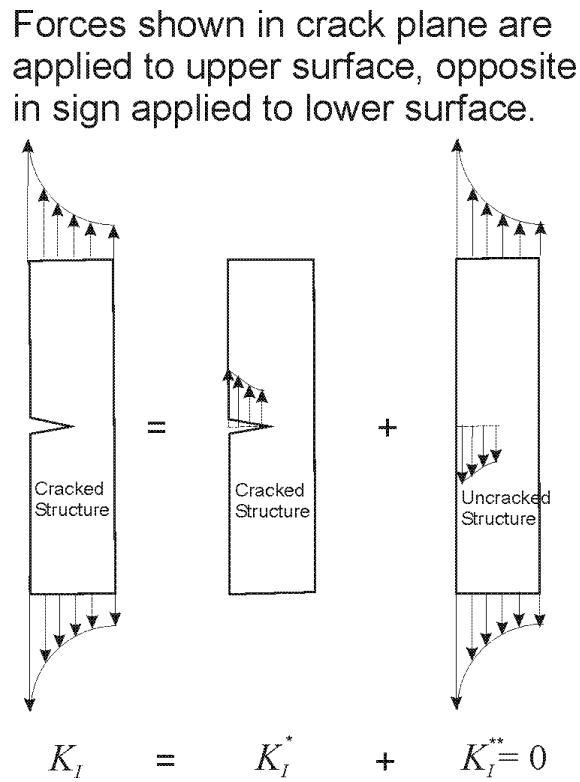

Fig. 26. Superposition allows the use of an equivalent problem to compute the stress intensity factor.

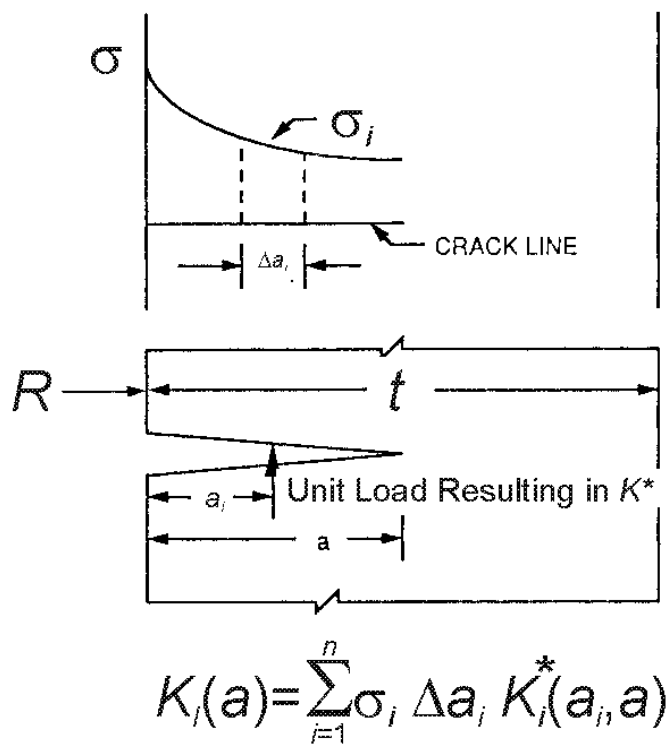

Fig. 27. Influence coefficients, *K, represent stress intensity factor per unit load applied to the crack face.**

4.1.3.3 Embedded Flaw Model

The computational methodology implemented in FAVOR for calculating Mode I stress-intensity factors, K_I , for embedded flaws [102] is the EPRI NP-1181 analytical interpretation [103] of the ASME Section XI-Appendix A [104] model for embedded (or "subsurface" in the nomenclature of Ref. [104]) flaws. Figure 28 is a schematic of the ASME embedded flaw model with the relevant descriptive variables.

The procedure for calculating Mode I stress-intensity factors, K_I , is based on the resolution of nonlinear applied stresses through the RPV wall thickness into the linear superposition of approximate membrane and bending stress components. The K_I factor is thus computed from the following relation:

$$K_I = (M_m \sigma_m + M_b \sigma_b)\sqrt{\pi a / Q} \tag{73}$$

where:

$2a =$ the minor axis of the elliptical subsurface flaw
$Q =$ flaw shape parameter
$M_m =$ free-surface correction factor for membrane stresses
$M_b =$ free-surface correction factor for bending stresses
$\sigma_m =$ membrane stress
$\sigma_b =$ bending stress

The stress-linearization procedure, depicted in Fig. 29 for a concave upward nonlinear stress profile, involves the interpolation of the applied stresses at two points on the flaw crack front – point 1 at a distance x_1 from the inner surface and point 2 at a distance x_2 from the inner surface. A straight line is fitted through these two points which represents a linear approximation, $\hat{\sigma}(x)$, of the original nonlinear stress profile, $\sigma(x)$, where x is the distance from the inner surface. The effective membrane stress, σ_m , is located at $x = t/2$ along this line, and the bending stress, σ_b, is the stress at the inner surface ($x = 0$) minus the membrane stress. The nonlinear stress profile, $\sigma(x)$, is resolved into the linear superposition of the membrane stress (σ_m) and bending stress (σ_b) (see Fig. 29) as follows:

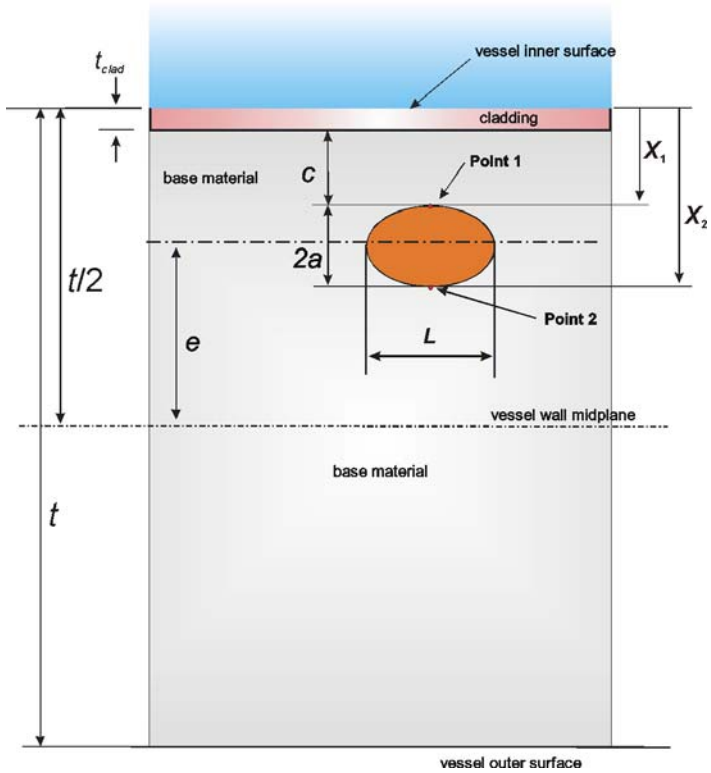

Fig. 28. Geometry and nomenclature used in embedded-flaw model.

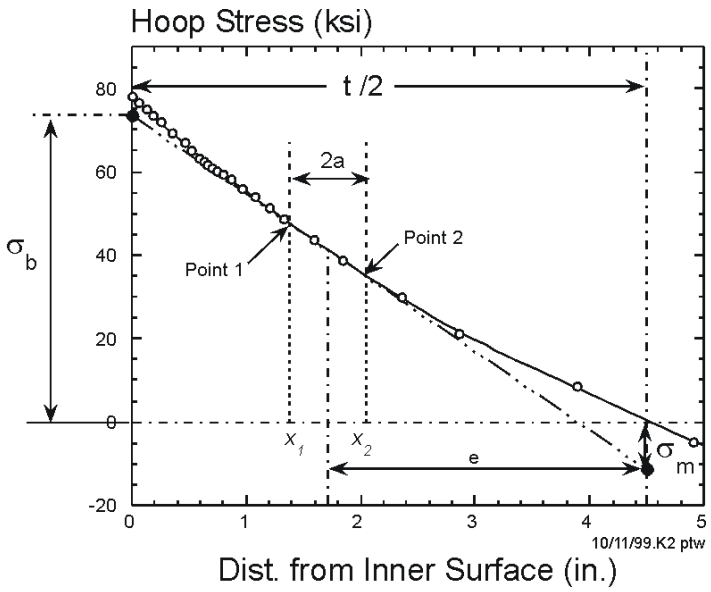

Fig. 29. Resolution of computed nonlinear stress profile into the linear superposition of effective membrane and bending stresses.

$$\sigma_m = \hat{\sigma}(t/2) = \frac{\left(\sigma(x_2) - \sigma(x_1)\right)}{2a} \times \left(t/2 - x_1\right) + \sigma(x_1) \tag{74}$$

$$\sigma_b = \hat{\sigma}(0) - \sigma_m = \frac{\left(\sigma(x_1) - \sigma(x_2)\right)}{2a} \times \left(t/2\right) \tag{75}$$

The formal definition of the shape parameter Q is based on the complete elliptic integral of the second kind, $E(x)$,

$$\begin{aligned} &Q(x) = E^2(x) \\ &E(x) = \int_0^{\pi/2} \sqrt{\left(1 - x\sin^2(\theta)\right)} d\theta \text{ for } 0 \le x \le 1 \\ &x = 1 - 4\left(\frac{a}{L}\right)^2 \end{aligned} \tag{76}$$

In ref. [103], the elliptic integral is replaced by an infinite-series approximation for Q of the form

$$Q \approx \frac{\pi^2}{4(1+m)^2}\left[1 + \frac{m^2}{4} + \frac{m^4}{64} + \frac{m^6}{256} + \left(\frac{5}{128}\right)^2 m^8 + \left(\frac{7}{256}\right)^2 m^{10}\right]^2 \tag{77}$$

where

$$m = \frac{1 - 2(a/L)}{1 + 2(a/L)}$$

Equation (77) has been implemented in FAVOR. The equation for the free-surface correction factor for the membrane stress (M_m) is as follows:

$$\begin{aligned} M_m = {} & D_1 + D_2(2a/t)^2 + D_3(2a/t)^4 + D_4(2a/t)^6 + D_5(2a/t)^8 + \\ & \frac{D_6(2a/t)^{20}}{\left[1 - \left(2e/t\right) - \left(2a/t\right)\right]^{1/2}} \end{aligned} \tag{78}$$

where:

$$\begin{aligned} D_1 &= 1 \\ D_2 &= 0.5948 \\ D_3 &= 1.9502\left(e/a\right)^2 + 0.7816\left(e/a\right) + 0.4812 \\ D_4 &= 3.1913\left(e/a\right)^4 + 1.6206\left(e/a\right)^3 + 1.8806\left(e/a\right)^2 + \\ &\quad 0.4207\left(e/a\right) + 0.3963 \\ D_5 &= 6.8410\left(e/a\right)^6 + 3.6902\left(e/a\right)^5 + 2.7301\left(e/a\right)^4 + \\ &\quad 1.4472\left(e/a\right)^3 + 1.8104\left(e/a\right)^2 + 0.3199\left(e/a\right) + \\ &\quad 0.3354 \end{aligned}$$

$D_6 = 0.303$

The equation for the free-surface correction factor for bending stresses (M_b) is:

$$M_b = E_1 + \frac{\begin{bmatrix} E_2\left(2e/t\right) + E_3(2e/t)^2 + E_4\left(2e/t\right)\left(2a/t\right) + \\ E_5\left(2a/t\right)\left(2e/t\right)^2 + E_6\left(2a/t\right) + \\ E_7\left(2a/t\right)^2 + E_8\left(2e/t\right)\left(2a/t\right)^2 + E_9 \end{bmatrix}}{\left[1-\left(2e/t\right)-\left(2a/t\right)\right]^{1/2}} \tag{79}$$

where:

$$E_1 = 0.8408685\,,\ E_2 = 1.509002\,,\ E_3 = -0.603778\,,$$
$$E_4 = -0.7731469\,, E_5 = 0.1294097,\ \ E_6 = 0.8841685\,,$$
$$E_7 = -0.07410377\,,\ E_8 = 0.04428577\ E_9 = -0.8338377$$

4.1.3.4 Inclusion of Residual Stresses in Welds

The through-wall weld residual stress distribution was derived in the HSST program from a combination of experimental measurements taken from an RPV shell segment made available from a cancelled pressurized-water reactor plant and finite-element thermal and stress analyses [105,106].

The residual stresses in an RPV structural weld stem from (a) the clad-shell differential thermal expansion (DTE) and (b) the residual stresses, generated by the structural welding process, that are not completely relaxed by the post-weld heat-treatment [107]. Data required for calculation of these residual stresses were obtained by cutting a radial slot in the longitudinal weld in a shell segment from an RPV and then measuring the deformation of the slot width after cutting. The measured slot openings were assumed to be the sums of the openings due to the clad-base material differential thermal expansion (DTE) and the weld residual stresses. To evaluate the residual stresses in an RPV structural weld, a combined experimental and analytical process was used. Slot opening measurements were made during the machining of full-thickness clad beam specimens with two-dimensional flaws. The blanks measured 54-inches long (circumferential direction), 9-inches wide (longitudinal direction), and 9-inches thick (radial direction). The blanks were cut so as to have a segment of a longitudinal seam weld from the original RPV at the mid-length of the blank. Using the wire-EDM process, a slot was cut along the weld centerline in a radial direction from the inside (clad) surface of the blank. Measurements were made on three specimens having final slot depths of 0.045 inches, 0.90 inches, or 4.50 inches, respectively. After machining, the widths of the slots were

measured along each radial face of the blanks. Finite-element analyses were used to develop a through-thickness stress distribution that gave a deformation profile matching the measured values. This distribution is shown in Fig. 30, where the contributions from clad and base DTE have been removed. The residual stress profile is modified to apply to an analysis of a vessel that has a wall thickness other than the one from which the stress distribution is derived. The through-wall weld residual stress distribution retains the shape and magnitude as derived from experiment/analysis; however, it is compressed or expanded to fit the current wall thickness by modifying the residual profile data by the ratio of the current RPV wall thickness to 8.936, i.e., the wall thickness from which the stress distribution was derived. The user has the option in the input deck for FAVLoad [45] to specify whether or not the weld residual stress profile will be superimposed on either the axial or circumferential through-wall stress distributions, or both.

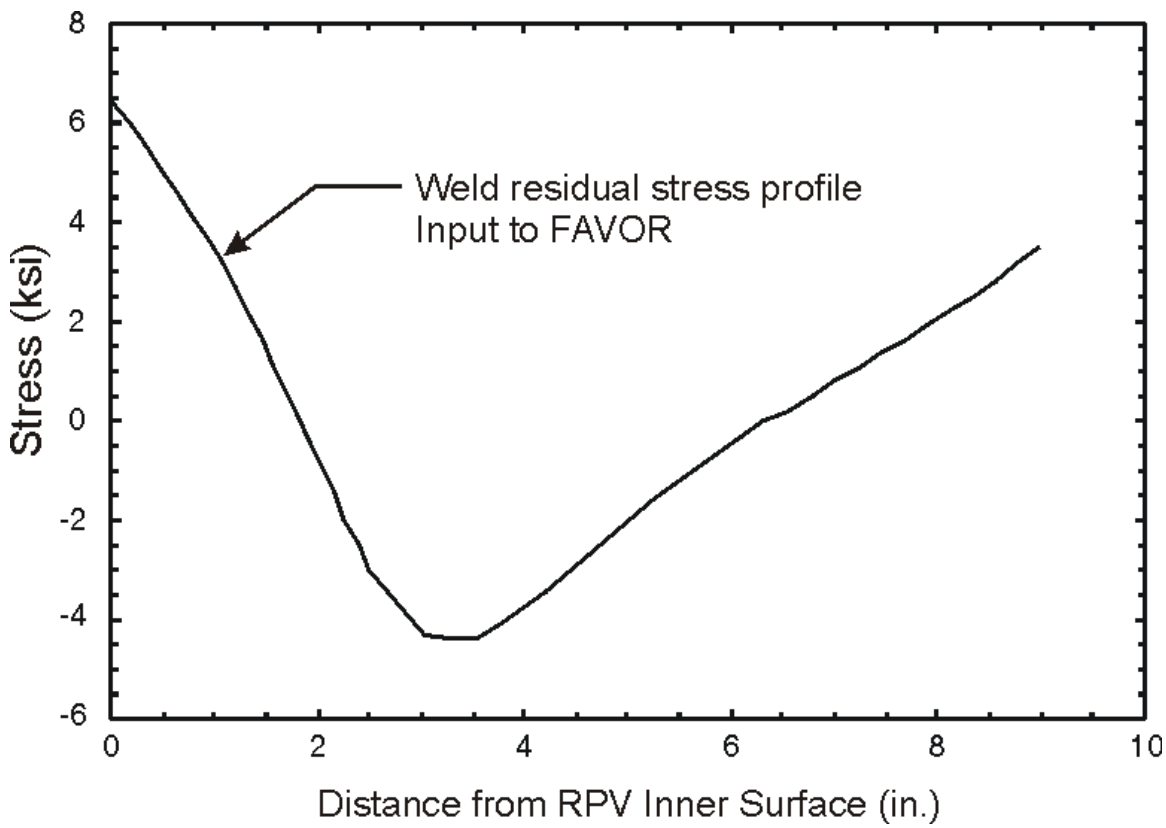

Fig. 30. Weld residual stress through-thickness distribution developed for use in RPV integrity analyses.

4.1.3.5 Inclusion of Crack-Face Pressure Loading for Surface-Breaking Flaws

Crack-face pressure loading on the exposed faces of internal surface-breaking flaws is included as an option in the mechanical loading of the family of surface-breaking flaws in a FAVLoad deterministic analysis. The Mode I Stress Intensity Factor database provides a simple but accurate mechanism for including the effects of crack-face pressure loading.

Semi-Elliptic Finite Surface Flaws

For semi-elliptic finite surface flaws, the uniform unit-load 3D-flaw influence coefficients can be applied to calculate the contribution, K_{I-cfp}, of the crack-face pressure loading to the total stress intensity factor at the deepest point of the flaw $(\phi = 90°)$ by

$$K_{I-cfp} = \sqrt{\pi a}\ K_0^*\ p(\tau)$$

where $p(\tau)$ is the coolant pressure in ksi at time τ in the transient. By linear superposition, the crack-face pressure component, K_{I-cfp}, is then added to the total stress intensity factor.

Infinite-Length Surface Flaws

A similar procedure can be followed for infinite-length surface flaws.

for axial flaws

$$K_{I-cfp}(a) = \sum_{i=1}^{n} p(\tau)\ \Delta a_i K_i^*(a_i', a)$$

for circumferential flaws

$$K_{I-cfp}(a) = \sum_{i=1}^{n} 2\pi(R + a_i')\ p(\tau)\ \Delta a_i K_i^*(a_i', a)$$

where

$\Delta a_i =$ an increment of a about a_i' such that $\sum_{i=1}^{n} \Delta a_i = a$

$a_i' =$ radial distance from open end of crack to point of application of unit load,

$p(\tau) =$ coolant pressure at time τ uniformly applied over the crack face

$K_{I-cfp} =$ opening Mode I stress-intensity factor contribution due to crack-face pressure

$K_I^* =$ stress-intensity factor per unit load applied at a_i', where load has dimensions of force/length for axial flaws and force for circumferential flaws

$n =$ number of points along length of crack for which K_i^* are available,

$R =$ inside radius of vessel.

4.2 Sampled LEFM Material and Correlative Properties

A detailed description of the technical bases for the models in this section is presented in Ref. [108]. A summary of the material in [108] is presented here with emphasis on the implementation of these models into FAVOR.

4.2.1 Reference Nil-Ductility Transition Temperature, RT_{PTS}, at EOL Fluence

For each major region, FAVOR calculates and reports a value of RT_{NDT} (designated as RT_{PTS}). The value of RT_{PTS} that is reported for each major region corresponds to the subregion within that major region that has the highest value of RT_{PTS}. This value of RT_{PTS} is not sampled from a distribution and is reported for comparison purposes only and is not used in any subsequent analyses.

There are two minor differences between the definition of RT_{PTS} as utilized in FAVOR and as currently defined by 10CFR50.61 [10], where RT_{PTS} is defined as follows:

$$RT_{PTS} = RT_{NDT(U)} + M + \Delta RT_{PTS} \tag{80}$$

where M is the margin term added to account for uncertainties in the values of the unirradiated $RT_{NTD(U)}$ and ΔRT_{PTS}. The margin term, M, is determined by

$$\begin{aligned} M &= 2\sqrt{\sigma_U^2 + \sigma_\Delta^2} \\ \sigma_U &= \text{ the standard deviation for } RT_{NDT(U)} \\ \sigma_\Delta &= \text{ the standard deviation for } \Delta RT_{NDT} \end{aligned} \tag{81}$$

In 10CFR50.61 [10], ΔRT_{PTS} is the mean value of the transition temperature shift due to irradiation at the *EOL* (end-of-licensing) fast-neutron fluence attenuated to the clad-base interface; whereas, in FAVOR, ΔRT_{PTS} is the mean value of the transition temperature shift due to the irradiation corresponding to the attenuated neutron fluence at the time in the operating life of the vessel for which the PFM analysis is being performed.

Currently, in 10CFR50.61, ΔRT_{PTS} is calculated from the irradiation shift model taken from Regulatory Guide 1.99, revision 2 [12], where

$$\Delta RT_{PTS} = (CF)\, f(\delta)^{(0.28-0.10\log_{10}(f(\delta)))}$$

$$\begin{aligned} CF &= \text{chemistry factor, a continuous function of copper and nickel} \\ f(\delta) &= \text{best-estimate neutron fluence } [10^{19}\ \text{n/cm}^2;\ E > 1\ \text{MeV}] \text{ attenuated} \\ &\quad \text{from the inner surface to the clad/base metal interface} \\ \delta &= \text{distance from the inner surface to the clad/base metal interface [in.]} \end{aligned} \tag{82}$$

The fast-neutron fluence is attenuated through the wall by the relation

$$f(\delta) = f(0)\exp(-0.24 \times \delta) \tag{83}$$

where δ is in inches and $f(0)$ is the neutron fluence at the inner surface. Look-up tables for the chemistry factor, *CF*, taken from 10CFR50.61 [10], are included in FAVOR for the calculation of RT_{PTS}.

In FAVOR, ΔRT_{PTS} may be calculated using either Regulatory Guide 1.99, Rev 2 (RG 1.99, Rev 2) [12], as defined above, or by ΔT_{30} (see Eq. (84)) as calculated by the Eason and Wright irradiation-shift model [86] to be discussed in the following section. The intent is to provide for the generality of using the current RG 1.99, Rev 2 or the Eason and Wright irradiation-shift model [86]. It is anticipated that the Eason and Wright model [86] may supersede the current RG 1.99, Rev 2 model discussed above.

4.2.2 Radiation Embrittlement

Irradiation damage of RPV steels in U.S. PWRs occurs as a consequence of two hardening mechanisms: *matrix hardening* and *age hardening*. Details of these mechanisms are taken from [108]:

> **Matrix Hardening** – Matrix damage develops continuously during irradiation, producing hardening that has a square root dependence on fluence. Matrix damage can be divided into two components: unstable matrix defects (UMD), and stable matrix defects (SMD). Unstable matrix defects are formed at relatively low fluence and are small vacancy or interstitial clusters, complexed with solutes such as phosphorous. UMDs are produced in displacement cascades. Increasing flux causes increasing hardening due to these defects, but they occur relatively independently of alloy composition. In low copper alloys, at low fluence and high flux, UMD is the dominant source of hardening; however, in high copper steels, these defects delay the copper-rich precipitate contribution to hardening by reducing the efficiency of radiation-enhanced diffusion. Stable matrix features form at high fluence and include nanovoids and more highly complexed clusters. These defects cause hardening that increases with the square root of exposure and is especially important at high fluence levels.
>
> **Age Hardening** – Radiation accelerates the precipitation of copper held in solid solution, forming copper-rich precipitates (CRPs) that inhibit dislocation motion and, thereby, harden the material. This hardening rises to a peak value and is then unaffected by subsequent irradiation because no copper remains in solid solution to precipitate out and

cause damage. The magnitude of this peak depends on the amount of copper initially in solution. This copper is available for subsequent precipitation. Post-weld heat treatment (PWHT) performed before the RPV is placed into service can also precipitate copper, removing its ability to cause further damage during irradiation. Thus, different materials are expected to have different peak hardening values due to differing pre-service thermal treatments. Additionally, the presence of nickel in the alloy further enhances its age-hardening capacity. Nickel precipitates together with copper, forming larger second-phase particles that present greater impediments to dislocation motion and, thereby, produce a greater hardening effect.

These physical insights helped to establish the functional form of a relationship between basic material composition, irradiation-condition variables, and measurable quantities such as yield-strength increase, Charpy-transition-temperature shift, and toughness-transition-temperature shift. A quantitative relationship was developed from the database of Charpy shift values, ΔT_{30}, generated in US commercial reactor surveillance programs. Eason and Wright [86] recently developed the following physically motivated fit from these data.[8]

$$\Delta T_{30}(\bar{Ni}, \bar{Cu}, \bar{P}, \bar{f}_0(r), \tau_{\text{exposure}}, T_c, \text{product form}) =$$

$$A\exp\left(\frac{19310}{T_c + 460}\right)\left(1 + 110\bar{P}\right)\left(\bar{f}_0(r)\right)^{0.4601} + B\left(1 + 2.40\bar{Ni}^{1.250}\right) f(\bar{Cu}) g\left(\bar{f}_0(r)\right) + Bias$$

$$A = \begin{Bmatrix} 8.86\times10^{-17} \text{ for welds} \\ 9.30\times10^{-17} \text{ for forgings} \\ 12.7\times10^{-17} \text{ for plates} \end{Bmatrix}$$

$$B = \begin{Bmatrix} 230 \text{ for welds} \\ 132 \text{ for forgings} \\ 206 \text{ for plates in CE vessels} \\ 156 \text{ for other plates} \end{Bmatrix}$$

$$g(\bar{f}_0(r)) = \frac{1}{2} + \frac{1}{2}\tanh\left[\frac{\log_{10}\left(\bar{f}_0(r) + 4.579\times10^{12}\tau_{\text{exposure}}\right) - 18.265}{0.713}\right]$$

$$f\left(\bar{Cu}\right) = \begin{Bmatrix} 0 & \text{for } \bar{Cu} \le 0.072 \text{ wt \%} \\ \left(\bar{Cu}\text{-}0.072\right)^{0.659} & \text{for } \bar{Cu} > 0.072 \text{ wt \%} \end{Bmatrix} \tag{84}$$

subject to

[8] A curved overbar, $\bar{X}$, indicates a sampled random variate.

$$Cu_{\max} = \begin{Bmatrix} 0.25 \text{ for welds with Linde 80 or Linde 0091 flux} \\ 0.305 \text{ for everything else} \end{Bmatrix}$$

and

$$Bias = \begin{Bmatrix} 0 \text{ for } \tau_{\text{exposure}} < 97000 \text{ h} \\ 9.4 \text{ for } \tau_{\text{exposure}} \geq 97000 \text{ h} \end{Bmatrix}$$

where $\widehat{Cu}$ is the sampled copper content in wt%, $\widehat{Ni}$ is the sampled nickel content in wt%, $\widehat{P}$ is the sampled phosphorous content in wt%, $\widehat{f}_0(r)$ is the sampled and then attenuated neutron fluence in n/cm^2, r is the position from the inner surface of RPV wall, $\tau_{exposure}$ is exposure time in hours (input to FAVOR in EFPY), and T_c is coolant temperature in °F. The fast-neutron fluence at the inner surface of the vessel, $f_0(0)$, is sampled using the protocol given in Sect. 4.2.3. The sampled neutron fluence for the flaw is then attenuated (but not resampled) as the crack grows through the wall. The sampling distributions and protocols for plate and weld chemistry are presented in Sect. 4.2.9.

Reference [108] recommends that the uncertainty in the CVN transition shift values, ΔT_{30}, be treated as *epistemic*. Having used information concerning composition and irradiation conditions to estimate the CVN transition temperature shift using Eq. (84), it is necessary to transform these ΔT_{30} values into shifts in the fracture-toughness transition temperature. Figure 31 provides an empirical basis for the following least-squares fits for $\widehat{\Delta RT}_{NDT}$ using data extracted from the literature as discussed in [108].

$$\widehat{\Delta RT}_{NDT}(r,\ldots) = \begin{cases} 0.99\widehat{\Delta T}_{30}(r,\ldots) & \text{welds} \\ 1.10\widehat{\Delta T}_{30}(r,\ldots) & \text{plates and forgings} \end{cases} \tag{85}$$

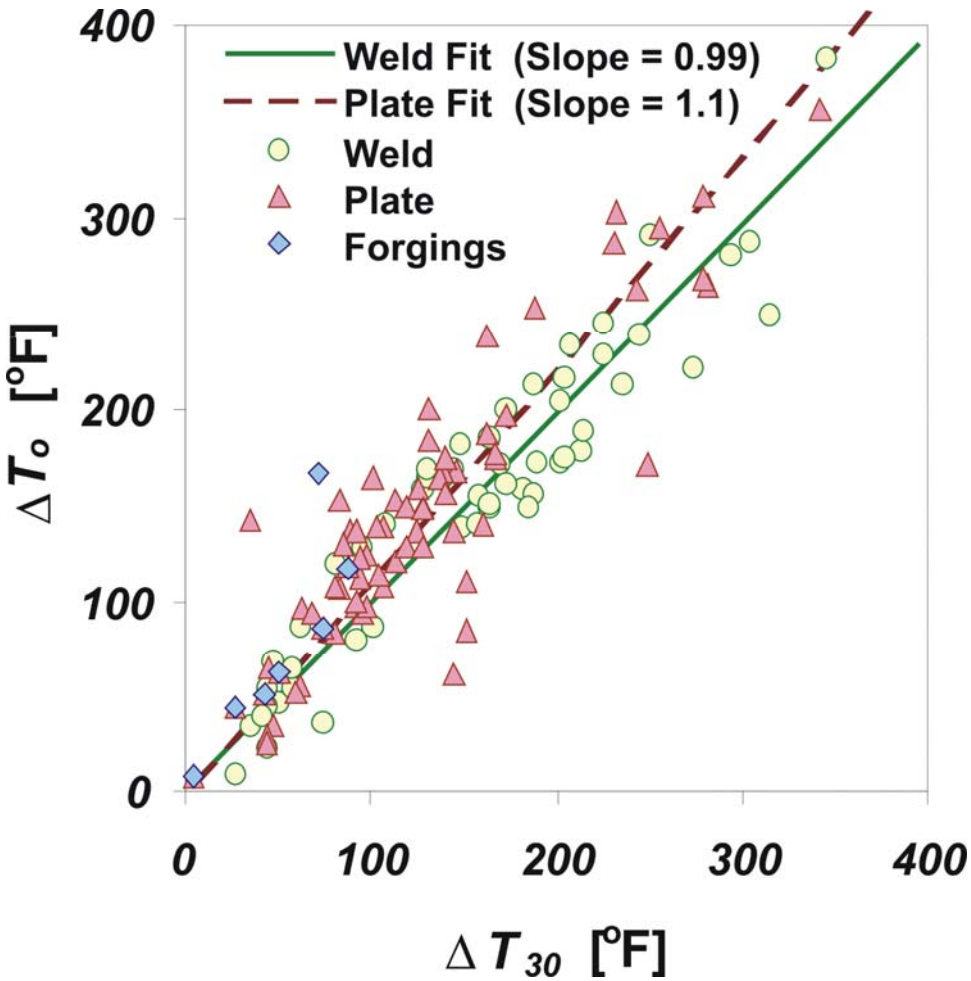

Fig. 31. Relationship between the change in the fracture-toughness index temperature ($\Delta T_0 \approx \Delta RT_{NDT}$) change in the 30 ft-lbf CVN transition temperature (ΔT_{30}) for welds and plates/forgings produced by irradiation. The difference in the best-fit slopes is statistically significant (from [108]).

4.2.3 Fast-Neutron Fluence Attenuation and Sampling Distribution

The sampled fast-neutron fluence at the crack tip is attenuated from its sampled reference value, $\tilde{f}_0(0)$, at the inner surface of the RPV wall. This attenuation takes the following form

$$\tilde{f}_0(a) = \hat{f}_0(0) \times \exp(-0.24a) \tag{86}$$

where a is the position of the flaw tip (in inches) relative to the inner surface.

The inner surface fluence is sampled from two normal distributions such that

$$\begin{aligned}
\sigma_{global} &= SIGFGL \times fluence_{subregion} \\
\hat{f}_{mean} &\leftarrow N(fluence_{subregion}, \sigma_{global}) \\
\tilde{\sigma}_{local} &= SIGFLC \times \hat{f}_{mean} \\
\tilde{f}_0(0) &\leftarrow N(\hat{f}_{mean}, \tilde{\sigma}_{local})
\end{aligned} \tag{87}$$

where the best-estimate fluence, $fluence_{subregion}$, is input by the user at the subregion level. The global *SIGFGL* and local *SIGFLC* multipliers are supplied as input by the user. Recommended values are *SIGFGL* = 0.056 and *SIGFLC* = 0.118. Negative values of sampled fast-neutron fluence are handled as nonphysical exceptions in FAVOR using the truncation protocol described in Sect. 3.3.6, with 0.0 as a one-sided truncation boundary.

4.2.4 ORNL 99/27 K_{Ic} and K_{Ia} Databases

The EPRI K_{Ic} database [73] as amended by Nanstad et al. [109] consists of 171 data points and includes data from 11 unirradiated pressure-vessel steels. These data were taken using compact tension C(T) and wedge-open-loading (WOL) test specimens ranging in size from 1T to 11T. A survey was recently conducted by ORNL to identify additional K_{Ic} and K_{Ia} data to augment the EPRI database. The result of this survey has been designated as the ORNL 99/27 extended K_{Ic}/K_{Ia} database [74].

The candidate K_{Ic} data were evaluated using the following criteria: (a) satisfaction of validity requirements given in ASTM Standard E 399 [110] to maintain consistency with the LEFM driving forces applied in the fracture model, (b) availability in tabular form, and (c) availability of unirradiated RT_{NDT0}, determined according to the *ASME Boiler and Pressure Vessel Code,* Section III, NB-2331 [111]. The ORNL survey produced an additional 84 K_{Ic} fracture-toughness values obtained from Refs. [112-116]. The extended K_{Ic} database, compiled from the amended EPRI data and from the ORNL survey, provided a total of 255 fracture-toughness data points from 18 materials for input

to the statistical model development procedures described in Ref. [74] and applied herein. A plot of the extended K_{Ic} database versus $(T - RT_{NDT0})$ is given in Fig. 32; the complete tabulation of the database is included in Appendix C of this report with a summary presented in Table 7.

A similar survey was carried out to compile an extended K_{Ia} database that would include those data in the EPRI report (see Fig. 33a). Because the ASTM Standard E 1221 [117] is relatively new, many of the existing data were generated before the adoption of the standard. Thus, it was agreed that candidate K_{Ia} data would be evaluated in a more general context, including engineering judgment of acknowledged experts and general acceptance by the nuclear technology community. The ORNL survey produced an additional 62 fracture-toughness, K_{Ia}, data points [118-120] to augment the existing 50 data points [121,122] in EPRI NP-719-SR. A complete tabulation of the 112 fracture-toughness values is given in Appendix C of this report with a summary presented in Table 8. A description of the chemistry and heat treatment of the principal steels in the ORNL 99/27 database is shown in Table 9.

In conjunction with the development of a ductile-tearing model, arrest data from large-specimen experiments carried out in the 1980s were also added to the K_{Ia} database (see Fig. 33b). These additional large-specimen arrest data came from the HSST Wide Plate test program (WP-1 [38] and WP2 [39]), the HSST Pressurized Thermal Shock Experiments (PTSE-1[26] and PTSE-2 [27]), and the HSST Thermal Shock Experiments (TSE) [123].

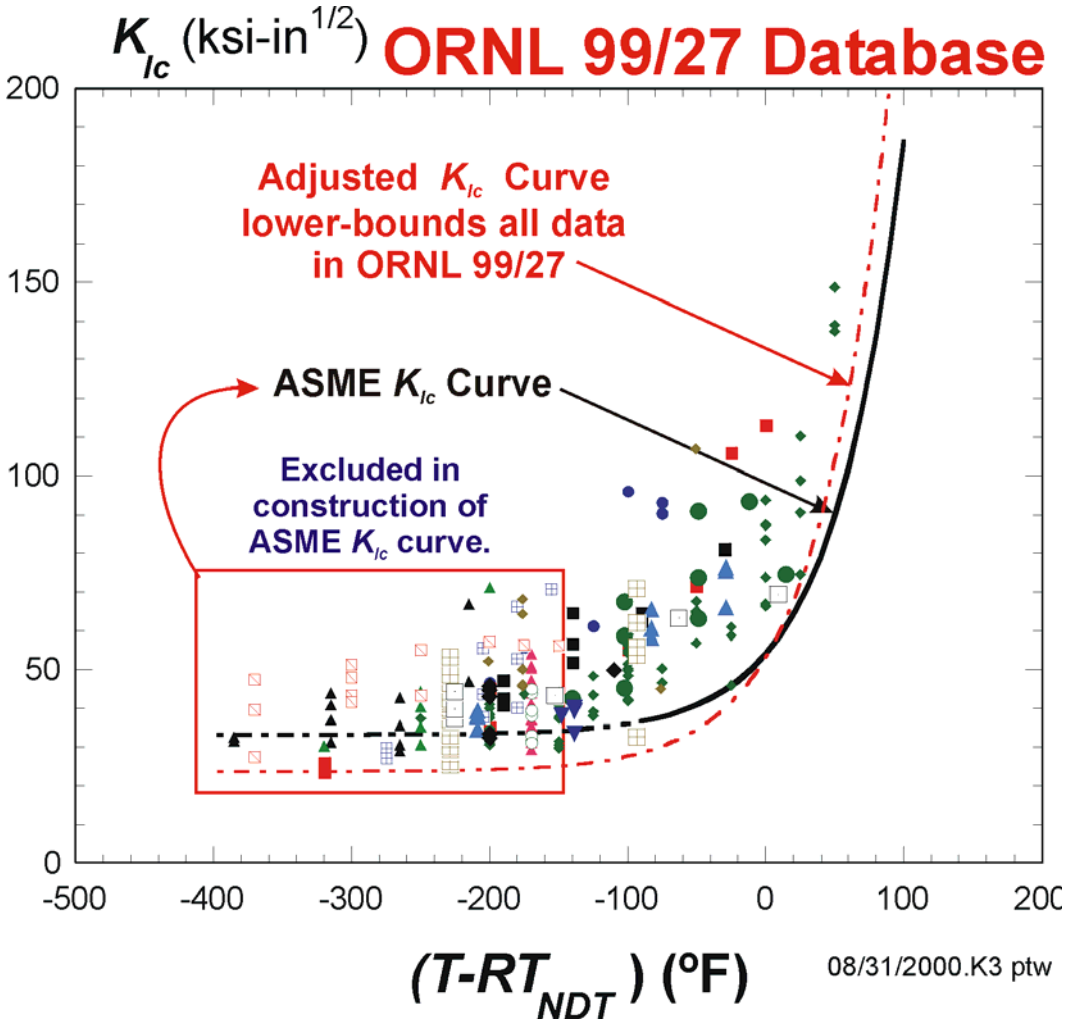

Fig. 32. ORNL 99/27 K_{Ic} database including modified ASME K_{Ic} curve that served as a lower-bounding reference curve in the development of a new transition index temperature.

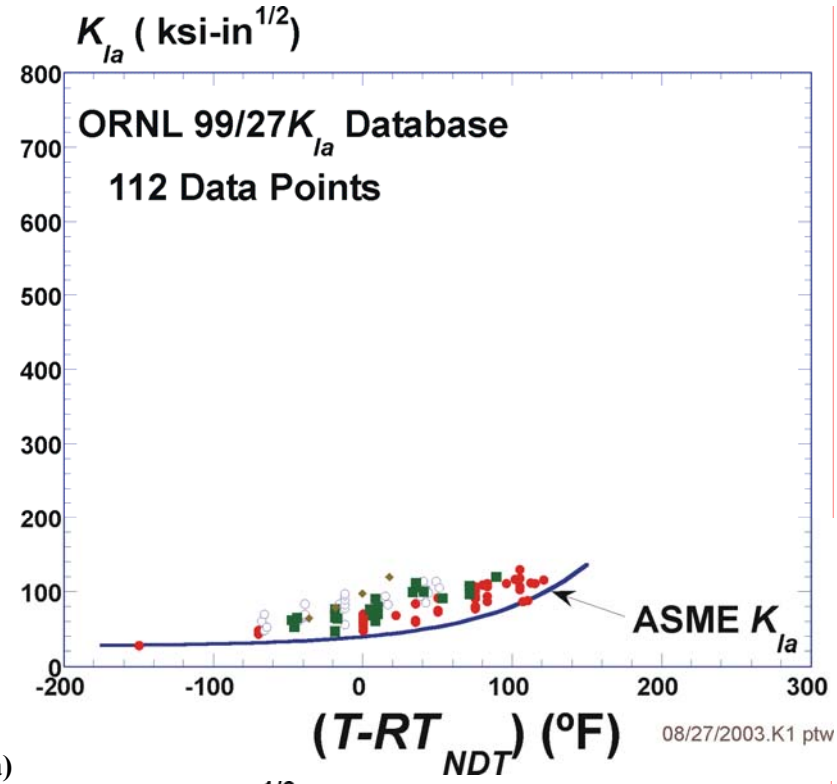

(a)

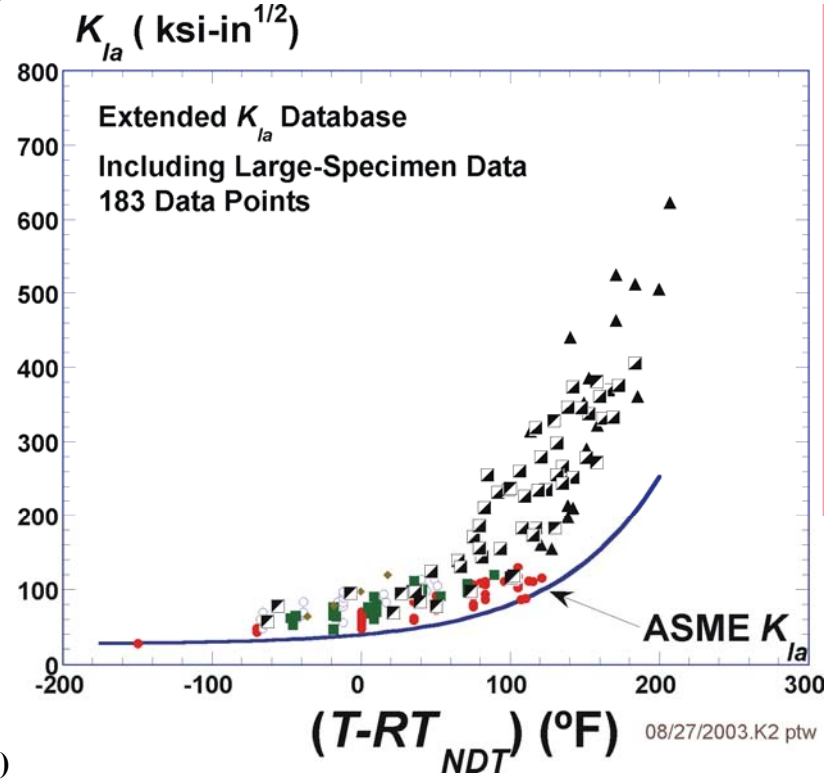

(b)

Fig. 33. K_{Ia} databases (a) ORNL 99/27 K_{Ia} database and (b) Extended K_{Ia} database.

Table 7. Summary of ORNL 99/27 K_{Ic} Extended Database

	Material	Source	Specimen Type	Size Range	Temp. Range (°F)	(T-RT_{NDT0}) Range (°F)	No. of Data Points
EPRI	**Database**	EPRI NP-719-SR					
1	HSST 01 subarc weldment	Shabbits (1969)	C(T)	1T - 6T	-200 to -50	-200 to -50	8
2	A533B Cl. 1 subarc weld	Shabbits (1969)	C(T)	1T - 8T	-200 to 0	-200 to 0	8
3	HSST 01	Mager (1970)	C(T)	1T	-150	-170	17
4	HSST 03	Mager (1970)	C(T)	1T	-150	-170	9
5	A533B Cl. 1	Mager (1969)	WOL	1T - 2T	-320 to -150	-385 to -215	13
6	HSST 02	Mager (1969)	WOL & C(T)	1T - 2T	-200 to 0	-200 to 0	41
6	HSST 02	Shabbits (1969)	C(T)	1T - 11T	-250 to 50	-250 to 50	28
7	A533B Cl. 1 weldment	Mager (1969)	WOL	1T - 2T	-320 to -200	-275 to -155	10
8	A533 B Cl. 1 weldment/HAZ	Mager (1969)	WOL	1T - 2T	-320 to -200	-320 to -200	6
9	A508 Cl.2 European Forging	Mager (1969)	WOL	1T - 2T	-320 to -100	-370 to -150	12
10	A508 Class 2	unpublished	C(T)	2T - 6T	-150 to 0	-201 to -51	9
11	A508 Class 2	unpublished	C(T)	2T - 8T	-125 to -75	-190 to -30	10
						Total	171
Additional	**Data**						
12	HSSI Weld 72W	NUREG/CR-5913.	C(T)	1T-6T	-238 to 50	-229 to 59	13
13	HSSI Weld 73W	NUREG/CR-5913	C(T)	1T-4T	-238 to -58	-209 to -29	10
14	HSST Plate 13A	NUREG/CR-5788	C(T)	½T-4T	-238 to -103	-229 to -94	43
15	A508 Cl. 3	ASTM STP 803	Bx2B C(T)	1T-4T	-238 to -4	-225 to 9	6
16	Midland Nozzle Course Weld	NUREG/CR-6249	C(T)	1T	-148 to -58	-200 to -110	6
17	Midland Beltline	NUREG/CR-6249	C(T)	1T	-148	-171	2
18	Plate 02 4th Irr. Series (68-71W)	NUREG/CR-4880	C(T)	1T	-148 to -139	-148 to -139	4
						Total	84
						Grand Total	255

Table 8. Summary of K_{Ia} Extended Database

	Material	Source	Specimen Type	Size Range	Test Temp. Range (°F)	(T-$RTNDT$) Range (°F)	No. of Data Points
EPRI	**Database**	**EPRI NP-719-SR**					
1	**HSST 02**	**Ripling (1971)**	**CCA crack arrest**	**1T-3T**	**-150 to 121**	**-150 to 121**	**50**
Additional Data	**Additional Data**						
2	**HSSI Weld 72W**	**NUREG/CR-5584**	**CCA crack arrest**		**-78 to 41**	**-68 to 51**	**32**
3	**HSSI Weld 73W**	**NUREG/CR-5584**	**CCA crack arrest**		**-78 to 59**	**-48 to 89**	**26**
4	**MW15J**	**NUREG/CR-6621**	**CCA crack arrest**		**-4 to 50**	**-36 to 18**	**4**
Large Specimen Data							
5	**HSST WP1**	**NUREG/CR-5330**	**Wide Plate Tests**	**(-)**	**84 to 198**	**94 to 207**	**18**
6	**HSST WP2**	**NUREG/CR-5451**	**Wide Plate Tests**	**(-)**	**142 tp 324**	**2 to 184**	**38**
7	**HSST PTSE-1**	**NUREG/CR-4106**	**Pressurized Vessel**	**(-)**	**326 to 354**	**100 to 158**	**2**
8	**HSST PTSE-2**	**NUREG/CR-4888**	**Pressurized Vessel**	**(-)**	**267 tp 325**	**130 to 158**	**3**
9	**HSST TSE**	**NUREG/CR-4249**	**Thermally-Shocked Cylinder**	**(-)**	**72 to 268**	**-63 to 103**	**10**
						Total =	**183**

Table 9. Chemistry and Heat Treatment of Principal Materials: ORNL 99/27 Database

Material ID	Specification	Source	Chemistry – wt (%) C	P	Mn	Ni	Mo	Si	Cr	Cu	S	Al	Heat Treatment
HSST 01	A533B Cl. 1	Mager (1970)	.22	.012	1.48	.68	.52	.25	-	-	.018	-	Note 1
HSST 02	A533B Cl. 1	Mager (1969)	.22	.012	1.48	.68	.52	.25	-	-	.018	-	Note 2
HSST 03	A533B Cl. 1	Mager (1970)	.20	.011	1.26	.56	.45	.25	.10	.13	.018	.034	Note 3
HSST 02	A533B Cl. 1	Shabbits (1969)	.22	.012	1.48	.68	.52	.25	-	-	.018	-	Note 4
HSST 01 subarc weld	A533B Cl. 1	Shabbits (1969)	.12	.014	1.35	.65	.52	.23	-	-	.012	-	Note 5
B&W subarc weldment	A533B Cl. 1	Shabbits (1969)	.10	.009	1.77	.64	.42	.36	-	-	.015	-	Note 6
PW/PH weldment	A533B Cl. 1	Mager (1969)	.09	.019	1.25	1.08	.52	.23	.05	.22	.13	.037	Note 7
MD07 European	A508 Cl. 2 Ring forging	Mager (1969)	.18	.009	1.16	.72	.51	.24	.28	-	.10	-	Note 8
-	A533B Cl. 1	Mager (1969)	.19	.012	1.37	.52	.45	.25	.13	.15	.016	.048	Note 9
72W	A533B weld	5788	.09	.006	1.66	.60	.58	.04	.27	.23	.006	-	
73W	A533B weld	5788	.10	.005	1.56	.60	.58	.04	.25	.21	.005	-	

Notes:

1.	Normalizing:	1675 °F	4 hr, air cooled
	Austentizing:	1600 °F	4 hr
	Quenching:	Water quench	
	Tempering:	1225 °F	4 hr, furnace cooled
	Stress Relief:	1150 °F	40 hr, furnace cooled
2.	Normalizing:	1675 °F	4 hr, air cooled
	Austentizing:	1600 °F	4 hr
	Quenching:	Water quench	
	Tempering:	1225 °F	4 hr, furnace cooled
	Stress Relief:	1150 °F	40 hr, furnace cooled
3.	Normalizing:	1675 °F	12 hr, air cooled
	Austentizing:	1575 °F	12 hr
	Quenching:	Water quench	
	Tempering:	1175 °F	12 hr, furnace cooled
	Stress Relief:	1125 °F	40 hr, furnace cooled
4.	Normalizing:	1675 ± 25 °F	4 hr
	Austentizing:	1520 °F – 1620 °F	4 hr
	Quenching:	Water quench.	
	Tempering:	1200 °F – 1245 °F	4 hr, air cooled
	Stress Relief:	1150 ± 25 °F	40 hr, furnace cooled to 600 °F
5.	Post Weld:	1150 ± 25 °F	12 hr
	Intermediate	1100 ± 25 °F	15 min
6.	Post Weld	1100 °F – 1150 °F	12 hr
	Intermediate	1100 °F – 1150 °F	15 min
7.		620 °C	27 hr, air cooled
8.		925 °C	5 hr
	Quenching:	Water quench	
		650 °C	3 hr, furnace cooled
		620 °C	24 hr, air cooled
9.		910 °C	8 hr
	Quenching:	Water quench	
		680 °C	10 hr, furnace cooled
		850 °C	8 hr
	Quenching:	Water quench	
		690 °C	8 hr, air cooled
		620 °C	24 hr, air cooled

4.2.5 Index Temperature RT_{NDT} – Uncertainty Classification and Quantification

Values of RT_{NDT} are uncertain both due to epistemic and aleatory causes. The *epistemic* uncertainty is due to the conservative bias implicit in the ASME NB-2331 [111] definition of RT_{NDT}, the variety of inconsistent transition temperature metrics used to define RT_{NDT}, the lack of prescription in the test methods used to define RT_{NDT}, and the fact that the *CVN* and *NDT* values used to define RT_{NDT} do not themselves measure fracture toughness. *Aleatory* uncertainties are due to material variability. It is expected that epistemic uncertainty sources outnumber aleatory ones [108]; however, this expectation alone is inadequate to classify the uncertainty in RT_{NDT} as being primarily aleatory or primarily epistemic. To make this distinction, a comparison of the RT_{NDT} index temperature to an exemplar index temperature (such as the *Master Curve* index T_0 [124]) associated with a physically motivated model of crack initiation toughness is needed.

The Master Curve index temperature T_0 is estimated directly from fracture-toughness data, and, by definition, it is therefore associated with the same location on the transition temperature curve of every steel, suggesting that the sources of epistemic uncertainty that are associated with RT_{NDT} do not influence T_0. Thus, the uncertainty in T_0 is expected to be primarily aleatory, and a comparison between T_0 and RT_{NDT} values can be used to quantify the epistemic uncertainty in RT_{NDT}. The numerical difference between RT_{NDT} and T_0 has been used to quantify how far away from measured fracture-toughness data RT_{NDT} positions a model of fracture toughness for a given heat of steel [108]. Figure 34 shows a cumulative distribution function (CDF) constructed from the difference between values of RT_{NDT} and T_0 reported in the literature [125] for the RPV steels in the ORNL 99/27 database. See Appendix E for a description of the statistical procedures applied in the construction of this CDF. These data (see Table 10) demonstrate that the epistemic uncertainty in RT_{NDT} almost always produces a high estimate of the actual fracture-toughness transition temperature.

Even though it quantifies the epistemic uncertainty in RT_{NDT}, the CDF illustrated in Fig. 34 cannot be used directly in FAVOR because of inconsistencies between T_0 and the requirements of the PTS re-evaluation project. Consequently, an alternative CDF (see Fig. 35) was developed that avoids the explicit treatment of size effects and the use of elastic-plastic fracture mechanics (EPFM) toughness data, but retains the important concept from the Master Curve that the index temperature should be quantitatively linked to the measured toughness data. This alternative CDF was determined based on the temperature shift values ($\Delta RT_{epistemic}$ in Table 11) needed to make a NB-2331 RT_{NDT}-positioned K_{Ic} curve lower-bound the ASTM E-399 valid K_{Ic} data for each of the 18 heats of RPV steel in the ORNL 99/27 database. See Fig. 36 for an example of this lower-bounding shift procedure for HSST Plate 02.

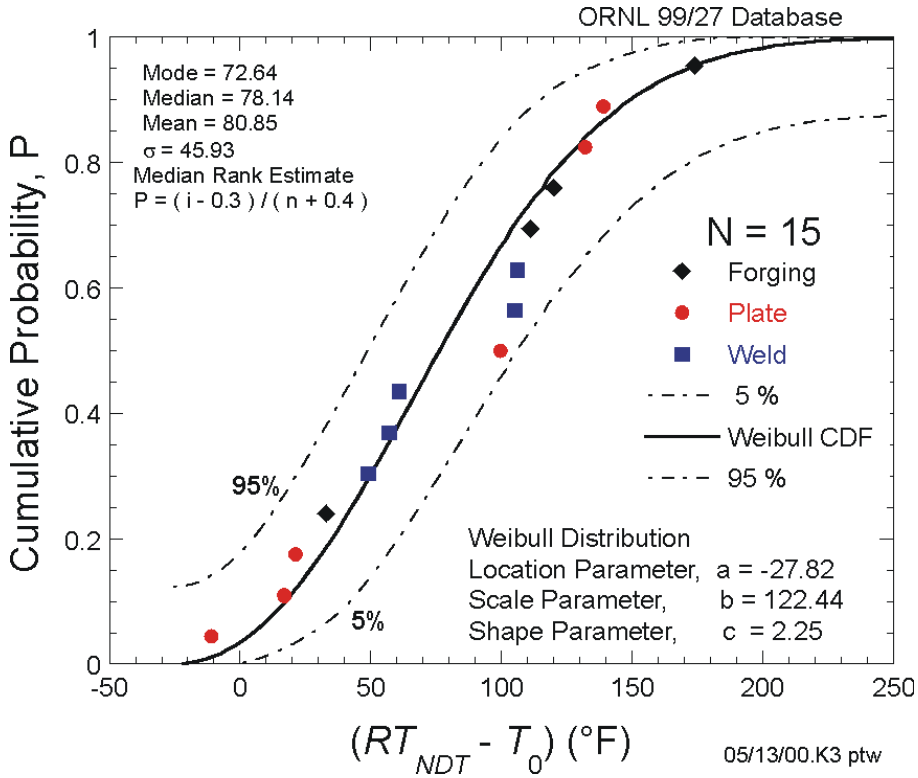

Fig. 34. Cumulative distribution function of the observed difference in RT_{NDT0} and T_o (with a size of 1T) using data in the ORNL 99/27 database.

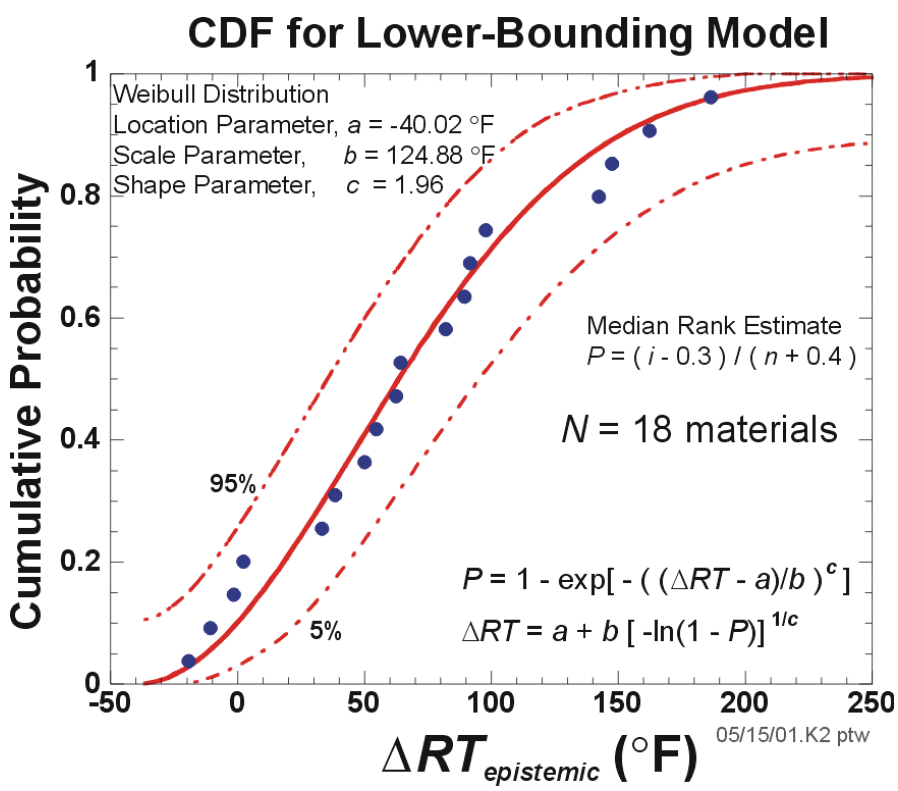

Fig. 35. Cumulative distribution function of the difference (designated as $\Delta RT_{epistemic}$) between RT_{NDT0} and a new lower-bounding reference index designated RT_{LB}.

Table 10. Materials Used from the ORNL 99/27 K_{Ic} Extended Database

ID	Form	RT_{NDT} (°F)	T_0 (°F)*	RT_{NDT} - T_0	P	T_q (°F)**
HSST-03	Plate	20	31	-11	0.0455	26.1
HSST-02	Plate	0	-17	17	0.1104	-17.4
HSST-01	Plate	20	-1	21	0.1753	-2.9
A508 Cl. 3	Forging	-13	-46	33	0.2403	
73W	Weld	-29.2	-78	48.8	0.3052	
A533B Cl. 1	Weld	0	-57	57	0.3701	-56.7
72W	Weld	-9.4	-70	60.6	0.4351	
A533B Cl. 1	Plate	-9.4	-109	99.6	0.5000	
HSST-01	Weld	0	-105	105	0.5649	-104.4
A533B Cl. 1	Weld	-45	-151	106	0.6299	-151.5
A508 Cl. 2	Forging	51	-60	111	0.6948	-59.9
A508 Cl. 2	Forging	65	-55	120	0.7597	-5.8
A533B Cl. 1	HAZ	0	-132	132	0.8247	-132.3
A533B Cl. 1	Plate	65	-74	139	0.8896	-73.8
A508 Cl. 2	Forging	50	-124	174	0.9545	-119.3

*T_0 values reported in [125]. Calculated using ASTM E-1921 valid data.
**Provisional T_q values calculated using ASTM E-399 valid K_{Ic} data in [74].

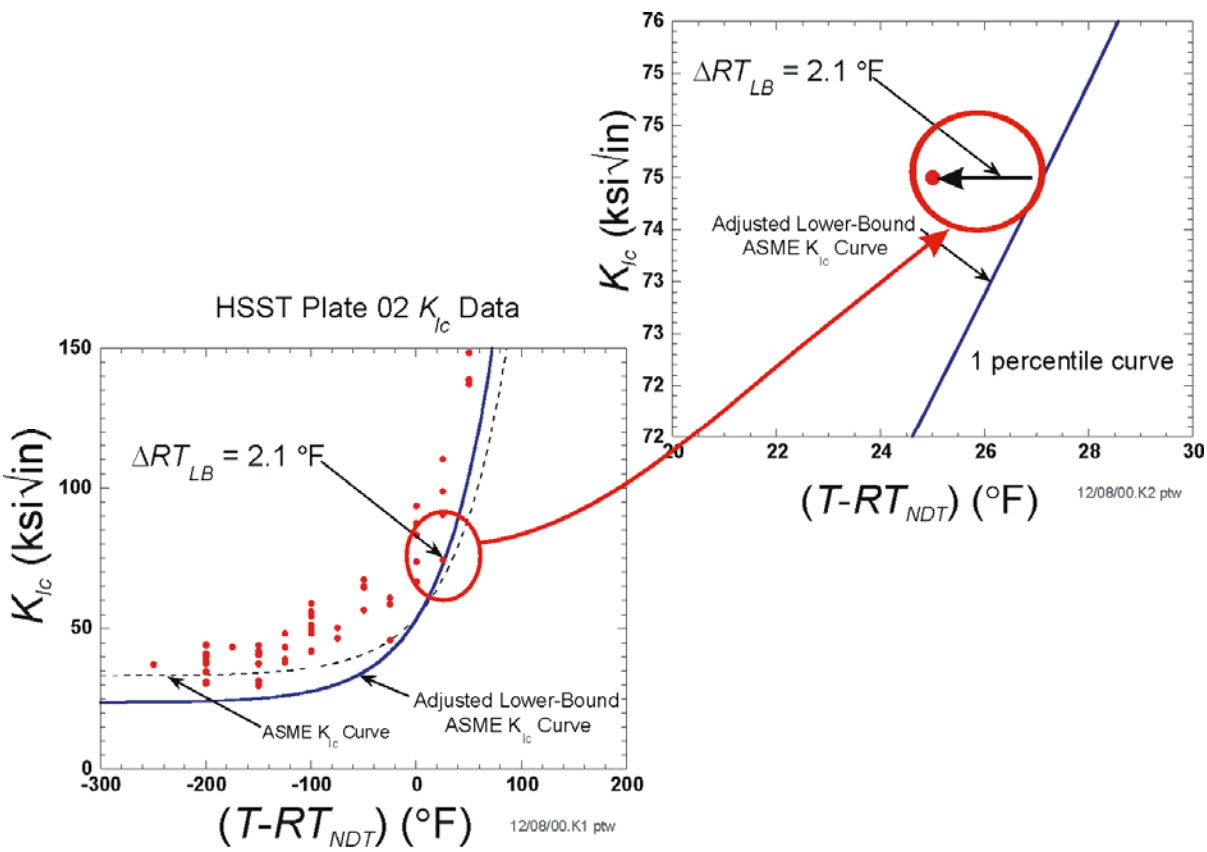

Fig. 36. The ΔRT_{LB} for HSST Plate 02. The lower-bounding transition reference temperature, RT_{LB}, was developed from 18 materials in the ORNL 99/27 database, where for each material $RT_{LB} = RT_{NDT0} - \Delta RT_{LB}$.

Table 11. Values of Lower-Bounding Reference Temperature with and without Sample-Size Adjustment: ORNL 99/27 Database

Material ID No. k	Sample Size, N	RT_{NDT0} (°F)	$RT_{LB}{}^{(k)*}$ (°F)	$\Delta RT_{LB}{}^{(k)*}$ (°F)	Size Correct. (°F)	$RT_{LB}{}^{(k)**}$ (°F)	$\Delta RT_{epistemic}{}^{(k)**}$ (°F)
1	8	0.0	-75.2	75.2	10.9	-64.3	64.3
2	8	0.0	0.0	0	10.9	10.9	-10.9
3	17	20.0	-82.4	102.4	4.6	-77.8	97.8
4	9	20.0	-81.1	101.1	9.6	-71.5	91.5
5	13	65.0	-127.6	192.6	6.4	-121.2	186.2
6	69	0.0	-2.1	2.1	0	-2.1	2.1
7	10	-45.0	-195.7	150.7	8.5	-187.2	142.2
8	6	0.0	-176.9	176.9	14.5	-162.4	162.4
9	12	50.0	-104.5	154.5	6.9	-97.6	147.6
10	9	51.0	-8.7	59.7	9.6	0.9	50.1
11	10	65.0	1.9	63.1	8.5	10.4	54.6
12	13	-9.4	3.6	-13.0	6.4	10.0	-19.4
13	10	-29.2	-76.1	46.9	8.5	-67.6	38.4
14	43	-9.4	-43.5	34.1	0.9	-42.6	33.2
15	6	-13.0	-25.8	12.8	14.5	-11.3	-1.7
16	6	52.0	-51.9	103.9	14.5	-37.4	89.4
17	2	23.0	-99.7	122.7	40.8	-58.9	81.9
18	4	0.0	-83.8	83.8	21.5	-62.3	62.3

$RT_{LB}^{(k)*}$ = lower-bounding reference temperature for the kth material without sample size-adjustment

$\Delta RT_{LB}^{(k)*} = RT_{NDT(0)}^{(k)} - RT_{LB}^{(k)*}$

$RT_{LB}^{(k)**}$ = lower-bounding reference temperature for the kth material with sample size-adjustment

$\Delta RT_{epistemic}^{(k)**} = RT_{NDT0}^{(k)} - RT_{LB}^{(k)**}$

The adjusted ASME lower-bounding curve shown in Fig. 36 has the following form:

$$K_{Ic} = 23.65 + 29.56 \exp\left[0.02(T - RT_{NDT})\right] \text{ ksi}\sqrt{\text{in.}} \tag{88}$$

with $(T - RT_{NDT})$ in °F. The adjustment for sample size indicated in Table 11 assumes that Eq. (88) represents a 0.01 fractile. The $RT_{NDT0} - T_0$ CDF (Figs. 34 and 37) is a Weibull distribution with a flaw-size dependence

$$\begin{aligned}
&(RT_{NDT0} - T_0) \leftarrow W(a_{xT}, 122.4, 2.25) \\
&a_{xT} = a_{1T} - \frac{1.8}{0.019} \ln\left[\frac{80\left(B_{xT}/B_{1T}\right)^{1/4} - 10}{70}\right] \text{ [°F]} \\
&a_{1T} = -27.82 \text{ °F} \\
&B_{xT} = \text{ flaw length [in.]} \\
&B_{1T} = \text{ 1.0 in.}
\end{aligned} \tag{89}$$

The lower-bounding CDF, Eq. (90), quantifies the epistemic uncertainty in RT_{NDT} in a manner fully consistent with the constraints placed on the toughness models used in the PTS re-evaluation effort. In Fig. 37, we also compare this quantification of epistemic uncertainty with that based on the Master Curve. This comparison illustrates that the implicit treatment of size effects adopted when developing the alternative CDF using ASTM E 399 valid data produces a result quite similar in form to that based on the Master Curve. The similarity of the alternative CDF to the Master Curve-based CDF provides a link between the RT_{LB} concept developed to conform to the requirements of the PTS re-evaluation and the physical and empirical underpinnings of the Master Curve, thereby demonstrating that aleatory and epistemic uncertainties can be reasonably distinguished using RT_{LB} and ΔRT_{LB}. The epistemic uncertainty in the unirradiated value of RT_{NDT0} is estimated by sampling from the following Weibull distribution (see Appendix F for details on the development of Eq. (90)):

$$\begin{aligned} &\Delta RT_{epistemic} \leftarrow W(-45.586, 131.27, 2.177) \\ &\Delta RT_{epistemic} = -45.586 + 131.27\left[-\ln\left(1-\Phi\right)\right]^{1/2.177} \quad [°\mathrm{F}] \\ &\text{where } \Phi \leftarrow \mathrm{U}(0,1) \end{aligned} \tag{90}$$

Combined with the sampled irradiation-shift term described in Sect. 4.2.2, the irradiated value of RT_{NDT} is calculated by

$$RT_{NDT}(r,\ldots) = RT_{NDT0} - \Delta RT_{epistemic} + \Delta RT_{NDT}(r,\ldots) \tag{91}$$

where $RT_{NDT0} \leftarrow N(\overline{RT}_{NDT0}, \sigma_{RT_{NDT0}})$ and RT_{NDT} is a function of the position of the crack tip due to the attenuation of the fast-neutron fluence at position r in the vessel wall.

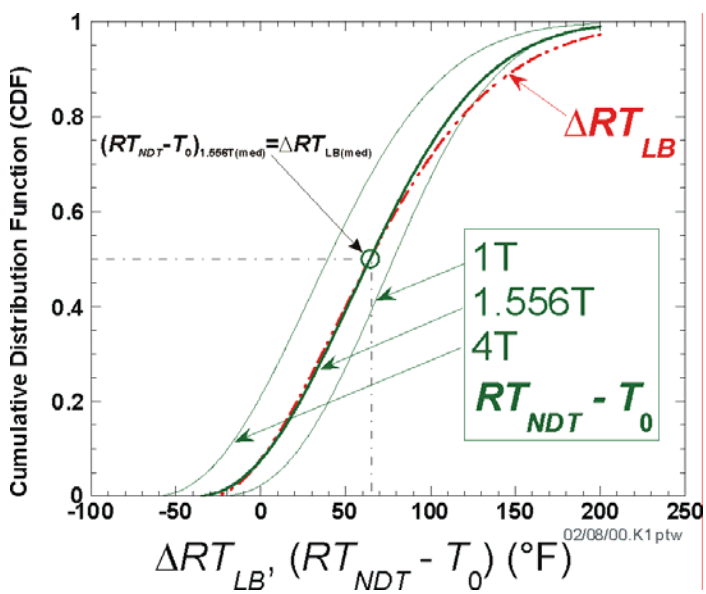

Fig. 37. Comparison of cumulative distribution functions developed for RT_{NDT0}-T_0 and RT_{NDT0}-RT_{LB} .

4.2.6 Index Temperature RT_{Arrest} – Uncertainty Classification and Quantification

To enable all commercial operators of pressurized water reactors to assess the state of their RPV relative to new PTS screening criteria without the need to make new material property measurements, the arrest fracture toughness of the RPV needs to be estimated using only currently available unirradiated RT_{NDT0} values. These restrictions suggest that very limited information, specifically a value of RT_{NDT0}, is available to define the arrest fracture-toughness model appropriate to a particular steel in a particular RPV. Consequently, the temperature dependency and uncertainty of the arrest fracture-toughness model will either have to be demonstrated or assumed to be invariant over a wide range of conditions because sufficient information is not available to establish these features on a heat-specific basis [108].

The information presented in [108] suggests that a relevant arrest reference temperature can be defined based on (a) an index temperature that defines the position of the plane-strain crack arrest toughness, K_{Ia} , transition curve on the temperature axis and (b) a relationship between the index temperatures for the initiation and arrest fracture-toughness curves (assuming such a relationship exists). For this study, the temperature dependency of K_{Ia} data was assumed to be universal to all reactor pressure vessel steels, or, more specifically, within this class of materials the temperature dependency was assumed to be insensitive to all individual and combined effects of alloying, heat treatment (and other thermal processing), mechanical processing, and irradiation. These material variables only influence the temperature range over which a particular steel experiences a transition from brittle behavior (at low temperatures) to ductile behavior (at higher temperatures), this being quantified by a heat-specific index temperature value. Furthermore, the information presented in [108] suggests that the relationship between the index temperatures for crack initiation and crack arrest toughness is also not expected to be influenced strongly by heat-specific factors.

From [108]:

> **Crack arrest occurs when dislocations can move faster than the crack propagates, resulting in crack tip blunting and arrest. Dislocation mobility therefore controls the ability of a ferritic steel to arrest a running cleavage crack, and thus its crack arrest toughness. The atomic lattice structure is the only feature of the material that controls the temperature dependence of the material properties that are controlled by dislocation motion. Consequently, as was the case for crack initiation toughness, the temperature dependency of crack arrest toughness depends only on the short-range barriers to dislocation motion established by the BCC lattice structure. Other features that vary with steel composition, heat treatment, and irradiation include grain size/boundaries, point defects, inclusions, precipitates, and dislocation substructures. These features all influence dislocation motion, and thereby both strength and toughness, but their large inter-barrier spacing relative to the atomic scale associated with the lattice structure makes these effects completely athermal.**

This understanding suggests that the myriad of metallurgical factors that can influence absolute strength and toughness values, and thereby the transition temperature, exert no control over the temperature dependency of arrest toughness in fracture mode transition. Additionally, since K_{Ic} and K_{Ia} both depend on the ability of the material to absorb energy via dislocation motion, K_{Ic} and K_{Ia} are both expected to exhibit a similar temperature dependence.

As described in [108], a strong physical basis supports a temperature dependency in arrest fracture-toughness data that is universal to all ferritic steels; this temperature dependence has a similar functional form to that of crack-initiation toughness. Mathematically, Wallin and co-workers proposed [126,127]:

$$K_{Ia(mean)} = 30 + 70\exp\left[0.019\left(T - T_{KIa}\right)\right] \ \ [\mathrm{MPa}\sqrt{\mathrm{m}}] \tag{92}$$

where $(T - T_{KIa})$ is in $^{\circ}\mathrm{C}$. Equation (92) describes the temperature (T) dependency of the mean arrest toughness ($K_{Ia(mean)}$). In this equation, temperature is normalized to the index temperature T_{KIa}, where T_{KIa} is defined as the temperature at which the mean arrest toughness is $100\ \mathrm{MPa}\sqrt{\mathrm{m}}$ ($91\ \mathrm{ksi}\sqrt{\mathrm{in.}}$). Wallin found that a lognormal distribution having a lognormal standard deviation of 0.18 fits the extensive database used in his study.

The physical understanding of the relationship between crack initiation and crack arrest presented in [108] suggests that the temperature separation between the K_{Ic} and K_{Ia} transition curves should progressively diminish as the material is hardened (e.g. by cold work, irradiation, etc.). Available empirical evidence supports this expectation, as illustrated in Fig. 38. An exponentially decaying functional form for the mean was selected to represent these data, because this relationship had the mathematical form anticipated from physical considerations (i.e. the separation between the K_{Ic} and K_{Ia} curves diminishes as T_o increases). This nonlinear regression fit was:

$$\Delta RT_{ARREST(mean)} \equiv T_{K_{Ia}} - T_o = 44.123 \cdot \exp\left\{-0.006T_0\right\} \ \ [^{\circ}\mathrm{C}] \tag{93}$$

where ΔRT_{ARREST} is distributed lognormally about the mean given by Eq. (93), with an estimated log-normal standard deviation of 0.39 (see Fig. 39). Table 12 presents several reference-transition temperature indices for the steels in the ORNL 99/27 K_{Ia} database including $\overline{RT}_{Arrest}$ calculated from Eq. (93).

Table 12. ORNL 99/27 K_{Ia} Database – Reference-Transition Temperatures

Material ID	Product Form	Sample Size	RT_{NDT0} (°F)	RT_{LB} (°F)	T_0 (°F)	RT_{Arrest} (°F)	T_{KIa} (°F)
HSST-02	Plate	50	0	-2.1	-17	76.8	75.2
72W	Weld	32	-9.4	-42.6	-70	49.8	8.6
73W	Weld	26	-29.2	-67.6	-78	34.1	6.8
Midland	Weld	4	32.2	-58.9	NA	NA	NA

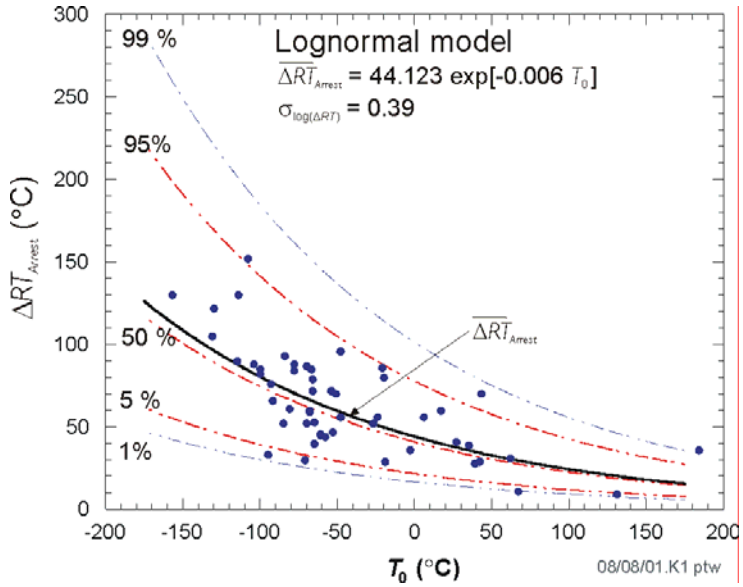

Fig. 38. Lognormal distribution of $\Delta RT_{ARREST} = T_{K_{Ia}} - T_0$ as a function of T_0

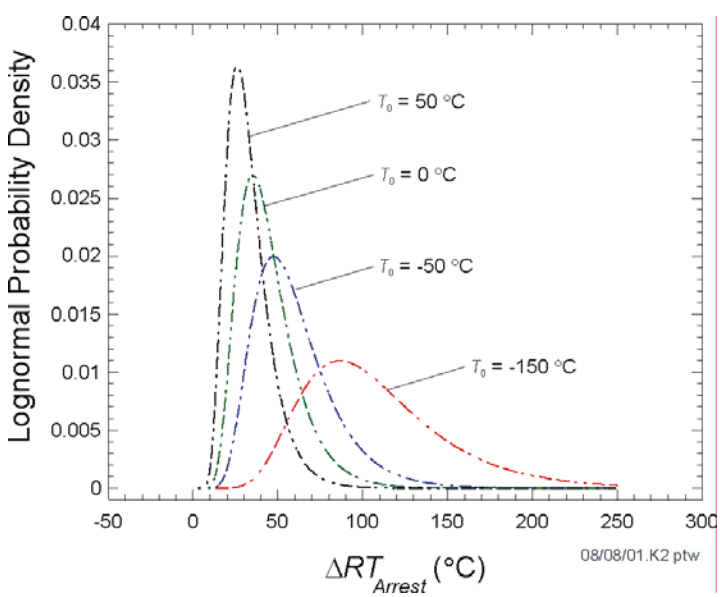

Fig. 39. Lognormal probability densities for ΔRT_{Arrest} as function of T_0.

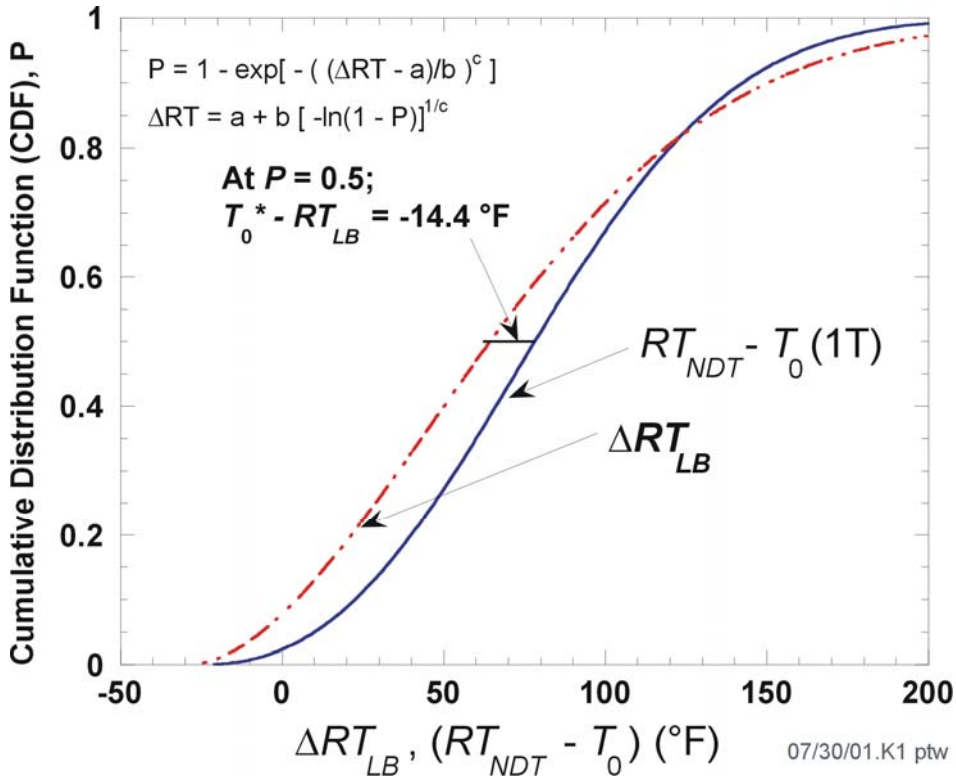

Fig. 40. Proposed adjustment to RT_{LB} arises from observed offset between ΔRT_{LB} CDF and $RT_{NDT} - T_0$ CDF at median (P = 0.5).

An approximate connection between T_0 and the initiation reference temperature RT_{LB} can be established from the observed offset of 14.4 °F between the medians of the RT_{NDT0}-T_0 CDF and the ΔRT_{LB} CDF in Fig. 40. This observation allows us to apply Eq. (93) to develop a distribution for the epistemic uncertainty in the arrest reference temperature linked to the epistemic uncertainty in the initiation reference temperature.

$$\Delta RT_{epist-arrest} = \Delta RT_{epistemic} - 14.4 \quad [°F] \tag{94}$$

where $\Delta RT_{epistemic}$ has been sampled from the distribution given by Eq. (90). The sampled arrest reference temperature can now be calculated by

$$RT_{ARREST}(r,\ldots) = RT_{NDT0} - \Delta RT_{epist-arrest} + \Delta RT_{ARREST} + \Delta RT_{NDT}(r,\ldots) \tag{95}$$

where RT_{NDT0}, $\Delta RT_{epist-arrest}$, and $\Delta RT_{NDT}(r,\cdots)$ have not been re-sampled from their initiation values and $\Delta RT_{ARREST} \leftarrow \Lambda(\mu_{\ln(\Delta RT_{ARREST})}, \sigma_{\ln(\Delta RT_{ARREST})})$ is sampled from the following lognormal distribution:

$$\mu_{\ln(\Delta RT_{ARREST})} = \ln\left[\Delta RT_{ARREST(mean)}\right] - \frac{\sigma^2_{\ln(\Delta RT_{ARREST})}}{2}$$

where

$$T_0 = \left(RT_{NDT_0} - \Delta RT_{epist-arrest} - 32\right)/1.8 \quad [°\mathrm{C}]$$

$$\Delta RT_{ARREST(mean)} = 44.122\exp\left[-0.005971 \times T_0\right] \quad [°\mathrm{C}] \tag{96}$$

$$\sigma_{\ln(\Delta RT_{ARREST})} = \sqrt{\ln\left\{\exp\left[0.38998^2 + 2\ln(\Delta RT_{ARREST(mean)})\right] - \mathrm{var}\left(T_0\right)\right\} - 2\ln\left[\Delta RT_{ARREST(mean)}\right]}$$

where

$$\mathrm{var}(T_0) = \begin{cases} (12.778)^2 & \text{for } T_0 < -35.7\ °\mathrm{C} \\ 99.905972 - 1.7748073 T_0 & \text{for } -35.7\ °\mathrm{C} \le T_0 \le 56\ °\mathrm{C} \\ 0 & \text{for } T_0 > 56\ °\mathrm{C} \end{cases}$$

and ΔRT_{ARREST} is sampled from (see Step 11 in Sect. 4.5)

$$\Delta RT_{ARREST} = 1.8\exp\left[\sigma_{\ln(\Delta RT_{Arrest})} Z_{P_f} + \mu_{\ln(\Delta RT_{Arrest})}\right] \quad [°\mathrm{F}]$$

$Z_{P_f} \leftarrow N(0,1)$; Z_{P_f} is the standard normal deviate corresponding to the P_f fractile $(0 < P_f < 1)$ for this trial in the crack *Initiation - Growth - Arrest* model.

See Appendix F for the details of the development of Eq. (96).

4.2.7 Plane-Strain Static Cleavage Initiation Toughness – K_{Ic}

Using the K_{Ic} data in the ORNL 99/27 fracture-toughness database (see Fig. 41) and the new lower-bounding reference temperature, RT_{LB}, a statistical model based on a Weibull distribution was developed by applying the statistical procedures given in [74]. The cumulative distribution function (CDF) for the Weibull model has the following form:

$$\Pr(K_{Ic} < K_I) = \Phi_{K_{Ic}}(K_I \mid a_{K_{Ic}}, b_{K_{Ic}}) = \begin{cases} 0; & K_I \le a_{K_{Ic}} \\ 1 - \exp\left[-\left(\dfrac{K_I - a_{K_{Ic}}(\Delta T_{RELATIVE})}{b_{K_{Ic}}(\Delta T_{RELATIVE})}\right)^{c_{K_{Ic}}}\right]; & a_{K_{Ic}} < K_I < \infty \end{cases} \tag{97}$$

where the inverse CDF or percentile function is given by

$$K_{Ic}(\Delta T) = a_{K_{Ic}}(\Delta T) + b_{K_{Ic}}(\Delta T)\left[-\ln(1 - \Phi_{K_{Ic}})\right]^{1/c_{K_{Ic}}} \quad \text{for } 0 < \Phi_{K_{Ic}} < 1$$
$$\text{for } a \le K_{Ic} \le K_{Ic(\max)} \tag{98}$$

where the bounding value of $K_{Ic(\max)}$ is input by the user to FAVOR (typically $K_{Ic(\max)} = 200\ \mathrm{ksi}\sqrt{\mathrm{in.}}$). The parameters of the distribution are

$$
\begin{aligned}
a_{K_{Ic}}(\Delta T_{RELATIVE}) &= 19.35 + 8.335\exp\left[0.02254(\Delta T_{RELATIVE})\right] \ [\text{ksi}\sqrt{\text{in.}}] \\
b_{K_{Ic}}(\Delta T_{RELATIVE}) &= 15.61 + 50.132\exp\left[0.008(\Delta T_{RELATIVE})\right] \ [\text{ksi}\sqrt{\text{in.}}] \\
c_{K_{Ic}} &= 4
\end{aligned}
\tag{99}
$$

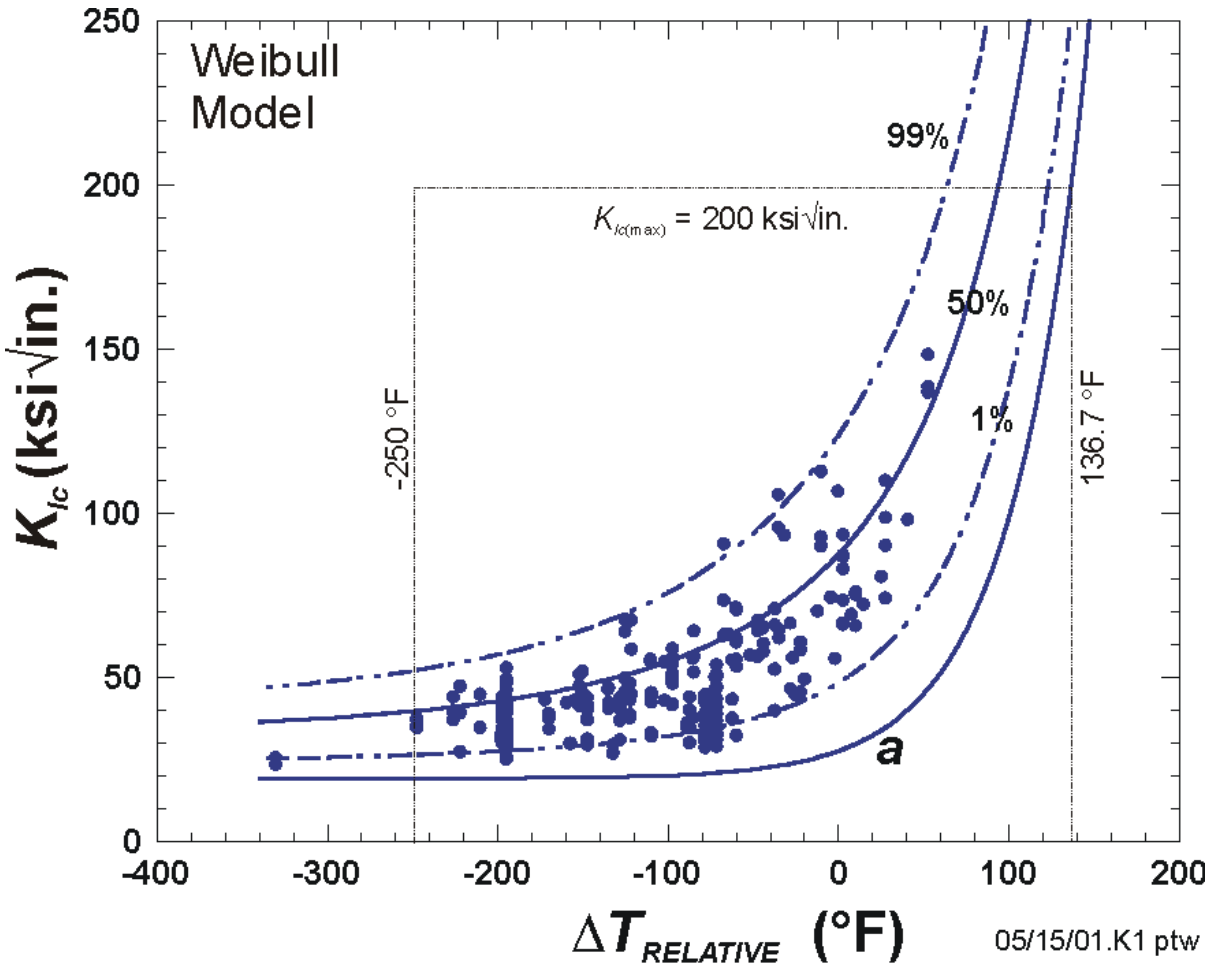

Fig. 41. Weibull statistical distribution for plane-strain cleavage initiation fracture toughness, K_{Ic}, with prescribed validity bounds. The ORNL 99/27 K_{Ic} database was used in the construction of the model.

with K_{Ic} in ksi√in and $\Delta T_{RELATIVE} = T(\tau) - RT_{NDT}(r,\cdots)$ in °F. Note that this Weibull statistical model describes the *aleatory* uncertainty in the plane-strain static initiation fracture toughness, since it is assumed that the *epistemic* uncertainty has been reduced by the sampled $\Delta RT_{epistemic}$ in Eq. (90).

4.2.8 Plane-Strain Crack Arrest Toughness – K_{Ia}

Two lognormal distributions (see Fig. 42) are available in FAVOR to describe the aleatory uncertainty in the plane-strain crack arrest toughness, K_{Ia}. For a lognormal distribution with random variate, x, the cumulative distribution function is expressed by

$$\begin{aligned} \Pr\{X \le x\} &= \frac{1}{\sigma x\sqrt{2\pi}} \int_{-\infty}^{\ln(x)} \exp\left[-\left(\frac{(\xi-\mu)^2}{2\sigma^2}\right)\right] \mathrm{d}\xi = \\ \Phi\left(\frac{\ln(x)-\mu}{\sigma}\right) &= \frac{1}{\sqrt{2\pi}} \int_{-\infty}^{(\ln(x)-\mu)/\sigma} \exp\left[-\frac{\varsigma^2}{2}\right] \mathrm{d}\varsigma \end{aligned} \tag{100}$$

The function Φ can be evaluated numerically through its relation to the *error function*, erf(x), such that for a given applied stress intensity factor, K_I, and normalized temperature, $\Delta T = T\text{-}RT_{Arrest}$,

$$\Pr\left\{K_{Ia} \le K_I\right\} = \Phi_{K_{Ia}}\left(\frac{\ln(K_I) - \mu_{\ln(K_{Ia})}(\Delta T)}{\sigma_{\ln(K_{Ia})}}\right) = \frac{1}{2}\left[\operatorname{erf}\left(\frac{\ln(K_I) - \mu_{\ln(K_{Ia})}(\Delta T)}{\sigma_{\ln(K_{Ia})}\sqrt{2}}\right) + 1\right] \tag{101}$$

where $\Phi_{K_{Ia}}$ is now the cumulative probability of crack extension and the error function (a special case of the incomplete gamma function, $P(a,x^2)$) is defined by

$$\begin{aligned} P\left(0.5, x^2\right) &= \operatorname{erf}(x) = \frac{2}{\sqrt{\pi}} \int_0^x \exp(-\xi^2)\, \mathrm{d}\xi \\ \operatorname{erf}(-x) &= -\operatorname{erf}(x) \end{aligned} \tag{102}$$

The inverse CDF for the lognormal distribution allows sampling of K_{Ia} by

$$\begin{aligned} K_{Ia}(\Phi_{K_{Ia}}, \Delta T_{RELATIVE}) &= \exp\left[\sigma_{\ln(K_{Ia})} \widehat{Z}_{\Phi K_{Ia}} + \mu_{\ln(K_{Ia})}(\Delta T_{RELATIVE})\right] \\ \widehat{Z}_{\Phi_{K_{Ia}}} &= \text{standard normal deviate} \\ &\quad \text{corresponding to the } \Phi_{K_{Ia}} \text{ fractile} \\ \Phi_{K_{Ia}} &\leftarrow U(0,1) \end{aligned} \tag{103}$$

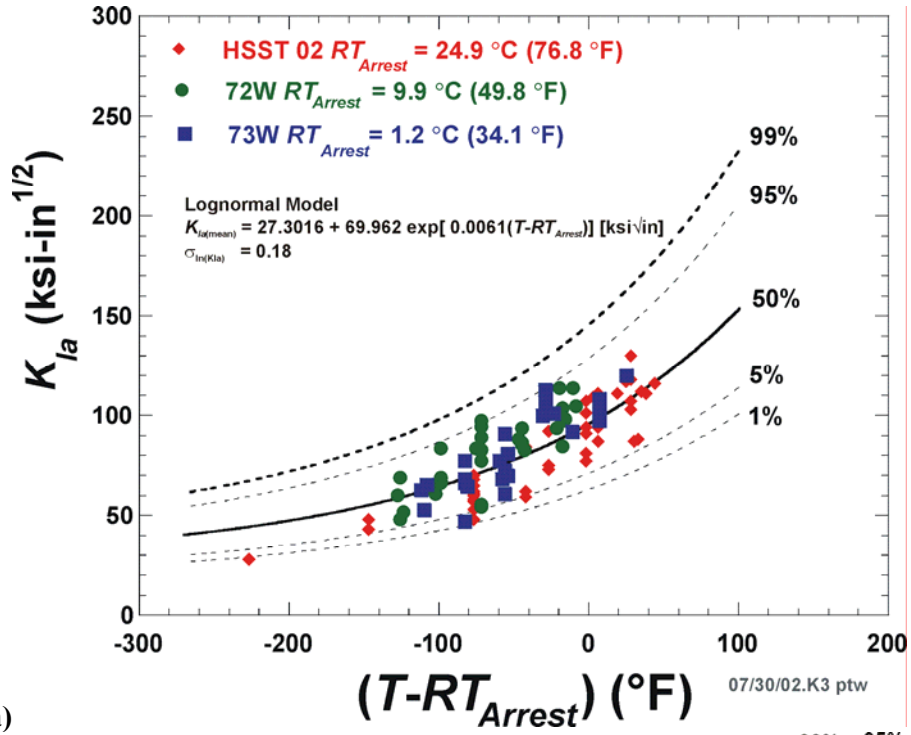

(a)

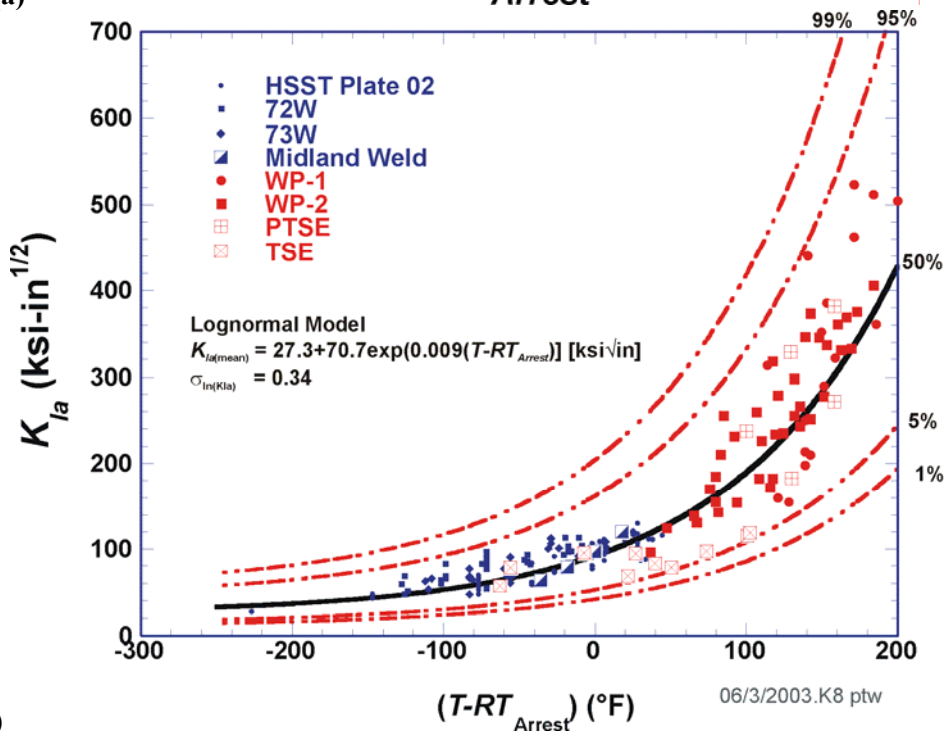

(b)

Fig. 42. Lognormal statistical distribution for plane-strain crack arrest fracture toughness, K_{Ia}, constructed using the (a) Model 1: ORNL 99/27 K_{Ia} database normalized by the arrest reference temperature, RT_{Arrest} and (b) Model 2: Extended K_{Ia} database normalized by the arrest reference temperature, RT_{Arrest}.

Model 1 is based on the ORNL 99/27 K_{Ia} database of 112 data points which were taken using CCA specimens. The parameters of the Model 1 K_{Ia} lognormal distribution, shown in Fig. 42a, are

$$\mu_{\ln(K_{Ia})}(\Delta T_{RELATIVE}) = \ln\left[\bar{K}_{Ia}(\Delta T_{RELATIVE})\right] - \frac{\sigma^2_{\ln(K_{Ia})}}{2}$$

where

$$\sigma_{\ln(K_{Ia})} = 0.18 \tag{104}$$

$$K_{Ia(\text{mean})}(\Delta T_{RELATIVE}) = 27.302 + 69.962\exp\left[0.006057(\Delta T_{RELATIVE})\right] \quad [\text{ksi}\sqrt{\text{in.}}]$$

$$\Delta T_{RELATIVE} = T(r,\tau) - RT_{Arrest}(r,\cdots) \quad [°\text{F}]$$

The equation for the mean was developed by nonlinear regression of the data shown in Fig. 42a. Model 1 is recommended to be used when the ductile-tearing model is not activated, and an upper bound for K_{Ia} of 200 $\text{ksi}\sqrt{\text{in.}}$ should be set in the FAVPFM input file.

Model 2 is based on the Extended K_{Ia} database of 183 data points which were taken using both CCA specimens and Large-Specimen experiments. The parameters of the Model 2 K_{Ia} lognormal distribution, shown in Fig. 42b, are

$$\mu_{\ln(K_{Ia})}(\Delta T_{RELATIVE}) = \ln\left[\bar{K}_{Ia}(\Delta T_{RELATIVE})\right] - \frac{\sigma^2_{\ln(K_{Ia})}}{2}$$

where

$$\sigma_{\ln(K_{Ia})} = 0.34 \tag{105}$$

$$K_{Ia(\text{mean})}(\Delta T_{RELATIVE}) = 27.302 + 70.6998\exp\left[0.008991(\Delta T_{RELATIVE})\right] \quad [\text{ksi}\sqrt{\text{in.}}]$$

$$\Delta T_{RELATIVE} = T(r,\tau) - RT_{Arrest}(r,\cdots) \quad [°\text{F}]$$

Model 2 will be automatically selected when the ductile-tearing model is activated, and any specified upper bound on K_{Ia} is ignored.

4.2.9 Material Chemistry –Sampling Protocols

The sampling protocol used by FAVOR, v04.1, requires estimated chemistry (Cu, Ni, and P) content values for each weld and plate subregion used to model the beltline shells of the vessel. The user will, therefore, input best-heat estimates designated as HE_{Cu}, HE_{Ni}, and HE_P in wt%.

FAVOR treats the vessel beltline as a collection of major regions of plates, forgings, and welds. These major regions are then discretized into subregions, where within a given subregion flaws are analyzed through Monte Carlo *realizations* of the RPV subjected to the PTS transients under study. The sampling protocols for plate and weld chemistry distinguish between the first flaw simulated in a subregion, designated as *Flaw*1, and all subsequent flaws in the subregion, designated as *Flawx*. The plate or weld chemistry for the set of *Flawx's* will be perturbations of the sampled *Flaw*1 chemistry for this subregion. This variation in chemistry is intended to simulate *local variability* in the subregion chemistry.

<u>Plate Subregion Chemistry</u>

Flaw1

The Cu, Ni, and P content (expressed in wt%) for the first flaw in a subregion are sampled from the following normal distributions:

$$\begin{aligned} \widehat{Cu}_{Flaw1} &\leftarrow N(HE_{Cu}, \sigma_{Cu}) \\ \widehat{Ni}_{Flaw1} &\leftarrow N(HE_{Ni}, \sigma_{Ni}) \\ \widehat{P}_{Flaw1} &\leftarrow N(HE_P, \sigma_P) \end{aligned} \tag{106}$$

where the recommended constant standard deviations are

$$\begin{aligned} \sigma_{Cu} &= 0.0073 \text{ wt\%} \\ \sigma_{Ni} &= 0.0244 \text{ wt\%} \\ \sigma_P &= 0.0013 \text{ wt\%} \end{aligned} \tag{107}$$

The triplet $(\sigma_{Cu}, \sigma_{Ni}, \sigma_P)$ is supplied by the user in the input file for the FAVPFM module. Negative values of sampled $\widehat{Cu}_{Flaw1}$, $\widehat{Ni}_{Flaw1}$, and $\widehat{P}_{Flaw1}$ are handled as nonphysical exceptions in FAVOR using the truncation protocol described in Sect. 3.3.6, with 0.0 applied as a one-sided truncation boundary.

Flawx – local variability

All subsequent flaws in a given subregion should contain small local variability in Cu, Ni, and P content. This local variability is determined by sampling values from the following logistic distributions:

$$\begin{aligned} Cu_{Flawx} &\leftarrow Cu_{Flaw1} + L(-3.89\times10^{-7}, 0.00191) \\ Ni_{Flawx} &\leftarrow Ni_{Flaw1} + L(-1.39\times10^{-7}, 0.00678) \\ P_{Flawx} &\leftarrow P_{Flaw1} + L(1.30\times10^{-5}, 0.000286) \end{aligned} \tag{108}$$

$$\begin{aligned} \Delta_{Cu-Flawx} &= -3.89\times10^{-7} - 0.00191\ln\left[\frac{1}{\Phi_{Cu}} - 1\right] \text{ for } \Phi_{Cu} \leftarrow U(0,1) \\ Cu_{Flawx} &= Cu_{Flaw1} + \Delta_{Cu-Flawx} \\ \Delta_{Ni-Flawx} &= -1.39\times10^{-7} - 0.00678\ln\left[\frac{1}{\Phi_{Ni}} - 1\right] \text{ for } \Phi_{Ni} \leftarrow U(0,1) \\ Ni_{Flawx} &= Ni_{Flaw1} + \Delta_{Ni-Flawx} \\ \Delta_{P-Flawx} &= 1.3\times10^{-5} - 0.000286\ln\left[\frac{1}{\Phi_{P}} - 1\right] \text{ for } \Phi_{P} \leftarrow U(0,1) \\ P_{Flawx} &= P_{Flaw1} + \Delta_{P-Flawx} \end{aligned} \tag{109}$$

Negative values of sampled Cu_{Flawx}, Ni_{Flawx}, and P_{Flawx} are handled as nonphysical exceptions in FAVOR using the truncation protocol described in Sect. 3.3.6, with 0.0 applied as a one-sided truncation boundary.

Through-thickness sampling for Plates

There is no resampling protocol for flaws growing through the thickness of plate subregions.

Weld Subregion Chemistry

Flaw1

Copper, Cu_{Flaw1}:

The Cu content for the first flaw in a weld subregion is sampled from a normal distribution with mean equal to the heat estimate for Cu and a sampled standard deviation:

$$\begin{aligned} Cu_{Flaw1} &\leftarrow N(HE_{Cu}, \sigma_{Cu}) \\ \sigma_{Cu} &\leftarrow N\left(0.167\times HE_{Cu},\ \min\left(0.0718\times HE_{Cu}, 0.0185\right)\right) \end{aligned} \tag{110}$$

Nickel, Ni_{Flaw1}:

<u>Ni-addition welds (heats 34B009 and W5214)</u>

The Ni content for the first flaw in a weld subregion is sampled from a normal distribution with mean equal to the heat estimate for Ni and standard deviation equal to 0.162.

$$\hat{Ni}_{Flaw1} \leftarrow N(HE_{Ni}, 0.162) \tag{111}$$

<u>All other heats</u>

The Ni content for the first flaw in a weld subregion is sampled from a normal distribution with mean equal to the heat estimate for Ni and standard deviation sampled from a normal distribution with mean equal to 0.029 wt% and standard deviation equal to 0.0165 wt%.

$$\begin{aligned} \hat{Ni}_{Flaw1} &\leftarrow N(HE_{Ni}, \hat{\sigma}_{Ni_{Flaw1}}) \\ \hat{\sigma}_{Ni_{Flaw1}} &\leftarrow N(0.029, 0.0165) \end{aligned} \tag{112}$$

Phosphorous, P_{Flaw1}:

The phosphorous content for the first flaw in a weld subregion is sampled from a normal distribution with mean equal to the heat estimate for phosphorous and standard deviation equal to 0.0013.

$$\hat{P}_{Flaw1} \leftarrow N(HE_P, 0.0013) \tag{113}$$

Negative values of sampled $\hat{Cu}_{Flaw1}, \hat{Ni}_{Flaw1}$, and $\hat{P}_{Flaw1}$ are handled as nonphysical exceptions in FAVOR using the truncation protocol described in Sect. 3.3.6, with 0.0 applied as a one-sided truncation boundary.

<u>Flawx – local variability</u>

All subsequent flaws in a given weld subregion should contain small local variability in Cu, Ni, and P content.

Copper, Cu_{Flawx}:

The local variability for Cu is determined by sampling a Δ_{Cu} value drawn from a logistic distribution with parameters $\alpha = 6.85 \times 10^{-8}$ and $\beta = 0.0072$ such that

$$\begin{aligned} \hat{\Delta}_{Cu-Flawx} &\leftarrow L(6.85 \times 10^{-8}, 0.0072) \\ \hat{\Delta}_{Cu-Flawx} &= 6.85 \times 10^{-8} - 0.0072 \ln\left[\frac{1}{\Phi_{Cu}} - 1\right] \text{ for } \Phi_{Cu} \leftarrow U(0,1) \\ \hat{Cu}_{Flawx} &= Cu_{Flaw1} + \hat{\Delta}_{Cu-Flawx} \end{aligned} \tag{114}$$

Nickel, Ni_{Flawx}:

The local variability for Ni is determined by sampling a Δ_{Ni} value drawn from a logistic distribution with parameters $\alpha = -0.0014$ and $\beta = 0.00647$ such that

$$\begin{aligned}
&\widehat{\Delta}_{Ni-Flawx} \leftarrow L(-0.0014, 0.00647) \\
&\widehat{\Delta}_{Ni-Flawx} = -0.0014 - 0.00647 \ln\left[\frac{1}{\Phi_{Ni}} - 1\right] \text{ for } \Phi_{Ni} \leftarrow U(0,1) \\
&\widehat{Ni}_{Flawx} = Ni_{Flaw1} + \widehat{\Delta}_{Ni-Flawx}
\end{aligned} \tag{115}$$

The same local variability samplings are applied to Ni-addition and non-Ni-addition welds.

Phosphorous, P_{Flawx}:

The local variability for phosphorous is determined by sampling a Δ_P value drawn from a logistic distribution with parameters $\alpha = 3.27 \times 10^{-6}$ and $\beta = 0.000449$.

$$\begin{aligned}
&\widehat{\Delta}_{P-Flawx} \leftarrow L(3.27 \times 10^{-6}, 0.000449) \\
&\widehat{\Delta}_{P-Flawx} = 3.27 \times 10^{-6} - 0.000449 \ln\left[\frac{1}{\Phi_P} - 1\right] \text{ for } \Phi_P \leftarrow U(0,1) \\
&\widehat{P}_{Flawx} = P_{Flaw1} + \widehat{\Delta}_{Ni-Flawx}
\end{aligned} \tag{116}$$

Negative values of sampled $\widehat{Cu}_{Flawx}, \widehat{Ni}_{Flawx}$, and $\widehat{P}_{Flawx}$ are handled as nonphysical exceptions in FAVOR using the truncation protocol described in Sect. 3.3.6, with 0.0 applied as a one-sided truncation boundary.

Through-thickness re-sampling for Weld Layers

Due to their thickness, RPV welds were typically constructed using multiple coils of weld wire. The variability in chemistry from one coil or weld layer to another is resampled in FAVOR as a given crack grows through the wall and enters a new weld layer. The weld-layer thickness in which this variability is imposed is every 1/4T of the RPV. In general, when a flaw has initiated, the weld chemistry content is not resampled for each growth increment. However, if the inner crack tip of the flaw has moved from one 1/4T of the vessel wall thickness to an adjoining 1/4T region, then the chemistry of the weld is sampled as if the flaw had advanced into a new material.

Additional Comments on Chemistry Sampling in Plate and Weld Subregions

When a sampled chemistry value for the first flaw in a subregion (*for the current RPV trial*) is truncated internally by FAVPFM, the non-truncated chemistry value for *Flaw1* continues to be used as the basis for subsequent *local variability* perturbation samplings. As an example, for a given RPV trial and first flaw in a given subregion, the sampled value of Cu_{Flaw1} might be truncated back to 0.25 for Linde welds or to 0.305 for all other welds, plates, and forgings, when applying the Eason and Wright correlation [86] to calculate $\Delta RT_{NDT.}$ However, FAVPFM will utilize the non-truncated value for Cu_{Flaw1} in the determination of the local variability copper content, $\hat{C}u_{Flawx}$, for all subsequent flaws located in this subregion for the current RPV trial. The rationale for this procedure is that the local variability random perturbation sampled for copper, $\hat{\Delta}_{Cu-Flawx}$, as determined from its logistic distribution, could possibly be sufficiently negative such that the perturbed value of $\hat{C}u_{Flawx}$ might take on a value below the truncation upper bound. However, if the value of $\hat{C}u_{Flawx}$ should exceed the upper truncation boundary, then FAVPFM will automatically truncate back to the appropriate upper bound.

4.3 NRC RVID2 Database

The *Reactor Vessel Integrity Database*, RVID [128] , developed following the NRC staff review of licensee responses to Generic Letter (GL) 92-01, Revision 1, provides a key source of input data for FAVOR. The most recent update of the database, RVID2 [129], was released in July of 2000. The RIVD2 summarizes the properties of the reactor vessel beltline materials for each operating commercial nuclear power plant. The RVID includes four tables for each plant: (1) background information table, (2) chemistry data table, (3) upper-shelf energy table, and (4) pressure-temperature limits or pressurized thermal shock table. References and notes follow each table to document the source(s) of data and to provide supplemental information. Appendix D presents a selection of RVID2 data relevant to FAVOR for the four power plants included in the PTS Re-evaluation Project. As of this writing, they are: (1) Beaver Valley 1, (2) Calvert Cliffs 1, (3) Oconee 1, and (4) Pallisades 1.

4.4 Discrete Flaw Density and Size Distributions

The method used to quantify the uncertainty in the flaw characterization is to include 1000 flaw-characterization records in each of the three data files: (1) inner surface-breaking flaws (2) embedded flaws in weld material, and (3) embedded flaws in plate material. The flaw-characterization file for inner surface- breaking flaws is applicable to weld and plate material. Each of these records contains separate discrete flaw-density and flaw-size distributions.

During the Monte Carlo PFM analysis, the RPV flaw-characterization data for the first stochastically generated RPV trial are taken from the first group of records, i.e., the first inner surface-breaking record, the first embedded-flaw weld material record, and the first embedded-flaw plate material record. The RPV flaw characterization for the second stochastically generated RPV trial is determined from the second group of records, etc. The RPV trials cycle through the flaw-characterization records sequentially up to 1000, and then restart at the first record.

Inner surface-breaking flaw density data are expressed in flaws per unit RPV-inner-surface area and weld subregion embedded flaws are flaws per unit area on the fusion line between the weld and adjacent plate subregions. These conventions are consistent with the physical model utilized by Pacific Northwest National Laboratory to derive the flaw characterization data input to FAVOR. Embedded flaws in plate regions are expressed on a volumetric basis.

Figures 43a and 43b illustrate axial and circumferential weld subregion elements, respectively. The number of flaws in each of these weld elements is calculated (internally by FAVOR) as the sum of the number of inner- surface breaking flaws and the number of embedded flaws as follows:

$$\begin{pmatrix}\text{Number of Flaws}\\ \text{in Weld Subregions}\end{pmatrix} = \rho_{SB}\left[\left(\frac{2\pi}{360}\right)R_i\ dz\ d\theta\right] + \rho_{EW}\left[2\left(\frac{3}{8}\right)dA\right]$$

$$\begin{aligned}
\rho_{SB} &= \text{inner surface-breaking flaw density (per unit surface area - flaws/in}^2\text{)}\\
\rho_{EW} &= \text{weld embedded-flaw density (per unit weld-fusion area - flaws/in}^2\text{)}\\
dA &= \text{user-input weld-fusion area (for one side of weld) (in}^2\text{ - input by user)}\\
R_i &= \text{internal radius of RPV (in. - input by user)}\\
dz &= \text{height of subregion element (in. - input by user)}\\
d\theta &= \text{subtended angle of subregion element (degrees - input by user)}
\end{aligned} \tag{117}$$

where ρ_{SB} and ρ_{EW} are summed over all flaw depths.

For axial welds, the fusion lines are on the sides of the weld, whereas for circumferential welds, the fusion lines are on the top and bottom of the welds. In the term {2 (3/8) *dA* }, the factor of 2 accounts for the fact that the user input data is the area on one side of the fusion line whereas flaws reside in fusion lines on both sides of the welds. The (3/8) accounts for the fact that embedded flaws that reside beyond the first 3/8 of the base metal are not included in a PTS analysis. All flaw densities are assumed to be uniform through the RPV wall thickness.

Figure 43c illustrates a plate subregion element. The number of flaws in each of these plate elements is calculated (internally by FAVOR) as the sum of the number of inner surface-breaking flaws and the number of embedded flaws as follows:

$$\begin{pmatrix}\text{Number of Flaws}\\ \text{in Plate Subregions}\end{pmatrix} = \rho_{SB}\left[\left(\frac{2\pi}{360}\right)R_i\ dz\ d\theta\right] + \rho_{EP}\left[\left(\frac{3}{8}\right)\pi\left(R_o^2 - \left(R_i - CLTH\right)^2\right)dz\left(\frac{d\theta}{360}\right)\right]$$

$$\begin{aligned}
\rho_{SB} &= \text{inner surface-breaking flaw density (per unit surface area - flaws/in}^2\text{)}\\
\rho_{EP} &= \text{plate embedded-flaw density summed over all flaw depths}\\
&\quad\ \text{(flaws per unit volume - flaws/in}^3\text{)}\\
R_o &= \text{external radius of RPV (in - input by user)}\\
R_i &= \text{internal radius of RPV (in. - input by user)}\\
CLTH &= \text{cladding thickness (in. - input by user)}\\
dz &= \text{height of subregion element (in. - input by user)}\\
d\theta &= \text{subtended angle of subregion element}\\
&\quad\ \text{(degrees - input by user)}
\end{aligned} \tag{118}$$

where ρ_{SB} and ρ_{EP} are summed over all flaw depths.

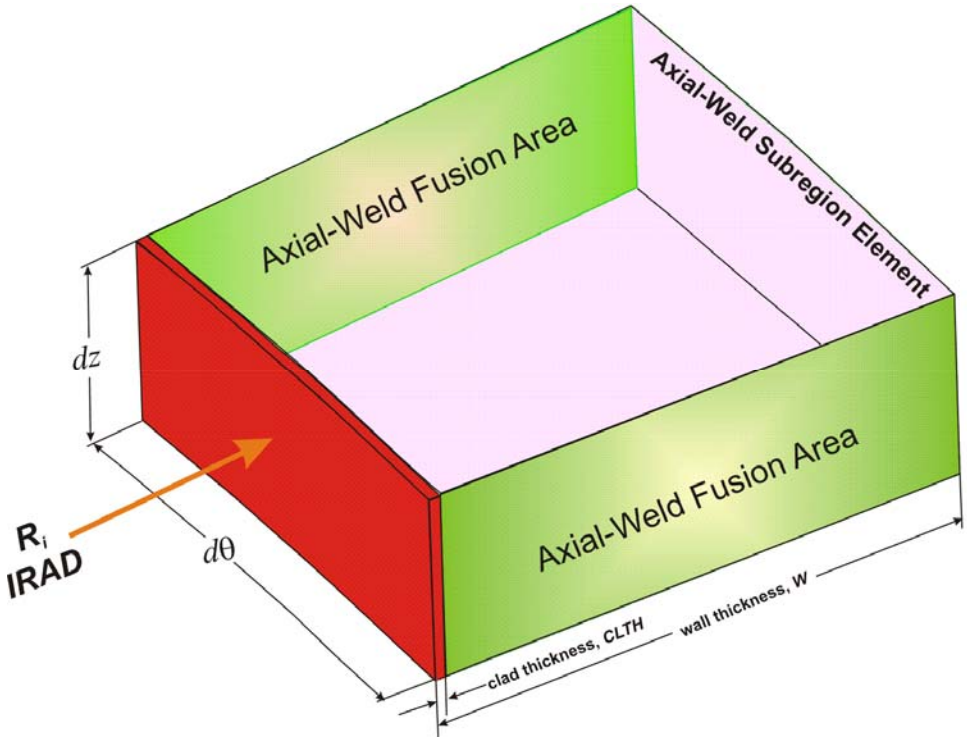

(a)

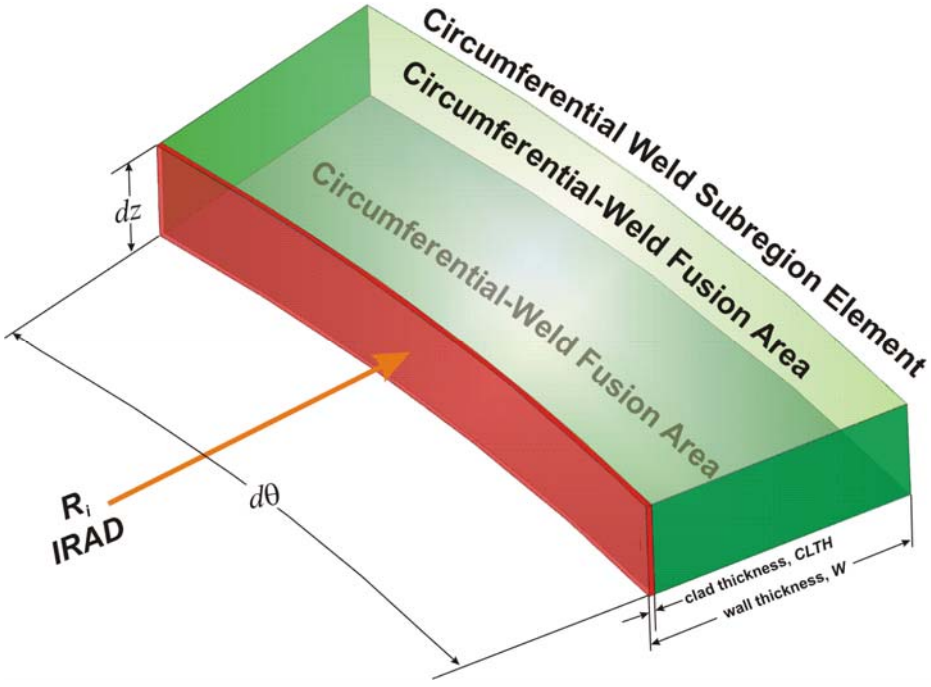

(b)

Fig. 43. Weld fusion area definitions for (a) axial-weld subregion elements and (b) circumferential subregion elements.

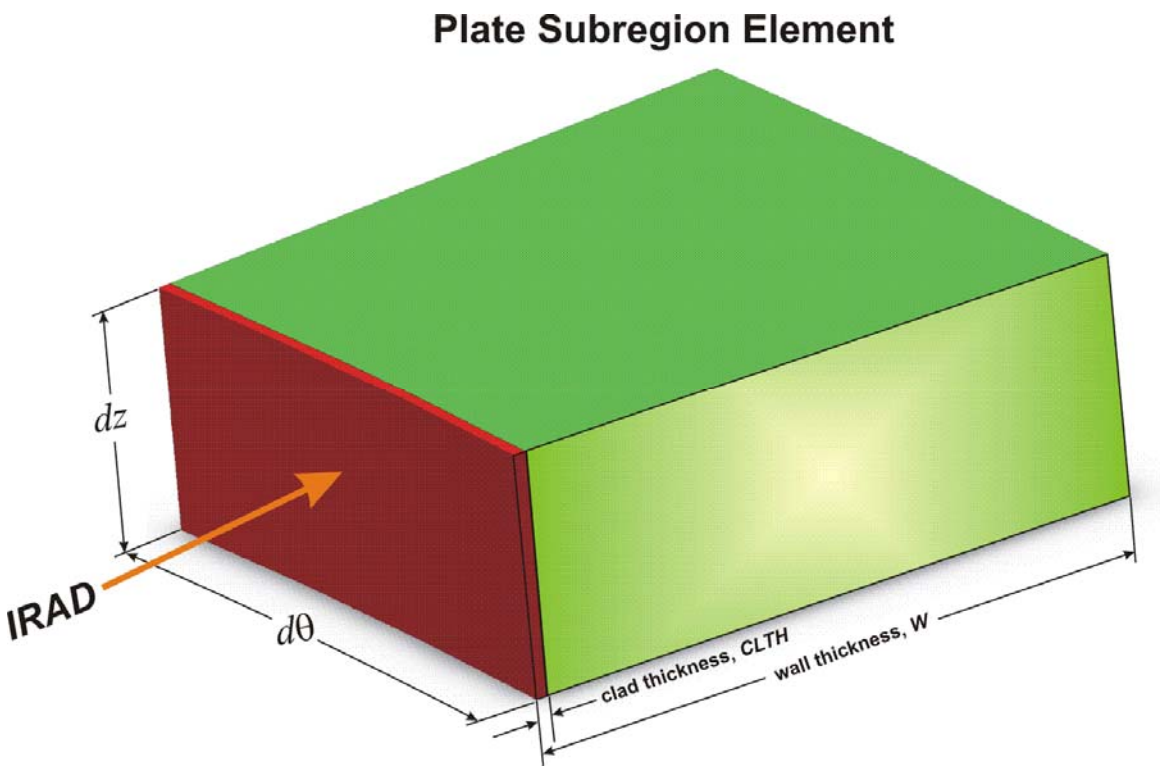

Fig. 43. (continued) (c) Plate subregion element.

4.5 Summary of Sampling Distributions and Protocols

Plane-Strain Static Initiation

The following sampling distribution and protocols have been implemented in the FAVOR code (FAVPFM) to represent (for a given flaw at a given time in the specific PTS transient under study) the epistemic and aleatory uncertainties in the plane-strain static initiation fracture-toughness values used in determining the probability of cleavage initiation:

Step 1. For plate, forging, and weld product forms, provide the following input to FAVOR:

Provide best estimates for the mean and standard deviation for normal distributions of copper, nickel, and phosphorous content, $N(\overline{Cu},\sigma_{Cu}), N(\overline{Ni},\sigma_{Ni}), N(\overline{P},\sigma_P)$.[9]

Provide a best estimate for the mean and standard deviation for a normal distribution of fluence at the inside surface of the vessel, $N(\overline{f_0}(0),\sigma_{f_0(0)})$.

Provide a best estimate for the standard deviations, $\sigma_{RT_{NDT0}}$, of unirradiated RT_{NDT0} and $\sigma_{\Delta RT_{NDT}}$ of the irradiation shift model ΔRT_{NDT}. The value of $\sigma_{\Delta RT_{NDT}}$ is used only to calculate the regulatory value of RT_{PTS} for reporting purposes.

Provide the coolant temperature, T_c in °F, and RPV exposure time in EFPY, where T_c is the temperature of the coolant on the inner surface of the RPV beltline region (adjacent to the active core) at the time the transient originates (at time = 0).

Determine the current regulatory estimate of the mean value of the unirradiated RT_{NDT} from the Reactor Vessel Integrity Database (RVID2) [129] for the material of interest (see Appendix D).

a) If this RT_{NDT} value was determined using either the ASME NB-2331 or MTEB 5-2 methods, designate the value of $RT_{NDT(RVID)}$ from RVID as RT_{RTND0} and proceed directly to Step 2.

b) If this RT_{NDT} value was determined using the *Generic* method, assign $\overline{RT}_{NDT0}$ as –8 °F for welds and 0 °F for plates and forgings; sample $\widehat{RT}_{NDT0} \leftarrow N(\overline{RT}_{NDT0},\sigma_{RT_{NDT0}})$; then proceed to Step 2.

[9] Note that negative values of $\widehat{Cu}, \widehat{Ni}$, and $\widehat{P}$ sampled from normal distributions are handled as nonphysical exceptions in FAVOR using the truncation protocol described in Sect. 3.3.6 with 0.0 as the truncation boundary.

Step 2. Generate a random number, Φ, between 0 and 1 from a uniform distribution. Use this random number to sample[10] a value of $\Delta RT_{epistemic}$ from the following Weibull percentile function (inverse CDF):

$$\begin{aligned} \Delta RT_{epistemic} &\leftarrow W(-45.586, 131.27, 2.177) \\ \Delta RT_{epistemic} &= -45.586 + 131.27\left[-\ln\left(1-\Phi\right)\right]^{1/2.177} \quad [°\text{F}] \end{aligned} \tag{119}$$

$\Delta RT_{epistemic}$ represents the epistemic uncertainty in RT_{NDT_0}.

Step 3. Sample the irradiation shift, ΔRT_{NDT}, using the Eason and Wright [86] embrittlement correlation from sampled values (sampled for each flaw) of neutron fluence, $\hat{f}_0(r)$; copper content, $Cu \leftarrow N(\overline{Cu}, \sigma_{Cu})$; nickel content, $Ni \leftarrow N(\overline{Ni}, \sigma_{Ni})$; phosphorous content, $\hat{P} \leftarrow N(\overline{P}, \sigma_P)$; and product form.

$$\Delta RT_{NDT}(r,\ldots) = \begin{cases} 0.99\Delta T_{30}(r,\ldots) & \text{weld} \\ 1.10\Delta T_{30}(r,\ldots) & \text{plate and forgings} \end{cases} \tag{120}$$

where

$$\Delta T_{30}(Ni, Cu, \hat{P}, f_0(r), \tau_{\text{exposure}}, T_c, \text{product form}) =$$

$$A\exp\left(\frac{19310}{T_c + 460}\right)\left(1 + 110\hat{P}\right)\left(f_0(r)\right)^{0.4601} + B\left(1 + 2.40Ni^{1.250}\right) f(Cu)\, g\left(f_0(r)\right) + Bias$$

$$A = \begin{Bmatrix} 8.86\times10^{-17} & \text{for welds} \\ 9.30\times10^{-17} & \text{for forgings} \\ 12.7\times10^{-17} & \text{for plates} \end{Bmatrix}$$

$$B = \begin{Bmatrix} 230 & \text{for welds} \\ 132 & \text{for forgings} \\ 206 & \text{for plates in CE vessels} \\ 156 & \text{for other plates} \end{Bmatrix}$$

$$g(f_0(r)) = \frac{1}{2} + \frac{1}{2}\tanh\left[\frac{\log_{10}\left(f_0(r) + 4.579\times10^{12}\tau_{\text{exposure}}\right) - 18.265}{0.713}\right]$$

$$f\left(Cu\right) = \begin{Bmatrix} 0 & \text{for } Cu \le 0.072 \text{ wt \%} \\ \left(Cu\text{-}0.072\right)^{0.659} & \text{for } Cu > 0.072 \text{ wt \%} \end{Bmatrix}$$

[10] A curved overbar, X, indicates a sampled random variate. A braced overbar, $\overline{X}$, indicates that sampling has occurred in a prior step but not in the current step.

subject to

$$Cu_{\max} = \begin{Bmatrix} 0.25 \text{ for welds with Linde 80 or Linde 0091 flux} \\ 0.305 \text{ for everything else} \end{Bmatrix}$$

and

$$Bias = \begin{Bmatrix} 0 \text{ for } t_{\text{exposure}} < 97000 \text{ h} \\ 9.4 \text{ for } t_{\text{exposure}} \geq 97000 \text{ h} \end{Bmatrix}$$

where $\hat{Cu}$ is the sampled copper content in wt%, $\hat{Ni}$ is the sampled nickel content in wt%, $\hat{P}$ is the sampled phosphorous content in wt%, $\hat{f}_0(r)$ is the sampled and then attenuated neutron fluence in n/cm^2, r is the position from the inner surface of RPV wall, $\tau_{exposure}$ is exposure time in hours (input to FAVOR in EFPY), and T_c is coolant temperature in °F. The fast-neutron fluence at the inner surface of the vessel is sampled using the protocol described in Sect. 4.2.3. The sampled neutron fluence for the flaw is then attenuated (but not resampled) as the crack grows through the wall to produce $\hat{f}_0(r)$.

Step 4. Calculate the sampled, irradiated value of RT_{NDT} from

$$\hat{RT}_{NDT}(r,\ldots) = \hat{RT}_{NDT0} - \hat{\Delta RT}_{epistemic} + \hat{\Delta RT}_{NDT}(r,\ldots) \tag{121}$$

where $\hat{RT}_{NDT0} = \begin{cases} \hat{RT}_{NDT0} \leftarrow N(\overline{RT}_{NDT0}, \sigma_{RT_{NDT0}}) \text{ if RVID2 method is } \textit{Generic} \\ \text{Heat Estimate of } \hat{RT}_{NDT0} \text{ if RVID2 method is NB-2331 or MTEB 5-2} \end{cases}$

Step 5. Calculate the normalized temperature of the vessel at the current location, r, of the crack tip in the RPV wall as

$$\hat{\Delta T}_{RELATIVE}(r,\ldots) = T(r,\tau) - \hat{RT}_{NDT}(r,\ldots) \tag{122}$$

Step 6. Calculate the parameters of the Weibull distribution of the K_{Ic} Weibull statistical distribution by

$$\boxed{\begin{aligned} a_{K_{Ic}}(\hat{\Delta T}_{RELATIVE}) &= 19.35 + 8.335\exp\left[0.02254(\hat{\Delta T}_{RELATIVE})\right] \text{ [ksi}\sqrt{\text{in.}}] \\ b_{K_{Ic}}(\hat{\Delta T}_{RELATIVE}) &= 15.61 + 50.132\exp\left[0.008(\hat{\Delta T}_{RELATIVE})\right] \text{ [ksi}\sqrt{\text{in.}}] \\ c_{K_{Ic}} &= 4 \end{aligned}} \tag{123}$$

with K_{Ic} in ksi√in and $\Delta T = (T\text{-}RT_{NDT})$ in °F.

Note that this Weibull statistical model describes the *aleatory* uncertainty in plane-strain static initiation.

Step 7. For a given applied K_I, calculate the instantaneous conditional probability of crack initiation, $\Pr\{K_{Ic} \le K_I\}$ with *aleatory* uncertainty, from the following Weibull distribution

$$\Pr(K_{Ic} < K_I) = \widehat{cpi} = \begin{cases} 0; & K_I \le a_{K_{Ic}} \\ 1 - \exp\left[-\left(\dfrac{K_I - a_{K_{Ic}}(\widehat{\Delta T}_{RELATIVE})}{b_{K_{Ic}}(\widehat{\Delta T}_{RELATIVE})} \right)^{c_{K_{Ic}}} \right]; & K_I > a_{K_{Ic}} \end{cases} \tag{124}$$

If the flaw is determined to be in a warm-prestressing state (and the WPS option has been turned on by the user), then the conditional probability of initiation is set to zero. See Sect. 3.3.4 for a complete discussion of warm prestressing.

Plane-Strain Static Crack Arrest

Assuming that the given flaw at a given time (for the specific PTS transient under study) has a finite conditional probability of initiation that is increasing with time, the following protocol has been implemented in FAVOR as a part of the *Initiation-Growth-Arrest* (IGA) submodel (see Sect. 3.3.12) to represent the epistemic and aleatory uncertainties in plane-strain crack arrest fracture-toughness values.

Step 8. For plate, forging, and weld product forms, the following input will have been provided to FAVOR:

Best estimates for the mean and standard deviation for normal distributions of copper, nickel, and phosphorous content: $N(\overline{Cu}, \sigma_{Cu}), N(\overline{Ni}, \sigma_{Ni}), N(\overline{P}, \sigma_P)$.[11]

Best estimate for the mean and standard deviation for a normal distribution of fluence at the inside surface of the vessel, $N(\overline{f_0}(0), \sigma_{f_0(0)})$.[12]

Best estimate for the standard deviation, $\sigma_{RT_{NDT0}}$, of unirradiated RT_{NDT}.

The coolant temperature, T_c in °F, and RPV exposure time in EFPY.

From the initiation procedure for this flaw, the current regulatory estimate of the unirradiated RT_{NDT} will have already been determined from the Reactor Vessel Integrity Database (RVID2) [129] for the material of interest (see Appendix D) and designated as either RT_{NDT0} if the RVID2 $RT_{NDT(u)}$ method is NB-2331 or MTEB 5-2 or sampled from a normal distribution $\widehat{RT}_{NDT0} \leftarrow N(\overline{RT}_{NDT(RVID)}, \sigma_{RT_{NDT0}})$ if the RVID2 $RT_{NDT(u)}$ method is *Generic*.

---

[11] Note that negative values of chemistry content ($\widehat{Cu}, \widehat{Ni}$, and $\widehat{P}$) sampled from normal distributions are handled as nonphysical exceptions in FAVOR using the truncation protocol described in Sect. 3.3.4 with 0 as the truncation boundary.

[12] Note that sampled negative values of fluence, $\widehat{f_0}(0)$, are handled as nonphysical exceptions in FAVOR using the truncation protocol described in Sect. 3.3.4 with 0 as the truncation boundary.

Step 9. Retrieve the value of $\Delta RT_{epistemic}$ determined from Step 2 in the initiation procedure applied for this flaw and adjust the epistemic uncertainty in RT_{NDT_0} by applying a shift of -14.4 °F

$$\Delta RT_{epist-arrest} = \Delta RT_{epistemic} - 14.4 \ \ [°F] \tag{125}$$

Note that this step does not involve a resampling of $\Delta RT_{epistemic}$.

Step 10. Retrieve the sampled value of the irradiation shift for this flaw, $\Delta RT_{NDT}(r,\ldots)$, determined from Step 3 in the initiation procedure applied for this flaw at its current position in the RPV wall. Note that this step does not involve a resampling of $\Delta RT_{NDT}(r,\ldots)$.

Step 11. Sample $\Delta RT_{ARREST} \leftarrow \Lambda(\mu_{\ln(\Delta RT_{ARREST})}, \sigma_{\ln(\Delta RT_{ARREST})})$ from a lognormal distribution (see Appendix F) where

$$\mu_{\ln(\Delta RT_{ARREST})} = \ln\left[\Delta RT_{ARREST(mean)}\right] - \frac{\sigma^2_{\ln(\Delta RT_{ARREST})}}{2}$$

where

$$T_0 = \left(RT_{NDT_0} - \Delta RT_{epist-arrest} - 32\right)/1.8 \ \ [°C]$$

$$\Delta RT_{ARREST(mean)} = 44.122 \exp\left[-0.005971 \times T_0\right] \ \ [°C] \tag{126}$$

$$\sigma_{\ln(\Delta RT_{ARREST})} = \sqrt{\ln\left\{\exp\left[0.38998^2 + 2\ln(\Delta RT_{ARREST(mean)})\right] - \mathrm{var}\left(T_0\right)\right\} - 2\ln\left[\Delta RT_{ARREST(mean)}\right]}$$

where

$$\mathrm{var}(T_0) = \begin{cases} (12.778)^2 & \text{for } T_0 < -35.7 \text{ °C} \\ 99.905972 - 1.7748073 T_0 & \text{for } -35.7 \text{ °C} \le T_0 \le 56 \text{ °C} \\ 0 & \text{for } T_0 > 56 \text{ °C} \end{cases}$$

ΔRT_{ARREST} is sampled from the lognormal percentile function and then converted into °F

$$\Delta RT_{ARREST} = 1.8 \exp\left[\sigma_{\ln(\Delta RT_{Arrest})} Z_{P_f} + \mu_{\ln(\Delta RT_{Arrest})}\right] \ \ [°F]$$

$Z_{P_f} \leftarrow N(0,1)$; Z_{P_f} is the standard normal deviate corresponding to the P_f fractile $(0 < P_f < 1)$ for this trial in the crack *Initiation - Growth - Arrest* model.

Step 12. Calculate the estimated arrest reference temperature, RT_{ARREST}

$$RT_{ARREST}(r,\ldots) = RT_{NDT_0} - \Delta RT_{epist-arrest} + \Delta RT_{ARREST} + \Delta RT_{NDT}(r,\ldots) \tag{127}$$

Step 13. Calculate the normalized (relative to RT_{ARREST}) temperature of the vessel at the current location, *r*, in the RPV wall

$$\Delta T_{RELATIVE}(r,\ldots) = T(r,t) - RT_{ARREST}(r,\ldots) \tag{128}$$

Step 14. Calculate the lognormal mean, $\mu_{\ln(K_{Ia})}(\Delta T_{RELATIVE})$, of the K_{Ia} statistical distribution by

$$\mu_{\ln(K_{Ia})}(\Delta T_{RELATIVE}) = \ln\left[K_{Ia(mean)}(\Delta T_{RELATIVE})\right] - \frac{\sigma^2_{\ln(K_{Ia})}}{2}$$

where

if K_{Ia}_Model is equal to 1

$$K_{Ia(\text{mean})}(\Delta T_{RELATIVE}) = 27.302 + 69.962\exp\left[0.006057(\Delta T_{RELATIVE})\right] \text{ [ksi}\sqrt{\text{in.}}\text{]} \tag{129}$$

$$\sigma_{\ln(K_{Ia})} = 0.18$$

else if K_{Ia}_Model is equal to 2

$$K_{Ia(\text{mean})}(\Delta T_{RELATIVE}) = 27.302 + 70.6998\exp\left[0.008991(\Delta T_{RELATIVE})\right] \text{ [ksi}\sqrt{\text{in.}}\text{]}$$

$$\sigma_{\ln(K_{Ia})} = 0.34$$

Step 15. Given the current value of $K_{I\text{-}initiation}$ from the initiation model, we first calculate the fractile, $\Phi_{K_{I-initiation}}$, associated with this value in the arrest model by

$$\Phi_{K_{I-initiation}} = \frac{1}{2}\left[\text{erf}\left(\frac{\ln(K_{I-initiation}) - \mu_{\ln(K_{Ia})}(\Delta T_{RELATIVE})}{\sigma_{\ln(K_{Ia})}\sqrt{2}}\right) + 1\right] \tag{130}$$

where $\text{erf}(x) \equiv \frac{2}{\sqrt{\pi}}\int_0^x \exp(-\xi^2)\,\text{d}\xi$. Using the same value of P_f from Step 11, scale by $\Phi_{K_{I-initiation}}$ such that

$$\Phi_{K_{Ia}} = (P_f)(\Phi_{K_{I-initiation}}) \tag{131}$$

With this $\Phi_{K_{Ia}}$ fractile, draw a value of K_{Ia} from its lognormal distribution

$$K_{Ia}(\Phi_{K_{Ia}}, \Delta T_{RELATIVE}) = \exp\left[\sigma_{\ln(K_{Ia})}\widehat{Z}_{\Phi_{K_{Ia}}} + \mu_{\ln(K_{Ia})}(\Delta T_{RELATIVE})\right] \tag{132}$$

$$\widehat{Z}_{\Phi_{K_{Ia}}} = \text{ standard normal deviate corresponding to the } \Phi_{K_{Ia}} \text{ fractile}$$

Notes:

Note on Step 3: The current sampled value of ΔT_{30} is also used to estimate the effects of irradiation on the unirradiated flow stress, $\sigma_{flow(u)}$, in the crack *Initiation-Growth-Arrest* model. After each resampling of ΔT_{30}, the flow stress is adjusted by the following relation:

$$\sigma_{flow} = \sigma_{flow(u)} + \gamma\Delta T_{30} \text{ where } \gamma = \begin{cases} 0.112 \text{ ksi/°F for welds} \\ 0.131 \text{ ksi/°F for plates} \end{cases}$$

This value of σ_{flow} is then used in the vessel-failure test against the pressure-induced membrane stress in the remaining ligament, checking for net-section plastic collapse.

Note on Step 11: The only random variate sampled in Step 11 is Z_{P_f} . All other variates have been sampled in previous steps.

Note on Step 15: The scaling procedure in Step 15 ensures that the initial value of K_{Ia} , calculated immediately after initiation, does not exceed the initiating value of K_I, thus ensuring an initial extension. For welds, the scaling procedure of Eq. (131) is used only in the weld layer in which the flaw originally initiated. If the flaw advances into other weld layers, then this scaling is not applied, since it is assumed that any linkage between the original initiation event and crack arrest is thereby broken.

For either an initiated (cpi > 0) surface-breaking or embedded flaw, the flaw is first assumed to extend to become an infinite-length flaw before it is allowed to advance through the RPV wall. It is the applied K_I of the infinite-length flaw (designated as $K_{I\text{-}initiation}$ in Step 15, Eq. (130)) that is taken as the operative initiating K_{Ic} to establish the required scaling factor and not the applied K_I of the surface-breaking or embedded flaw at initiation. It was determined that scaling by the lower embedded-flaw K_I at initiation was an overly restrictive constraint.

5. Summary and Conclusions

This report has provided a detailed description of the theory, algorithms, methods, and correlations that have been implemented in this baseline release of the FAVOR, v04.1, computer code for performing probabilistic fracture mechanics analyses of nuclear reactor pressure vessels subjected to pressurized thermal shock and other pressure-thermal events. In support of the PTS Re-evaluation Project, the following advanced technologies and new capabilities have been incorporated into FAVOR, v04.1:

- **the ability to incorporate new detailed flaw-characterization distributions from NRC research (with Pacific Northwest National Laboratory, PNNL),**
- **the ability to incorporate detailed neutron fluence regions – detailed fluence maps from Brookhaven National Laboratory, BNL,**
- **the ability to incorporate warm-prestressing effects into the analysis,**
- **the ability to include temperature-dependencies in the thermo-elastic properties of base and cladding,**
- **the ability to include crack-face pressure loading for surface-breaking flaws,**
- **a new ductile-fracture model simulating stable and unstable ductile tearing,**
- **a new embrittlement correlation,**
- **the ability to include multiple transients in one execution of FAVOR,**
- **input from the Reactor Vessel Integrity Database, Revision 2, (RVID2) of relevant RPV material properties,**
- **fracture-toughness models based on extended databases and improved statistical distributions,**
- **a variable failure criterion, i.e., how far must a flaw propagate into the RPV wall for the vessel simulation to be considered as "failed" ?**
- **semi-elliptic surface-breaking and embedded-flaw models,**
- **through-wall weld residual stresses, and an**
- **improved PFM methodology that incorporates modern PRA procedures for the classification and propagation of input uncertainties and the characterization of output uncertainties as statistical distributions.**

The companion report *Fracture Analysis of Vessels – Oak Ridge, FAVOR, v04.1 Computer Code: User's Guide* [45] gives complete details on input requirements and execution of FAVOR, v04.1.

References

1. T. L. Dickson, S. N. M. Malik, J. W. Bryson, and F. A. Simonen, "Revisiting the Integrated Pressurized Thermal Shock Studies of an Aging Pressurized Water Reactor," ASME PVP-Volume 388, *Fracture, Design Analysis of Pressure Vessels, Heat Exchangers, Piping Components, and Fitness for Service*, *ASME Pressure Vessels and Piping Conference*, August, 1999.

2. A. R. Foster and R. L. Wright, Jr., *Basic Nuclear Engineering*, 2nd ed., Allyn and Bacon, Inc., Boston, 1973.

3. K. Balkey, F. J. Witt, and B. A. Bishop, *Documentation of Probabilistic Fracture Mechanics Codes Used for Reactor Pressure Vessels Subjected to Pressurized Thermal Shock Loading, Parts 1 and 2*, EPRI TR-105001, Westinghouse Electric Corporation, Pittsburgh, PA, June 1995.

4. D. L. Selby, et al., *Pressurized Thermal Shock Evaluation of the H.B. Robinson Nuclear Power Plant,* NUREG/CR-4183 (ORNL/TM-9567), September 1985.

5. *Classification of TMI Action Plan Requirements*, U.S. Nuclear Regulatory Commission, NUREG-0737, November 1980.

6. D. L. Selby, et al., *Pressurized Thermal Shock Evaluation of the Calvert Cliffs Unit 1 Nuclear Power Plant*, NUREG/CR-4022 (ORNL/TM-9408), Oak Ridge National Laboratory, Oak Ridge, TN, September 1985.

7. T. J. Burns, et al., *Preliminary Development of an Integrated Approach to the Evaluation of Pressurized Thermal Shock as Applied to the Oconee Unit 1 Nuclear Power Plant*, NUREG/CR-3770 (ORNL/TM-9176), May 1986.

8. Policy Issue from J. W. Dircks to NRC Commissioners, *Enclosure A: NRC Staff Evaluation of Pressurized Thermal Shock, November 1982*, SECY-82-465, November 23, 1982, Division of Nuclear Reactor Regulation, U.S. Nuclear Regulatory Commission, Washington, D.C.

9. T. L. Dickson, *Review of Pressurized Thermal Shock Screening Criteria for Embrittled Pressurized Water Reactor Pressure Vessels,* ORNL/NRC/LTR-95/39, December, 1995.

10. *U.S. Code of Federal Regulations,* Title 10, Part 50, Section 50.61 and Appendix G.

11. U.S. Nuclear Regulatory Commission, Regulatory Guide 1.154 (1987), *Format and Content of Plant-Specific Pressurized Thermal Shock Safety Analysis Reports for Pressurized Water Reactors*.

12. U. S. Nuclear Regulatory Commission, Regulatory Guide 1.99, Revision 2 (1988), *Radiation Embrittlement of Reactor Vessel Materials*.

13. C. E. Pugh and B. R. Bass, *A Review of Large-Scale Fracture Experiments Relevant to Pressure Vessel Integrity Under Pressurized Thermal Shock Conditions,* NUREG/CR-6699 (ORNL/TM-2000/360), Oak Ridge National Laboratory, January 2001.

14. B. R. Bass, C. E. Pugh, J. Keeney-Walker, H. Schulz, and J. Sievers, *CSNI Project for Future Analyses of Large-Scale International Reference Experiments (Project FALSIRE),* NUREG/CR-5997 (ORNL/TM-12307), Oak Ridge National Laboratory, December 1992.

15. B. R. Bass, C. E. Pugh, J. Keeney-Walker, H. Schulz, and J. Sievers, *CSNI Project for Future Analyses of Large-Scale International Reference Experiments (FALSIRE II),* NUREG/CR-6460 (ORNL/TM-13207), Oak Ridge National Laboratory, April 1996.

16. J. Sievers and B. R. Bass, "Comparative Assessment of Project FALSIRE-Results," *Journal Nucl. Engr. Des.* **152**, (1994) 19-38.

17. B. R. Bass, et al., "CSNI Project for Fracture Analysis of Large-Scale International Reference Experiments (FALSIRE II)," *Proceedings of the International Conference on Nuclear Engineering-4 (ICONE-4),* Vol. 1, Part A, American society of Mechanical Engineers, (1996) 149-162.

18. B. R. Bass, C. E. Pugh, S. Crutzen, and R. Murgatroyd, *Relationship of NESC-1 to Other Large-Scale International Projects,* ORNL/NRC/LTR-99/20, Oak Ridge National Laboratory, Oak Ridge, TN, 1999.

19. J. G. Merkle, G. D. Whitman, and R. H. Bryan, *An Evaluation of the HSST Program Intermediate Pressure Vessel Tests in Terms of Light-Water-Reactor Pressure Vessel Safety*, ORNL/TM-5090, Oak Ridge National Laboratory, Oak Ridge, TN, November 1975.

20. G. D. Whitman, *Historical Summary of the Heavy-Section Steel Technology Program and Some Related Activities in Light-Water-Reactor Pressure Vessel Safety Research*, NUREG/CR-4489 (ORNL-6259), Oak Ridge National Laboratory, Oak Ridge, TN, March 1986.

21. R. W. Derby, et al., *Test of 6-Inch-Thick Pressure Vessels, Series 1: Intermediate Test Vessels V-1 and V-2*, ORNL-4895, Oak Ridge National Laboratory, Oak Ridge, TN, February 1974.

22. R. H. Bryan, et al., *Test of 6-Inch-Thick Pressure Vessels, Series 2: Intermediate Test Vessels V-3, V-4, and V-6*, ORNL-5059, Oak Ridge National Laboratory, Oak Ridge, TN, November 1975.

23. R. H. Bryan, et al., *Test of 6-Inch-Thick Pressure Vessels, Series 3: Intermediate Test Vessels V-7B*, NUREG/CR-0309 (ORNL/NUREG-38), Oak Ridge National Laboratory, Oak Ridge, TN, October 1978.

24. J. G. Merkle, et al., *Test of 6-Inch-Thick Pressure Vessels, Series 4: Intermediate Test Vessels V-5 and V-9 with Nozzle Corner Cracks,* ORNL/NUREG-7, Oak Ridge National Laboratory, Oak Ridge, TN, August 1977.

25. R. H. Bryan, et al., *Test of 6-Inch-Thick Pressure Vessels, Series 3: Intermediate Test Vessel V-8,* NUREG/CR-0675 (ORNL/NUREG-58), Oak Ridge National Laboratory, Oak Ridge, TN, December 1979.

26. R. H. Bryan, et al., *Pressurized-Thermal Shock Test of 6-Inch-Thick Pressure Vessel, PTSE-1: Investigations of Warm Prestressing and Upper-Shelf Arrest*, NUREG/CR-4106 (ORNL-6135), Oak Ridge National Laboratory, Oak Ridge, TN, April 1985.

27. R. H. Bryan, et al., *Pressurized Thermal Shock Test of 6-Inch-Thick Pressure Vessel PTSE-2: Investigation of Low Tearing Resistance and Warm Prestressing*, NUREG/CR-4888 (ORNL-6377), Oak Ridge National Laboratory, Oak Ridge, TN, December 1987.

28. H. Keinanen, et al., "Pressurized Thermal Shock Tests with Model Pressure Vessels Made of VVER-440 Reactor Steel," *IAEA/CSNI Specialists' Meeting on Fracture Mechanics Verification by Large-Scale Testing, Oak Ridge, Tennessee*, *October 26-29, 1992*, NUREG/CP-0131 (ORNL/TM-12413), October 1993, 275-288.

29. B. R. Bass, et al., *CSNI Project for Fracture Analyses of Large-Scale International Reference Experiments (FALSIRE II)*, NUREG/CR-6460 (ORNL/TM-13207), Oak Ridge National Laboratory, Oak Ridge, TN, April 1996.

30. L. Stumpfrock, "FALSIRE Results for NKS-3 and NKS-4," *IAEA/CSNI Specialists' Meeting on Fracture Mechanics Verification by Large-Scale Testing, Oak Ridge, Tennessee*, *October 26-29, 1992*, NUREG/CR-0131 (ORNL/TM-12413), October 1993, 151-188.

31. L. Stumpfrock, et al., "Fracture Mechanics Investigations on Cylindrical Large-Scale Specimens under Thermal-Shock Loading," *Journal of Nuclear Engineering Design* **144**, (1993) 31-44.

32. E. Morland, "Spinning Cylinder Experiments SC-I and SC-II: A Review of Results and Analyses Provided to the FALSIRE Project," *IAEA/CSNI Specialists' Meeting on Fracture Mechanics Verification by Large-Scale Testing, Oak Ridge, Tennessee*, *October 26-29, 1992*, NUREG/CR-0131 (ORNL/TM-12413), October 1993, 39-74.

33. D. J. Lacey, et al., *Spinning Cylinder Test 4: An Investigation of Transition Fracture Behavior for Surface Breaking Defects in Thick-Section Steel Specimens*, AEA Technology Report AEA TRS 4098, June 1991.

34. R. D. Cheverton, et al., "Review of Pressurized-Water-Reactor-Related Thermal Shock Studies," *Fracture Mechanics: Nineteenth Symposium (June 30-July 2, 1986)*, ASTM STP-969, American Society for Testing and Materials, (1988) 752-766.

35. R. D. Cheverton, "Thermal Shock Experiments with Flawed Clad Cylinders," *Journal of Nuclear Engineering and Design* **124**, (1990) 109-119.

36. B. R. Bass, J. Wintle, R. C. Hurst, and N. Taylor (eds), *NESC-1 Project Overview*, EUR 19051EN, European Commission, Directorate-General Joint Research Centre, Institute for Advanced Materials, Petten, The Netherlands, 2001.

37. H. Okumura, et al., "PTS Integrity Study in Japan," *Ninth International Conference on Structural Mechanics in Reactor Technology*, Vol. F, (1989) 7-12.

38. D. J. Naus, et al., *High-Temperature Crack Arrest Behavior in 152-mm-Thick SEN Wide Plates of Quenched and Tempered A533 Grade B Class 1 Steel*, NUREG/CR-5330 (ORNL-11083), Oak Ridge National Laboratory, Oak Ridge, TN, April 1989.

39. D. J. Naus, et al., *Crack-Arrest Behavior in SEN Wide Plates of Low-Upper-Shelf Base Metal Tested Under Nonisothermal Conditions: WP-2 Series*, NUREG/CR-5451 (ORNL-6584), Oak Ridge National Laboratory, Oak Ridge, TN, April 1989.

40. K. Kussmaul, R. Gillot, and T. Elenz, "Full Thickness Crack Arrest Investigations on Compact Specimens and a Heavy-Wide Plate," *IAEA/CSNI Specialists' Meeting on Fracture Mechanics Verification by Large-Scale Testing, Oak Ridge, Tennessee*, *October 26-29, 1992*, NUREG/CR-0131 (ORNL/TM-12413), October 1993, 551-572.

41. D. Moinerau, et al., "Cleavage Fracture of Specimens Containing an Underclad Crack, PVP Vol. 233, *Pressure Vessel Fracture, Fatigue and Life Management,* American Society of Mechanical Engineers, 1992.

42. J. A. Keeney, B. R. Bass, and W. J. McAfee, "Fracture Assessment of Weld Material from a Full-Thickness Clad RPV Shell Segment," *Fatigue and Fracture Mechanics, 20th Volume,* ASTM STP-1321, eds., J. H. Underwood, B. D. McDonald, and M. R. Mitchell, American Society of Materials and Testing, 1997.

43. J. A. Keeney and P. T. Williams, "Fracture Analysis of Ductile Crack Growth in Weld Material from a Full-Thickness Clad RPV Shell Segment," *Fatigue and Fracture Mechanics, 29th Volume*, ASTM STP-1332, eds. T. L. Panontin and S. D. Sheppard, American Society of Materials and Testing, 1998.

44. B. R. Bass, et al., "Evaluation of Constraint Methodologies Applied to Shallow-Flaw Cruciform Bend Specimens Tested under Biaxial Loading Conditions," PVP Vol. 365, *Proceedings of the 1998 ASME Pressure Vessel and Piping Conference,* San Diego, CA, July 1998, 11-26.

45. T. L. Dickson, P. T. Williams, and S. Yin, *Fracture Analysis of Vessels – FAVOR (v04.1): User's Guide*, NUREG/CR-6855 (ORNL/TM-2004/245), Oak Ridge National Laboratory, Oak Ridge, TN, 2004.

46. M. G. Morgan and M. Henrion, *Uncertainty – A Guide to Dealing with Uncertainty in Quantitative Risk and Policy Analysis*, Cambridge University Press, Cambridge, UK, 1990.

47. F.A. Simonen, S.R. Doctor, G.J. Schuster, and P.G. Heasler, "A Generalized Procedure for Generating Flaw Related Inputs for the FAVOR Code," NUREG/CR-6817, Rev. 1, U.S. Nuclear Regulatory Commission, October 2003.

48. G. J. Schuster, S. R. Doctor, S. L. Crawford, and A. F. Pardini, *Characterization of Flaws in U.S. Reactor Pressure Vessels: Density and Distribution of Flaw Indications in PVRUF*, USNRC Report NUREG/CR-6471, Vol. 1, U.S. Nuclear Regulatory Commission, Washington, D.C. (1998).

49. G. J. Schuster, S. R. Doctor, and P. G. Heasler, *Characterization of Flaws in U.S. Reactor Pressure Vessels: Validation of Flaw Density and Distribution in the Weld Metal of the PVRUF Vessel,* USNRC Report NUREG/CR-6471, Vol. 2, U.S. Nuclear Regulatory Commission, Washington, D.C. (2000).

50. G. J. Schuster, S. R. Doctor, S. L. Crawford, and A. F. Pardini, *Characterization of Flaws in U.S. Reactor Pressure Vessels: Density and Distribution of Flaw Indications in the Shoreham Vessel,* USNRC Report NUREG/CR-6471, Vol. 3, U.S. Nuclear Regulatory Commission, Washington, D.C. (1999).

51. A. M. Law and W. D. Kelton, *Simulation Modeling and Analysis*, 3rd ed., McGraw-Hill, New York, NY, (2000).

52. A. J. Brothers and S. Yukawa, "The Effect of Warm Prestressing on Notch Fracture Strength," *Journal of Basic Engineering*, *Transaction of the ASME*, Series D, **85**(1), (1963) 87-104.

53. R. W. Nichols, "The Use of Overstressing Techniques to Reduce the Risk of Subsequent Brittle Fracture: Parts 1 and 2," *British Welding Journal*, January and February 1968.

54. J. J. McGowan, "An Assessment of the Beneficial Effects of Warm Prestressing on the Fracture Properties of Nuclear Reactor Pressure Vessels Under Severe Thermal Shock," Westinghouse Electric Company, WCAP-9178, March 1978.

55. G. C. Chell, "A Theory of Warm Prestressing: Experimental Validation and the Implication for Elastic-Plastic Failure Criteria," CERL Lab Note RD/L/N78/79, September 1979.

56. G. C. Chell, "Some Fracture Mechanics Applications of Warm Prestressing to Pressure Vessels," *4th International Conference on Pressure Vessel Technology*, Paper C22/80, London, May 1980.

57. B. W. Pickles and A. Cowan, "A Review of Warm Prestressing Studies," *International Journal of Pressure Vessels and Piping* **14**, (1983) 95-131.

58. D. Lidbury and P. Birkett, "Effect of Warm Prestressing on the Transition Toughness Behaviour of an A533 Grade B Class 1 Pressure Vessel Steel," *ASTM STP 1074, Fracture Mechanics: 21st Symposium*, American Society for Testing and Materials, Philadelphia, PA, (1990) 264-285.

59. F. M. Burdekin and D. P. G. Lidbury, "Views of TAGSI on the Current Position with Regard to Benefits of Warm Prestressing," *International Journal of Pressure Vessels and Piping* **76**, (1999) 885-890.

60. H. Kordisch, R. Böschen, J. G. Blauel, W. Schmitt, and G. Nagel, "Experimental and Numerical Investigation of the Warm-Prestressing (WPS) Effect Considering Different Load Paths," *Nuclear Engineering Design* **198**, (2000) 89-96.

61. J. H. Chen, V. B. Wang, G. Z. Wang, and X. Chen, "Mechanism of Effects of Warm Prestressing on Apparent Toughness of Precracked Specimens of HSLA Steels," *Engineering Fracture Mechanics* **68**, (2001) 1669-1689.

62. W. Lefevre, G. Barbier, R. Masson, and G. Rousselier, "A Modified Beremin Model to Simulate the Warm Pre-Stress Effect," *Nuclear Engineering and Design* **216**, (2002) 27-42.

63. M. T. Kirk, "Inclusion of Warm Prestressing Effects in Probabilistic Fracture Mechanics Calculations Performed to Assess the Risk of RPV Failure Produced by Pressurized Thermal Shock Events: An Opinion," presented at the *NATO Advanced Research Workshop – Scientific Fundamentals for the Life Time Extension of Reactor Pressure Vessels*, Kiev, Ukraine, April 22-25, 2002.

64. B. W. Brown and J. Lovato, *RANLIB – A Library of Fortran Routines for Random Number Generation*, Department of Biomathematics, University of Texas, Houston, TX, 1994.

65. P. L'Ecuyer, "Efficient and Portable Combined Random Number Generators," *Communications of the ACM* **31**(6), (1988) 742-774.

66. P. L'Ecuyer and S. Cote, "Implementing a Random Number Package with Splitting Facilities." *ACM Transactions on Mathematical Software* **17**, (1991) 98-111.

67. A. Rukhin, et al., *A Statistical Test Suite for Random and Pseudorandom Number Generators for Cryptographic Applications*, NIST Special Publication 800-22, National Institute of Standards and Technology, Gaithersburg, MD, May 15, 2001.

68. G. E. P. Box and M. E. Müller, "A Note on the Generation of Random Normal Deviates," *Annals of Mathematical Statistics*, **29** (1958), 610-611.

69. M. E. Müller, "An Inverse Method for the Generation of Random Normal Deviates on Large Scale Computers," *Math. Tables Aids Comp.* **63**, (1958) 167-174.

70. M. Abramowitz and I. A. Stegun, *Handbook of Mathematical Functions*, Dover Publications, Inc., New York, (1972) 931.

71. J. H. Ahrens and U. Dieter, "Extensions of Forsythe's Method for Random Sampling from the Normal Distribution," *Math. Comput.* **27**(124), (1973) 927-937.

72. Kennedy and Gentle, *Statistical Computing*, Marcel Dekker, NY, (1980) 95.

73. EPRI Special Report, 1978, *Flaw Evaluation Procedures: ASME Section XI*, EPRI NP-719-SR, Electric Power Research Institute, Palo Alto, CA.

74. K. O. Bowman and P. T. Williams, *Technical Basis for Statistical Models of Extended K_{Ic} and K_{Ia} Fracture Toughness Databases for RPV Steels*, ORNL/NRC/LTR-99/27, Oak Ridge National Laboratory, Oak Ridge, TN, February, 2000.

75. R. D. Cheverton, et al., *Pressure Vessel Fracture Studies Pertaining to the PWR Thermal-Shock Issue: Experiment TSE-7,* NUREG/CR-4304 (ORNL/TM-6177), Oak Ridge National Laboratory, Oak Ridge, TN, August 1985.

76. F. Li, *Assessment of Pressure Vessel Failure Due to Pressurized Thermal Shock with Consideration of Probabilistic-Deterministic Screening and Uncertainty Analysis,* Ph.D. Dissertation, Center for Technology Risk Studies, University of Maryland, 2001.

77. T. Fang and M. Modarres, "Probabilistic and Deterministic Treatments for Multiple Flaws in Reactor Pressure Vessel Safety Analysis," *Transactions of the 17th International Conference on Structural Mechanics in Reactor Technology (SMiRT 17),* August 17-22, 2003, Prague, Czech Republic.

78. A. L. Hiser, et al., "J-R Curve Characterization of Irradiated Low Upper Shelf Welds," NUREG/CR-3506, U. S. Nuclear Regulatory Commission, 1984.

79. D. E. McCabe, R. K. Nanstad, S. K. Iskander, D. W. Heatherly, and R. L. Swain, *Evaluation of WF-70 Weld Metal From the Midland Unit 1 Reactor Vessel*, USNRC Report NUREG/CR-5736 (ORNL/TM-13748), Oak Ridge National Laboratory, Oak Ridge, TN, November 2000.

80. J. R. Hawthorne, J.R., "Investigations of Irradiation-Anneal-Reirradiation (IAR) Properties Trends of RPV Welds: Phase 2 Final Report," NUREG-CR/5492, U. S. Nuclear Regulatory Commission, 1990.

81. *Standard Test Method for Measurement of Fracture Toughness*, ASTM E 1820-1, Annual Book of ASTM Standards 2002, Section Three, Metals Test Methods and Analytical Procedures, Volume 03.01, American Society for Testing and Materials, West Conshohocken, PA (2002).

82. M. EricksonKirk and M. T. EricksonKirk, "The Relationship Between the Transition and Upper-shelf Fracture Toughness of Ferritic Steels," *Fatigue Fract Engng Mater Struct* **29**, (2006) 1–13.

83. M. T. EricksonKirk, B. R. Bass, T. L. Dickson, C. E. Pugh, T. Santos, and P. T. Williams, "Probabilistic Fracture Mechanics: Models, Parameters, and Uncertainty Treatment Used in FAVOR Version 04.1," U.S. Nuclear Regulatory Commission, NUREG-1807, 2006.

84. M. T. EricksonKirk and M. EricksonKirk, "An Upper-Shelf Fracture Toughness Master Curve for Ferritic Steels," to appear in the *International Journal of Pressure Vessels and Piping*, 2006.

85. E. D. Eason, J. E. Wright, and G. R. Odette, "Improved Embrittlement Correlations for Reactor Pressure Vessel Steels," NUREG/CR-6551, U. S. Nuclear Regulatory Commission, Washington, DC, 1998.

86. M. T. Kirk, C. S. Santos, E.D. Eason, J.E. Wright, and G. R. Odette, "Updated Embrittlement Trend Curve for Reactor Pressure Vessel Steels," Paper No. G01-5, *Transactions of the 17th International Conference on Structural Mechanics in Reactor Technology (SMiRT 17)*, Prague, Czech Republic, August 17-22, 2003.

87. N. Siu, S. Malik, D. Bessette, R. Woods, A. Mosleh, and M. Modarres, "Treating Aleatory and Epistemic Uncertainties in Analyses of Pressurized Thermal Shock," *Proceedings of PSAM 5, International Conference on Probabilistic Safety Assessment and Management*, Osaka, Japan, (2000) 377-382.

88. R. W. Lewis, K. Morgan, H. R. Thomas, and K. N. Seetharamu, *The Finite-Element Method in Heat Transfer Analysis*, John Wiley & Sons, New York, 1996.

89. R. D. Cook, D. S. Malkus, and M. E. Plesha, *Concepts and Applications of Finite Element Analysis, 3rd ed.,* John Wiley & Sons, New York, 1989.

90. H. F. Bückner, "A Novel Principle for the Computation of Stress Intensity Factors," *Z. angew. Math. Mech.* **50**, (1970) 529-546.

91. C. B. Buchalet and W. H. Bamford, "Stress Intensity Factor Solutions for Continuous Surface Flaws in Reactor Pressure Vessels," ASTM STP 590, *Mechanics of Crack Growth*, American Society for Testing and Materials, (1976) 385-402.

92. J. Heliot, R. C. Labbens, and A. Pellissier-Tanon, "Semi-Elliptical Cracks in a Cylinder Subjected to Stress Gradients," ASTM STP 677, *Fracture Mechanics,* ed. C. W. Smith, American Society for Testing and Materials, (1979) 341-364.

93. J. J. McGowan and M. Raymund, "Stress Intensity Factor Solutions for Internal Longitudinal Semi-Elliptical Surface Flaws in a Cylinder Under Arbitrary Loadings," ASTM STP 677, *Fracture Mechanics*, ed. C. W. Smith, American Society for Testing and Materials, (1979) 365-380.

94. I. S. Raju and J. C. Newman, Jr., "Stress Intensity Factor Influence Coefficients for Internal and External Surface Cracks in Cylindrical Vessels," PVP Vol. 58, *Aspects of Fracture Mechanics in Pressure Vessels and Piping*, ASME Pressure Vessels and Piping Conference, (1982) 37-48.

95. S. K. Iskander, R. D. Cheverton, and D. G. Ball, OCA-I, A Code for Calculating the Behavior of Flaws on the Inner Surface of a Pressure Vessel Subjected to Temperature and Pressure Transients, NUREG/CR-2113 (ORNL/NUREG-84), Oak Ridge National Laboratory, Oak Ridge, TN, 1981.

96. R. D. Cheverton and D. G. Ball, *OCA-P, A Deterministic and Probabilistic Fracture Mechanics Code for Application to Pressure Vessels,* NUREG/CR-3618 (ORNL-5991), Oak Ridge National Laboratory, Oak Ridge, TN, May 1984.

97. J. W. Bryson and T. L. Dickson, "Stress-Intensity-Factor Influence Coefficients for Axial and Circumferential Flaws in Reactor Pressure Vessels," PVP Vol. 250, ASME Pressure Vessels and Piping Conference, (1993) 77-88.

98. T. L. Dickson, J. A. Keeney, and J. W. Bryson, "Validation of FAVOR Code Linear-Elastic Fracture Solutions for Finite-Length Flaw Geometries," PVP-Vol. 304, *Fatigue and Fracture Mechanics in Pressure Vessels and Piping*, ASME Pressure Vessels and Piping Conference, (1995) 51-58.

99. J. W. Bryson and T. L. Dickson, *Stress-Intensity-Factor Influence Coefficients for Circumferentially Oriented Semielliptical Inner Surface Flaws in Clad Pressure Vessels*, ORNL/NRC/LTR-94/8, Oak Ridge National Laboratory, Oak Ridge, TN, April, 1994.

100. *ABAQUS Theory Manual, Version 4.8,* Hibbit, Karlson, and Sorenesen, Inc., Providence, RI, 1989.

101. S. Timoshenko, *Theory of Plates and Shells*, McGraw-Hill, New York, 1940.

102. T. L. Dickson, B. R. Bass, and P. T. Williams, "Validation of a Linear-Elastic Fracture Methodology for Postulated Flaws Embedded in the Wall of a Nuclear Reactor Pressure Vessel," PVP-Vol. 403, *Severe Accidents and Other Topics in RPV Design*, American Society of Mechanical Engineering Pressure Vessels and Piping Conference, (2000) 145-151.

103. R.C. Cipolla, et al., Failure Analysis Associates, Computational Method to Perform the Flaw Evaluation Procedure as Specified in the ASME Code, Section XI, Appendix A, EPRI Report NP-1181, September, 1979.

104. *American Society of Mechanical Engineers Boiler and Pressure Vessel Code,* Section XI, Rules for Inservice Inspection of Nuclear Power Plant Components, Appendix A, Analysis of Flaws, Article A-3000, Method for K_I Determination, American Society of Mechanical Engineers, New York, 1998.

105. T. L. Dickson, B. R. Bass, and W. J. McAfee, "The Inclusion of Weld Residual Stress In Fracture Margin Assessments of Embrittled Nuclear Reactor Pressure Vessels," PVP-Vol. 373, *Fatigue, Fracture, and Residual Stresses*, ASME Pressure Vessels and Piping Conference, (1998) 387-395.

106. T.L .Dickson, W.J. McAfee, W.E. Pennell, and P.T. Williams, *Evaluation of Margins in the ASME Rules for Defining the P-T Curve for an RPV*, NUREG/CP-0166, Oak Ridge National Laboratory, Oak Ridge, TN, *Proceedings of the Twenty-Sixth Water Reactor Safety Meeting* **1**, (1999) 47-72.

107. J. A. Keeney, et al., *Preliminary Assessment of the Fracture Behavior of Weld Material in Full-Thickness Clad Beams*, NUREG/CR-6228 (ORNL/TM-12735), Oak Ridge National Laboratory, Oak Ridge, TN, October 1994.

108. M. T. EricksonKirk, B. R. Bass, T. L. Dickson, C. E. Pugh, T. Santos, and P. T. Williams, "Probabilistic Fracture Mechanics: Models, Parameters, and Uncertainty Treatment Used in FAVOR Version 04.1," U.S. Nuclear Regulatory Commission, NUREG-1807, 2006.

109. R. K. Nanstad, J. A. Keeney , and D. E. McCabe, *Preliminary Review of the Bases for the K_{Ic} Curve in the ASME Code*, ORNL/NRC/LTR-93/15, Oak Ridge National Laboratory, Oak Ridge, TN, 1993.

110. *Standard Test Method for Plane-Strain Fracture Toughness of Metallic Materials,* E 399-90, Annual Book of ASTM Standards - Section 3: Metals Test Methods and Analytical Procedures, vol. 03.01, *Metals – Mechanical Testing; Elevated and Low-Temperature Tests; Metallography*, American Society for Testing and Materials, West Conshohocken, PA, 1998.

111. *ASME Boiler and Pressure Vessel Code*, Section III, Article NB-2331, American Society of Mechanical Engineers, New York, NY, (1998).

112. R. K. Nanstad, F. M. Haggag, and D. E. McCabe, *Irradiation Effects on Fracture Toughness of Two High-Copper Submerged-Arc Welds, HSSI Series 5,* USNRC Report NUREG/CR-5913 (ORNL/TM-12156/V1 and V2) Vols. 1 and 2, Oak Ridge National Laboratory, Oak Ridge, TN, October 1992.

113. D. E. McCabe, *A Comparison of Weibull and β_{Ic} Analysis of Transition Range Fracture Toughness Data,* USNRC Report NUREG/CR-5788 (ORNL/TM-11959), Oak Ridge National Laboratory, Oak Ridge, TN, January 1992.

114. T. Iawadate, Y. Tanaka, S. Ono, and J. Watanabe, "An Analysis of Elastic-Plastic Fracture Toughness Behavior for J_{Ic} Measurements in the Transition Region," *Elastic-Plastic Fracture: Second Symposium, Vol. II-Fracture Resistance Curves and Engineering Applications*, (edited by C. F. Shih and J. P. Gudas) ASTM STP 803, (1983) II531-II561.

115. D. E. McCabe, R. K. Nanstad, S. K. Iskander, and R. L. Swain, *Unirradiated Material Properties of Midland Weld WF-70,* USNRC Report NUREG/CR-6249 (ORNL/TM-12777), Oak Ridge National Laboratory, Oak Ridge, TN, October 1994.

116. J. J. McGowan, R. K. Nanstad, and K. R. Thoms, *Characterization of Irradiated Current-Practice Welds and A533 Grade B Class 1 Plate for Nuclear Pressure Vessel Service*, USNRC Report NUREG/CR-4880 (ORNL-6484/V1 and V2), Oak Ridge National Laboratory, Oak Ridge, TN, July 1988.

117. American Society for Testing and Materials, *Standard Test Method for Determining Plane-Strain Crack Arrest Toughness, K_{Ia}, of Ferritic Steels,* E 1221-88, Annual Book of ASTM Standards, Section 3: Metals Test Methods and Analytical Procedures, vol. 03.01, *Metals – Mechanical Testing; Elevated and Low-Temperature Tests; Metallography*, American Society for Testing and Materials, West Conshohocken, PA, 1998.

118. S. K. Iskander, W. R. Corwin, R. K. Nanstad, *Results of Crack-Arrest Tests on Two Irradiated High-Copper Welds,* USNRC Report NUREG/CR-5584 (ORNL/TM-11575), Oak Ridge National Laboratory, Oak Ridge, TN, December 1990.

119. S. K. Iskander, C. A. Baldwin, D. W. Heatherly, D. E. McCabe, I. Remec, and R. L. Swain, *Detailed Results of Testing Unirradiated and Irradiated Crack-Arrest Toughness Specimens from the Low Upper-Shelf Energy, High Copper Weld, WF-70,* NUREG/CR-6621 (ORNL/TM-13764) under preparation.

120. S. K. Iskander, R. K. Nanstad, D. E. McCabe, and R. L. Swain, "Effects of Irradiation on Crack-Arrest Toughness of a Low Upper-Shelf Energy, High-Copper Weld," *Effects of Radiation on Materials: 19th International Symposium, ASTM STP 1366*, M. L. Hamilton, A. S. Kumar, S. T. Rosinski, and M. L. Grossbeck, eds., American Society for Testing and Materials, to be published.

121. E. J. Ripling and P. B. Crosley, "Strain Rate and Crack Arrest Studies," *HSST 5th Annual Information Meeting*, Paper No. 9, 1971.

122. E. J. Ripling and P. B. Crosley, "Crack Arrest Studies," *HSST 6th Annual Information Meeting*, Paper No. 10, 1972.

123. R. D. Cheverton, D. G. Ball, S. E. Bolt, S. K. Iskander, and R. K. Nanstad, *Pressure Vessel Fracture Studies Pertaining to the PWR Thermal-Shock Issue: Experiments TSE-5, TSE-5A, and TSE-6,* NUREG/CR-4249 (ORNL-6163), Oak Ridge National Laboratory, Oak Ridge, TN, June 1985.

124. "Standard Test Method for Determination of Reference Temperature, T_0, for Ferritic Steels in the Transition Range," E 1921-97, Annual Book of ASTM Standards Section 3: Metals Test Methods and Analytical Procedures, vol. 03.01, *Metals – Mechanical Testing; Elevated and Low-Temperature Tests; Metallography*, American Society for Testing and Materials, West Conshohocken, PA, 1998.

125. M. Kirk, R. Lott, W. L. Server, R. Hardies, and S. Rosinski, "Bias and Precision of T_0 Values Determined Using ASTM Standard E 1921-97 for Nuclear Reactor Pressure Vessel Steels," *Effects of Radiation on Materials: 19th International Symposium, ASTM STP 1366,* M. L. Hamilton, A. S. Kumar, S. T. Rosinski, and M. L. Grossbeck, Eds., American Society for Testing and Materials, West Conshococken, PA, (2000) 143-161.

126. K. Wallin, "Master Curve Based Correlation Between Static Initiation Toughness, K_{Ic}, and Crack Arrest Toughness, K_{Ia}," presented at *24th MPA Seminar*, Stuttgart, Germany, October 8 and 9, 1998.

127. K. Wallin, "Application of the Master Curve Method to Crack Initiation and Crack Arrest," *Fracture, Fatigue, and Weld Residual Stress*, PVP Vol. 393, ASME Pressure Vessels and Piping Conference, Boston, MA, August 1-5, 1999.

128. *Reactor Vessel Integrity Database (RVID), User's Manual,* Version 1.1, U. S. Nuclear Regulatory Commission, July 1995.

129. *Reactor Vessel Integrity Database (RVID)*, Version 2.1.1, U. S. Nuclear Regulatory Commission July 6, 2000.

Appendix A – Background and Antecedents of FAVOR, v04.1

An important element of the PTS plant-specific analysis is the calculation of the conditional probability of failure of the vessel by performing probabilistic fracture mechanics (PFM) analyses. The term *conditional* refers here to two assumed preconditions: (1) the specific PTS event under study has in fact occurred, and (2) the postulated flaws do exist on the surface or embedded within the RPV wall. Combined with an estimate of the frequency of occurrence for the event, a predicted frequency of vessel failure can then be calculated. OCA-P [1] and VISA-II [2] are PTS PFM computer programs, independently developed at Oak Ridge National Laboratory (ORNL) and Pacific Northwest National Laboratory (PNNL), respectively, in the 1980s with NRC funding, that are currently referenced in Regulatory Guide 1.154 as acceptable codes for performing plant-specific analyses.

There have also been other proprietary and public-domain PTS PFM codes independently developed in the US and internationally by reactor vendors and research laboratories. The development of the OCA-P code [1] (and its deterministic predecessors, OCA-I [3], and OCA-II [4]) and the VISA II code [2] was preceded by two earlier probabilistic computer programs developed by the NRC, specifically OCTAVIA [5] (**O**perationally **C**aused **T**ransients **a**nd **V**essel **I**ntegrity **A**nalysis) and a second unnamed code developed by Gamble and Strosnider [6].

OCTAVIA [5] was developed in the mid-1970s to calculate the probability of RPV failure from operationally caused pressure transients which can occur in a PWR vessel at low operating temperatures. OCTAVIA computed the pressure at which the vessel would fail for different-sized flaws existing in the beltline region, where only axially oriented flaws in the vessel beltline were considered. The probability of vessel failure was then calculated as the product of two factors: the probability that the maximum-sized flaw in the beltline is of a given size, and the probability that the transient would occur and would have a pressure exceeding the vessel failure pressure associated with the flaw size. The probabilities of vessel failure were summed over the various sizes to obtain the total vessel failure probability.

The code developed by Gamble and Strosnider [6] calculates the probability of flaw-induced failure in the vessel beltline region using mathematical relationships based on linear-elastic fracture mechanics to model variable interaction and to estimate a failure rate. The RPV failure criterion was based on a comparison of the driving-force stress-intensity factor, K_I, with the static initiation toughness, K_{Ic}, of the material. Monte Carlo methods were used to simulate independently each of the several variables and model their interaction to obtain values of K_I and K_{Ic} to predict the probabilities of vessel failure. Near the end of this study, an *importance-*

sampling scheme was developed and incorporated into the computer code to increase the code's efficiency for performing calculations in the transition-temperature region and to allow greater accuracy for analyzing conditions associated with low-failure probabilities (see Appendix B of ref. [6]).

An early version of the VISA code [7] was used in the NRC staff evaluation of PTS as described in SECY-82-465 [8]. VISA is a simulation model, which means that the failure probability is assessed by performing a large number of deterministic evaluations with random variables selected for various parameters. The user can specify the thermal transient with either a polynomial representation or an exponential decay model, and the pressure transient can be specified with a polynomial function. The deterministic analysis in VISA assumes linear-elastic material behavior, implying that the total maximum stresses are less than the yield strength of the material. This assumption of linear-elastic deformation response allows stress components to be added through linear superposition, and the principles of linear-elastic fracture mechanics (LEFM) can be applied. For rapid thermal transients, high stresses (potentially above the yield strength of the cladding) can occur locally at the inside surface of the vessel wall; however, acceptable stress distributions can still be obtained over the remaining section if the overstressed region is relatively thin. Stress intensity factors are calculated from influence coefficients developed by Heliot, Labbens, and Pellissier-Tanon [9, 10].

Examples of internationally developed PFM/PTS codes include PASCAL (**P**FM **A**nalysis of **S**tructural **C**omponents in **A**ging **L**WR) [11-13], OPERA [14], and PARISH (**P**robabilistic **A**ssessment of **R**eactor **I**ntegrity under pressurized thermal **SH**ock) [15]. In addition, other PFM codes such as PRAISE [16] and STAR6 [17] have been developed to calculate failure probabilities considering the aged condition of RCW piping systems allowing for factors such as fatigue crack growth, stress corrosion crack growth, and changes in mechanical properties.

The above codes perform PFM/PTS analyses using Monte Carlo techniques to estimate the increase in failure probability as the vessel accumulates radiation damage over its operating life. The results of such analyses, when compared with the limit of acceptable failure probability, provide an estimate of the residual life of a reactor pressure vessel. Also results of such analyses can be used to evaluate the potential benefits of plant-specific mitigating actions designed to reduce the probability of reactor vessel failure, thus potentially extending the operating life of the vessel [18].

Previous efforts at obtaining the same probabilistic solutions to a specified PTS problem using different PFM codes have met with varying degrees of success [19-21]. Experience with the

application of OCA-P, VISA-II, and other PFM codes as well as advancements in the science of probabilistic risk assessment (PRA) over the past 15 years have provided insights into areas where the PTS PFM methodology could be improved. The FAVOR computer code was initially developed at ORNL in the early 1990s [22] (see Fig. A1) in an effort to combine the best attributes of OCA-P and VISA-II. In the ensuing years, the NRC-funded FAVOR code has continued its advancement with the goal of providing a computational platform for incorporating additional capabilities and new developments in relevant fracture-related disciplines, as illustrated in Fig. A1.

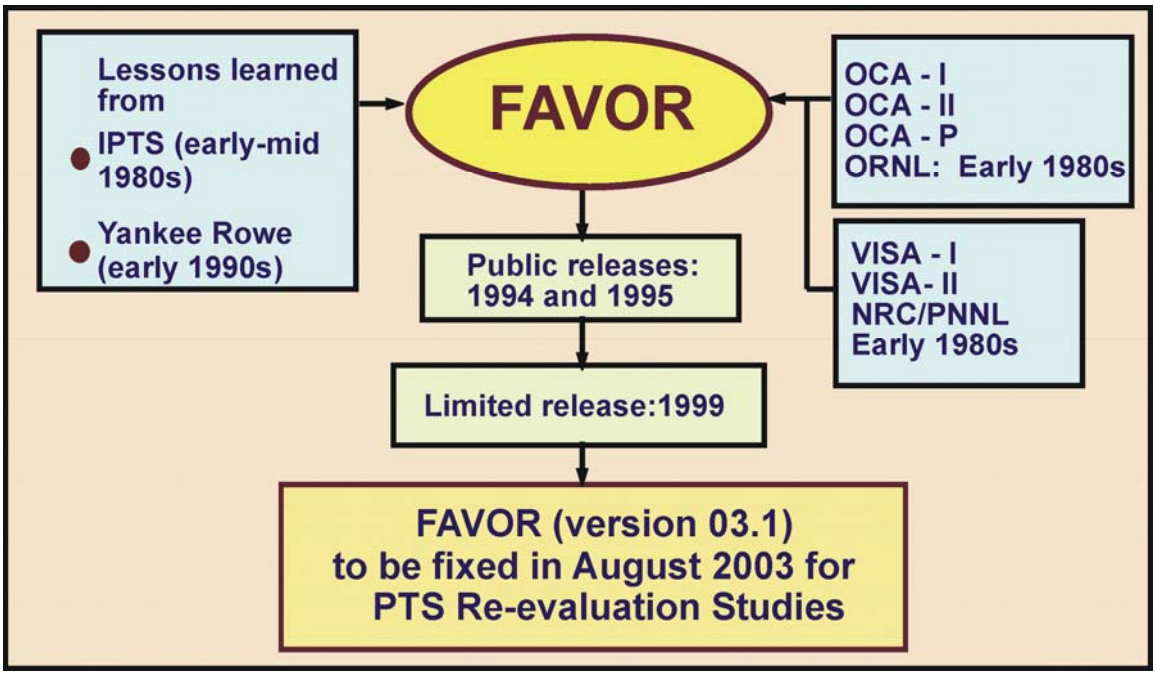

Fig. A1. Depiction of the development history of the FAVOR code

References to Appendix A

1. R. D. Cheverton and D. G. Ball, *OCA-P, A Deterministic and Probabilistic Fracture Mechanics Code for Application to Pressure Vessels,* NUREG/CR-3618 (ORNL-5991), Oak Ridge National Laboratory, Oak Ridge, TN, May 1984.

2. F. A. Simonen, et al., *VISA-II – A Computer Code for Predicting the Probability of Reactor Pressure Vessel Failure*, NUREG/CR-4486 (PNL-5775), Pacific Northwest Laboratory, Richland, Washington, March 1986.

3. S. K. Iskander, R. D. Cheverton, and D. G. Ball, OCA-I, A Code for Calculating the Behavior of Flaws on the Inner Surface of a Pressure Vessel Subjected to Temperature and Pressure Transients, NUREG/CR-2113 (ORNL/NUREG-84), Oak Ridge National Laboratory, Oak Ridge, TN, 1981.

4. D. G. Ball, R. D. Cheverton, J. B. Drake, and S. K. Iskander, *OCA-II, A Code for Calculating the Behavior of 2-D and 3-D Surface Flaws in a Pressure Vessel Subjected to Temperature and Pressure Transients*, NUREG/CR-3491 (ORNL-5934), Oak Ridge National Laboratory, Oak Ridge, TN, 1983.

5. W. E. Vesely, E. K. Lynn, and F. F. Goldberg, *The Octavia Computer Code: PWR Reactor Pressure Vessel Failure Probabilities Due to Operationally Caused Pressure Transients*, NUREG-0258, U. S. Nuclear Regulatory Commission, Washington, D.C., 1978.

6. R. M. Gamble and J. Strosnider, Jr., *An Assessment of the Failure Rate for the Beltline Region of PWR Pressure Vessels During Normal Operation and Certain Transient Conditions*, NUREG-0778, U. S. Nuclear Regulatory Commission, Washington, D.C., 1981.

7. D. L. Stevens, F. A. Simonen, J. Strosnider, Jr., R. W. Klecker, D. W. Engel, and K. I. Johnson, *VISA – A Computer Code for Predicting the Probability of Reactor Pressure Vessel Failure*, NUREG/CR-3384, (PNL-4774), Pacific Northwest Laboratory, Richland, Washington, 1983.

8. Policy Issue from J. W. Dircks to NRC Commissioners, *Enclosure A: NRC Staff Evaluation of Pressurized Thermal Shock, November 1982*, SECY-82-465, November 23, 1982, Division of Nuclear Reactor Regulation, U.S. Nuclear Regulatory Commission, Washington, D.C.

9. R. Labbens, A. Pellissier-Tanon, and J. Heliot, "Practical Method for Calculating Stress-Intensity Factors Through Weight Functions," ASTM STP-590, *Mechanics of Crack Growth*, American Society for Testing and Materials, (1976) 368-384.

10. J. Heliot, R. C. Labbens, and A. Pellissier-Tanon, "Semi-Elliptical Cracks in the Mendional Plane of a Cylinder Subjected to Stress Gradients, Calculation of Stress Intensity Factors by the Boundary Integral Equations Method," *XIth National Symposium on Fracture Mechanics*, Blacksburg, VA, 1978.

11. G. Yagawa, Y. Kanto, S. Yoshimura, H. Machida, and K. Shibata, "Probabilistic Fracture Mechanics Analysis of Nuclear Structural Components: A Review of Recent Japanese Activities," *Nuclear Engineering and Design* **207**, (2001) 269-286.

12. K. Shibata, D. Kato, and Y. Li, "Development of a PFM Code for Evaluating Reliability of Pressure Components Subject to Transient Loading," *Nuclear Engineering and Design* **208**, (2001) 1-13.

13. Y. Li, D. Kato, K. Shibata, and K. Onizawa, "Improvements to a Probabilistic Fracture Mechanics Code for Evaluating the Integrity of an RPV Under Transient Loading," *International Journal of Pressure Vessels and Piping* **78**, (2001) 271-282.

14. M. Persoz, S. Hugonnard-Bruyere, et al., "Deterministic and Probabilistic Assessment of the Reactor Pressure Vessel Structural Integrity with a User-Friendly Software," PVP-Vol. 403, *presented at the ASME Pressure Vessels and Piping Conference*, (2000) 137-144.

15. B. K. Dutta, H. S. Kushwaha, and V. V. Raj, "Probabilistic Assessment of Reactor Pressure Vessel Integrity Under Pressurised Thermal Shock," *International Journal of Pressure Vessels and Piping* **76**, (1999) 445-453.

16. D. O. Harris, E. Y. Lim, et al., "Probability of Pipe Fracture in the Primary Coolant Loop of a PWR Plant," NUREG/CR-2189, 1981.

17. R. Wilson and R. A. Ainsworth, "A Probabilistic Fracture Mechanics Assessment Procedure," SMiRT 11, vol. G, (1991) 325-330.

18. T. L. Dickson and F. A. Simonen, "The Application of Probabilistic Fracture Analysis to Residual Life Evaluation of Embrittled Reactor Vessels," AD-Vol. 28, Reliability Technology, *American Society of Mechanical Engineers,* (1992) 43-55.

19. B. A. Bishop, T. L. Dickson, and F. A. Simonen, *Benchmarking of Probabilistic Fracture Mechanics Analyses of Reactor Vessels Subjected to Pressurized Thermal Shock (PTS) Loading,* Research Project 2975-5, Final Report, February 1993.

20. T. L. Dickson and R. D. Cheverton, *Review of Reactor Pressure Vessel Evaluation Report for Yankee Rowe Nuclear Power Station (YAEC No. 1735), Appendix D,* NUREG/CR-5799 (ORNL/TM-11982), Oak Ridge National Laboratory, Oak Ridge, TN, March 1992.

21. B. R. Bass, et al., *International Comparative Assessment Study of Pressurized Thermal Shock in Reactor Pressure Vessels,* NUREG/CR-6651 (ORNL/TM-1999/231), Oak Ridge National Laboratory, Oak Ridge, TN, December 1999.

22. T. L. Dickson, *FAVOR: A Fracture Analysis Code for Nuclear Reactor Pressure Vessels, Release 9401*, ORNL/NRC/LTR/94/1, Oak Ridge National Laboratory, Oak Ridge, TN, 1994.

Appendix B – Stress-Intensity Factor Influence Coefficients

Table B1. Influence Coefficients for Inside Axial and Circumferential Semi-elliptical Surface Flaws: *R* / *t* =10 and *a/t*=0.01
Table B2. Influence Coefficients for Inside Axial and Circumferential Semi-elliptical Surface Flaws: *R* / *t* =10 and *a/t*=0.0184
Table B3. Influence Coefficients for Inside Axial and Circumferential Semi-elliptical Surface Flaws: *R* / *t* =10 and *a/t*=0.05
Table B4. Influence Coefficients for Inside Axial and Circumferential Semi-elliptical Surface Flaws: *R* / *t* =10 and *a/t*=0.075
Table B5. Influence Coefficients for Inside Axial and Circumferential Semi-elliptical Surface Flaws: *R* / *t* =10 and *a/t*=0.1
Table B6. Influence Coefficients for Inside Axial and Circumferential Semi-elliptical Surface Flaws: *R* / *t* =10 and *a/t*=0.2
Table B7. Influence Coefficients for Inside Axial and Circumferential Semi-elliptical Surface Flaws: *R* / *t* =10 and *a/t*=0.3
Table B8. Influence Coefficients for Inside Axial Semi-elliptical Surface Flaws: *R* / *t* =10 and *a/t*=0.5
Table B9. Influence Coefficients for Inside Circumferential Semi-elliptical Surface Flaws: *R* / *t* =10 and *a/t*=0.5
Table B10. Influence Coefficients for Inside Axial Infinite-Length Surface Flaws: *R* / *t* =10
Table B11. Influence Coefficients for Inside Circumferential 360-Degree Surface Flaws: *R* / *t* =10

Table B1. Influence Coefficients for Inside Axial and Circumferential Semi-elliptical Surface Flaws: R / t = 10 and a / t = 0.01

Aspect Ratio	Elliptic Angle (deg)	K_0 Uniform	K_1 Linear	K_2 Quadratic	K_3 Cubic	K_0 t_{cl}=0.25 in.	K_1 t_{cl}=0.25 in.	K_0 t_{cl}=0.156 in.	K_1 t_{cl}=0.156 in.
2:1	0.00	0.764	0.153	0.061	0.034	0.764	0.153	0.764	0.153
	2.37	0.754	0.165	0.062	0.032	0.754	0.165	0.754	0.165
	16.60	0.690	0.192	0.079	0.040	0.690	0.192	0.690	0.192
	30.80	0.669	0.264	0.127	0.069	0.669	0.264	0.669	0.264
	45.00	0.660	0.335	0.196	0.124	0.660	0.335	0.660	0.335
	59.20	0.653	0.393	0.269	0.198	0.653	0.393	0.653	0.393
	73.40	0.651	0.434	0.329	0.268	0.651	0.434	0.651	0.434
	87.60	0.649	0.463	0.366	0.310	0.649	0.463	0.649	0.463
	90.00	0.649	0.468	0.372	0.317	0.649	0.468	0.649	0.468
6:1	0.00	0.670	0.134	0.048	0.024	0.670	0.134	0.670	0.134
	2.37	0.667	0.134	0.043	0.019	0.667	0.134	0.667	0.134
	16.60	0.654	0.170	0.055	0.009	0.654	0.170	0.654	0.170
	30.80	0.741	0.269	0.109	0.029	0.741	0.269	0.741	0.269
	45.00	0.827	0.381	0.199	0.100	0.827	0.381	0.827	0.381
	59.20	0.893	0.481	0.302	0.197	0.893	0.481	0.893	0.481
	73.40	0.938	0.559	0.389	0.290	0.938	0.559	0.938	0.559
	87.60	0.970	0.594	0.435	0.341	0.970	0.594	0.970	0.594
	90.00	0.975	0.601	0.443	0.350	0.975	0.601	0.975	0.601
10:1	0.00	0.515	0.090	0.020	0.006	0.515	0.090	0.515	0.090
	2.37	0.529	0.094	0.010	0.005	0.529	0.094	0.529	0.094
	16.60	0.610	0.146	0.033	0.005	0.610	0.146	0.610	0.146
	30.80	0.762	0.258	0.060	0.019	0.762	0.258	0.762	0.258
	45.00	0.889	0.389	0.171	0.066	0.889	0.389	0.889	0.389
	59.20	0.979	0.507	0.290	0.136	0.979	0.507	0.979	0.507
	73.40	1.033	0.593	0.389	0.249	1.033	0.593	1.033	0.593
	87.60	1.064	0.635	0.439	0.307	1.064	0.635	1.064	0.635
	90.00	1.069	0.642	0.447	0.316	1.069	0.642	1.069	0.642

Table B2. Influence Coefficients for Inside Axial and Circumferential Semi-elliptical Surface Flaws: R / t = 10 and a / t = 0.0184

Aspect Ratio	Elliptic Angle (deg)	K_0 Uniform	K_1 Linear	K_2 Quadratic	K_3 Cubic	K_0 t_{cl}=0.25 in.	K_1 t_{cl}=0.25 in.	K_0 t_{cl}=0.156 in.	K_1 t_{cl}=0.156 in.
2:1	0.00	0.777	0.155	0.061	0.034	0.777	0.155	0.777	0.155
	2.37	0.767	0.167	0.062	0.032	0.767	0.167	0.767	0.167
	16.60	0.700	0.194	0.079	0.040	0.700	0.194	0.700	0.194
	30.80	0.677	0.266	0.127	0.069	0.677	0.266	0.677	0.266
	45.00	0.667	0.338	0.196	0.125	0.667	0.338	0.667	0.338
	59.20	0.660	0.397	0.270	0.198	0.660	0.397	0.660	0.397
	73.40	0.657	0.438	0.330	0.267	0.657	0.438	0.657	0.438
	87.60	0.654	0.467	0.366	0.310	0.654	0.467	0.654	0.467
	90.00	0.653	0.472	0.373	0.317	0.653	0.472	0.653	0.472
6:1	0.00	0.653	0.127	0.043	0.021	0.653	0.127	0.653	0.127
	2.37	0.654	0.128	0.038	0.016	0.654	0.128	0.654	0.128
	16.60	0.654	0.168	0.045	0.021	0.654	0.168	0.654	0.168
	30.80	0.758	0.271	0.099	0.026	0.758	0.271	0.758	0.271
	45.00	0.852	0.387	0.192	0.085	0.852	0.387	0.852	0.387
	59.20	0.920	0.492	0.298	0.187	0.920	0.492	0.920	0.492
	73.40	0.963	0.569	0.387	0.283	0.963	0.569	0.963	0.569
	87.60	0.994	0.609	0.434	0.335	0.994	0.609	0.994	0.609
	90.00	0.999	0.616	0.442	0.344	0.999	0.616	0.999	0.616
10:1	0.00	0.525	0.092	0.019	0.007	0.525	0.092	0.525	0.092
	2.37	0.538	0.096	0.009	0.005	0.538	0.096	0.538	0.096
	16.60	0.621	0.149	0.039	0.005	0.621	0.149	0.621	0.149
	30.80	0.777	0.262	0.050	0.022	0.777	0.262	0.777	0.262
	45.00	0.899	0.392	0.164	0.075	0.899	0.392	0.899	0.392
	59.20	0.982	0.509	0.283	0.127	0.982	0.509	0.982	0.509
	73.40	1.033	0.595	0.383	0.242	1.033	0.595	1.033	0.595
	87.60	1.063	0.637	0.433	0.300	1.063	0.637	1.063	0.637
	90.00	1.068	0.644	0.441	0.310	1.068	0.644	1.068	0.644

Table B3. Influence Coefficients for Inside Axial and Circumferential Semi-elliptical Surface Flaws: R / t = 10 and a / t = 0.05

Aspect Ratio	Elliptic Angle (deg)	K_0 Uniform	K_1 Linear	K_2 Quadratic	K_3 Cubic	K_0 t_{cl}=0.25 in.	K_1 t_{cl}=0.25 in.	K_0 t_{cl}=0.156 in.	K_1 t_{cl}=0.156 in.
2:1	0.00	0.779	0.155	0.061	0.034	0.708	0.184	0.636	0.205
	2.37	0.769	0.166	0.062	0.031	0.701	0.194	0.624	0.213
	16.60	0.701	0.194	0.079	0.040	0.659	0.264	0.509	0.232
	30.80	0.678	0.267	0.128	0.070	0.581	0.340	0.246	0.124
	45.00	0.668	0.339	0.199	0.126	0.326	0.188	0.159	0.083
	59.20	0.661	0.398	0.273	0.201	0.233	0.127	0.128	0.067
	73.40	0.658	0.440	0.333	0.270	0.204	0.110	0.115	0.060
	87.60	0.656	0.469	0.370	0.313	0.185	0.099	0.106	0.055
	90.00	0.655	0.474	0.377	0.320	0.182	0.097	0.104	0.054
6:1	0.00	0.655	0.128	0.043	0.021	0.631	0.151	0.576	0.176
	2.37	0.655	0.128	0.039	0.016	0.628	0.156	0.570	0.177
	16.60	0.655	0.167	0.049	0.019	0.646	0.221	0.537	0.213
	30.80	0.758	0.270	0.104	0.013	0.688	0.357	0.340	0.167
	45.00	0.851	0.386	0.197	0.091	0.494	0.263	0.271	0.138
	59.20	0.918	0.492	0.305	0.193	0.422	0.217	0.253	0.128
	73.40	0.962	0.569	0.395	0.290	0.396	0.201	0.241	0.121
	87.60	0.992	0.609	0.443	0.342	0.374	0.189	0.231	0.115
	90.00	0.997	0.616	0.450	0.351	0.370	0.186	0.229	0.115
10:1	0.00	0.523	0.092	0.021	0.005	0.533	0.119	0.496	0.149
	2.37	0.537	0.095	0.011	0.015	0.543	0.121	0.504	0.146
	16.60	0.622	0.147	0.033	0.050	0.631	0.149	0.547	0.199
	30.80	0.778	0.261	0.061	0.080	0.718	0.348	0.376	0.182
	45.00	0.898	0.391	0.171	0.065	0.550	0.286	0.349	0.156
	59.20	0.981	0.509	0.292	0.138	0.474	0.241	0.287	0.144
	73.40	1.034	0.596	0.392	0.252	0.444	0.224	0.273	0.136
	87.60	1.063	0.638	0.442	0.310	0.418	0.221	0.260	0.130
	90.00	1.068	0.645	0.450	0.320	0.414	0.221	0.257	0.128

Table B4. Influence Coefficients for Inside Axial and Circumferential Semi-elliptical Surface Flaws: $R / t = 10$ and $a / t = 0.075$

Aspect Ratio	Elliptic Angle (deg)	K_0 Uniform	K_1 Linear	K_2 Quadratic	K_3 Cubic	K_0 t_{cl}=0.25 in.	K_1 t_{cl}=0.25 in.	K_0 t_{cl}=0.156 in.	K_1 t_{cl}=0.156 in.
2:1	0.00	0.740	0.128	0.045	0.023	0.650	0.197	0.572	0.210
	7.03	0.737	0.147	0.055	0.028	0.629	0.220	0.529	0.217
	14.20	0.721	0.179	0.067	0.033	0.593	0.271	0.400	0.177
	35.90	0.671	0.298	0.155	0.086	0.219	0.120	0.118	0.060
	48.70	0.661	0.355	0.220	0.143	0.161	0.085	0.094	0.048
	61.50	0.656	0.404	0.285	0.212	0.137	0.071	0.081	0.042
	74.30	0.654	0.439	0.336	0.273	0.125	0.065	0.075	0.038
	87.00	0.651	0.468	0.372	0.313	0.114	0.065	0.068	0.035
	90.00	0.651	0.475	0.381	0.322	0.111	0.065	0.067	0.034
6:1	0.00	0.650	0.098	0.029	0.013	0.591	0.170	0.527	0.188
	2.37	0.635	0.104	0.031	0.013	0.571	0.180	0.495	0.179
	16.60	0.672	0.140	0.040	0.014	0.590	0.243	0.441	0.187
	30.80	0.786	0.309	0.139	0.048	0.334	0.171	0.195	0.098
	45.00	0.862	0.410	0.229	0.125	0.294	0.149	0.180	0.090
	59.20	0.918	0.501	0.326	0.219	0.275	0.138	0.170	0.085
	73.40	0.952	0.566	0.404	0.303	0.265	0.133	0.164	0.082
	87.60	0.980	0.602	0.446	0.351	0.265	0.133	0.159	0.080
	90.00	0.987	0.611	0.456	0.362	0.265	0.132	0.157	0.079
10:1	0.00	0.547	0.073	0.016	0.006	0.514	0.148	0.469	0.171
	2.37	0.551	0.074	0.016	0.003	0.514	0.145	0.458	0.131
	16.60	0.636	0.113	0.023	0.009	0.583	0.220	0.465	0.173
	30.80	0.812	0.303	0.124	0.018	0.375	0.189	0.223	0.112
	45.00	0.914	0.419	0.225	0.111	0.335	0.168	0.206	0.103
	59.20	0.982	0.522	0.332	0.216	0.310	0.156	0.193	0.096
	73.40	1.022	0.593	0.416	0.307	0.298	0.149	0.185	0.093
	87.60	1.048	0.631	0.461	0.356	0.295	0.147	0.185	0.092
	90.00	1.055	0.639	0.471	0.368	0.295	0.147	0.184	0.092

Table B5. Influence Coefficients for Inside Axial and Circumferential Semi-elliptical Surface Flaws: R / t = 10 and a / t = 0.1

Aspect Ratio	Elliptic Angle (deg)	K_0 Uniform	K_1 Linear	K_2 Quadratic	K_3 Cubic	K_0 t_{cl}=0.25 in.	K_1 t_{cl}=0.25 in.	K_0 t_{cl}=0.156 in.	K_1 t_{cl}=0.156 in.
2:1	0.00	0.729	0.124	0.044	0.023	0.596	0.195	0.519	0.205
	5.27	0.741	0.139	0.053	0.027	0.582	0.208	0.483	0.198
	17.10	0.722	0.230	0.096	0.048	0.366	0.213	0.168	0.086
	31.10	0.676	0.273	0.133	0.072	0.176	0.097	0.095	0.048
	45.10	0.664	0.339	0.201	0.127	0.122	0.064	0.072	0.037
	59.10	0.658	0.396	0.274	0.200	0.101	0.052	0.061	0.031
	73.10	0.655	0.436	0.333	0.268	0.091	0.047	0.056	0.028
	87.00	0.653	0.470	0.373	0.313	0.082	0.047	0.050	0.025
	90.00	0.652	0.477	0.382	0.323	0.080	0.047	0.049	0.025
6:1	0.00	0.641	0.094	0.029	0.014	0.550	0.175	0.485	0.188
	2.37	0.630	0.098	0.031	0.015	0.532	0.176	0.454	0.168
	16.60	0.701	0.196	0.067	0.015	0.427	0.232	0.211	0.108
	30.80	0.756	0.273	0.115	0.039	0.258	0.131	0.152	0.077
	45.00	0.848	0.385	0.207	0.109	0.224	0.112	0.138	0.069
	59.20	0.915	0.489	0.312	0.207	0.208	0.104	0.129	0.065
	73.40	0.958	0.565	0.402	0.302	0.200	0.100	0.125	0.062
	87.60	0.989	0.607	0.450	0.356	0.200	0.100	0.120	0.060
	90.00	0.996	0.616	0.461	0.367	0.200	0.100	0.119	0.060
10:1	0.00	0.543	0.067	0.016	0.007	0.490	0.148	0.443	0.168
	2.37	0.536	0.069	0.016	0.006	0.479	0.144	0.421	0.138
	16.60	0.670	0.175	0.047	0.027	0.443	0.220	0.229	0.117
	30.80	0.778	0.269	0.102	0.030	0.291	0.143	0.176	0.088
	45.00	0.897	0.395	0.202	0.089	0.256	0.128	0.159	0.080
	59.20	0.979	0.512	0.318	0.199	0.236	0.118	0.147	0.074
	73.40	1.029	0.597	0.416	0.302	0.226	0.113	0.141	0.071
	87.60	1.060	0.640	0.466	0.358	0.224	0.111	0.140	0.070
	90.00	1.066	0.649	0.477	0.370	0.223	0.111	0.140	0.070

Table B6. Influence Coefficients for Inside Axial and Circumferential Semi-elliptical Surface Flaws: R / t = 10 and a / t = 0.2

Aspect Ratio	Elliptic Angle (deg)	K_0 Uniform	K_1 Linear	K_2 Quadratic	K_3 Cubic	K_0 t_{cl}=0.25 in.	K_1 t_{cl}=0.25 in.	K_0 t_{cl}=0.156 in.	K_1 t_{cl}=0.156 in.
2:1	0.00	0.692	0.127	0.046	0.024	0.457	0.173	0.393	0.178
	19.80	0.695	0.214	0.089	0.044	0.155	0.080	0.071	0.031
	31.10	0.679	0.273	0.133	0.073	0.090	0.050	0.048	0.023
	42.50	0.671	0.332	0.192	0.120	0.061	0.031	0.038	0.019
	53.80	0.665	0.383	0.255	0.182	0.052	0.026	0.032	0.016
	65.20	0.660	0.423	0.312	0.245	0.047	0.023	0.029	0.014
	76.50	0.658	0.450	0.354	0.296	0.044	0.022	0.027	0.014
	87.90	0.656	0.475	0.384	0.329	0.041	0.021	0.025	0.013
	90.00	0.656	0.479	0.389	0.335	0.040	0.020	0.025	0.013
6:1	0.00	0.617	0.101	0.034	0.017	0.434	0.163	0.377	0.171
	2.37	0.699	0.194	0.066	0.019	0.180	0.090	0.093	0.043
	16.60	0.781	0.280	0.118	0.045	0.127	0.063	0.079	0.039
	30.80	0.856	0.375	0.195	0.101	0.116	0.058	0.072	0.036
	45.00	0.915	0.464	0.283	0.180	0.110	0.055	0.069	0.034
	59.20	0.958	0.538	0.366	0.265	0.106	0.053	0.066	0.033
	73.40	0.986	0.590	0.430	0.336	0.104	0.052	0.065	0.032
	87.60	1.010	0.619	0.464	0.373	0.102	0.051	0.064	0.032
	90.00	1.020	0.624	0.470	0.380	0.101	0.051	0.063	0.032
10:1	0.00	0.525	0.077	0.022	0.009	0.402	0.149	0.355	0.160
	2.37	0.694	0.183	0.050	0.025	0.200	0.100	0.106	0.050
	16.60	0.815	0.280	0.107	0.011	0.149	0.073	0.093	0.046
	30.80	0.915	0.387	0.190	0.083	0.137	0.068	0.085	0.043
	45.00	0.991	0.488	0.287	0.170	0.130	0.065	0.081	0.040
	59.20	1.045	0.572	0.379	0.263	0.125	0.062	0.078	0.039
	73.40	1.080	0.631	0.449	0.340	0.122	0.061	0.077	0.038
	87.60	1.103	0.660	0.483	0.378	0.120	0.060	0.075	0.037
	90.00	1.107	0.666	0.490	0.385	0.119	0.060	0.075	0.037

Table B7. Influence Coefficients for Inside Axial and Circumferential Semi-elliptical Surface Flaws: R / t = 10 and a / t = 0.3

Aspect Ratio	Elliptic Angle (deg)	K_0 Uniform	K_1 Linear	K_2 Quadratic	K_3 Cubic	K_0 t_{cl}=0.25 in.	K_1 t_{cl}=0.25 in.	K_0 t_{cl}=0.156 in.	K_1 t_{cl}=0.156 in.
2:1	0.00	0.723	0.127	0.048	0.026	0.404	0.188	0.334	0.176
	17.40	0.708	0.203	0.083	0.042	0.102	0.049	0.056	0.025
	29.10	0.690	0.264	0.126	0.068	0.058	0.028	0.034	0.016
	40.90	0.680	0.326	0.185	0.114	0.043	0.021	0.026	0.013
	52.60	0.673	0.381	0.251	0.177	0.036	0.018	0.022	0.011
	64.40	0.668	0.423	0.310	0.242	0.032	0.016	0.020	0.010
	76.10	0.665	0.452	0.355	0.297	0.030	0.015	0.018	0.009
	87.90	0.662	0.478	0.385	0.331	0.028	0.014	0.017	0.009
	90.00	0.662	0.482	0.391	0.337	0.027	0.014	0.017	0.009
6:1	0.00	0.665	0.112	0.041	0.022	0.380	0.181	0.315	0.167
	2.37	0.715	0.190	0.068	0.027	0.117	0.054	0.069	0.032
	16.60	0.804	0.277	0.118	0.051	0.093	0.045	0.057	0.028
	30.80	0.886	0.376	0.194	0.104	0.085	0.042	0.053	0.026
	45.00	0.951	0.470	0.284	0.182	0.081	0.040	0.050	0.025
	59.20	0.998	0.549	0.372	0.270	0.078	0.039	0.049	0.024
	73.40	1.028	0.605	0.439	0.345	0.077	0.038	0.048	0.024
	87.60	1.053	0.635	0.475	0.384	0.075	0.038	0.047	0.024
	90.00	1.058	0.640	0.481	0.391	0.075	0.037	0.047	0.023
10:1	0.00	0.562	0.085	0.029	0.014	0.344	0.168	0.290	0.153
	2.37	0.707	0.176	0.052	0.016	0.128	0.059	0.078	0.037
	16.60	0.848	0.276	0.104	0.016	0.110	0.054	0.068	0.034
	30.80	0.962	0.389	0.188	0.082	0.102	0.051	0.064	0.032
	45.00	1.051	0.498	0.288	0.169	0.098	0.049	0.062	0.031
	59.20	1.115	0.590	0.385	0.265	0.096	0.048	0.060	0.030
	73.40	1.157	0.653	0.460	0.346	0.095	0.047	0.060	0.030
	87.60	1.183	0.685	0.496	0.387	0.094	0.047	0.059	0.029
	90.00	1.187	0.691	0.503	0.394	0.094	0.047	0.059	0.029

Table B8. Influence Coefficients for Inside Axial Semi-elliptical Surface Flaws: R / t = 10 and a / t = 0.5

Aspect Ratio	Elliptic Angle (deg)	K_0 Uniform	K_1 Linear	K_2 Quadratic	K_3 Cubic	K_0 t_{cl}=0.25 in.	K_1 t_{cl}=0.25 in.	K_0 t_{cl}=0.156 in.	K_1 t_{cl}=0.156 in.
2:1	0.00	0.736	0.132	0.053	0.029	0.327	0.162	0.272	0.150
	15.40	0.746	0.203	0.083	0.043	0.079	0.037	0.045	0.020
	27.50	0.719	0.263	0.124	0.067	0.042	0.020	0.025	0.012
	39.60	0.704	0.327	0.183	0.112	0.029	0.014	0.018	0.009
	51.70	0.693	0.383	0.249	0.175	0.023	0.012	0.015	0.007
	63.70	0.685	0.426	0.311	0.242	0.021	0.010	0.013	0.006
	75.80	0.681	0.456	0.357	0.299	0.019	0.009	0.012	0.006
	87.90	0.676	0.483	0.389	0.334	0.018	0.009	0.011	0.006
	90.00	0.676	0.488	0.395	0.340	0.017	0.009	0.011	0.005
6:1	0.00	0.758	0.142	0.059	0.033	0.322	0.163	0.268	0.149
	2.37	0.814	0.213	0.083	0.040	0.091	0.041	0.054	0.025
	16.60	0.908	0.302	0.132	0.065	0.070	0.034	0.043	0.021
	30.80	0.998	0.405	0.208	0.116	0.065	0.032	0.040	0.020
	45.00	1.069	0.504	0.300	0.195	0.062	0.031	0.039	0.019
	59.20	1.120	0.588	0.392	0.285	0.061	0.030	0.038	0.019
	73.40	1.153	0.647	0.463	0.363	0.060	0.030	0.038	0.019
	87.60	1.182	0.679	0.500	0.404	0.059	0.029	0.037	0.018
	90.00	1.187	0.685	0.506	0.411	0.059	0.029	0.037	0.018
10:1	0.00	0.666	0.119	0.049	0.028	0.302	0.156	0.254	0.140
	2.37	0.822	0.208	0.077	0.033	0.097	0.044	0.060	0.028
	16.60	0.995	0.316	0.131	0.056	0.086	0.042	0.054	0.027
	30.80	1.138	0.440	0.216	0.112	0.083	0.041	0.052	0.026
	45.00	1.251	0.560	0.321	0.198	0.083	0.041	0.052	0.026
	59.20	1.335	0.662	0.425	0.298	0.083	0.041	0.052	0.026
	73.40	1.390	0.734	0.506	0.383	0.083	0.041	0.052	0.026
	87.60	1.423	0.770	0.546	0.427	0.083	0.041	0.052	0.026
	90.00	1.429	0.776	0.553	0.434	0.083	0.041	0.052	0.026

Table B9. Influence Coefficients for Inside Circumferential Semi-elliptical Surface Flaws: R / t = 10 and a / t = 0.5

Aspect Ratio	Elliptic Angle (deg)	K_0 Uniform	K_1 Linear	K_2 Quadratic	K_3 Cubic	K_0 t_{cl}=0.25 in.	K_1 t_{cl}=0.25 in.	K_0 t_{cl}=0.156 in.	K_1 t_{cl}=0.156 in.
2:1	0.00	0.741	0.134	0.054	0.030	0.324	0.162	0.269	0.151
	15.40	0.750	0.205	0.084	0.044	0.079	0.038	0.045	0.020
	27.50	0.721	0.264	0.124	0.067	0.042	0.020	0.025	0.012
	39.60	0.706	0.328	0.183	0.112	0.029	0.014	0.018	0.009
	51.70	0.698	0.384	0.250	0.175	0.024	0.012	0.015	0.007
	63.70	0.692	0.430	0.312	0.243	0.021	0.010	0.013	0.007
	75.80	0.686	0.461	0.360	0.301	0.019	0.010	0.012	0.006
	87.90	0.682	0.488	0.392	0.336	0.020	0.010	0.012	0.006
	90.00	0.682	0.493	0.398	0.343	0.020	0.009	0.013	0.006
6:1	0.00	0.727	0.132	0.053	0.030	0.315	0.161	0.262	0.147
	15.40	0.786	0.205	0.079	0.037	0.087	0.039	0.052	0.024
	27.50	0.882	0.295	0.128	0.062	0.067	0.032	0.041	0.020
	39.60	0.974	0.398	0.205	0.114	0.062	0.031	0.038	0.019
	51.70	1.049	0.499	0.298	0.193	0.060	0.030	0.037	0.019
	63.70	1.103	0.584	0.390	0.284	0.058	0.029	0.036	0.018
	75.80	1.138	0.644	0.462	0.362	0.057	0.029	0.036	0.018
	87.90	1.166	0.676	0.499	0.403	0.058	0.029	0.036	0.018
	90.00	1.171	0.682	0.506	0.410	0.058	0.029	0.036	0.018
10:1	0.00	0.616	0.101	0.040	0.023	0.291	0.152	0.247	0.138
	15.40	0.770	0.195	0.071	0.028	0.090	0.039	0.055	0.026
	27.50	0.936	0.301	0.125	0.053	0.078	0.038	0.049	0.024
	39.60	1.076	0.424	0.211	0.109	0.075	0.037	0.047	0.024
	51.70	1.190	0.544	0.315	0.196	0.075	0.037	0.047	0.023
	63.70	1.275	0.647	0.420	0.295	0.075	0.037	0.047	0.023
	75.80	1.330	0.719	0.501	0.381	0.075	0.037	0.047	0.023
	87.90	1.363	0.755	0.542	0.425	0.075	0.037	0.047	0.024
	90.00	1.368	0.762	0.549	0.433	0.075	0.037	0.047	0.024

Table B10. Influence Coefficients for Inside Axial Infinite-Length Surface Flaws, $R / t = 10$

	$0.1\ t^{1/2}\ K^*$					
a' / a	***a/t*=0.01**	***a/t*=0.02**	***a/t*=0.03**	***a/t*=0.05**	***a/t*=0.075**	***a/t*=0.10**
0	1.434	1.029	0.846	0.667	0.565	0.511
0.0556	1.435	1.029	0.846	0.667	0.564	0.510
0.1111	1.436	1.029	0.846	0.666	0.563	0.508
0.1667	1.436	1.028	0.846	0.665	0.562	0.506
0.2222	1.438	1.029	0.846	0.665	0.561	0.505
0.2778	1.442	1.032	0.848	0.666	0.561	0.504
0.3333	1.450	1.037	0.852	0.669	0.563	0.505
0.3888	1.463	1.046	0.859	0.674	0.566	0.507
0.4444	1.482	1.058	0.869	0.682	0.571	0.511
0.500	1.509	1.077	0.884	0.693	0.580	0.517
0.5556	1.546	1.103	0.905	0.708	0.592	0.527
0.6111	1.598	1.138	0.934	0.731	0.609	0.541
0.6666	1.669	1.188	0.974	0.761	0.633	0.561
0.7222	1.768	1.258	1.031	0.804	0.668	0.590
0.7778	1.913	1.360	1.113	0.868	0.718	0.632
0.8333	2.138	1.518	1.242	0.967	0.798	0.699
0.8888	2.534	1.798	1.470	1.143	0.940	0.821
0.9166	2.878	2.041	1.668	1.294	1.064	0.927
0.9444	3.499	2.624	2.187	1.749	1.385	1.224
0.9639	5.831	4.227	3.499	2.770	2.187	1.895
0.9778	11.225	7.289	5.685	4.227	3.426	2.916
0.9889	17.493	11.662	8.746	6.414	5.102	4.373

a'/a	**a/t=0.2**	**a/t=0.3**	**a/t=0.4**
0	0.461	0.510	0.617
0.0552	0.457	0.502	0.602
0.1103	0.452	0.492	0.586
0.1655	0.447	0.483	0.571
0.2206	0.443	0.475	0.556
0.2757	0.439	0.466	0.542
0.3309	0.436	0.459	0.527
0.3861	0.434	0.451	0.513
0.4412	0.432	0.445	0.500
0.4963	0.433	0.440	0.488
0.5515	0.435	0.436	0.477
0.6066	0.440	0.434	0.467
0.6618	0.450	0.435	0.460
0.7169	0.464	0.440	0.456
0.7721	0.487	0.453	0.457
0.8272	0.526	0.477	0.468
0.8824	0.598	0.527	0.501
0.9118	0.665	0.577	0.538
0.9412	0.875	0.729	0.671
0.9618	1.385	1.020	0.948
0.9765	2.187	1.749	1.604
0.9882	2.916	2.478	2.187

a'/a	**a/t=0.5**
0	0.781
0.059	0.755
0.118	0.730
0.176	0.704
0.235	0.679
0.294	0.654
0.353	0.630
0.412	0.605
0.471	0.582
0.529	0.559
0.588	0.538
0.647	0.518
0.706	0.501
0.750	0.491
0.794	0.485
0.838	0.486
0.882	0.501
0.912	0.526
0.941	0.656
0.962	0.875
0.976	1.312
0.988	2.041

Table B10. (continued) Influence Coefficients for Inside Axial Infinite-Length Surface Flaws, *R* / *t* = 10

$0.1\, t^{1/2} K^*$

a'/a	a/t=0.6	a'/a	a/t=0.7	a'/a	a/t=0.8	a'/a	a/t=0.9	a/t=0.95
0	1.021	0	1.35	0	1.739	0	1.952	1.902
0.0564	0.983	0.057	1.294	0.058	1.661	0.058	1.866	1.827
0.1127	0.946	0.115	1.238	0.116	1.583	0.117	1.779	1.752
0.1691	0.908	0.172	1.182	0.174	1.506	0.175	1.694	1.678
0.2255	0.871	0.229	1.127	0.232	1.428	0.233	1.608	1.604
0.2819	0.834	0.286	1.071	0.289	1.351	0.292	1.523	1.529
0.3382	0.798	0.343	1.016	0.347	1.275	0.35	1.438	1.456
0.3946	0.761	0.401	0.961	0.405	1.198	0.409	1.354	1.381
0.451	0.725	0.458	0.906	0.463	1.122	0.467	1.27	1.308
0.5074	0.69	0.515	0.852	0.521	1.047	0.526	1.186	1.234
0.5637	0.655	0.572	0.799	0.579	0.971	0.584	1.102	1.162
0.6201	0.622	0.63	0.747	0.637	0.897	0.643	1.019	1.088
0.6765	0.59	0.687	0.696	0.695	0.824	0.701	0.936	1.017
0.7328	0.561	0.744	0.648	0.753	0.752	0.759	0.854	0.947
0.7892	0.536	0.802	0.604	0.811	0.685	0.818	0.773	0.878
0.8456	0.521	0.859	0.569	0.869	0.627	0.876	0.699	0.815
0.902	0.528	0.916	0.562	0.927	0.598	0.935	0.651	0.768
0.9265	0.549	0.937	0.575	0.945	0.607	0.951	0.654	0.766
0.951	0.671	0.958	0.729	0.963	0.7	0.967	0.729	0.781
0.9681	0.933	0.973	1.02	0.976	1.02	0.979	0.875	0.826
0.9804	1.399	0.983	1.458	0.985	1.458	0.987	1.166	0.911
0.9902	2.041	0.992	2.041	0.993	2.041	0.993	1.749	1.093

Table B11. Influence Coefficients for Inside Circumferential 360 Degree Surface Flaws, R / t = 10

	10t $t^{1/2}$ K^*					
a' / a	***a / t*=0.01**	**a/t=0.02**	**a/t=0.03**	**a/t=0.05**	**a/t=0.075**	**a/t=0.10**
0	2.255	1.616	1.325	1.036	0.867	0.771
0.0556	2.256	1.616	1.324	1.036	0.865	0.769
0.1111	2.257	1.616	1.324	1.035	0.864	0.767
0.1667	2.258	1.616	1.323	1.034	0.863	0.765
0.2222	2.260	1.617	1.324	1.035	0.862	0.764
0.2778	2.267	1.621	1.327	1.037	0.863	0.764
0.3333	2.280	1.629	1.334	1.041	0.866	0.766
0.3888	2.300	1.642	1.344	1.049	0.872	0.770
0.4444	2.329	1.662	1.361	1.061	0.880	0.777
0.5000	2.372	1.691	1.384	1.079	0.894	0.788
0.5556	2.431	1.732	1.417	1.104	0.914	0.804
0.6111	2.511	1.788	1.462	1.138	0.941	0.826
0.6666	2.623	1.866	1.526	1.187	0.979	0.859
0.7222	2.779	1.975	1.615	1.255	1.034	0.905
0.7778	3.008	2.135	1.744	1.355	1.114	0.972
0.8333	3.361	2.383	1.946	1.510	1.239	1.079
0.8888	3.986	2.823	2.305	1.786	1.462	1.271
0.9166	4.520	3.199	2.611	2.022	1.654	1.425
0.9444	6.195	3.965	3.346	2.478	1.982	1.735
0.9639	8.674	5.948	4.956	3.717	2.974	2.602
0.9778	13.630	9.913	8.054	6.195	4.956	4.337
0.9889	18.586	14.249	11.771	9.045	7.682	6.567

a'/a	**a/t=0.2**	**a/t=0.3**	**a/t=0.4**	**a'/a**	**a/t=0.5**
0	0.645	0.644	0.691	0	0.764
0.0552	0.640	0.635	0.678	0.059	0.744
0.1103	0.635	0.626	0.664	0.118	0.724
0.1655	0.630	0.617	0.651	0.176	0.704
0.2206	0.625	0.609	0.638	0.235	0.684
0.2757	0.622	0.601	0.625	0.294	0.666
0.3309	0.619	0.594	0.613	0.353	0.647
0.3861	0.618	0.588	0.602	0.412	0.630
0.4412	0.618	0.584	0.592	0.471	0.614
0.4963	0.622	0.581	0.584	0.529	0.600
0.5515	0.628	0.581	0.578	0.588	0.589
0.6066	0.639	0.584	0.574	0.647	0.580
0.6618	0.656	0.592	0.575	0.706	0.577
0.7169	0.681	0.607	0.581	0.750	0.579
0.7721	0.721	0.633	0.596	0.794	0.588
0.8272	0.784	0.678	0.626	0.838	0.608
0.8824	0.900	0.764	0.691	0.882	0.650
0.9118	1.007	0.845	0.793	0.912	0.702
0.9412	1.363	1.078	0.954	0.941	0.843
0.9618	1.921	1.487	1.301	0.962	1.115
0.9765	2.912	2.354	1.982	0.976	1.859
0.9882	3.841	3.346	2.912	0.988	2.726

Table B11. (continued) Influence Coefficients for Inside Circumferential 360 Degree Surface Flaws, *R* / *t* = 10

10t $t^{1/2}$ *K**							
a'/a	**a/t=0.6**	**a'/a**	**a/t=0.7**	**a'/a**	**a/t=0.8**	**a'/a**	**a/t=0.9**
0	0.852	0	0.944	0	1.028	0	1.129
0.0564	0.827	0.057	0.913	0.058	0.995	0.058	1.099
0.1127	0.802	0.115	0.883	0.116	0.962	0.117	1.070
0.1691	0.778	0.172	0.853	0.174	0.929	0.175	1.041
0.2255	0.753	0.229	0.823	0.232	0.897	0.233	1.013
0.2819	0.729	0.286	0.794	0.289	0.866	0.292	0.986
0.3382	0.706	0.343	0.766	0.347	0.835	0.350	0.959
0.3946	0.684	0.401	0.739	0.405	0.805	0.409	0.932
0.4510	0.663	0.458	0.712	0.463	0.776	0.467	0.907
0.5074	0.642	0.515	0.687	0.521	0.748	0.526	0.882
0.5637	0.624	0.572	0.663	0.579	0.721	0.584	0.857
0.6201	0.608	0.630	0.641	0.637	0.695	0.643	0.832
0.6765	0.595	0.687	0.622	0.695	0.671	0.701	0.809
0.7328	0.586	0.744	0.607	0.753	0.651	0.759	0.786
0.7892	0.586	0.802	0.600	0.811	0.636	0.818	0.767
0.8456	0.601	0.859	0.608	0.869	0.637	0.876	0.757
0.9020	0.653	0.916	0.661	0.927	0.686	0.935	0.786
0.9265	0.703	0.937	0.709	0.945	0.729	0.951	0.820
0.9510	0.867	0.958	0.855	0.963	0.880	0.967	0.892
0.9681	1.140	0.973	1.155	0.976	1.128	0.979	1.115
0.9804	1.797	0.983	1.760	0.985	1.722	0.987	1.735
0.9902	2.602	0.992	2.602	0.993	2.466	0.993	2.478

Appendix C – Listings of K_{Ic} And K_{Ia} Extended Databases

Table C1 – Static Initiation Toughness K_{Ic} Extended Database

Table C2 - Crack Arrest Toughness K_{Ia} ORNL 99/27 Database

Table C3. Crack Arrest Toughness K_{Ia} Extended K_{Ia} Database – Large Specimen Data

Table C1. Static Initiation Toughness K_{Ic} Extended Database

Material	Reference Source	Specimen ID	Type No.	Orientation	T (°F)	RT_{NDT} (°F)	$T - RT_{NDT}$ (°F)	K_{Ic} (ksi√in)
HSST 01	Shabbits	1T-C(T)	1		-200	0	-200	46.6
subarc	(1969)	1T-C(T)	1		-175	0	-175	55.8
weldment		4T-C(T)	4		-150	0	-150	56.1
		4T-C(T)	4		-125	0	-125	61.1
		4T-C(T)	4		-100	0	-100	96.0
		4T-C(T)	4		-75	0	-75	90.3
		4T-C(T)	4		-75	0	-75	93.1
		6T-C(T)	6		-50	0	-50	72.6
A533B Class 1	Shabbits	1T-C(T)	1		-200	0	-200	35.1
subarc	(1969)	1T-C(T)	1		-200	0	-200	45.2
weldment		1T-C(T)	1		-320	0	-320	25.9
		1T-C(T)	1		-320	0	-320	23.7
		4T-C(T)	4		-100	0	-100	55.2
		4T-C(T)	4		-50	0	-50	71.6
		4T-C(T)	4		-25	0	-25	105.9
		8T-C(T)	8		0	0	0	113.1
HSST 01	Mager (1969)	1T-C(T)	1	RW	-150	20	-170	43.9
		1T-C(T)	1	RW	-150	20	-170	39.4
		1T-C(T)	1	RW	-150	20	-170	31.3
		1T-C(T)	1	RW	-150	20	-170	47.3
		1T-C(T)	1	RW	-150	20	-170	50.4
		1T-C(T)	1	RW	-150	20	-170	41.2
		1T-C(T)	1	RW	-150	20	-170	54.0
		1T-C(T)	1	RW	-150	20	-170	50.9
		1T-C(T)	1	RW	-150	20	-170	35.5
		1T-C(T)	1	RW	-150	20	-170	33.2
		1T-C(T)	1	RW	-150	20	-170	37.2
		1T-C(T)	1	RW	-150	20	-170	37.1
		1T-C(T)	1	RW	-150	20	-170	37.1
		1T-C(T)	1	RW	-150	20	-170	34.7
		1T-C(T)	1	RW	-150	20	-170	35.0
		1T-C(T)	1	RW	-150	20	-170	32.6
		1T-C(T)	1	RW	-150	20	-170	29.4
HSST 03	Mager (1969)	1T-C(T)	1	RW	-150	20	-170	44.0
		1T-C(T)	1	RW	-150	20	-170	31.4
		1T-C(T)	1	RW	-150	20	-170	39.3
		1T-C(T)	1	RW	-150	20	-170	31.3
		1T-C(T)	1	RW	-150	20	-170	33.0
		1T-C(T)	1	RW	-150	20	-170	38.1
		1T-C(T)	1	RW	-150	20	-170	31.1
		1T-C(T)	1	RW	-150	20	-170	44.9
		1T-C(T)	1	RW	-150	20	-170	39.4
A533B Class 1	Mager (1969)	1X-WOL	1	RW	-320	65	-385	31.6
		1T-WOL	1	RW	-320	65	-385	32.5
		1X-WOL	1	RW	-250	65	-315	40.9
		1X-WOL	1	RW	-250	65	-315	37.1
		1X-WOL	1	RW	-250	65	-315	44.0
		1T-WOL	1	RW	-250	65	-315	40.8
		1T-WOL	1	RW	-250	65	-315	31.2
		1X-WOL	1	RW	-200	65	-265	30.6

Material	Reference Source	Specimen ID	Type No.	Orientation	T (°F)	RT_{NDT} (°F)	$T - RT_{NDT}$ (°F)	K_{Ic} (ksi√in)
		1X-WOL	1	RW	-200	65	-265	29.0
		1T-WOL	1	RW	-200	65	-265	35.6
		1T-WOL	1	RW	-200	65	-265	42.8
		2T-WOL	2	RW	-150	65	-215	46.9
		2T-WOL	2	RW	-150	65	-215	66.9
HSST 02	Mager (1969)	1X-WOL	1	RW	-200	0	-200	30.5
		1X-WOL	1	RW	-200	0	-200	37.5
		1X-WOL	1	RW	-200	0	-200	41.0
		1T-WOL	1	RW	-200	0	-200	31.2
		1T-WOL	1	RW	-200	0	-200	30.8
		1T-WOL	1	RW	-175	0	-175	43.5
		1X-WOL	1	RW	-150	0	-150	29.7
		1X-WOL	1	RW	-150	0	-150	31.5
		1X-WOL	1	RW	-150	0	-150	41.2
		1X-WOL	1	RW	-150	0	-150	30.5
		1X-WOL	1	RW	-125	0	-125	39.1
		1T-WOL	1	RW	-125	0	-125	48.3
		1T-WOL	1	RW	-125	0	-125	43.4
		1T-WOL	1	RW	-125	0	-125	38.1
		2T-WOL	2	RW	-100	0	-100	51.4
		2T-WOL	2	RW	-100	0	-100	59.0
		2T-WOL	2	RW	-100	0	-100	56.2
		2T-WOL	2	RW	-100	0	-100	50.2
		2T-WOL	2	RW	-50	0	-50	65.1
		2T-WOL	2	RW	-50	0	-50	65.0
		2T-WOL	2	RW	-50	0	-50	67.5
		2T-WOL	2	RW	-50	0	-50	65.0
		1X-WOL	1	RW	-250	0	-250	37.3
		1X-WOL	1	RW	-200	0	-200	44.0
		1X-WOL	1	RW	-200	0	-200	34.6
		1X-WOL	1	RW	-200	0	-200	39.9
		1X-WOL	1	RW	-200	0	-200	38.5
		1T-C(T)	1	RW	-150	0	-150	42.1
		1T-C(T)	1	RW	-150	0	-150	37.7
		1T-C(T)	1	RW	-150	0	-150	40.7
		1T-C(T)	1	RW	-100	0	-100	42.2
		1T-C(T)	1	RW	-100	0	-100	48.5
		1T-C(T)	1	RW	-100	0	-100	48.5
		1T-C(T)	1	RW	-75	0	-75	50.3
		1T-C(T)	1	RW	-75	0	-75	46.6
		1T-C(T)	1	RW	-100	0	-100	54.8
		1T-C(T)	1	RW	-100	0	-100	54.4
		2T-WOL	2	RW	-50	0	-50	56.7
		2T-WOL	2	RW	0	0	0	66.4
		2T-WOL	2	RW	0	0	0	93.7
		2T-WOL	2	RW	0	0	0	83.4
A533B Class 1 weld	Mager (1969)	1X-WOL	1		-320	-45	-275	29.7
		1X-WOL	1		-320	-45	-275	27.2
		1X-WOL	1		-250	-45	-205	37.6
		1X-WOL	1		-250	-45	-205	37.8
		1T-WOL	1		-250	-45	-205	43.6
		2T-WOL	2		-250	-45	-205	55.6
		1T-WOL	1		-225	-45	-180	40.1
		1T-WOL	1		-225	-45	-180	52.8

Material	Reference Source	Specimen ID	Type No.	Orientation	T (°F)	RT_{NDT} (°F)	$T - RT_{NDT}$ (°F)	K_{Ic} (ksi√in)
		2T-WOL	2		-225	-45	-180	66.2
		2T-WOL	2		-200	-45	-155	70.7
A533B Class 1 weld-HAZ	Mager (1969)	1X-WOL	1		-320	0	-320	30.3
		1X-WOL	1		-250	0	-250	35.2
		1X-WOL	1		-250	0	-250	40.4
		1T-WOL	1		-250	0	-250	30.5
		1T-WOL	1		-250	0	-250	44.2
		2T-WOL	2		-200	0	-200	71.2
A508 Class 2 European Forging "ring forging"	Mager (1969)	1X-WOL	1		-320	50	-370	39.6
		1X-WOL	1		-320	50	-370	27.5
		1T-WOL	1		-320	50	-370	47.5
		1X-WOL	1		-250	50	-300	43.2
		1X-WOL	1		-250	50	-300	47.9
		1X-WOL	1		-250	50	-300	41.6
		1T-WOL	1		-250	50	-300	51.3
		1T-WOL	1		-200	50	-250	55.0
		2T-WOL	2		-200	50	-250	43.3
		2T-WOL	2		-150	50	-200	57.2
		2T-WOL	2		-125	50	-175	56.2
		2T-WOL	2		-100	50	-150	56.0
HSST 02	Shabbits (1969)	6T-C(T)	6	RW	25	0	25	98.9
		6T-C(T)	6	RW	25	0	25	74.5
		6T-C(T)	6	RW	25	0	25	90.5
		6T-C(T)	6	RW	0	0	0	73.9
		6T-C(T)	6	RW	0	0	0	66.9
		11T-C(T)	11	RW	50	0	50	148.6
		10T-C(T)	10	RW	50	0	50	137.3
		10T-C(T)	10	RW	50	0	50	139.0
		4T-C(T)	4	RW	0	0	0	87.2
		4T-C(T)	4	RW	-25	0	-25	61.0
		4T-C(T)	4	RW	-25	0	-25	58.7
		4T-C(T)	4	RW	-25	0	-25	45.9
		10T-C(T)	10	RW	0	0	0	87.5
		10T-C(T)	10	RW	25	0	25	110.3
		1T-C(T)	1	RW	-250	0	-250	37.3
		1T-C(T)	1	RW	-200	0	-200	44.4
		1T-C(T)	1	RW	-200	0	-200	34.6
		1T-C(T)	1	RW	-200	0	-200	39.9
		1T-C(T)	1	RW	-200	0	-200	34.8
		1T-C(T)	1	RW	-150	0	-150	44.1
		1T-C(T)	1	RW	-150	0	-150	37.4
		1T-C(T)	1	RW	-150	0	-150	41.8
		1T-C(T)	1	RW	-100	0	-100	48.3
		1T-C(T)	1	RW	-100	0	-100	48.3
		1T-C(T)	1	RW	-100	0	-100	41.9
		2T-C(T)	2	RW	-100	0	-100	49.7
		2T-C(T)	2	RW	-50	0	-50	64.6
		2T-C(T)	2	RW	-50	0	-50	64.7
A508 Class 2	unpublished outside of EPRI NP-719-SR	2T-C(T)	2		-150	51	-201	52.2
		2T-C(T)	2		-150	51	-201	45.5
		2T-C(T)	2		-125	51	-176	46.0
		2T-C(T)	2		-125	51	-176	64.3
		2T-C(T)	2		-125	51	-176	50.0
		4T-C(T)	4		-25	51	-76	45.0

Material	Reference Source	Specimen ID	Type No.	Orientation	T (°F)	RT_{NDT} (°F)	$T - RT_{NDT}$ (°F)	K_{Ic} (ksi√in)
		6T-C(T)	6		0	51	-51	107.0
		2T-C(T)	2		-125	51	-176	45.6
		2T-C(T)	2		-125	51	-176	68.0
A508 Class 2	unpublished	2T-C(T)	2		-75	65	-140	52.0
	outside of	2T-C(T)	2		-75	65	-140	64.6
	EPRI NP-719-SR	2T-C(T)	2		-75	65	-140	56.6
		2T-C(T)	2		-25	65	-90	64.7
		2T-C(T)	2		-25	65	-90	62.4
		8T-C(T)	8		35	65	-30	81.0
		2T-C(T)	2		-125	65	-190	47.2
		2T-C(T)	2		-125	65	-190	40.9
		2T-C(T)	2		-125	65	-190	42.5
		2T-C(T)	2		-125	65	-190	42.5
HSSI Weld	NUREG/CR-	1T-C(T)	1	T-L	-238	-9.4	-228.6	35.09
72W	5913	1T-C(T)	1	T-L	-238	-9.4	-228.6	35.45
		1T-C(T)	1	T-L	-238	-9.4	-228.6	37.82
		1T-C(T)	1	T-L	-149.8	-9.4	-140.4	42.55
		1T-C(T)	1	T-L	-112	-9.4	-102.6	45.09
		2T-C(T)	2	T-L	-112	-9.4	-102.6	58.73
		2T-C(T)	2	T-L	-112	-9.4	-102.6	67.64
		2T-C(T)	2	T-L	-58	-9.4	-48.6	63.27
		4T-C(T)	4	T-L	-58	-9.4	-48.6	73.82
		4T-C(T)	4	T-L	-58	-9.4	-48.6	90.91
		4T-C(T)	4	T-L	-22	-9.4	-12.6	93.45
		4T-C(T)	4	T-L	5	-9.4	14.4	74.64
HSSI	NUREG/CR-	1T-C(T)	1	T-L	-238	-29.2	-208.8	34.64
73W	5913	1T-C(T)	1	T-L	-238	-29.2	-208.8	37.82
		1T-C(T)	1	T-L	-238	-29.2	-208.8	38.18
		1T-C(T)	1	T-L	-238	-29.2	-208.8	39.45
		2T-C(T)	2	T-L	-112	-29.2	-82.8	58.18
		2T-C(T)	2	T-L	-112	-29.2	-82.8	60.64
		2T-C(T)	2	T-L	-112	-29.2	-82.8	65.55
		2T-C(T)	2	T-L	-58	-29.2	-28.8	66.09
		4T-C(T)	4	T-L	-58	-29.2	-28.8	75.55
		4T-C(T)	4	T-L	-58	-29.2	-28.8	76.45
HSST Plate 13	NUREG/CR-	1T-C(T)	1	L-T	-103	-9.4	-93.6	32.64
	5788 (A533B	2T-C(T)	2	L-T	-103	-9.4	-93.6	55.82
	Plate 13A)	4T-C(T)	4	L-T	-103	-9.4	-93.6	53.73
		4T-C(T)	4	L-T	-103	-9.4	-93.6	62.09
		4T-C(T)	4	L-T	-103	-9.4	-93.6	70.82
		½T-C(T)	0.5	L-T	-238	-9.4	-228.6	25.36
		½T-C(T)	0.5	L-T	-238	-9.4	-228.6	26.18
		½T-C(T)	0.5	L-T	-238	-9.4	-228.6	29.27
		½T-C(T)	0.5	L-T	-238	-9.4	-228.6	29.45
		½T-C(T)	0.5	L-T	-238	-9.4	-228.6	30.18
		½T-C(T)	0.5	L-T	-238	-9.4	-228.6	31.00
		½T-C(T)	0.5	L-T	-238	-9.4	-228.6	32.82
		½T-C(T)	0.5	L-T	-238	-9.4	-228.6	33.82
		½T-C(T)	0.5	L-T	-238	-9.4	-228.6	36.00
		½T-C(T)	0.5	L-T	-238	-9.4	-228.6	36.36
		1T-C(T)	1	L-T	-238	-9.4	-228.6	32.09
		1T-C(T)	1	L-T	-238	-9.4	-228.6	33.73
		1T-C(T)	1	L-T	-238	-9.4	-228.6	34.27
		1T-C(T)	1	L-T	-238	-9.4	-228.6	34.91

Material	Reference Source	Specimen ID	Type No.	Orientation	T (°F)	RT_{NDT} (°F)	$T - RT_{NDT}$ (°F)	K_{Ic} (ksi√in)
		1T-C(T)	1	L-T	-238	-9.4	-228.6	35.09
		1T-C(T)	1	L-T	-238	-9.4	-228.6	36.00
		1T-C(T)	1	L-T	-238	-9.4	-228.6	37.45
		1T-C(T)	1	L-T	-238	-9.4	-228.6	37.45
		1T-C(T)	1	L-T	-238	-9.4	-228.6	39.55
		1T-C(T)	1	L-T	-238	-9.4	-228.6	39.73
		1T-C(T)	1	L-T	-238	-9.4	-228.6	40.36
		1T-C(T)	1	L-T	-238	-9.4	-228.6	42.36
		1T-C(T)	1	L-T	-238	-9.4	-228.6	43.73
		1T-C(T)	1	L-T	-238	-9.4	-228.6	46.45
		1T-C(T)	1	L-T	-238	-9.4	-228.6	49.55
		1T-C(T)	1	L-T	-238	-9.4	-228.6	49.64
		2T-C(T)	2	L-T	-238	-9.4	-228.6	30.09
		2T-C(T)	2	L-T	-238	-9.4	-228.6	33.00
		2T-C(T)	2	L-T	-238	-9.4	-228.6	36.55
		2T-C(T)	2	L-T	-238	-9.4	-228.6	37.00
		2T-C(T)	2	L-T	-238	-9.4	-228.6	39.36
		2T-C(T)	2	L-T	-238	-9.4	-228.6	39.91
		2T-C(T)	2	L-T	-238	-9.4	-228.6	40.91
		2T-C(T)	2	L-T	-238	-9.4	-228.6	41.45
		2T-C(T)	2	L-T	-238	-9.4	-228.6	42.18
		2T-C(T)	2	L-T	-238	-9.4	-228.6	46.45
		2T-C(T)	2	L-T	-238	-9.4	-228.6	48.64
		2T-C(T)	2	L-T	-238	-9.4	-228.6	53.18
A508 Class 3	Iwadate, et al.	Bx2B	1	NA	-238	-13	-225	37.29
	ASTM STP	Bx2B	1	NA	-238	-13	-225	39.89
	803	Bx2B	1	NA	-238	-13	-225	44.22
		Bx2B	4	NA	-166	-13	-153	43.36
		Bx2B	4	NA	-76	-13	-63	63.30
		Bx2B	3	NA	-4	-13	9	69.37
Midland Nozzle	NUREG/CR-	1T-C(T)	1		-58	52	-110	49.81
Course Weld	6249	1T-C(T)	1		-148	52	-200	45.63
		1T-C(T)	1		-148	52	-200	44.63
		1T-C(T)	1		-148	52	-200	42.81
		1T-C(T)	1		-148	52	-200	33.45
		1T-C(T)	1		-148	52	-200	32.36
Midland Beltline	NUREG/CR-	1T-C(T)	1		-148	23	-171	36.45
	6249	1T-C(T)	1		-148	23	-171	34.91
Plate 02 4th Irr.	NUREG/CR-	1T-C(T)	1	T-L	-148	0	-148	38.09
Series	4880, 1988	1T-C(T)	1	T-L	-139	0	-139	33.45
	Plate 02	1T-C(T)	1	T-L	-139	0	-139	39.27
	(68-71W)	1T-C(T)	1	T-L	-139	0	-139	40.09

References for Table C1

EPRI Special Report, 1978, *Flaw Evaluation Procedures: ASME Section XI*, EPRI NP-719-SR, Electric Power Research Institute, Palo Alto, CA.

W. O. Shabbits, W. H. Pryle, and E. T. Wessel, *Heavy Section Fracture Toughness Properties of A533, Grade B, Class-1 Steel Plate and Submerged Arc Weldments*, HSST Technical Report 6, WCAP-7414, December 1969.

T. R. Mager, F. O. Thomas, and W. S. Hazelton, *Evaluation by Linear Elastic Fracture Mechanics of Radiation Damage to Pressure Vessel Steels,* HSST Technical Report 5, WCAP-7328, Revised, October 1969.

T. R. Mager, *Fracture Toughness Characterization Study of A533, Grade B, Class-1 Steel*, HSST Technical Report 10, WCAP-7578, October 1970.

R. K. Nanstad, F. M. Haggag, and D. E. McCabe, *Irradiation Effects on Fracture Toughness of Two High-Copper Submerged-Arc Welds, HSSI Series 5,* USNRC Report NUREG/CR-5913 (ORNL/TM-12156/V1 and V2) Vol. 1 and 2, Oak Ridge National Laboratory, Oak Ridge, TN, October 1992.

D. E. McCabe., *A Comparison of Weibull and β_{Ic} Analysis of Transition Range Fracture Toughness Data,* USNRC Report NUREG/CR-5788 (ORNL/TM-11959), Oak Ridge National Laboratory, Oak Ridge, TN, January 1992.

T. Iawadate, Y. Tanaka, S. Ono, and J. Watanabe, "An Analysis of Elastic-Plastic Fracture Toughness Behavior for J_{Ic} Measurements in the Transition Region," *Elastic-Plastic Fracture: Second Symposium, Vol. II-Fracture Resistance Curves and Engineering Applications*, ASTM STP 803, (1983) II531-II561.

D. E. McCabe, R. K. Nanstad, S. K. Iskander, R. L. Swain, *Unirradiated Material Properties of Midland Weld WF-70,* USNRC Report NUREG/CR-6249 (ORNL/TM-12777), Oak Ridge National Laboratory, Oak Ridge, TN, October 1994.

J. J. McGowan, R. K. Nanstad, and K. R. Thoms, *Characterization of Irradiated Current-Practice Welds and A533 Grade B Class 1 Plate for Nuclear Pressure Vessel Service*, USNRC Report NUREG/CR-4880 (ORNL-6484/V1 and V2), Oak Ridge National Laboratory, Oak Ridge, TN, July 1988.

Table C2. Crack Arrest Toughness K_{Ia} ORNL 99/27 Database

Material	Reference Source	Specimen ID	Size No.	Orientation	T (°F)	RT_{NDT} (°F)	T-RT_{NDT} (°F)	K_{Ia} (ksi√in)
HSST-02	EPRI NP	CCA	1.4	L-T	-150	0	-150	28.0
HSST-02	719-SR	CCA	1	L-T	-70	0	-70	43.0
HSST-02	Ripling (1971)	CCA	2	L-T	-70	0	-70	48.0
HSST-02		CCA	2	L-T	-70	0	-70	43.0
HSST-02		CCA	1	L-T	0	0	0	68.0
HSST-02		CCA	1	L-T	0	0	0	58.0
HSST-02		CCA	1	L-T	0	0	0	48.0
HSST-02		CCA	1	L-T	0	0	0	57.0
HSST-02		CCA	1	L-T	0	0	0	62.0
HSST-02		CCA	1.3	L-T	0	0	0	58.0
HSST-02		CCA	1.3	L-T	0	0	0	60.0
HSST-02		CCA	1.3	L-T	0	0	0	65.0
HSST-02		CCA	1.6	L-T	0	0	0	60.0
HSST-02		CCA	1.6	L-T	0	0	0	58.0
HSST-02		CCA	2	L-T	0	0	0	53.0
HSST-02		CCA	2	L-T	0	0	0	58.0
HSST-02		CCA	2	L-T	0	0	0	70.0
HSST-02		CCA	2	L-T	0	0	0	57.0
HSST-02		CCA	3	L-T	0	0	0	57.0
HSST-02		CCA	3	L-T	0	0	0	61.0
HSST-02		CCA	2	L-T	22	0	22	68.0
HSST-02		CCA	1.4	L-T	35	0	35	59.0
HSST-02		CCA	1.6	L-T	35	0	35	84.0
HSST-02		CCA	2	L-T	35	0	35	62.0
HSST-02		CCA	1.4	L-T	50	0	50	92.0
HSST-02		CCA	2	L-T	50	0	50	73.0
HSST-02		CCA	3	L-T	50	0	50	75.0
HSST-02		CCA	1	L-T	75	0	75	94.0
HSST-02		CCA	1.6	L-T	75	0	75	107.0
HSST-02		CCA	2	L-T	75	0	75	77.0
HSST-02		CCA	2	L-T	75	0	75	81.0
HSST-02		CCA	2	L-T	75	0	75	91.0
HSST-02		CCA	2	L-T	75	0	75	102.3
HSST-02		CCA	2	L-T	80	0	80	109.0
HSST-02		CCA	2	L-T	83	0	83	87.0
HSST-02		CCA	3	L-T	83	0	83	94.0
HSST-02		CCA	3	L-T	83	0	83	107.0
HSST-02		CCA	3	L-T	83	0	83	111.0
HSST-02		CCA	2	L-T	96	0	96	111.0
HSST-02		CCA	2	L-T	102	0	102	117.0
HSST-02		CCA	1.8	L-T	105	0	105	118.0
HSST-02		CCA	2	L-T	105	0	105	103.0
HSST-02		CCA	2	L-T	105	0	105	107.0
HSST-02		CCA	3	L-T	105	0	105	130.0
HSST-02		CCA	2	L-T	107	0	107	87.0
HSST-02		CCA	2	L-T	110	0	110	88.0
HSST-02		CCA	2	L-T	110	0	110	88.0
HSST-02		CCA	1.1	L-T	112	0	112	112.0
HSST-02		CCA	2	L-T	115	0	115	111.0
HSST-02		CCA	1.1	L-T	121	0	121	116.0
72W	NUREG/CR-5584	CCA		Crack	-77.8	-10	-68	60.1

Material	Reference Source	Specimen ID	Size No.	Orientation	T (°F)	RT_{NDT} (°F)	T-RT_{NDT} (°F)	K_{Ia} (ksi√in)
72W		CCA		runs	-76	-10	-66	48.2
72W		CCA		in	-76	-10	-66	69.2
72W		CCA		welding	-74.2	-10	-64.2	51.9
72W		CCA		direction	-52.6	-10	-42.6	61.0
72W		CCA			-52.6	-10	-42.6	64.6
72W		CCA			-49	-10	-39	66.4
72W		CCA			-49	-10	-39	67.3
72W		CCA			-49	-10	-39	69.2
72W		CCA			-49	-10	-39	83.7
72W		CCA			-25.6	-10	-15.6	83.7
72W		CCA			-22	-10	-12	54.6
72W		CCA			-22	-10	-12	55.5
72W		CCA			-22	-10	-12	77.4
72W		CCA			-22	-10	-12	82.8
72W		CCA			-22	-10	-12	89.2
72W		CCA			-22	-10	-12	94.6
72W		CCA			-22	-10	-12	97.4
72W		CCA			3.2	-10	13.2	88.3
72W		CCA			5	-10	15	85.5
72W		CCA			5	-10	15	85.5
72W		CCA			5	-10	15	86.5
72W		CCA			5	-10	15	93.7
72W		CCA			6.8	-10	16.8	82.8
72W		CCA			28.4	-10	38.4	93.7
72W		CCA			30.2	-10	40.2	113.8
72W		CCA			32	-10	42	84.6
72W		CCA			32	-10	42	97.4
72W		CCA			32	-10	42	103.7
72W		CCA			33.8	-10	43.8	98.3
72W		CCA			39.2	-10	49.2	113.8
72W		CCA			41	-10	51	104.7
73W	NUREG/CR-5584	CCA		Crack	-77.8	-30	-47.8	62.8
73W		CCA		runs	-76	-30	-46	52.8
73W		CCA		in	-74.2	-30	-44.2	65.5
73W		CCA		welding	-49	-30	-19	47.3
73W		CCA		direction	-49	-30	-19	66.4
73W		CCA			-49	-30	-19	68.3
73W		CCA			-49	-30	-19	77.4
73W		CCA			-47.2	-30	-17.2	64.6
73W		CCA			-25.6	-30	4.4	77.4
73W		CCA			-23.8	-30	6.2	68.3
73W		CCA			-22	-30	8	61.0
73W		CCA			-22	-30	8	72.8
73W		CCA			-22	-30	8	91.0
73W		CCA			-20.2	-30	9.8	70.1
73W		CCA			-20.2	-30	9.8	81.0
73W		CCA			3.2	-30	33.2	100.1
73W		CCA			5	-30	35	106.5
73W		CCA			5	-30	35	111.9
73W		CCA			5	-30	35	112.8
73W		CCA			10.4	-30	40.4	102.3
73W		CCA			23	-30	53	91.9
73W		CCA			41	-30	71	97.4
73W		CCA			41	-30	71	101.9

Material	Reference Source	Specimen ID	Size No.	Orientation	T (°F)	RT_{NDT} (°F)	T-RT_{NDT} (°F)	K_{Ia} (ksi√in)
73W		CCA			41	-30	71	102.8
73W		CCA			41	-30	71	108.3
73W		CCA			59	-30	89	120.1
MW15JC	NUREG/CR-6621	CCA		Crack	-4	32.2	-36.2	63.7
MW15JB*r*		CCA		runs	14	32.2	-18.2	79.0
MW15JE*r1*		CCA		in welding	32	32.2	-0.2	97.1
MW15JF		CCA		direction	50	32.2	17.8	119.7

References for Table C2

EPRI Special Report, 1978, *Flaw Evaluation Procedures: ASME Section XI*, EPRI NP-719-SR, Electric Power Research Institute, Palo Alto, CA.

E. J. Ripling and P. B. Crosley, "Strain Rate and Crack Arrest Studies," *HSST 5th Annual Information Meeting*, Paper No. 9, 1971.

S. K. Iskander, W. R. Corwin, R. K. Nanstad, *Results of Crack-Arrest Tests on Two Irradiated High-Copper Welds,* USNRC Report NUREG/CR-5584 (ORNL/TM-11575), Oak Ridge National Laboratory, Oak Ridge, TN, December 1990.

S. K. Iskander, C. A. Baldwin, D. W. Heatherly, D. E. McCabe, I. Remec, and R. L. Swain, *Detailed Results of Testing Unirradiated and Irradiated Crack-Arrest Toughness Specimens from the Low Upper-Shelf Energy, High Copper Weld, WF-70,* NUREG/CR-6621 (ORNL/TM-13764) under preparation.

S. K. Iskander, R. K. Nanstad, D. E. McCabe, and R. L. Swain, "Effects of Irradiation on Crack-Arrest Toughness of a Low Upper-Shelf Energy, High-Copper Weld," *Effects of Radiation on Materials: 19th International Symposium, ASTM STP 1366*, M. L. Hamilton, A. S. Kumar, S. T. Rosinski, and M. L. Grossbeck, eds., American Society for Testing and Materials, 2000.

Table C3. Crack Arrest Toughness K_{Ia} Extended K_{Ia} Database – Large Specimen Data

Material Test No.	Reference Source	T (°F)	RT_{NDT} (°F)	$T\text{-}RT_{NDT}$ (°F)	K_{Ia} (ksi-in$^{1/2}$)
WP 1.2A	NUREG/CR-4930	-9.4	143.6	153.0	385.81
WP 1.2B		-9.4	197.6	207.0	623.29
WP 1.3		-9.4	129.2	138.6	213.83
WP 1.4B		-9.4	140.0	149.4	352.14
WP 1.5A		-9.4	132.8	142.2	210.19
WP 1.5B		-9.4	161.6	171.0	463.15
WP 1.6A		-9.4	129.2	138.6	250.23
WP 1.6B		-9.4	176.0	185.4	361.24
WP 1.7A	NUREG/CR-5330	-9.4	141.8	151.2	290.26
WP 1.7B		-9.4	190.4	199.8	505.00
WP 1.8A		-9.4	104.0	113.4	313.92
WP 1.8B		-9.4	131.0	140.4	440.40
WP 1.8C		-9.4	174.2	183.6	512.28
WP CE-1		-31.0	96.8	127.8	154.69
WP CE-2A		-31.0	107.6	138.6	198.36
WP CE-2B		-31.0	127.4	158.4	322.11
WP CE-2C		-31.0	140.0	171.0	524.11
SP 1.3	Smirt 10 Vol F, p37	-9.4	111.2	120.6	160.15
WP 2.1A	NUREG/CR-5451	140.0	176.0	36.0	96.45
WP 2.1B		140.0	204.8	64.8	139.22
WP 2.1D		140.0	221.0	81.0	143.77
WP 2.1E		140.0	233.6	93.6	154.69
WP 2.1F		140.0	257.0	117.0	182.89
WP 2.1H		140.0	275.0	135.0	266.61
WP 2.1I		140.0	293.0	153.0	337.58
WP 2.1J		140.0	305.6	165.6	369.43
WP 2.2A		140.0	248.0	108.0	182.89
WP 2.2B		140.0	264.2	124.2	235.67
WP 2.2C		140.0	271.4	131.4	255.69
WP 2.2D		140.0	282.2	142.2	252.05
WP 2.2E		140.0	287.6	147.6	345.77
WP 2.2F		140.0	302.0	162.0	331.21
WP 2.2G		140.0	323.6	183.6	405.82
WP 2.3A		140.0	206.6	66.6	131.03
WP 2.3B		140.0	222.8	82.8	211.10
WP 2.3D		140.0	231.8	91.8	232.03
WP 2.3F		140.0	258.8	118.8	234.76
WP 2.4B		140.0	186.8	46.8	124.66
WP 2.4C		140.0	215.6	75.6	171.06
WP 2.4D		140.0	224.6	84.6	255.69
WP 2.4E		140.0	249.8	109.8	226.57
WP 2.4F		140.0	260.6	120.6	279.34
WP 2.4G		140.0	278.6	138.6	346.68
WP 2.4H		140.0	300.2	160.2	361.24
WP 2.5B		140.0	219.2	79.2	155.60
WP 2.5C		140.0	255.2	115.2	172.88
WP 2.5D		140.0	275.0	135.0	243.86
WP 2.5E		140.0	291.2	151.2	278.43
WP 2.5F		140.0	309.2	169.2	333.03
WP 2.6A		140.0	219.2	79.2	185.62
WP 2.6B		140.0	239.0	99.0	235.67
WP 2.6C		140.0	246.2	106.2	260.24
WP 2.6D		140.0	257.0	117.0	318.47
WP 2.6F		140.0	271.4	131.4	298.45
WP 2.6G		140.0	282.2	142.2	373.98
WP 2.6H		140.0	312.8	172.8	375.80
PTSE 1B	NUREG/CR-4106	196.3	326.3	130.0	182.80
PTSE 1C		196.3	354.2	157.9	271.97
PTSE 2A	NUREG/CR-4888	167.0	267.1	100.1	237.85
PTSE 2B		167.0	296.2	129.2	329.03
PTSE 2C		167.0	325.2	158.2	381.53
TSE 4	NUREG/CR-4249	167.0	267.8	100.8	115.56
TSE 5-1		152.6	96.8	-55.8	78.25
TSE 5-2		152.6	179.6	27.0	94.63
TSE 5-3		152.6	192.2	39.6	83.71
TSE 5A-1		50.0	71.6	21.6	69.15
TSE 5A-2		50.0	100.4	50.4	78.25
TSE 5A-3		50.0	123.8	73.8	97.36
TSE 5A-4		50.0	152.6	102.6	118.29
TSE 6-1		152.6	89.6	-63.0	57.32
TSE 6-2		152.6	145.4	-7.2	95.54

References for Table C3

D. J. Naus, et al., *High-Temperature Crack Arrest Behavior in 152-mm-Thick SEN Wide Plates of Quenched and Tempered A533 Grade B Class 1 Steel*, NUREG/CR-5330 (ORNL-11083), Oak Ridge National Laboratory, Oak Ridge, TN, April 1989.

D. J. Naus, et al., *Crack-Arrest Behavior in SEN Wide Plates of Low-Upper-Shelf Base Metal Tested Under Nonisothermal Conditions: WP-2 Series*, NUREG/CR-5451 (ORNL-6584), Oak Ridge National Laboratory, Oak Ridge, TN, April 1989.

R. H. Bryan, et al., *Pressurized-Thermal Shock Test of 6-Inch-Thick Pressure Vessel, PTSE-1: Investigations of Warm Prestressing and Upper-Shelf Arrest*, NUREG/CR-4106 (ORNL-6135), Oak Ridge National Laboratory, Oak Ridge, TN, April 1985.

R. H. Bryan, et al., *Pressurized Thermal Shock Test of 6-Inch-Thick Pressure Vessel PTSE-2: Investigation of Low Tearing Resistance and Warm Prestressing*, NUREG/CR-4888 (ORNL-6377), Oak Ridge National Laboratory, Oak Ridge, TN, December 1987.

R. D. Cheverton, D. G. Ball, S. E. Bolt, S. K. Iskander, and R. K. Nanstad, *Pressure Vessel Fracture Studies Pertaining to the PWR Thermal-Shock Issue: Experiments TSE-5, TSE-5A, and TSE-6,* NUREG/CR-4249 (ORNL-6163), Oak Ridge National Laboratory, Oak Ridge, TN, June 1985.

Appendix D – Summary of RVID2 Data for Use in FAVOR Calculations

Product Form	Heat	Beltline	$\sigma_{flow(u)}$ [ksi]	$RT_{NDT(u)}$ [°F]			Composition(2)			
				$RT_{NDT(u)}$ Method	$RT_{NDT(u)}$ Value	$\sigma_{(u)}$ Value	Cu	Ni	P	USE_0 (ft-lbf)
Beaver Valley 1, (Designer: Westinghouse, Manufacturer: CE) Coolant Temperature = 547°F, Vessel Thickness = 7-7/8 in.										
PLATE	C4381-1	INTERMEDIATE SHELL B6607-1	83.8	MTEB 5-2	43	0	0.14	0.62	0.015	90
	C4381-2	INTERMEDIATE SHELL B6607-2	84.3	MTEB 5-2	73	0	0.14	0.62	0.015	84
	C6293-2	LOWER SHELL B7203-2	78.8	MTEB 5-2	20	0	0.14	0.57	0.015	84
	C6317-1	LOWER SHELL B6903-1	72.7	MTEB 5-2	27	0	0.2	0.54	0.01	80
LINDE 1092 WELD	305414	LOWER SHELL AXIAL WELD 20-714	75.3	Generic	-56	17	0.337	0.609	0.012	98
	305424	INTER SHELL AXIAL WELD 19-714	79.9	Generic	-56	17	0.273	0.629	0.013	112
LINDE 0091 WELD	90136	CIRC WELD 11-714	76.1	Generic	-56	17	0.269	0.07	0.013	144
Calvert Cliffs 1, (Designer and Manufacturer: CE) Coolant Temperature = 545°F, Vessel Thickness = 8 5/8-in.										
PLATE	B-8489-1	LOWER SHELL D-7207-3	78.8	MTEB 5-2	-20	0	0.11	0.53	0.008	81
	B-8489-2	LOWER SHELL D-7207-2	80.3	MTEB 5-2	-10	0	0.11	0.56	0.009	90
	C-4351-2	INTERMEDIATE SHELL D-7206-1	74.7	MTEB 5-2	20	0	0.11	0.55	0.011	90
	C-4420-1	LOWER SHELL D-7207-1	78.0	MTEB 5-2	10	0	0.13	0.54	0.01	77
	C-4441-1	INTERMEDIATE SHELL D-7206-3	78.5	ASME NB-2331	10	0	0.12	0.64	0.011	112
	C-4441-2	INTERMEDIATE SHELL D-7206-2	82.6	ASME NB-2331	-30	0	0.12	0.64	0.011	81
LINDE 1092 WELD	20291/12008	INTERMEDIATE SHELL AXIAL WELD 2-203	78.8	ASME NB-2331	-50	0	0.22	0.83	0.01	110
	21935	LOWER SHELL AXIAL WELD 3-203A/C	78.6	Generic	-56	17	0.18	0.72	0.015	109
LINDE 0091 WELD	33A277	INT. TO LOWER SHELL CIRC. WELD 9-203	78.6	ASME NB-2331	-80	0	0.24	0.16	0.014	160
Oconee 1, (Designer and Manufacturer: B&W) Coolant Temperature = 556°F, Vessel Thickness = 8.44-in.										
FORGING	AHR54 (ZV2861)	LOWER NOZZLE BELT	(4)	B&W Generic	3	31	0.16	0.65	0.006	109
PLATE	C2197-2	INTERMEDIATE SHELL	(4)	B&W Generic	1	26.9	0.15	0.5	0.008	81
	C2800-1	LOWER SHELL	(4)	B&W Generic	1	26.9	0.11	0.63	0.012	81
	C2800-2	LOWER SHELL	69.9	B&W Generic	1	26.9	0.11	0.63	0.012	119
	C3265-1	UPPER SHELL	75.8	B&W Generic	1	26.9	0.1	0.5	0.015	108
	C3278-1	UPPER SHELL	(4)	B&W Generic	1	26.9	0.12	0.6	0.01	81
LINDE 80 WELD	1P0962	INTERMEDIATE SHELL AXIAL WELDS SA-1073	79.4	B&W Generic	-5	19.7	0.21	0.64	0.025	70
	299L44	INT./UPPER SHL CIRC WELD (OUTSIDE 39%) WF-25	(4)	B&W Generic	-7	20.6	0.34	0.68	(3)	81
	61782	NOZZLE BELT/INT. SHELL CIRC WELD SA-1135	(4)	B&W Generic	-5	19.7	0.23	0.52	0.011	80
	71249	INT./UPPER SHL CIRC WELD (INSIDE 61%) SA-1229	76.4	ASME NB-2331	10	0	0.23	0.59	0.021	67
	72445	UPPER/LOWER SHELL CIRC WELD SA-1585	(4)	B&W Generic	-5	19.7	0.22	0.54	0.016	65
	8T1762	LOWER SHELL AXIAL WELDS SA-1430	75.5	B&W Generic	-5	19.7	0.19	0.57	0.017	70
	8T1762	UPPER SHELL AXIAL WELDS SA-1493	(4)	B&W Generic	-5	19.7	0.19	0.57	0.017	70
	8T1762	LOWER SHELL AXIAL WELDS SA-1426	75.5	B&W Generic	-5	19.7	0.19	0.57	0.017	70

Product Form	Heat	Beltline	$\sigma_{flow(u)}$ [ksi]	$RT_{NDT(u)}$ [°F]			Composition(2)			USE_0 (ft-lbf)
				$RT_{NDT(u)}$ Method	$RT_{NDT(u)}$ Value	$\sigma_{(u)}$ Value	Cu	Ni	P	
Palisades, (Designer and Manufacturer: CE) **Coolant Temperature = 532°F, Vessel Thickness = 8½ in.**										
PLATE	A-0313	D-3803-2	(4)	MTEB 5-2	-30	0	0.24	0.52	0.01	87
	B-5294	D-3804-3	(4)	MTEB 5-2	-25	0	0.12	0.55	0.01	73
	C-1279	D-3803-3	(4)	ASME NB-2331	-5	0	0.24	0.5	0.011	102
	C-1279	D-3803-1	74.7	ASME NB-2331	-5	0	0.24	0.51	0.009	102
	C-1308A	D-3804-1	(4)	ASME NB-2331	0	0	0.19	0.48	0.016	72
	C-1308B	D-3804-2	(4)	MTEB 5-2	-30	0	0.19	0.5	0.015	76
LINDE 0124 WELD	27204	CIRC. WELD 9-112	76.9	Generic	-56	17	0.203	1.018	0.013	98
LINDE 1092 WELD	34B009	LOWER SHELL AXIAL WELD 3-112A/C	76.1	Generic	-56	17	0.192	0.98	(3)	111
	W5214	LOWER SHELL AXIAL WELDS 3-112A/C	72.9	Generic	-56	17	0.213	1.01	0.019	118
	W5214	INTERMEDIATE SHELL AXIAL WELDS 2-112 A/C	72.9	Generic	-56	17	0.213	1.01	0.019	118

Notes:

(1) Information taken directly from the July 2000 release of the NRCs Reactor Vessel Integrity [RVID2] database.

(2) These composition values are as reported in RVID2. In FAVOR calculations these values should be treated as the central tendency of the Cu, Ni, and P distributions.

(3) No values of phosphorus are recorded in RVID2 for these heats. A generic value of 0.012 should be used, which is the mean of 826 phosphorus values taken from the surveillance database used to calibrate the embrittlement trend curve [Kirk].

(4) No values strength measurements are available in PREP4 for these heats [PREP]. A value of 77 ksi should be used, which is the mean of other flow strength values reported in this Appendix.

References:

RVID2 U.S. Nuclear Regulatory Commission Reactor Vessel Integrity Database, Version 2.1.1, July 6, 2000.

PREP PREP4: Power Reactor Embrittlement Program, Version 1.0," EPRI, Palo Alto, CA: 1996. SW-106276

Kirk M. T. Kirk, C. S. Santos, E.D. Eason, J.E. Wright, and G. R. Odette, “Updated Embrittlement Trend Curve for Reactor Pressure Vessel Steels,” Paper No. G01-5, Transactions of the 17th International Conference on Structural Mechanics in Reactor Technology (SMiRT 17), Prague, Czech Republic, August 17-22, 2003.

Appendix E – Statistical Point-Estimation Techniques for Weibull Distributions

The three parameters for the Weibull distributions of $RT_{NDT} - T_0$ and ΔRT_{LB} were calculated using a combination of two point-estimation procedures, *Maximum Likelihood* and the *Method of Moments*. The parameters to estimate are the location parameter, *a*, of the random variate, the scale parameter, *b*, of the random variate, and the shape parameter, *c*.

Maximum likelihood estimators for the shape parameter c' and the scale parameter b' can be derived from the likelihood function, *L*, for the Weibull distribution. The Weibull density is given by

$$w(\Delta RT \,|\, a,b,c) = \frac{c}{b} y^{c-1} \exp\left(-y^c\right), \quad \text{for} \quad (y = (\Delta RT - a)/b, \Delta RT > a,\ b,c > 0) \tag{E1}$$

and the corresponding likelihood function is the joint density (see Ref.[E1]) (given the location parameter, *a*)

$$L(b,c \,|\, \Delta RT, a) = \prod_{i=1}^{N} \frac{c}{b}\left(\frac{\Delta RT_{(i)} - a}{b}\right)^{c-1} \exp\left[-\left(\frac{\Delta RT_{(i)} - a}{b}\right)^{c}\right] \tag{E2}$$

The maximum likelihood (*ML*) estimators for the scale, b', and shape parameters, c', are defined as the unique values of (b', c') that maximize the joint probability that the *N* members of the sample set all come from the same parent population. The *ML* estimators are, therefore, calculated by finding the stationary point of Eq. (E2). Upon taking the logarithm of Eq. (E2), the derivatives with respect to the individual parameters (b', c') are set to zero. The resulting *ML* estimator for the shape parameter, c', is found by solving iteratively for c' in the following nonlinear equation

$$\frac{\partial(\ln(L(c')))}{\partial c'} = \frac{\sum_{i=1}^{N} (\Delta RT_{(i)} - a)^{c'} \ln(\Delta RT_{(i)} - a)}{\sum_{i=1}^{N} (\Delta RT_{(i)} - a)^{c'}} - \frac{1}{N}\sum_{i=1}^{N} \ln(\Delta RT_{(i)} - a) - \frac{1}{c'} = 0 \tag{E3}$$

Upon obtaining a solution for c', the *ML* estimator for the scale parameter, b', follows directly from

$$\frac{\partial(\ln(L))}{\partial b'} = b' - \left[\sum_{i=1}^{N} \frac{\left(\Delta RT_{(i)} - a\right)^{c'}}{N} \right]^{\frac{1}{c'}} = 0 \tag{E4}$$

For the *ML* point estimators for (b', c'), the location parameter, *a*, was assumed given. The *Method of Moments* (*MM*) can now be applied to provide a point estimate for the location parameter, a^*. In the *Method of Moments*, the sample moments are used as estimators for the population moments. The *MM* point estimator for the scale parameter, b^*, is (given the shape parameter, *c*),

$$b^* = \sqrt{m_2 / [\Gamma(1+2/c) - \Gamma^2(1+1/c)]} \tag{E5}$$

where m_2 is the second moment of the sample about the sample mean and Γ is Euler's gamma function. The *MM* estimator for the location parameter, a^*, follows from

$$a^* = m_1' - b^* \Gamma(1+1/c) \tag{E6}$$

where m_1' is the 1st crude moment of the sample (the sample mean) and the sample moments are defined by

$$\begin{aligned} m_1' &= \sum_{i=1}^{N} \frac{\Delta RT_{NDT(i)}}{N} \\ m_2 &= \sum_{i=1}^{N} \frac{\left(\Delta RT_{NDT}(i) - m_1'\right)^2}{N} \end{aligned} \tag{E7}$$

From Ref. [B.2], a moment estimator for the shape parameter, c^*, also exists

$$c^* = \frac{4.104683 - 1.148513\sqrt{b_1} + 0.44326(\sqrt{b_1})^2 - 0.053025(\sqrt{b_1})^3}{\sqrt{b_1} + 1.139547} \tag{E8}$$

where $\sqrt{b_1}$ is the sample skewness. However, for sample sizes as small as 20, there will be a high level of uncertainty in the (a^*, b^*, c^*) estimates derived from c^* (Ref. [B.2]).

The three parameters for the Weibull distribution of ΔRT were estimated through the following iterative sequence:

1) For the discrete set $(\Delta RT_{(i)}, i = 1, N)$, calculate the sample moments, (m_1', m_2) from Eqs. (E7).
2) Select a trial value for the location parameter, a_{trial} where $a_{trial} < \min(\Delta RT_{(i)}, i = 1, 2, \ldots N)$.
3) Calculate *ML* estimates for (c', b') from Eqs. (E3)-(E4) by letting $a = a_{trial}$.

4) Calculate MM estimates for (a^*, b^*) from Eqs. (E5)-(E6) by letting $c = c'$ as determined in Step 3.

5) Calculate a relative deviation between the trial a_{trial} and the MM estimate of a^* from Step 4 by

$$\delta = \frac{a_{trial} - a^*}{a_{trial}} \tag{E9}$$

6) Given $\varepsilon_{tolerance}$, as a pre-selected convergence tolerance, if $\delta > \varepsilon_{tolerance}$, then select a new trial location parameter, a_{trial}, and repeat Steps 3-6 until convergence, defined as $\delta \le \varepsilon_{tolerance}$.

Upon convergence, there will be two triplets (a_{trial}, b', c') and (a^*, b^*, c') where in general $a_{trial} \approx a^*$ and $b' \ne b^*$ although b' was typically close to b^* in this study. The triplet (a^*, b', c') was taken as the converged estimate for the parameters of the Weibull distribution for ΔRT.

References

E1. A. Ghosh, "A FORTRAN Program for Fitting Weibull Distribution and Generating Samples," *Computers & Geosciences* **25**, (1999) 729-738.

E2. K. O. Bowman and P. T. Williams, *Technical Basis for Statistical Models of Extended K_{Ic} and K_{Ia} Fracture Toughness Databases for RPV Steels*, ORNL/NRC/LTR-99/27, Oak Ridge National Laboratory, Oak Ridge, TN, February 2000.

Appendix F – Development of Stochastic Models for $\Delta RT_{epistemic}$ and ΔRT_{arrest}

F.1 Stochastic Model for $\Delta RT_{epistemic}$

F.1.1 Initial Weibull Model for $\Delta RT_{epistemic}$

Initially, the epistemic uncertainty in the unirradiated value for RT_{NDTo} was modeled by a continuous 3-parameter Weibull distribution of the form

$$\begin{aligned} f_W(\Delta RT \mid a,b,c) &= \frac{c}{b}\left(\frac{\Delta RT - a}{b}\right)^{c-1} \exp\left[-\left(\frac{\Delta RT - a}{b}\right)^{c}\right], \qquad \left(\Delta RT > a,\ \ (b,c) > 0\right) \\ \Pr\left(X \le \Delta RT\right) &= F_W(\Delta RT \mid a,b,c) = P = 1 - \exp\left[-\left(\frac{\Delta RT - a}{b}\right)^{c}\right],\ \left(\Delta RT > a,\ \ (b,c) > 0\right) \end{aligned} \tag{F1}$$

where f_W is the probability density function (PDF), F_W is the cumulative distribution function (CDF), and *a, b,* and *c* are the location, scale, and shape parameters, respectively, of the Weibull distribution. In FAVOR, the epistemic uncertainty term is sampled using the inverse CDF

$$\Delta RT = a + b\left[-\ln\left(1-P\right)\right]^{\frac{1}{c}}; \quad 0 < P < 1 \tag{F2}$$

where P is randomly sampled from a uniform distribution on the open interval (0,1). The *epistemic* uncertainty in $RT_{NDT(\mathrm{u})}$ can then be reduced by

$$RT_{LB} = RT_{NDT(\mathrm{u})} - \Delta RT \tag{F3}$$

Using a combination of the *Maximum Likelihood* and *Method of Moments* point-estimation procedures (as described in Appendix E, the following values were determined for the three Weibull parameters in Eqs. (F1) and (F2):

$$\begin{aligned} a &= -40.02\ ^\circ\mathrm{F} \\ b &= \ 124.88\ ^\circ\mathrm{F} \\ c &= \ 1.96 \end{aligned} \tag{F4}$$

based on the sample (N = 18) given in Table 8 and repeated in Table F1.

Table F1. $\Delta RT_{epistemic}$ **Ranked Data with Order-Statistic Estimates of *P***

i	ΔRT_i, (°F)	$\boldsymbol{P_i}$	$\ln(-\ln(1-\boldsymbol{P_i}))$
1	-19.4	0.03804	-3.24970
2	-10.9	0.09239	-2.33364
3	-1.7	0.14674	-1.84080
4	2.1	0.20109	-1.49387
5	33.2	0.25543	-1.22093
6	38.4	0.30978	-0.99223
7	50.1	0.36413	-0.79239
8	54.6	0.41848	-0.61229
9	62.3	0.47283	-0.44594
10	64.3	0.52717	-0.28898
11	81.9	0.58152	-0.13796
12	89.4	0.63587	0.01019
13	91.5	0.69022	0.15861
14	97.8	0.74457	0.31100
15	142.2	0.79891	0.47251
16	147.6	0.85326	0.65186
17	162.4	0.90761	0.86782
18	186.2	0.96196	1.18449

Sample
mean = 70.67
variance = 3669.77
stdv = 60.58

$P_i = (i - 0.3)/(n + 0.4)$

From the following asymptotic relations for the mean and variance of a Weibull distribution,

$$\mu = a + b\,\Gamma\left(1 + \frac{1}{c}\right)$$
$$\sigma^2 = b^2\left[\Gamma\left(1 + \frac{2}{c}\right) - \Gamma^2\left(1 + \frac{1}{c}\right)\right] \quad , \qquad \text{(F5)}$$
$$\Gamma(x) = \int_0^\infty t^{x-1} e^{-t}\,dt$$

the mean and variance for the Weibull model for $\Delta RT_{epistemic}$ compared to the corresponding sample estimators are:

Model	Sample
μ = 70.70 °F	m_1' = 70.67 °F
σ^2 = 3473.65	s^2 = 3669.77
σ = 58.94 °F	s = 60.58 °F

F.1.2 New Model Developed Using Orthogonal Distance Regression (ODR)

The initial statistical model for $\Delta RT_{epistemic}$ was developed using point-estimation procedures that did not take into account any uncertainty in the data sample of Table F1. An analytical procedure, called *orthogonal distance regression* (ODR), can be employed to solve the *errors-in-variables* problem in which uncertainties are assumed to exist in the data. The computational procedure implemented into the software package, ODRPACK [F1], can be used to fit a model equation to data using orthogonal distance regression.

The explicit ODR problem is defined as follows. Let $(x_i, y_i), i = 1, 2, \ldots n$ be an observed set of data. Assume that the values y_i are a (possibly nonlinear) function of x_i and a set of unknown parameters $\beta \in \Re^p$, where both y_i and x_i contain the uncertainties, $\varepsilon_i^* \in \Re^1$ and $\delta_i^* \in \Re^1$, respectively. The superscript "*" denotes an actual but unknown value. The observed value, y_i, can be expressed in terms of a *model equation*

$$y_i + \varepsilon_i^* = f_i\left(x_i + \delta_i^* \middle| \left\{\beta_k^*\right\}\right); \quad \left(i = 1, 2, \ldots n\right) \tag{F6}$$

for some actual values of the parameter vector $\left(\left\{\beta_k^*\right\}; k = 1, 2, \ldots p\right)$. The variables y_i are sometimes referred to as the *dependent* or *response* variables, and x_i are the *independent* (*regressor* or *explanatory*) variables.

The explicit *orthogonal distance regression* problem approximates $\left\{\beta^*\right\}$ by finding the estimate $\left\{\beta\right\}$ for which the sum of the squares of the n orthogonal distances from the curve $f(x\,;\{\beta\})$ to the n data points is minimized [F1]. This can be accomplished by the following minimization problem

$$\min_{\beta,\delta,\varepsilon} \sum_{i=1}^{n} \left(\varepsilon_i^2 + \delta_i^2\right) \tag{F7}$$

subject to the constraints

$$y_i = f_i\left(x_i + \delta_i \middle| \left\{\beta\right\}\right) - \varepsilon_i \qquad i = 1, 2, \ldots n. \tag{F8}$$

Since the constraints are linear in ε_i, they and thus ε_i can be eliminated from the minimization problem, obtaining

$$\min_{\{\beta\},\{\delta\}} \sum_{i=1}^{n} \left(\left[f_i\left(x_i + \delta_i \middle| \left\{\beta\right\}\right) - y_i\right]^2 + \delta_i^2\right) \tag{F9}$$

The algorithm implemented in ODRPACK uses the Levenberg-Marquardt *trust region* method to iteratively solve the nonlinear minimization problem of Eq. (F9).

Derivation of the Model Equation Form

To proceed, the form of the problem-specific model equation must be derived. The CDF in Eq.(F1) can be rewritten as

$$
\begin{aligned}
P &= 1-\exp\left[-\left(\frac{\Delta RT-a}{b}\right)^{c}\right] \\
1-P &= \exp\left[-\left(\frac{\Delta RT-a}{b}\right)^{c}\right] \\
-\ln\left(1-P\right) &= \left(\frac{\Delta RT-a}{b}\right)^{c} \\
\ln\left[-\ln\left(1-P\right)\right] &= c\ln\left(\Delta RT-a\right)-c\ln(b)
\end{aligned}
\tag{F10}
$$

The location parameter, a, is related to the scale, b, and shape, c, parameters through its *moment estimator*

$$
a \approx m_1' - b\,\Gamma\left(1+\frac{1}{c}\right) \tag{F11}
$$

where m_1' is the 1st crude moment of the sample (or sample mean). The use of the Eq. (F11) as a constraint in the model equation forces the mean of the resulting Weibull model to be identical to the sample mean, m_1'. Introducing Eq. (F11) into Eq. (F10), the final form of the nonlinear model equation is

$$
y_i = \beta_1 \ln\left[x_i - m_1' + \beta_2\,\Gamma\left(1+\frac{1}{\beta_1}\right)\right] - \beta_1 \ln(\beta_2);\ (i=1,2,\ldots n)
$$

where (F12)

$$
\left(\{\beta\} = \begin{Bmatrix}\beta_1\\ \beta_2\end{Bmatrix} = \begin{Bmatrix}c\\ b\end{Bmatrix};\quad \{x_i\} = \left\{\Delta RT_{(i)}\right\};\{y_i\} = \left\{\ln\left[-\ln\left(1-P_i\right)\right]\right\}\right)
$$

Values for P_i can be estimated by ranking the data in Table F1 and applying the median-rank order statistic

$$
P_i \approx \frac{i-0.3}{n+0.4} \tag{F13}
$$

ODRPACK iteratively solves for the solution vector $\begin{Bmatrix} \beta_1 \\ \beta_2 \\ \delta_1 \\ \delta_2 \\ \vdots \\ \delta_n \end{Bmatrix}_{n+2}$

The results of the ODRPACK analysis are presented in Table F2. In summary, the ODR analysis produced the following estimates for the Weibull model for $\Delta RT_{epistemic}$:

Location Parameter, $a =$	-45.586	95% Confidence Intervals
Scale Parameter, $b =$	130.899 ± 10.259	109.15 to 152.65
Shape Parameter, $c =$	1.855 ± 0.227	1.374 to 2.337
$\Delta RT_{ODR} =$	$-45.586 + 130.899\left[-\ln\left(1-P\right)\right]^{\frac{1}{1.855}}$;	$0 < P < 1$
Sample Mean, $m'_1 =$	70.67	
Weibull Mean, $\mu =$	70.667	
Sample Stdv, $s =$	60.58	
Weibull Stdv, $\sigma =$	65.036	
Sample Variance, $s^2 =$	3669.77	
Weibull Variance, $\sigma^2 =$	4229.692	

The 95% confidence intervals for the two parameters $\beta_1 = c$ and $\beta_2 = b$ are calculated by ODRPACK using $\beta_k \pm t_{(0.975,\mu)}\sigma_{\beta_k}$ where $t_{(0.975,\mu)}$ is the appropriate value for constructing a two-sided confidence interval using Student's t distribution with μ degrees of freedom. The computational procedure used by ODRPACK to calculate the standard deviations for the parameters, σ_{β_k}, is given in [F2]. See Fig. F1 for a comparison of the initial Weibull model and the model produced by the ODR analysis. The application of ODR has resulted in an increase in the Weibull model's standard deviation from 58.94 °F to 65.04 °F compared to the sample's standard deviation of 60.58 °F.

Table F2. ODRPACK Results of ODR Analysis of $\Delta RT_{epistemic}$ Model Equation

```
*****************************************************
* ODRPACK VERSION 2.01 OF 06-19-92 (DOUBLE PRECISION) *
*****************************************************

    ODR Analysis of DRTLB Weibull Model Parameters

   BETA(1) = c >> Shape Parameter
   BETA(2) = b >> Scale Parameter

   a = M1 - b*Gamma[1 + 1/c]

 *** INITIAL SUMMARY FOR FIT BY METHOD OF ODR ***

 --- PROBLEM SIZE:
           N =    18          (NUMBER WITH NONZERO WEIGHT =    18)
          NQ =     1
           M =     1
          NP =     2          (NUMBER UNFIXED =     2)

 --- CONTROL VALUES:
         JOB = 00010
             = ABCDE, WHERE
                      A=0 ==> FIT IS NOT A RESTART.
                      B=0 ==> DELTAS ARE INITIALIZED TO ZERO.
                      C=0 ==> COVARIANCE MATRIX WILL BE COMPUTED USING
                              DERIVATIVES RE-EVALUATED AT THE SOLUTION.
                      D=1 ==> DERIVATIVES ARE ESTIMATED BY CENTRAL
DIFFERENCES.
                      E=0 ==> METHOD IS EXPLICIT ODR.
      NDIGIT =    16          (ESTIMATED BY ODRPACK)
      TAUFAC =     1.00D+00

 --- STOPPING CRITERIA:
       SSTOL =     1.49D-08   (SUM OF SQUARES STOPPING TOLERANCE)
      PARTOL =     3.67D-11   (PARAMETER STOPPING TOLERANCE)
       MAXIT =    50          (MAXIMUM NUMBER OF ITERATIONS)

 --- INITIAL WEIGHTED SUM OF SQUARES        =   1.15671908D+00
         SUM OF SQUARED WEIGHTED DELTAS     =   0.00000000D+00
         SUM OF SQUARED WEIGHTED EPSILONS   =   1.15671908D+00

 *** ITERATION REPORTS FOR FIT BY METHOD OF ODR ***


        CUM.                 ACT. REL.   PRED. REL.
  IT.  NO. FN     WEIGHTED   SUM-OF-SQS   SUM-OF-SQS              G-N
 NUM.   EVALS   SUM-OF-SQS    REDUCTION    REDUCTION  TAU/PNORM  STEP
 ----  ------  -----------  -----------  -----------  ---------  ----

    1      12  5.36253D-01   5.3640D-01   5.3739D-01  1.333D-01   YES
    2      19  5.33419D-01   5.2849D-03   4.2184D-03  4.265D-02   YES
    3      26  5.33152D-01   4.9976D-04   3.9259D-04  1.461D-02   YES
    4      33  5.33130D-01   4.1577D-05   3.2561D-05  4.323D-03   YES
    5      40  5.33128D-01   3.2902D-06   2.5746D-06  1.224D-03   YES
    6      47  5.33128D-01   2.5647D-07   2.0064D-07  3.423D-04   YES
    7      54  5.33128D-01   1.9907D-08   1.5572D-08  9.542D-05   YES
    8      61  5.33128D-01   1.5432D-09   1.2072D-09  2.657D-05   YES
```

Table F2. ODRPACK Results of ODR Analysis of $\Delta RT_{epistemic}$ Model Equation (continued)

```
*** FINAL SUMMARY FOR FIT BY METHOD OF ODR ***

 --- STOPPING CONDITIONS:
        INFO =     1 ==> SUM OF SQUARES CONVERGENCE.
       NITER =     8          (NUMBER OF ITERATIONS)
        NFEV =    67          (NUMBER OF FUNCTION EVALUATIONS)
       IRANK =     0          (RANK DEFICIENCY)
       RCOND =     1.20D-01   (INVERSE CONDITION NUMBER)
       ISTOP =     0          (RETURNED BY USER FROM SUBROUTINE FCN)

 --- FINAL WEIGHTED SUMS OF SQUARES       =    5.33127879D-01
        SUM OF SQUARED WEIGHTED DELTAS   =    7.67684538D-04
        SUM OF SQUARED WEIGHTED EPSILONS =    5.32360195D-01

 --- RESIDUAL STANDARD DEVIATION          =    1.82539016D-01
        DEGREES OF FREEDOM               =    16

 --- ESTIMATED BETA(J), J = 1, ..., NP:

           BETA        S.D. BETA     ---- 95%  CONFIDENCE INTERVAL ----

 1   1.85530498D+00     2.2706D-01     1.37390691D+00 TO  2.33670305D+00
 2   1.30899017D+02     1.0259D+01     1.09149592D+02 TO  1.52648443D+02

 --- ESTIMATED EPSILON(I) AND DELTA(I,*), I = 1, ..., N:

        I    EPSILON(I,1)      DELTA(I,1)

        1  2.62841903D-01 -1.86361603D-02
        2 -1.29977011D-01  6.95094427D-03
        3 -1.86382404D-01  7.87802505D-03
        4 -3.79012096D-01  1.47415688D-02
        5  2.78865897D-01 -6.56742977D-03
        6  1.68817068D-01 -3.72942044D-03
        7  2.10949482D-01 -4.09035239D-03
        8  1.16154880D-01 -2.15105581D-03
        9  8.71915578D-02 -1.49943300D-03
       10 -3.56507199D-02  6.01915026D-04
       11  8.89342397D-02 -1.29426169D-03
       12  4.68465281D-02 -6.43875329D-04
       13 -7.29122682D-02  9.86768713D-04
       14 -1.41925842D-01  1.83636941D-03
       15  1.97009129D-01 -1.94642622D-03
       16  7.02764840D-02 -6.74910438D-04
       17 -8.73096746D-03  7.78822029D-05
       18 -1.24381318D-01  9.95579717D-04
```

F.1.3. Final Stochastic Model for $\Delta RT_{epistemic}$ in FAVOR

The epistemic uncertainty in $RT_{NDT(u)}$ is estimated in FAVOR by

$$\Delta RT_{epistemic} = RT_{NDT(u)} - RT_{LB} \tag{F14}$$

where $RT_{NDT(u)}$ is the unirradiated reference nil-ductility transition temperature and RT_{LB} is a new temperature index developed for FAVOR analyses. If we assume that $RT_{NDT(u)}$ and RT_{LB} are statistically independent and, therefore, uncorrelated, then the variance of $\Delta RT_{epistemic}$ is

$$\mathrm{var}(\Delta RT_{epistemic}) = \mathrm{var}(RT_{NDT}) + \mathrm{var}(RT_{LB}) \tag{F15}$$

where the $\mathrm{cov}\left(RT_{NDT(u)} RT_{LB}\right)$ has been assumed to be zero. The statistical model developed for $\Delta RT_{epistemic}$ using the ODR procedure contains the following four sources of uncertainty

1. Measurement uncertainty and material variability in $RT_{NDT(u)}$, $\sigma^2_{(1)}$
2. Measurement uncertainty and material variability in RT_{LB} , $\sigma^2_{(2)}$
3. Model uncertainty in $RT_{NDT(u)}$, $\sigma^2_{(3)}$
4. Model uncertainty in RT_{LB} , $\sigma^2_{(4)}$

such that the components of the variances for $RT_{NDT(u)}$ and RT_{LB} are the following:

$$\begin{aligned} \mathrm{var}(RT_{NDT(u)}) &= \sigma^2_{(1)} + \sigma^2_{(3)} \\ \mathrm{var}(RT_{LB}) &= \sigma^2_{(2)} + \sigma^2_{(4)} \end{aligned} \tag{F16}$$

Therefore, the variance (uncertainty) in the ODR-developed Weibull distribution for $\Delta RT_{epistemic}$ can be expressed as

$$\sigma^2_{\Delta RT} = \sigma^2_{(1)} + \sigma^2_{(2)} + \sigma^2_{(3)} + \sigma^2_{(4)} = 4229.69 \tag{F17}$$

As a result of the sampling protocols in FAVOR, the uncertainties associated with sources (1) and (2) have already been accounted for at the point in FAVOR where $\Delta RT_{epistemic}$ is sampled. The Weibull model for $\Delta RT_{epistemic}$ can be revised such that it reflects the uncertainties associated with sources (3) and (4) only, specifically

$$\sigma^2_{\Delta RT(rev)} = \sigma^2_{(3)} + \sigma^2_{(4)} = \sigma^2_{\Delta RT} - \sigma^2_{(1)} - \sigma^2_{(2)} \tag{F18}$$

Two cases were examined:

Case 1:

$$\sigma_{(1)}^2 = (23°\text{F})^2$$
$$\sigma_{(2)}^2 = 0$$

Case 2:

$$\sigma_{(1)}^2 = (23°\text{F})^2$$
$$\sigma_{(2)}^2 = (23°\text{F})^2$$

The required adjustments to the Weibull model for $\Delta RT_{epistemic}$ can be calculated by solving the following nonlinear system of equations

$$\begin{aligned} \mu_{\Delta RT} - a - b\Gamma\left(1+\frac{1}{c}\right) &= 0 \\ \sigma_{\Delta RT(rev)}^2 - b^2\left[\Gamma\left(1+\frac{2}{c}\right) - \Gamma^2\left(1+\frac{1}{c}\right)\right] &= 0 \end{aligned} \tag{F19}$$

for the new parameters b and c, where $\mu_{\Delta RT} = 70.67$ °F and the location parameter for the ODR-developed model, a = -45.586 °F, remain fixed. Equations (F19) are the asymptotic relations for the mean and variance of a Weibull distribution.

Case 1:

$$\sigma_{\Delta RT(rev)}^2 = \sigma_{\Delta RT}^2 - \sigma_{(1)}^2 - \sigma_{(2)}^2$$
$$\sigma_{\Delta RT(rev)}^2 = 4229.692 - 23^2 - 0 = 3700.692$$
$$\sigma_{\Delta RT(rev)} = 60.83 \text{ °F}$$

The solutions for (b,c) are

$$b = 131.18 \text{ °F}$$
$$c = 1.998$$

Case 2:

$$\sigma^2_{\Delta RT(rev)} = \sigma^2_{\Delta RT} - \sigma^2_{(1)} - \sigma^2_{(2)}$$
$$\sigma^2_{\Delta RT(rev)} = 4229.692 - 23^2 - 23^2 = 3171.692$$
$$\sigma_{\Delta RT(rev)} = 56.32\ °\text{F}$$

The solutions for (b,c) are

$$b = 131.27\ °\text{F}$$
$$c = 2.177$$

See Fig. F2 for a comparison of the ODR-derived model with the revised models of Cases 1 and 2. Figure F3 compares the CDF of the initial Weibull model to that of Case 2 with emphasis placed on the lower-left tail. Note that Case 2 produces a more negative $\Delta RT_{epistemic}$ adjustment than the initial model for cumulative probabilities less than approximately 3.5%. A comparison between the ODR-derived model and Case 2 is shown in Fig. F4. For cumulative probabilities less than approximately 60%, Case 2 produces more positive values of $\Delta RT_{epistemic}$ than the ODR model.

In summary the revised Weibull models for Cases (1) and (2) are:

Summary:

Case 1:

$$\Delta RT_{(rev)} = -45.586 + 131.18\left[-\ln\left(1-P\right)\right]^{\frac{1}{1.998}}; \quad 0 < P < 1$$

Case 2:

$$\Delta RT_{(rev)} = -45.586 + 131.27\left[-\ln\left(1-P\right)\right]^{\frac{1}{2.177}}; \quad 0 < P < 1$$

Case 2 was selected for implementation into FAVOR.

F.2. Stochastic Model for ΔRT_{arrest} in FAVOR

F.2.1 Initial Model for ΔRT_{arrest}

The initial stochastic model developed for FAVOR to describe the statistical distribution of $\Delta RT_{arrest} = T_0 - T_{K_{Ia}}$ was based on a lognormal distribution (see Fig. F5) with the parameters

$$\begin{aligned} &\overline{\Delta RT}_{arrest} = \mu(T_0) = 44.123\exp(-0.006\,T_0); \quad T_0[°c] \\ &\sigma_{\log}^2 = 0.39^2 = 0.1521 \text{ (constant)} \end{aligned} \tag{F20}$$

The asymptotic relations for the log-mean and variance of the model are:

$$\begin{aligned} &\mu_{\log}(T_0) = \ln\left[\mu(T_0)\right] - \frac{\sigma_{\log}^2}{2} \\ &\mathrm{var}(\Delta RT_{arrest}) = \sigma^2(T_0) = \omega(\omega-1)\exp\left[2\mu_{\log}(T_0)\right]; \quad \omega = \exp(\sigma_{\log}^2) \end{aligned} \tag{F21}$$

The initial model was derived from an ordinary least squares regression analysis using the log-transformed data shown in Table F3.

F.2.2 Model Developed Using Orthogonal Distance Regression (ODR)

The ORDPACK program was used to reanalyze the following model equation

$$\ln(\overline{\Delta RT}_{arrest}) = \beta_1 T_0 + \beta_2 \tag{F22}$$

where, upon reversing the log-transformation, the mean value for ΔRT_{arrest} is

$$\overline{\Delta RT}_{arrest} = \exp(\beta_2)\exp\left(\beta_1 T_0\right) \tag{F23}$$

The results of the ODR analysis are presented in Table F4 with the following ODR estimates for the model parameters:

$$\begin{aligned} &\beta_1 = -0.00597110744 \pm 0.00082458 \\ &\beta_2 = 3.78696343 \pm 0.065299 \\ &\exp(\beta_2) = 44.12221645 \pm 2.908036613 \\ \\ &\overline{\Delta RT}_{arrest} = 44.1222\exp(-0.00597T_0); \quad [°\mathrm{C}] \\ &\sigma_{\log} = 0.389987535; \quad \sigma_{\log}^2 = 0.1520903 \end{aligned} \tag{F24}$$

Table F3. Data Used in the Development of the ΔRT_{arrest} Model

N	T_0 (°C)	T_{KIa} (°C)	T_{KIa}-T_0 (°C)	ln(T_{KIa}-T_0)
1	-114	16	130	4.8675
2	131	140	9	2.1972
3	-66	13	79	4.3694
4	-78	6	84	4.4308
5	-104	-16	88	4.4773
6	-108	44	152	5.0239
7	43	113	70	4.2485
8	-20	60	80	4.3820
9	-71	-41	30	3.4012
10	-66	6	72	4.2767
11	-84	9	93	4.5326
12	-21	65	86	4.4543
13	-53	-6	47	3.8501
14	-54	18	72	4.2767
15	62	93	31	3.4340
16	-65	-12	53	3.9703
17	-100	-15	85	4.4427
18	-130	-8	122	4.8040
19	-100	-18	82	4.4067
20	-27	25	52	3.9512
21	-78	10	88	4.4773
22	-115	-25	90	4.4998
23	-68	-9	59	4.0775
24	-70	17	87	4.4659
25	-65	-25	40	3.6889
26	-51	19	70	4.2485
27	17	77	60	4.0943
28	-48	48	96	4.5643
29	-92	-26	66	4.1897
30	-70	-18	52	3.9512
31	-81	-20	61	4.1109
32	-157	-27	130	4.8675
33	67	78	11	2.3979
34	-84	9	93	4.5326
35	-67	18	85	4.4427
36	-58	-14	44	3.7842
37	35	74	39	3.6636
38	39	67	28	3.3322
39	-61	-15	46	3.8286
40	6	62	56	4.0254
41	-61	-16	45	3.8067
42	-48	8	56	4.0254
43	-24	32	56	4.0254
44	-19	10	29	3.3673
45	-85	-33	52	3.9512
46	-131	-26	105	4.6540
47	-3	33	36	3.5835
48	-95	-62	33	3.4965
49	-93	-17	76	4.3307
50	-68	-8	60	4.0943
51	184	220	36	3.5835
52	42	71	29	3.3673
53	27	68	41	3.7136

Table F4. ODRPACK Results of ODR Analysis of ΔRT_{arrest} Model Equation

```
*******************************************************
* ODRPACK VERSION 2.01 OF 06-19-92 (DOUBLE PRECISION) *
*******************************************************

    ODR Analysis of DARTarrest Lognormal Model

   BETA(1) = slope
   BETA(2) = intercept of log-transformed data

   LN(DRTarrest) = BETA(1)*T0 + BETA(2)

   DRTArrest = EXP(BETA(2))*EXP(BETA(1)*T0)


*** DERIVATIVE CHECKING REPORT FOR FIT BY METHOD OF ODR ***


    FOR RESPONSE  1 OF OBSERVATION     1

                              USER
                          SUPPLIED     RELATIVE    DERIVATIVE
       DERIVATIVE WRT        VALUE   DIFFERENCE    ASSESSMENT

            BETA(  1)    -1.57D+02     4.25D-07    VERIFIED
            BETA(  2)     1.00D+00     7.87D-08    VERIFIED
         DELTA( 1, 1)    -5.84D-03     4.30D-07    VERIFIED

    NUMBER OF RELIABLE DIGITS IN FUNCTION RESULTS          16
       (ESTIMATED BY ODRPACK)

    NUMBER OF DIGITS OF AGREEMENT REQUIRED BETWEEN
    USER SUPPLIED AND FINITE DIFFERENCE DERIVATIVE FOR
    USER SUPPLIED DERIVATIVE TO BE CONSIDERED VERIFIED      4

    ROW NUMBER AT WHICH DERIVATIVES WERE CHECKED            1

      -VALUES OF THE EXPLANATORY VARIABLES AT THIS ROW

         X( 1, 1)  -1.57000000D+02
*******************************************************
* ODRPACK VERSION 2.01 OF 06-19-92 (DOUBLE PRECISION) *
*******************************************************


*** INITIAL SUMMARY FOR FIT BY METHOD OF ODR ***

--- PROBLEM SIZE:
           N =    53          (NUMBER WITH NONZERO WEIGHT =    53)
          NQ =     1
           M =     1
          NP =     2          (NUMBER UNFIXED =     2)

--- CONTROL VALUES:
         JOB = 00020
             = ABCDE, WHERE
                      A=0 ==> FIT IS NOT A RESTART.
                      B=0 ==> DELTAS ARE INITIALIZED TO ZERO.
                      C=0 ==> COVARIANCE MATRIX WILL BE COMPUTED USING
                              DERIVATIVES RE-EVALUATED AT THE SOLUTION.
                      D=2 ==> DERIVATIVES ARE SUPPLIED BY USER.
                              DERIVATIVES WERE CHECKED.
                              RESULTS APPEAR CORRECT.
                      E=0 ==> METHOD IS EXPLICIT ODR.
      NDIGIT =    16          (ESTIMATED BY ODRPACK)
      TAUFAC =     1.00D+00
```

Table F4. ODRPACK Results of ODR Analysis of ΔRT_{arrest} Model Equation (continued)

```
--- STOPPING CRITERIA:
       SSTOL =     1.49D-08   (SUM OF SQUARES STOPPING TOLERANCE)
      PARTOL =     3.67D-11   (PARAMETER STOPPING TOLERANCE)
       MAXIT =    50          (MAXIMUM NUMBER OF ITERATIONS)

--- INITIAL WEIGHTED SUM OF SQUARES        =   7.76381810D+00
        SUM OF SQUARED WEIGHTED DELTAS     =   0.00000000D+00
        SUM OF SQUARED WEIGHTED EPSILONS   =   7.76381810D+00

*** ITERATION REPORTS FOR FIT BY METHOD OF ODR ***


        CUM.                 ACT. REL.   PRED. REL.
 IT.  NO. FN     WEIGHTED   SUM-OF-SQS   SUM-OF-SQS              G-N
NUM.   EVALS   SUM-OF-SQS    REDUCTION    REDUCTION  TAU/PNORM  STEP
----  ------  -----------  -----------  -----------  ---------  ----

   1      15  7.75660D+00   9.2916D-04   9.2766D-04  3.063D-02   YES
   2      16  7.75660D+00   1.7592D-08   1.7540D-08  5.224D-05   YES
   3      17  7.75660D+00   6.0973D-13   6.0818D-13  1.064D-06   YES


*** FINAL SUMMARY FOR FIT BY METHOD OF ODR ***

--- STOPPING CONDITIONS:
        INFO =     1 ==> SUM OF SQUARES CONVERGENCE.
       NITER =     3          (NUMBER OF ITERATIONS)
        NFEV =    17          (NUMBER OF FUNCTION EVALUATIONS)
        NJEV =     4          (NUMBER OF JACOBIAN EVALUATIONS)
       IRANK =     0          (RANK DEFICIENCY)
       RCOND =     1.02D-01   (INVERSE CONDITION NUMBER)
       ISTOP =     0          (RETURNED BY USER FROM SUBROUTINE FCN)

--- FINAL WEIGHTED SUMS OF SQUARES       =    7.75660416D+00
        SUM OF SQUARED WEIGHTED DELTAS   =    2.76544656D-04
        SUM OF SQUARED WEIGHTED EPSILONS =    7.75632762D+00

--- RESIDUAL STANDARD DEVIATION          =    3.89987535D-01
        DEGREES OF FREEDOM               =   51

--- ESTIMATED BETA(J), J = 1, ..., NP:

            BETA          S.D. BETA     ---- 95%  CONFIDENCE INTERVAL ----

   1  -5.97110744D-03     8.2458D-04    -7.62651413D-03 TO -4.31570076D-03
   2   3.78696343D+00     6.5299D-02     3.65587019D+00 TO  3.91805666D+00
   2a  44.1222164         1.06747815    38.70118385     TO 50.30259469
```

Table F4. ODRPACK Results of ODR Analysis of ΔRT_{arrest} Model Equation (continued)

```
--- ESTIMATED EPSILON(I) AND DELTA(I,*), I = 1, ..., N:

        I    EPSILON(I,1)      DELTA(I,1)

        1 -1.43102053D-01 -8.54477100D-04
        2 -8.47788261D-02 -5.06223103D-04
        3 -2.40805066D-01 -1.43787185D-03
        4 -2.61679548D-02 -1.56251554D-04
        5 -3.99850519D-01 -2.38754864D-03
        6 -5.92016383D-01 -3.53499080D-03
        7 -6.93757401D-02 -4.14249691D-04
        8 -5.85749970D-02 -3.49757341D-04
        9 -2.26442691D-02 -1.35211263D-04
       10  8.57680493D-01  5.12129857D-03
       11  1.15426669D-02  6.89224532D-05
       12  1.46645341D-01  8.75634434D-04
       13  3.43251602D-01  2.04959067D-03
       14 -2.44054340D-01 -1.45727360D-03
       15 -2.44054340D-01 -1.45727360D-03
       16  1.59743570D-01  9.53845309D-04
       17 -1.78100642D-01 -1.06345728D-03
       18 -2.24618999D-01 -1.34122318D-03
       19  8.09685804D-01  4.83471734D-03
       20 -2.60957867D-01 -1.55820631D-03
       21  2.53688183D-01  1.51479827D-03
       22  1.15457172D-01  6.89406666D-04
       23  9.86506532D-02  5.89053212D-04
       24 -2.55614517D-01 -1.52630061D-03
       25 -1.88384618D-01 -1.12486396D-03
       26 -9.56061927D-02 -5.70874424D-04
       27  2.04786195D-01  1.22279946D-03
       28  4.86188622D-01  2.90308234D-03
       29  3.22548084D-01  1.92596784D-03
       30  3.44526207D-01  2.05720147D-03
       31  3.49085578D-01  2.08442594D-03
       32 -1.67256927D-01 -9.98708341D-04
       33  2.53275489D-01  1.51233403D-03
       34 -1.56999738D-01 -9.37461609D-04
       35 -4.90754110D-01 -2.93034334D-03
       36  4.82231733D-02  2.87945535D-04
       37 -3.06028247D-03 -1.82732618D-05
       38 -9.50782960D-02 -5.67722299D-04
       39 -5.41971290D-01 -3.23616640D-03
       40 -4.75624102D-01 -2.84000050D-03
       41  5.33099631D-01  3.18319281D-03
       42  2.21349919D-01  1.32170317D-03
       43 -2.74205133D-01 -1.63730709D-03
       44 -4.08875384D-01 -2.44143703D-03
       45 -8.78254100D-02 -5.24414570D-04
       46 -8.55839285D-02 -5.11030452D-04
       47  2.21877816D-01  1.32485529D-03
       48  1.68875063D-01  1.00837040D-03
       49 -7.18263826D-01 -4.28882729D-03
       50 -1.72318244D-02 -1.02892998D-04
       51  9.88968694D-01  5.90523394D-03
       52  8.07494984D-01  4.82163573D-03
       53 -8.95207363D-01 -5.34537537D-03
```

Comparison of Eqs. (F20) with Eqs. (F24) indicates that the ODR analysis produced essentially the same model as resulted from the ordinary least squares analysis (see Fig. F6).

F.2.3 Final Model for ΔRT_{arrest}

The variance of $\Delta RT_{arrest} = T_0 - T_{K_{Ia}}$ is

$$\mathrm{var}(\Delta RT_{arrest}) = \mathrm{var}(T_0) + \mathrm{var}(T_{K_{Ia}}) - 2\,\mathrm{cov}(T_0 T_{K_{Ia}}) \tag{F25}$$

In the absence of data to the contrary, we assume the statistical independence of T_0 and T_{KIa} such that $\mathrm{cov}(T_0 T_{K_{Ia}}) = 0$, and Eq. (F25) becomes

$$\mathrm{var}(\Delta RT_{arrest}) = \mathrm{var}(T_0) + \mathrm{var}(T_{K_{Ia}}) \tag{F26}$$

The variance of both the initial and ODR lognormal model is a decreasing function of increasing T_0

$$\begin{aligned}\mathrm{var}(\Delta RT_{arrest(ODR)}) &= \sigma^2_{ODR}(T_0) \\ &= \exp(0.38998^2)\times\left[\exp(0.38998^2)-1\right]\times\exp\left[2\ln\left[\mu(T_0)\right]-0.38998^2\right]\end{aligned} \tag{F27}$$

as shown in Fig. F7. By $T_0 \approx$ 56 °C, $\mathrm{var}(\Delta RT_{arrest}) = (12.78\ ^\circ\mathrm{C})^2$.

The variance for T_0 has been accounted for in a separate sampling protocol prior to the sampling of ΔRT_{arrest}, and the statistical model for ΔRT_{arrest} should, therefore, reflect only the remaining variance in $T_{K_{Ia}}$. If we assume that the $\mathrm{var}(T_0) = (23\,^\circ\mathrm{F})^2 = (12.778\ ^\circ\mathrm{C})^2$, then

$$\begin{aligned}&\mathrm{var}(\Delta RT_{arrest(rev)}) = \mathrm{var}(T_{K_{Ia}}) = \mathrm{var}(\Delta RT_{arrest}) - \mathrm{var}(T_0) \\ &\mathrm{var}(\Delta RT_{arrest(rev)}) = \sigma^2_{rev}(T_0) = \\ &\left\{\exp(0.38998^2)\times\left[\exp(0.38998^2)-1\right]\times\exp\left[2\mu_{\log}(T_0)\right]\right\} - \mathrm{var}(T_0) = \\ &\qquad \exp\left[\sigma^2_{\log}(T_0)_{rev}\right]\times\left\{\exp\left[\sigma^2_{\log}(T_0)_{rev}\right]-1\right\}\times\exp\left[2\mu_{\log}(T_0)_{rev}\right]\end{aligned} \tag{F28}$$

where

$$\mu_{\log}(T_0)_{rev} = \ln\left[\mu(T_0)\right] - \frac{\sigma^2_{\log}(T_0)_{rev}}{2}$$

and $\mu(T_0)$ remains a fixed function of T_0. Solving Eq. (F28) for $\sigma^2_{\log}(T_0)_{rev}$ results in

$$\sigma^2_{\log}(T_0)_{rev} = \ln\left\{\exp\left[0.38998^2 + 2\ln(\mu(T_0)\right] - \mathrm{var}(T_0)\right\} - 2\ln\left[\mu(T_0)\right] \tag{F29}$$

and solving for $\mathrm{var}(\Delta RT_{arrest(rev)}) = \sigma^2(T_0)_{rev}$ gives

$$\sigma^2(T_0)_{rev} = \exp\left[\sigma^2_{\log}(T_0)_{rev}\right] \times \left\{\exp\left[\sigma^2_{\log}(T_0)_{rev}\right] - 1\right\} \times \exp\left\{2\ln\left[\mu(T_0)\right] - \sigma^2_{\log}(T_0)_{rev}\right\} \tag{F30}$$

However, as noted earlier and indicated in Fig. F7, at $T_0 \approx 56$ °C, $\mathrm{var}(\Delta RT_{arrest}) = \mathrm{var}(T_0) = (12.78\ °\mathrm{C})^2$ which would produce $\sigma^2(T_0)_{rev} = 0$. In order to prevent a nonphysical zero variance at this point, the assumed constant value of $\mathrm{var}(T_0)$ can be replaced by the following function with a transition region:

$$\mathrm{var}(T_0) = \begin{cases} (12.778)^2 & \text{for } T_0 < -35.7\ °\mathrm{C} \\ 99.905972 - 1.7748073T_0 & \text{for } -35.7\ °\mathrm{C} \le T_0 \le 56\ °\mathrm{C} \\ 0 & \text{for } T_0 > 56\ °\mathrm{C} \end{cases} \tag{F31}$$

Figure F7 plots Eq. (F30) as the final model variance with Eq. (F31) used in Eq. (F29) to produce the final log-variance as a function of T_0. Figure F8 compares the 1% and 99% percentiles of the ODR and final models for ΔRT_{arrest}.

<u>Summary of Stochastic Model for ΔRT_{arrest}</u>

The lognormal model for ΔRT_{arrest} is, therefore,

$$\begin{aligned} &\overline{\Delta RT}_{arrest} = \mu(T_0) = 44.122\exp(-0.005971T_0); \quad T_0[°\mathrm{C}] \\ &\sigma_{\log}(T_0)_{rev} = \sqrt{\ln\left\{\exp\left[0.38998^2 + 2\ln(\mu(T_0)\right] - \mathrm{var}\left(T_0\right)\right\} - 2\ln\left[\mu(T_0)\right]} \\ &\text{where} \\ &\mathrm{var}(T_0) = \begin{cases} (12.778)^2 & \text{for } T_0 < -35.7\ °\mathrm{C} \\ 99.905972 - 1.7748073T_0 & \text{for } -35.7\ °\mathrm{C} \le T_0 \le 56\ °\mathrm{C} \\ 0 & \text{for } T_0 > 56\ °\mathrm{C} \end{cases} \end{aligned} \tag{F32}$$

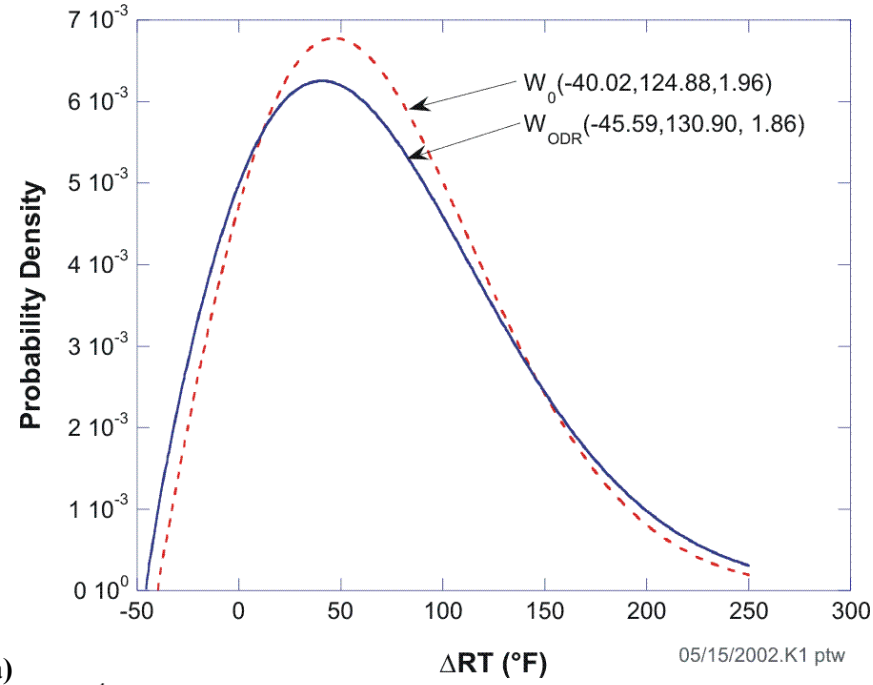

(a)

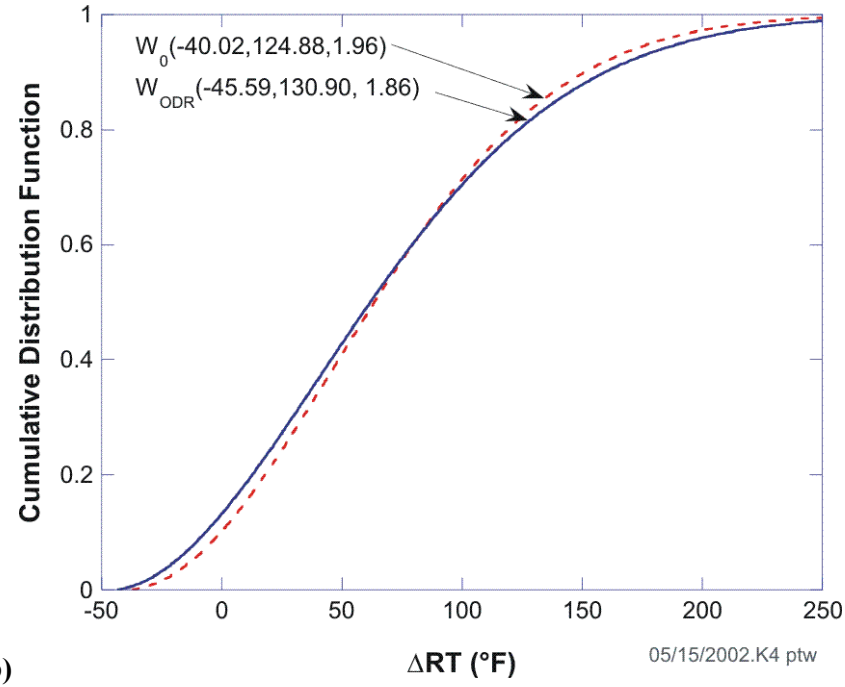

(b)

Fig. F1. Comparison of the initial Weibull model, W_0, for $\Delta RT_{epistemic}$ with the ODR model: (a) probability density functions and (b) cumulative distribution functions.

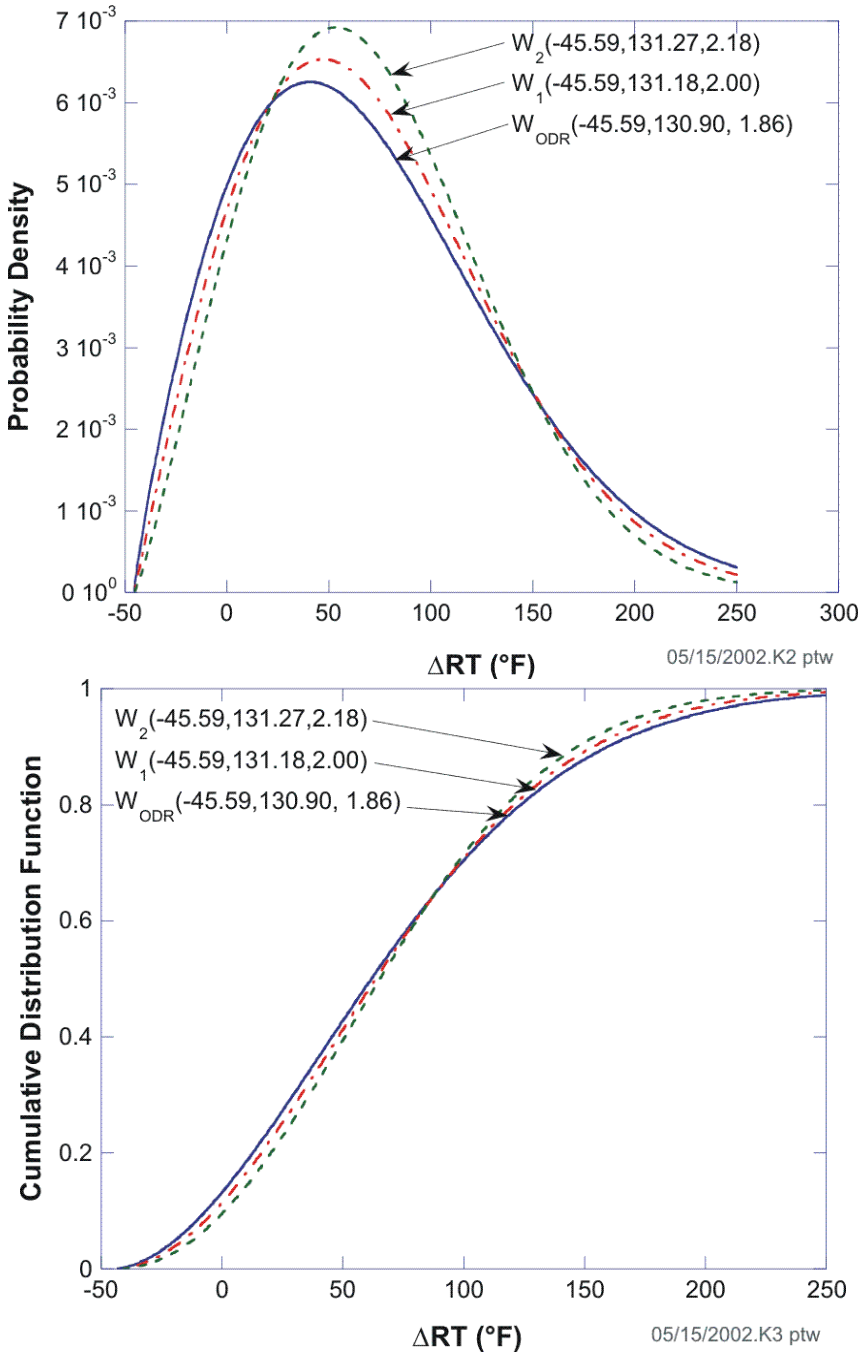

Fig. F2. Comparison of ODR Weibull model, W_{ODR}, for $\Delta RT_{epistemic}$ with the models for Case 1 (W_1) and Case 2 (W_2): (a) probability density functions and (b) cumulative distribution functions.

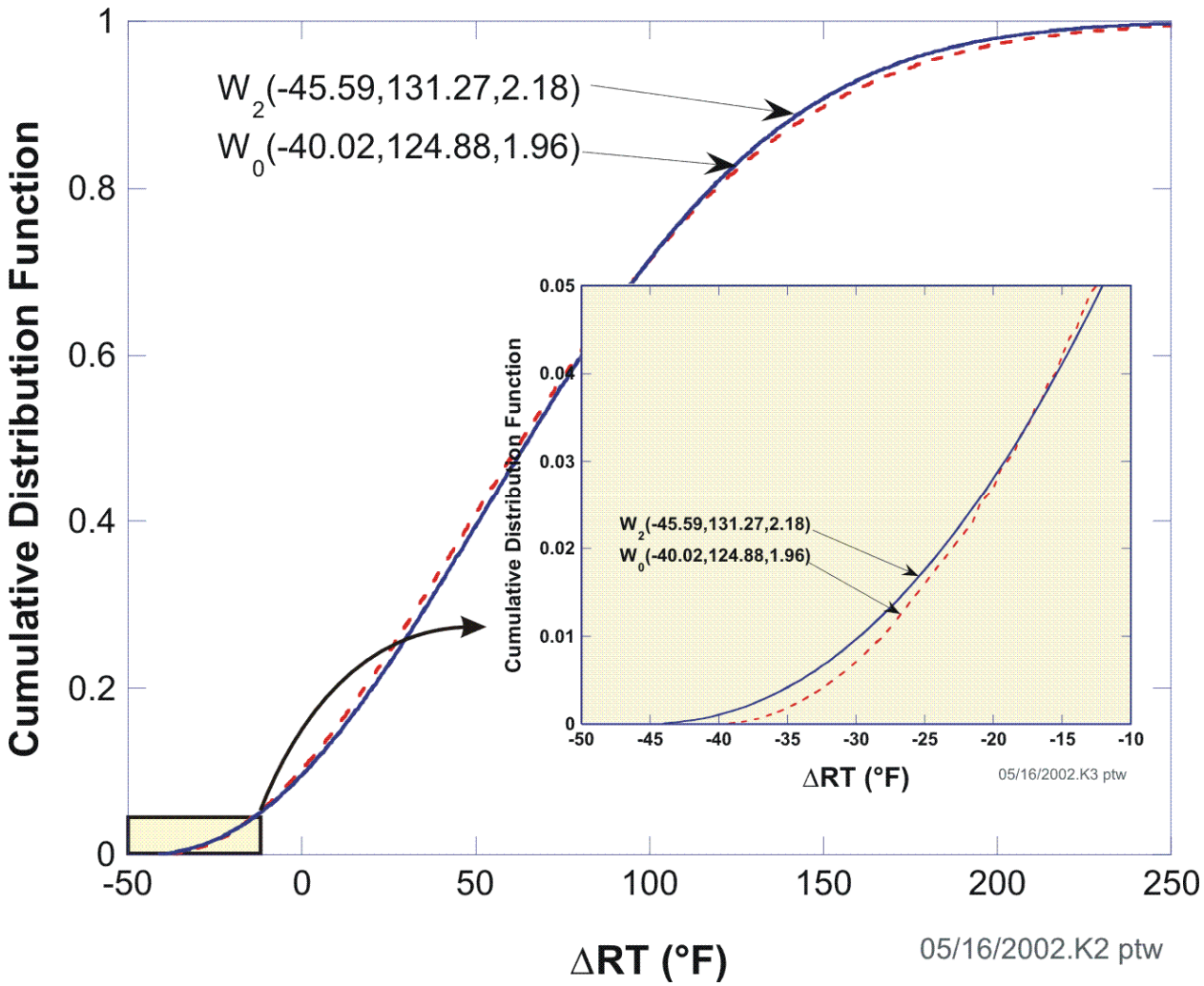

Fig. F3. Comparison of initial model in FAVOR, W_0, with Case 2, W_2.

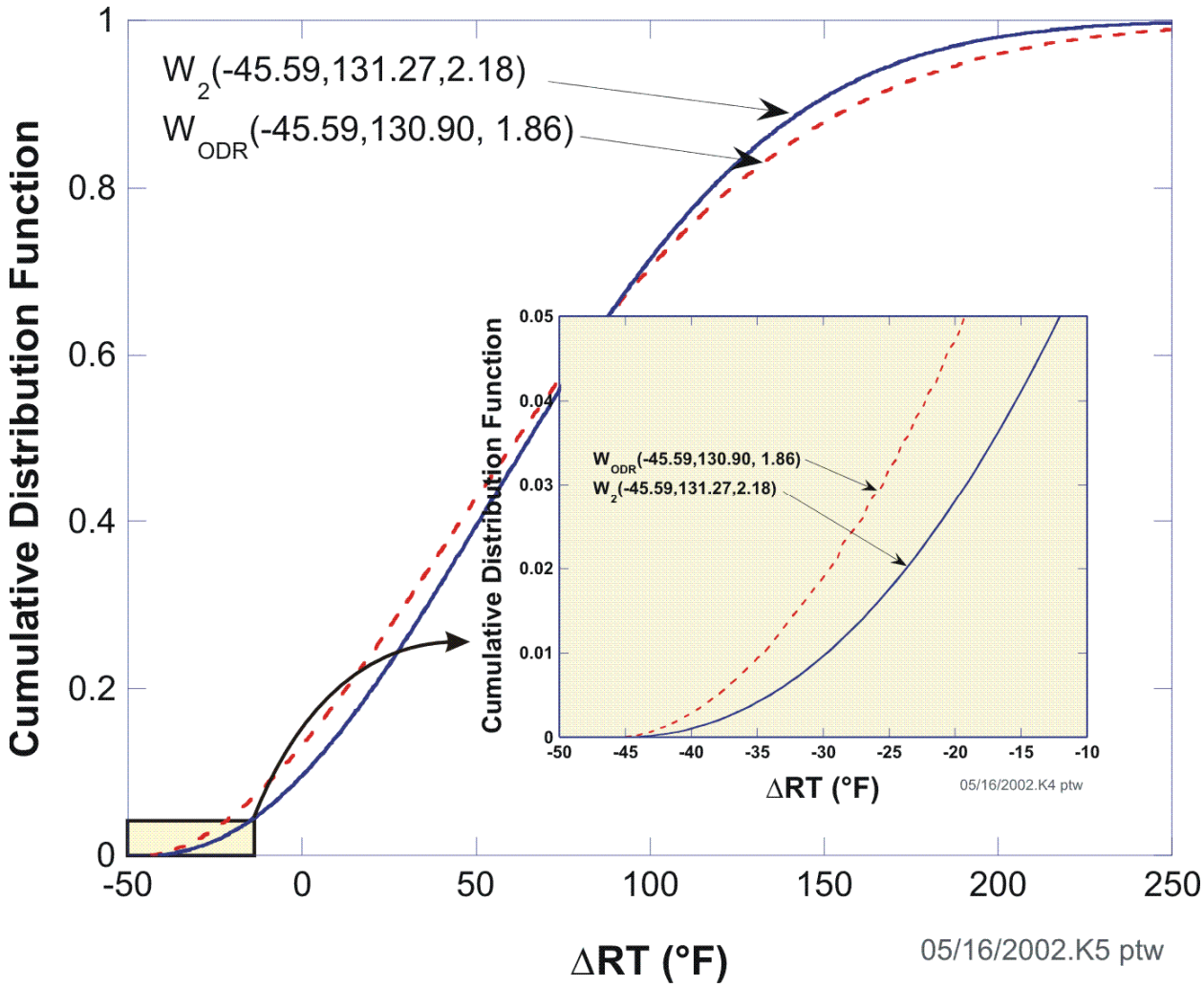

Fig. F4. Comparison of ODR model, W_{ODR}, with Case 2, W_2.

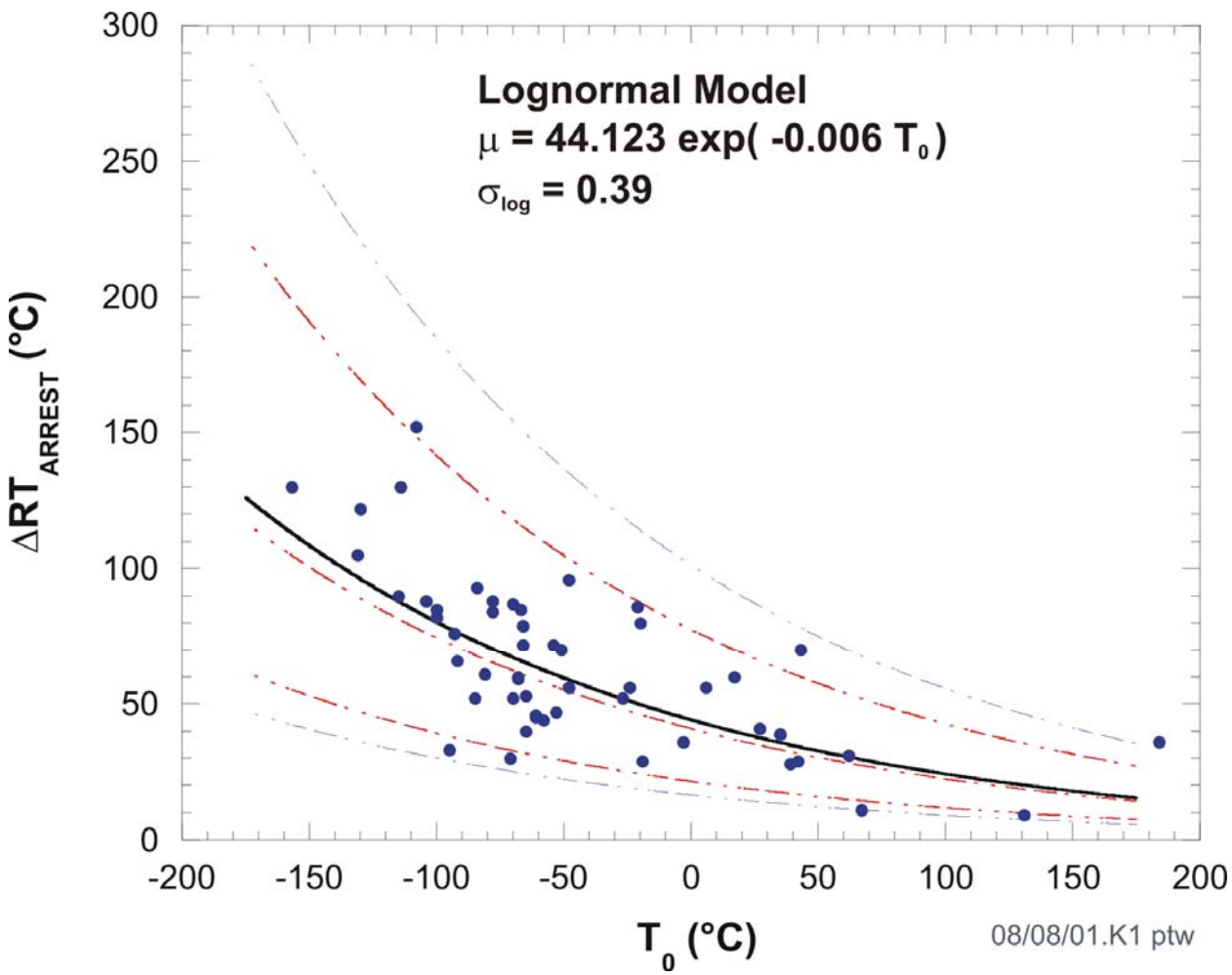

Fig. F5. Data used to develop the lognormal statistical model for ΔRT_{arrest} as a function of T_0.

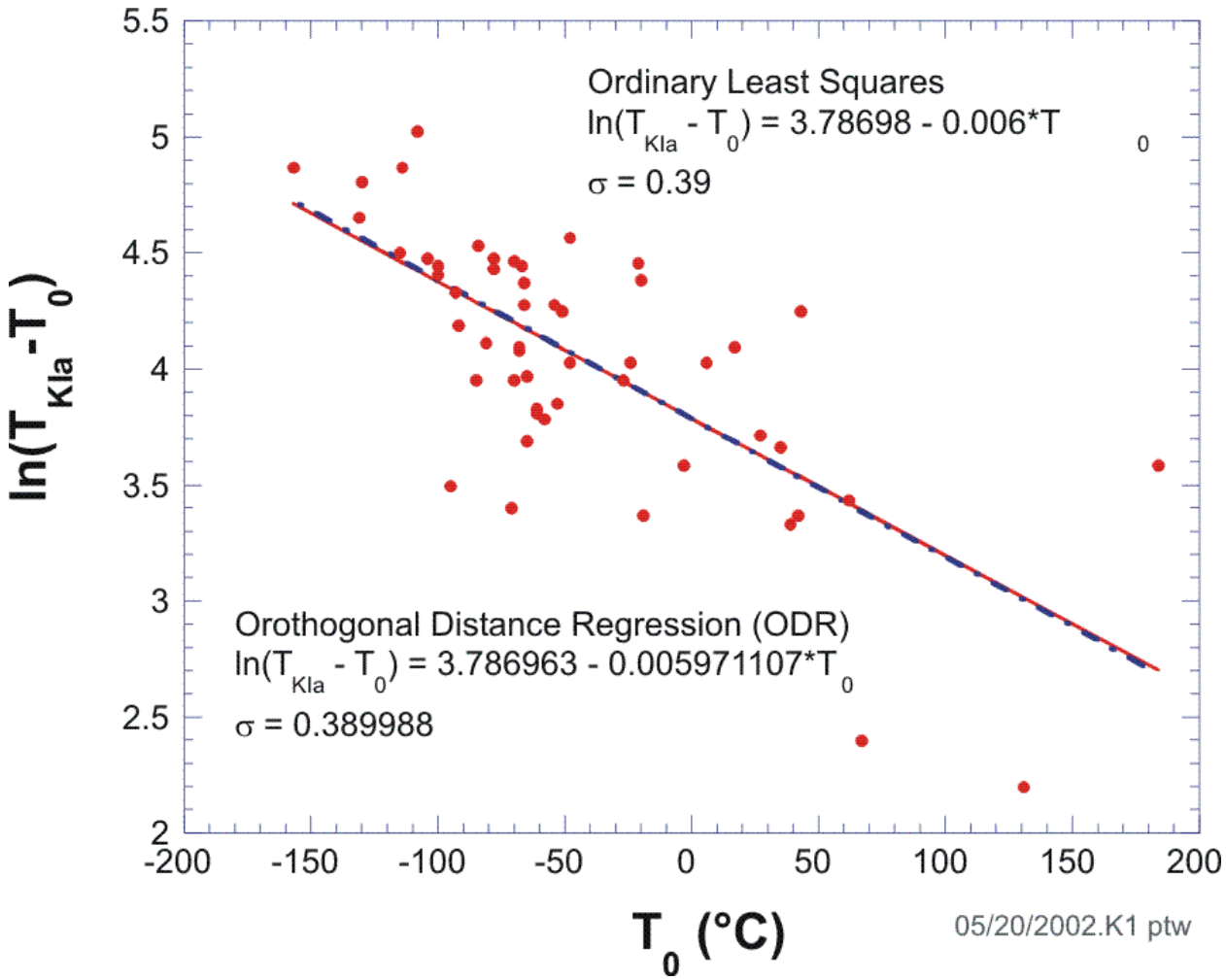

Fig. F6. Model developed from ODR analysis of log-transformed data.

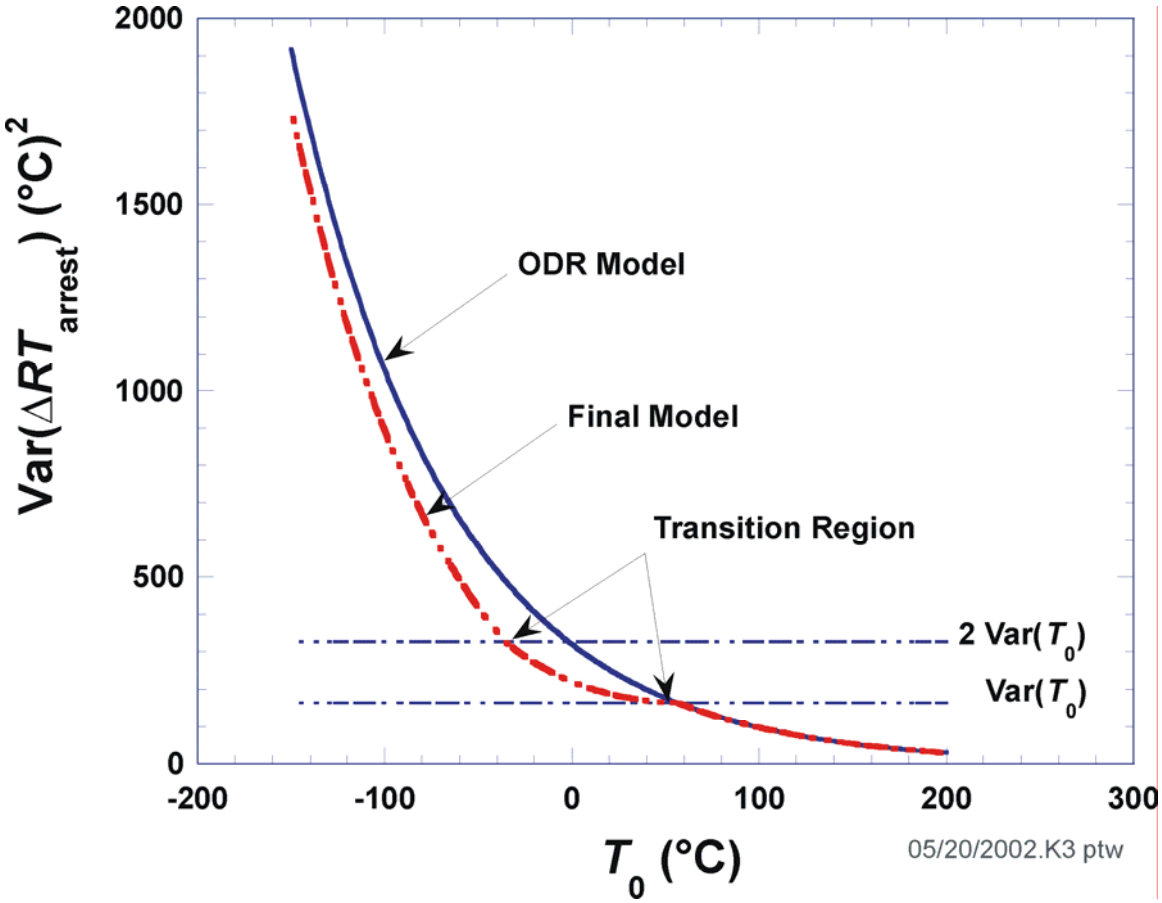

Fig. F7. Variance of ODR model compared to final model.

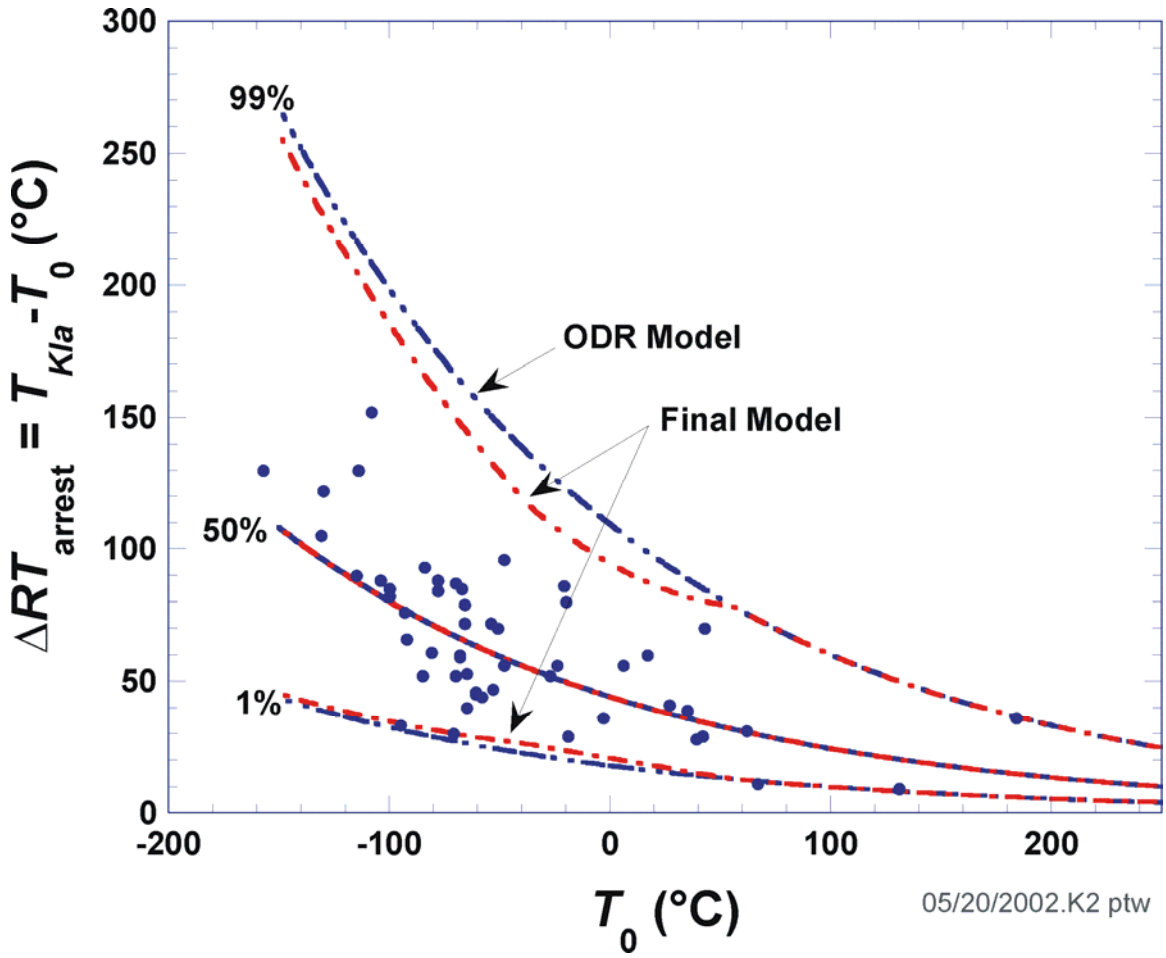

Fig. F8. Comparison of ODR model with final model.

REFERENCES

F1. P. T. Boggs, R. H. Byrd, J. E. Rogers, R. B. Schnabel, *User's Reference Guide for ODRPACK Version 2.01: Software for Weighted Orthogonal Distance Regression*, NISTIR 92-4834, National Institute of Standards and Technology, Gaithersburg, MD, 1992.

F2. P. T. Boggs and J. E. Rogers, "The Computation and Use of the Asymptotic Covariance Matrix for Measurement Error Models," Internal Report 89-4102, Applied and Computational Mathematics Division, National Institute of Standards and Technology, Gaithersburg, MD, 1990.

NRC FORM 335
(2-89)
NRCM 1102,
3201,3202

U.S. NUCLEAR REGULATORY COMMISSION

BIBLIOGRAPHIC DATA SHEET

(See instructions on the reverse)

1. REPORT NUMBER
(Assigned by NRC, Add Vol., Supp., Rev., and Addendum Numbers, if anv.1

NUREG/CR-6854
ORNL/TM-2004/244

2. TITLE AND SUBTITLE

Fracture Analysis of Vessels – Oak Ridge (FAVOR, v04.1):
Theory and Implementation of Algorithms, Methods, and Correlations

3. DATE REPORT PUBLISHED

MONTH	YEAR
	2006

4. FIN OR GRANT NUMBER
Y6533

5. AUTHOR(S)

P. T. Williams, T. L. Dickson, and S. Yin

6. TYPE OF REPORT
Final, technical

7. PERIOD COVERED *(Inclusive Dates)*

8. PERFORMING ORGANIZATION - NAME AND ADDRESS *(If NRC, provide Division, Office or Region, U.S. Nuclear Regulatory Commission, and mailing address; if contractor, provide name and mailing address.)*

Heavy Section Steel Technology Program
Oak Ridge National Laboratory
P. O. Box 2008, Mail Stop 6085
Oak Ridge, TN 37831-6085

9. SPONSORING ORGANIZATION - NAME AND ADDRESS *(If NRC, type "Same as above"; if contractor, provide NRC Division, Office or Region, U.S. Nuclear Regulatory Commission, and mailing address.)*

Division of Fuel, Engineering, and Radiological Research
Office of Nuclear Regulatory Research
U. S. Nuclear Regulatory Commission
Washington, DC 2055-0001

10. SUPPLEMENTARY NOTES

1 1. ABSTRACT *(200 words or less)*

The current regulations to insure that nuclear reactor pressure vessels (RPVs) maintain their structural integrity when subjected to transients such as pressurized thermal shock (PTS) events were derived from computational models developed in the early-to-mid 1980s. Since that time, advancements and refinements in relevant technologies that impact RPV integrity assessment have led to an effort by the NRC to re-evaluate its PTS regulations. Updated computational methodologies have been developed through interactions between experts in the relevant disciplines of thermal hydraulics, probabilistic risk assessment, materials embrittlement, fracture mechanics, and inspection (flaw characterization). Contributors to the development of these methodologies include the NRC staff, their contractors, and representatives from the nuclear industry. These updated methodologies have been integrated into the Fracture Analysis of Vessels – Oak Ridge (FAVOR, v04.1) computer code developed for the NRC by the Heavy Section Steel Technology (HSST) program at Oak Ridge National Laboratory (ORNL). The FAVOR, v04.1, code represents the baseline NRC-selected applications tool for re-assessing the current PTS regulations. This report is intended to document the technical bases for the assumptions, algorithms, methods, and correlations employed in the development of the FAVOR, v04.1, code.

12. KEY WORDS/DESCRIPTORS *(List words or phrases that will assist researchers in locating the report.)*

pressurized thermal shock, probabilistic fracture mechanics, reactor pressure vessels

13. AVAILABILITY STATEMENT
unlimited

14. SECURITY CLASSIFICATION
(This Page)
unclassified
(This Report)
unclassified

15. NUMBER OF PAGES

16. PRICE